



Faculteit Farmaceutische Wetenschappen

PHOTOBLEACHING WITH THE CONFOCAL LASER  
SCANNING MICROSCOPE FOR MOBILITY MEASUREMENTS  
AND THE ENCODING OF MICROBEADS

FOTOBLEKING MET DE CONFOCALE LASER  
SCANNING MICROSCOOP VOOR MOBILITEITSMETINGEN  
EN HET CODEREN VAN MICROSFEREN

**Lic. Kevin Braeckmans**

Thesis submitted in fulfillment of the requirements for the degree of  
Doctor in Pharmaceutical Sciences

Proefschrift voorgedragen tot het bekomen van de graad van  
Doctor in de Farmaceutische Wetenschappen

**2004**

**Decaan**

Prof. dr. apr. Jean-Paul Remon

**Promotoren**

Prof. dr. apr. Joseph Demeester

Prof. dr. apr. Stefaan De Smedt

The author and the promoters give the authorization to consult and to copy parts of this thesis for personal use only. Any other use is limited by the laws of copyright, especially concerning the obligation to refer to the source whenever results from this thesis are cited.

De auteur en de promotoren geven de toelating dit proefschrift voor consultatie beschikbaar te stellen en delen ervan te kopiëren voor persoonlijk gebruik. Elk ander gebruik valt onder de beperkingen van het auteursrecht, in het bijzonder met betrekking tot de verplichting uitdrukkelijk de bron te vermelden bij het aanhalen van resultaten uit dit proefschrift.

Gent, 14 April 2004

De auteur

De promotoren

Lic. Kevin Braeckmans

Prof. dr. apr. J. Demeester

Prof. dr. apr. S. De Smedt

# Voor- en dankwoord

Zo lang als ik me kan herinneren heb ik steeds het verlangen gevoeld om te zoeken naar het waarom van de dingen, naar waarheid. Ongetwijfeld is het ditzelfde verlangen dat aan de basis ligt van mijn uitgesproken interesse voor natuurkunde. Van alle takken van de wetenschap is het immers de natuurkunde die tracht door te dringen tot de meest fundamentele wetten die aan de basis van deze schepping liggen. Een eerste voeling met deze wetten kwam echter pas bij het uitvoeren van mijn licentiaatsthesis. Het was toen dat ik het plezier ontdekte om enerzijds een verklaring te zoeken voor wetenschappelijke waarnemingen en anderzijds deze kennis te gaan gebruiken voor nuttige toepassingen. Al gauw rees dan ook het verlangen om voort te gaan met toegepast wetenschappelijk onderzoek waarin deze beide aspecten verenigd worden. Deze mogelijkheid werd me toen vanuit onverwachtse hoek geboden aan het Labo Algemene Biochemie en Fysische Farmacie in de vorm van een doctoraat waarvan het resultaat nu aan de lezer aangeboden wordt.

Als vreemde ‘fysische’ eend in de farmaceutische bijt, hebben de voorbije doctoraatsjaren me voornamelijk het belang en potentieel doen inzien van het combineren van wetenschappelijke disciplines. Daar het onmogelijk is voor een individu om alle deze disciplines in detail te kennen, is interdisciplinaire samenwerking de aangewezen weg. Niet alleen verruimt dit de blik van de onderzoeker buiten het eigen vakgebied, het biedt tevens de mogelijkheid om tot nieuwe inzichten en toepassingen te komen. Om deze redenen zijn de voorbije doctoraatsjaren een zeer boeiende en leerrijke ervaring geweest. Het is dan ook een plezier om de vele collega’s, vrienden en familieleden van harte te bedanken die dit alles mogelijk gemaakt hebben.

Het spreekt voor zich dat er van dit werk geen sprake zou zijn zonder mijn beide promotoren, Prof. J. Demeester en Prof. S. De Smedt. Ik herinner me nog goed de lovende woorden van mijn echtgenote, toen nog mijn ‘vriendin’, over de vriendelijke en behulpzame begeleiding tijdens haar stage bij jullie. Na een hartelijk en open eerste sollicitatiegesprek

heb ik wat mij betreft dan ook geen seconde getwijfeld om bij jullie aan de slag te gaan. Behalve voor de uitstekende wetenschappelijke begeleiding ben ik in het bijzonder dankbaar voor het voortdurende vertrouwen dat jullie betoond hebben. Dit heeft ervoor gezorgd dat ik dit werk in alle vrijheid heb kunnen uitvoeren en geduldig te blijven bij succes en falen. Wat de toekomst ook brengt, ik zal steeds met diepe genegenheid aan jullie beiden en deze periode terugdenken.

Evenzeer ben ik veel dank verschuldigd aan Dr. C. Roelant die het microbead project geleid heeft vanuit de zijde van eerst Tibotec en later MemoBead Technologies. Zonder zijn voortdurende steun en vertrouwen in het project zou dit doctoraat niet tot stand kunnen komen zijn. Vooral zijn nooit aflatend enthousiasme en doorzettingsvermogen zullen me steeds bijblijven.

Tevens zou ik graag Dr. M. Leblans willen bedanken die eveneens van bij het begin aanwezig was bij het microbead project. Ik was steeds weer onder de indruk van zijn grondige en uitgebreide kennis van fysica en optica in het bijzonder, waarvan ik dan ook heel wat opgestoken heb. In het bijzonder ben ik hem ook dankbaar voor het kritisch nalezen van het theoretisch gedeelte van de microbeads (Hoofdstuk 6). Zo was hij het die voorgesteld heeft om de fundamentele Gauss distributie te bekijken, wat een goede keuze gebleken is. Verder heeft hij onlangs welwillend de besturing van de codeermodule volledig herschreven en gemoderniseerd, waarvoor speciale dank.

Verder wens ik ook de collega's van het Laboratorium voor Algemene Biochemie en Fysische Farmacie te bedanken, zowel zij die nu aanwezig zijn als zij die ondertussen reeds elders tewerkgesteld zijn, voor de goede sfeer en samenwerking. In het bijzonder dank ik mijn bureau-genoten Katrien en Tinneke voor hun vriendschap en collegialiteit. Het is een genoegen om met jullie dagelijks samen te mogen werken.

Ook een speciaal woord van dank voor Prof. P. Van Oostveldt bij wie ik mijn eerste stappen in de wereld van de confocale microscopie gezet heb. Zijn generositeit in het ter beschikking stellen van de confocale microscoop in de eerste twee jaren van het doctoraat ligt mee aan de basis van dit eindresultaat. Ook had ik graag Dr. N. Van Bruaene bedankt voor de aangename samengewerking in de beginfase van de FRAP experimenten.

Met genoegen betuig ik ook dank aan de thesisstudenten die meegewerkt hebben aan dit project: Nicolas Naert, Stefanie Quintelier, Philippe Keppens, Pascal Van Lierde, Ine

Darras, Isabelle Van de Reviere en Bart Huyck. Ik ben jullie in het bijzonder erkentelijk voor het geduld en doorzettingsvermogen. Jullie bijdrage is ten zeerste gewaardeerd.

Verder dank ik ook Tibotec, Memobead Technologies, het Vlaams Instituut voor de Bevordering van het Wetenschappelijk en Technologisch Onderzoek in de Industrie (IWT), het Fonds voor Wetenschappelijk Onderzoek-Vlaanderen (FWO) en het Bijzonder Onderzoeksfonds (BOF) van de Universiteit Gent voor hun financiële steun.

Van ganser harte wens ik mijn ouders te bedanken voor hun voortdurende steun op elk mogelijk gebied. Zonder jullie zou van dit alles geen sprake zijn. Met grote genegenheid dank ik ook de vele familieleden en vrienden voor hun niet aflatende steun en vriendschap.

Er zijn geen woorden die de dankbaarheid en liefde kunnen uitdrukken die ik voel voor mijn echtgenote Tiny en onze twee zoons Sebastiaan en Elewout. Toch wens ik de grootste bewondering uit te drukken voor hun geduld en nooit aflatende liefde. Hoewel er slechts één auteur vermeld staat op dit werk, is dit het resultaat van onze gezamenlijke inspanning. Want liefde maakt tot één.

Kevin Braeckmans  
Lokeren, april 2004

# General introduction, aim and structure of the thesis

## General introduction

Fluorescence recovery after photobleaching (FRAP) is a well-known, yet ever-evolving fluorescence technology that is used for measuring the mobility of molecules on a microscopic scale [1]. Basically, the fluorescent molecules are at first photobleached in a certain region of the sample (see Fig. 1). Photobleaching is a photo-induced process where fluorescent molecules lose their fluorescent properties, resulting in a fading of the fluorescent colour. Immediately after the bleaching phase, fluorescent molecules from the surrounding unbleached areas will start to diffuse into the bleached area. The resulting recovery of the fluorescence in the bleached area is subsequently measured by a highly attenuated light beam. The rate of fluorescence recovery reflects the mobility of the species in the system, expressed by the apparent translational diffusion coefficient. Additionally, the amount of recovery is a measure of the fraction of mobile species in the observed region.

In a pharmaceutical context, for example, a lot of research is being done on the delivery of macromolecular drugs, from the release from a matrix to the uptake of the drug at a certain location in the body. As it is still difficult to predict theoretically the dynamic behaviour of macromolecular drugs in solutions and networks, there is the need to experimentally determine their mobility properties in the different media. FRAP offers the possibility to do so. The FRAP-technique has also been applied to biological cells and tissues to elucidate the reaction and signalling pathways *in vivo* which are determined by properties such as viscosity, steric hindrance, binding and compartmentation.

The diffusion coefficient and mobile fractions are extracted from an experimental recovery curve by fitting of an appropriate FRAP model. FRAP models for use with regular

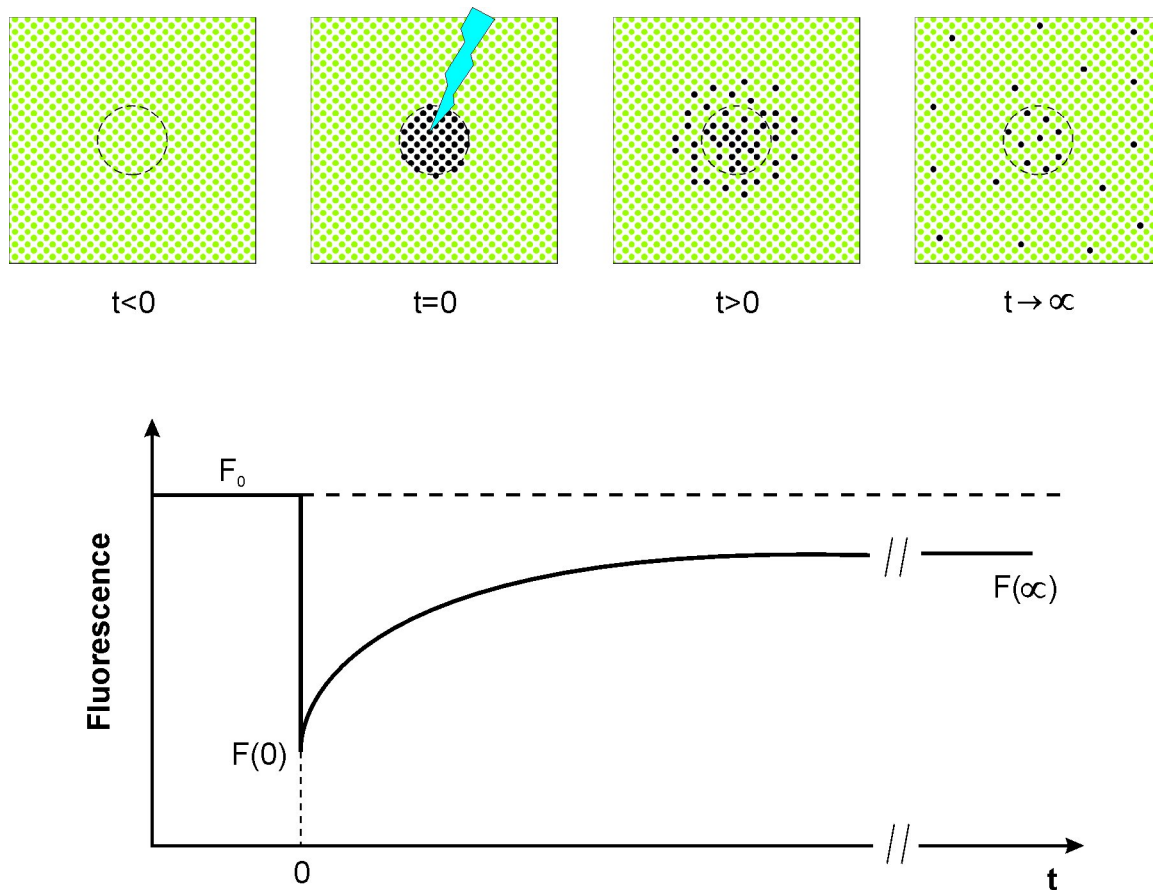


**Figure 1:** Schematic representation of a FRAP experiment. Just before bleaching, the fluorescence is measured in a specific area (circular in this example) of the sample. The initial fluorescence before bleaching is denoted on the fluorescence recovery curve as  $F_0$ . At  $t = 0$  a high intensity light beam instantly bleaches the molecules in the observed area causing a drop in fluorescence to  $F(0)$ . Due to diffusion, the bleached molecules will be gradually replaced in the bleached area by non bleached fluorescent molecules from the surrounding. This results in a recovery of the observed fluorescence within the observed area. At the end of the experiment ( $t \rightarrow \infty$ ), the fluorescence will recover to a level  $F(\infty)$ , which is equal to  $F_0$  if all fluorescent molecules in the observed area are mobile or less than  $F_0$  (as in this example) when a part of the fluorescent molecules are immobile in the observed area.

(i.e. *non scanning*) fluorescence microscopes have been developed earlier. They describe the relation between the diffusion into a two-dimensional (2-D) bleached region and the fluorescence recovery as observed by the fluorescence microscope. Nowadays, however, bleaching experiments can be done on confocal *scanning* laser microscopes (CSLM's) as they are usually equipped with the feature to bleach arbitrary regions in the sample. Such confocal microscopes make use of a relatively powerful laser beam whose intensity can be quickly modulated by an acousto optical modulator (AOM). When the bleaching geometry is defined in the software, the microscope scans the laser beam over the sample in a raster pattern, pixel by pixel and line by line, and meanwhile the AOM modulates the beam intensity according to the designed pattern. The regions that are hit by the high intensity beam will be bleached, while the surroundings that are illuminated by the low intensity beam remain in tact. The ability to bleach arbitrary regions makes such CSLM's an excellent standard tool to perform bleaching studies, such as FRAP measurements. Few FRAP models exist, however, for use with a CSLM. Moreover, despite CSLMs being widespread amongst pharmaceutical and biology labs, their application to FRAP studies is often limited to qualitative results because of the often complicated mathematics involved. Therefore, it would be an advantage to have FRAP models which are readily applicable on commercial confocal microscopes and which are based on straightforward mathematical expressions that can be easily programmed in a standard fitting routine and with very small computation times.

**In Part I of this thesis two such new FRAP models will be presented for use with the CSLM. The first model, as described in Chapter 1, is based on the photobleaching of a uniform disk, while the second model, which is described in Chapter 3, uses a long line segment. Both models are suited for measurements in 3-D samples.** They will be evaluated in great detail in order to understand the influence of the various experimental conditions such as noise, power of the bleaching beam, confocal aperture etc.

**An unexpected but important phenomenon was observed during the experimental evaluation of the FRAP models: the illumination intensity distribution, which results from focusing the laser beam with an objective lens, cannot be considered to be invariant in combination with first order photobleaching kinetics, as has always been assumed in FRAP models so far. Instead we have observed that the dimensions of the bleaching intensity distribution seemingly increase with increasing bleaching power.** Indirect evidence of this phenomenon will



already be presented in Chapter 1, but it is explained and examined separately in great detail, both theoretically and experimentally, in Chapter 2. The line model from Chapter 3 is especially designed to take this effect into account, which has never done before in FRAP models, but which is essential to obtain valid measurements of the diffusion coefficient. It also follows that the line model is the first method to measure directly the effective size of the bleaching beam as a function of the bleaching power.

**Part II of this thesis deals with a new technique for the encoding of microbeads.** As explained in Chapter 4, encoded microcarriers are used for ‘bead-based’ assays on very large numbers of molecules in gene expression studies, drug screening and clinical diagnostics. If each microbead is encoded according to the particular ligand bound to its surface, they can be subjected to an assay simultaneously. When a particular microsphere gives a positive reaction, the substance on its surface can be identified by reading the code. A new method for the encoding of microcarriers which is based on photobleaching has been invented at the Laboratory of General Biochemistry and Physical Pharmacy. Actually, this technique has arisen as a corollary of FRAP experiments. As already explained above, one of the characteristics that can be assessed with FRAP is the (im)mobile fraction of a system. After photobleaching, the mobile molecules will diffuse out of the bleached region and will be replaced by intact fluorophores from the unbleached regions. When all molecules are mobile, the fluorescence will recover completely. However, **when a fraction of the molecules are immobilized, they cannot be replaced after photobleaching and an imprint of the photobleached area will remain visible. This property can therefore be used to write patterns into fluorescent microbeads.**

**An extensive review of competing encoding technologies is presented in Chapter 4.** The pro’s and con’s of the different technologies are explained and compared with the new technique of encoding by photobleaching. **The new technique itself is discussed in detail in Chapter 5.** This chapter should allow the reader to fully understand the different aspects of the new bead-encoding technology. **The process of encoding by spatial selective photobleaching itself is considered from a theoretical point of view in Chapter 6.** The theory is incorporated into a computer program for the simulation of the encoding and decoding of the microbeads with a CSLM. Some thoughts on the design of suitable codes for microbeads are also provided in the same chapter. **Finally, encoding experiments are presented in Chapter 7 which aim to assess**

**the optimal conditions for writing and reading of the microbeads.** In addition, the experimental results are used to evaluate the theory of the previous chapter.

## **Aim of this thesis**

In the last decade, confocal scanning laser microscopes (CSLMs) have become very popular in biological, medical, pharmaceutical and material research. Because of their optical sectioning ability they can give insight in the three-dimensional structure of fluorescently labeled samples. Many CSLMs of the latest generation have the additional ability of scanning user-defined regions. This very feature makes them a convenient tool for fluorescence recovery after photobleaching (FRAP) experiments. In fact, it is thanks to this wide-spread new generation of CSLMs that nowadays FRAP is within reach of many scientists of various disciplines, whereas it was limited to a number of specialized labs in the past. However, there is a lack of clear and practical FRAP models for direct use with commercial CSLMs. **The first part of this thesis therefore aims at developing FRAP models which can be readily used with CSLMs equipped with the feature of bleaching user-defined regions. In particular we are interested in finding FRAP models which can be used for both two-dimensional and three-dimensional samples.**

The same feature of photobleaching user-defined regions can be used for the encoding of fluorescent microbeads. Encoding of microcarriers is required for ‘bead-based’ assays on very large numbers of molecules in gene expression studies, drug screening and clinical diagnostics. If each microbead is encoded according to the particular ligand bound to its surface, they can be subjected to an assay simultaneously. When a particular microsphere gives a positive reaction, the substance on its surface can be identified by reading the code. Previously reported techniques for colour encoding polymer microspheres only allow for a limited number of unique codes. Other methods use metallic particles, which are rather uncommon in screening applications. **In the second part of this thesis, a promising alternative technology will therefore be examined for the encoding of microbeads which are commonly used in screening applications. The method is based on writing patterns inside fluorescently dyed microspheres by ‘spatial selective photobleaching’. In particular we aim at understanding and examining the different aspects that will lead to the design and development of a fully automated encoding and decoding device for high-throughput screening and**

diagnostic applications.

## Structure of the manuscript

This thesis is divided into two main parts. Part I deals with the use of CSLMs for FRAP measurements. In **Chapter 1** a FRAP model is described for use with the CSLM based on the photobleaching of a uniform disk. **Chapter 2** relates on the unexpected observation of the bleaching intensity distribution being dependent on the bleaching power. A second model for FRAP with the CSLM is presented in **Chapter 3** which is based on the photobleaching of a long line segment. In Part II of this thesis, a new method for the encoding of microbeads is reported based on ‘spatial selective photobleaching’. First, a review is presented of the related field in **Chapter 4**. The new technology itself is explained in **Chapter 5**. A theory which describes the encoding and decoding process is presented in **Chapter 6**. Encoding experiments are finally discussed in **Chapter 7** which aim to assess the optimal conditions for writing and reading of the microbeads. The experiments are also used to evaluate the theory presented in the previous chapter.

The mathematical derivations and concepts are, as much as possible, deferred to the Appendices. In **Appendix A**, the mathematical formulation for the bleaching by a scanning beam is outlined. The different expressions for the illumination and detection intensity distributions as they are used throughout this thesis are briefly discussed in **Appendix B**. In **Appendix C**, finally, the mathematical derivation of the disk model from Chapter 1 is outlined.

# Contents

<b>I Fluorescence recovery after photobleaching with the confocal laser scanning microscope</b>	<b>1</b>
<b>1 A uniform disk model for three-dimensional fluorescence recovery after photobleaching with the confocal scanning laser microscope</b>	<b>2</b>
1.1 Introduction . . . . .	3
1.2 Theoretical framework: derivation of the FRAP model . . . . .	4
1.2.1 Bleaching a geometry with a scanning beam . . . . .	4
1.2.2 Bleaching of a disk by a scanning beam . . . . .	6
1.2.3 Three-dimensional fluorescence recovery after bleaching of a uniform disk . . . . .	8
1.3 Materials and methods . . . . .	12
1.3.1 FRAP equipment . . . . .	12
1.3.2 Test solutions . . . . .	12
1.3.3 Bovine vitreous . . . . .	13
1.3.4 Cystic fibrosis sputum . . . . .	13
1.3.5 Experimental FRAP protocol . . . . .	14
1.3.6 Data extraction and fitting . . . . .	16
1.4 Results and discussion . . . . .	16
1.4.1 The bleaching parameter $K_0$ . . . . .	16
1.4.2 The interline distance $\Delta y$ . . . . .	19
1.4.3 The radius $w$ of the bleached disk . . . . .	21
1.4.4 Validation of the disk model . . . . .	21
1.4.5 FRAP measurements with the CSLM in bovine vitreous and cystic fibrosis sputum . . . . .	25
1.5 Conclusions . . . . .	27

<b>2</b>	<b>Implications of anomalous photobleaching behaviour of fluorescein on FRAP measurements</b>	<b>29</b>
2.1	Introduction . . . . .	30
2.2	Theoretical background: photobleaching of fluorescein in microscopy . . . .	32
2.2.1	The photobleaching process of fluorescein . . . . .	32
2.2.2	Photobleaching of fluorescein by a focused laser beam . . . . .	34
2.3	Materials and methods . . . . .	37
2.3.1	The bleaching and imaging apparatus . . . . .	37
2.3.2	Photobleaching experiments . . . . .	37
2.3.3	Photobleaching simulations . . . . .	38
2.4	Results . . . . .	40
2.4.1	Photobleaching of immobilized FD2000 . . . . .	40
2.4.2	Simulation of photobleaching immobilized fluorescein . . . . .	44
2.5	Discussion . . . . .	50
2.6	Conclusions . . . . .	55
<b>3</b>	<b>A line model for fluorescence recovery after photobleaching with the confocal laser scanning microscope.</b>	<b>56</b>
3.1	Introduction . . . . .	57
3.2	Theoretical framework: derivation of the FRAP line model . . . . .	58
3.2.1	Photobleaching of a long line segment . . . . .	58
3.2.2	Fluorescence recovery after photobleaching of a long line segment . . . .	60
3.3	Materials and methods . . . . .	64
3.3.1	FRAP equipment . . . . .	64
3.3.2	Test solutions . . . . .	64
3.3.3	Experimental FRAP protocol . . . . .	65
3.3.4	Data extraction and fitting . . . . .	65
3.4	Results and discussion . . . . .	67
3.4.1	Influence of noise . . . . .	67
3.4.2	Influence of the confocal aperture . . . . .	67
3.4.3	Influence of the bleaching power . . . . .	70
3.4.4	Validation of the line model . . . . .	72
3.5	Conclusions . . . . .	78

<b>II</b>	<b>Encoding of microbeads</b>	<b>80</b>
<b>4</b>	<b>Introduction to the encoding of microcarriers</b>	<b>81</b>
4.1	The necessity of encoding microcarriers . . . . .	81
4.2	Methods for encoding microcarriers . . . . .	83
4.2.1	Spectrometric encoding . . . . .	83
4.2.2	Electronic encoding . . . . .	91
4.2.3	Graphical Encoding . . . . .	92
4.2.4	Physical encoding . . . . .	98
4.3	Conclusions . . . . .	98
<b>5</b>	<b>Encoding microbeads by spatial selective photobleaching</b>	<b>99</b>
5.1	Introduction . . . . .	100
5.2	Encoding by ‘Spatial Selective Photobleaching’ . . . . .	101
5.3	Code design . . . . .	103
5.4	Position and orientation of the microspheres . . . . .	106
5.5	Photochroming . . . . .	107
5.6	Putting the code to work . . . . .	110
5.7	Conclusions . . . . .	111
<b>6</b>	<b>Theoretic considerations on the encoding by photobleaching of fluorescent microcarriers</b>	<b>112</b>
6.1	Theory of first-order photobleaching by a scanning beam applied to the writing of a barcode . . . . .	112
6.1.1	First-order photobleaching . . . . .	112
6.1.2	Bleaching of a 2-D barcode . . . . .	113
6.1.3	Bleaching of a 1-D barcode or ‘dotcode’ . . . . .	116
6.1.4	Mobile fraction and multiple illumination scans . . . . .	117
6.1.5	Relation between two systems with different bleaching efficiencies . . . . .	117
6.1.6	The imaging process . . . . .	119
6.2	Code simulation program . . . . .	120
6.3	Codes for microcarriers . . . . .	126
6.3.1	‘Black And White’ codes . . . . .	127
6.3.2	Intensity codes . . . . .	128
6.3.3	Length and intensity encoding . . . . .	129

<b>7</b>	<b>Encoding and decoding of fluorescent microspheres: experiments and simulations</b>	<b>131</b>
7.1	Experimental verification of first-order photobleaching in fluorescent microspheres . . . . .	132
7.1.1	Aim and objectives . . . . .	132
7.1.2	Materials and methods . . . . .	132
7.1.3	Experiment and discussion . . . . .	133
7.1.4	Conclusions . . . . .	133
7.2	The experimental illumination and detection intensity distribution . . . . .	134
7.2.1	Aim and objectives . . . . .	134
7.2.2	Materials and methods . . . . .	134
7.2.3	Results and discussion . . . . .	136
7.2.4	Conclusions . . . . .	142
7.3	Focal shift and spherical aberrations in microspheres . . . . .	142
7.3.1	Aims and objectives . . . . .	142
7.3.2	Materials and methods . . . . .	143
7.3.3	Experiments and discussion . . . . .	143
7.3.4	Conclusions . . . . .	146
7.4	Encoding experiments and simulations . . . . .	146
7.4.1	Aim and objectives . . . . .	146
7.4.2	Materials and methods . . . . .	147
7.4.3	Experiments and discussion . . . . .	147
7.4.4	Conclusions . . . . .	160
<b>A</b>	<b>Bleaching with a scanning beam</b>	<b>162</b>
A.1	First-order photobleaching . . . . .	162
A.2	Bleaching of a single line segment . . . . .	162
A.3	Bleaching of a 2D geometry . . . . .	164
A.4	Discrete vs. continuous photobleaching solution . . . . .	167
<b>B</b>	<b>The illumination and detection intensity distribution</b>	<b>171</b>
B.1	The three-dimensional light distribution near focus . . . . .	171
B.2	The modified Gaussian intensity distribution . . . . .	176
B.3	The fundamental Gaussian-beam solution . . . . .	178

<b>C Mathematical derivation of the FRAP disk model</b>	<b>179</b>
C.1 Diffusion after bleaching of a uniform disk . . . . .	179
C.2 Fluorescence recovery after photobleaching of a uniform disk as observed by the CSLM . . . . .	182
<b>Bibliography</b>	<b>187</b>
<b>Summary</b>	<b>198</b>
<b>Samenvatting</b>	<b>204</b>
<b>Curriculum Vitae</b>	<b>210</b>
<b>List of publications</b>	<b>211</b>



# Part I

## Fluorescence recovery after photobleaching with the confocal laser scanning microscope

# Chapter 1

## A uniform disk model for three-dimensional fluorescence recovery after photobleaching with the confocal scanning laser microscope

### Summary

Confocal scanning laser microscopes (CSLMs) are equipped with the feature to photobleach user-defined regions. This makes them a convenient tool to perform fluorescence recovery after photobleaching (FRAP) measurements. To allow quantification of such FRAP experiments, we have developed a three-dimensional model that describes the fluorescence recovery process for a disk-shaped geometry that is photobleached by the scanning beam of a CSLM. First, the general mathematical basis will be outlined describing the bleaching process for an arbitrary geometry bleached by a scanning laser beam. Next, these general expressions are applied to the bleaching by a CSLM of a disk-shaped geometry and an analytical solution is derived that describes three-dimensional fluorescence recovery in the bleached area as observed by the CSLM. The FRAP model is validated through both the Stokes-Einstein relation and the comparison of the measured diffusion coefficients with their theoretical estimates. Finally, the FRAP model is used to characterize the transport of FITC-dextran through bulk three-dimensional biological materials: vitreous body isolated from bovine eyes, and lung sputum expectorated by cystic fibrosis patients.

## 1.1 Introduction

Recent advancements in the biomedical and pharmaceutical field have stimulated the development of macromolecular therapeutics [2, 3, 4] and colloidal nanoscopic drug carriers [5, 6]. The delivery and the transport of macromolecular therapeutics and colloidal drug carriers in vivo requires overcoming major biological barriers [7]. For example, nanoscopic liposome/DNA complexes for gene therapy of cystic fibrosis (CF) have to cross the mucus layer in the patients lungs before being effective [8, 9, 10]. Also, anticancer drugs entrapped in nanoscopic carriers have to move within the tumor interstitial matrix, which acts as a barrier to drug delivery [11, 12, 13, 14].

An ideal tool for studying the mobility characteristics of molecules and particles on a microscopic level is fluorescence recovery after photobleaching (FRAP). For a long time FRAP has been successfully used to assess the translational mobility of all kinds of solutes in cytoplasm, nuclei, and membranes [15, 16, 17, 18]. Besides its cellular applications, FRAP has also been used to study the mobility of molecules in interstitial spaces of (tumor) tissues [13, 19] and extracellular matrices such as cervical mucus and biofilms [20, 7, 21]. For an extensive review covering many applications of FRAP and its advantages over other techniques for the measurement of diffusion coefficients, see [1].

FRAP models for use with regular (i.e., *non-scanning*) fluorescence microscopes have already been developed. They describe the relation between the diffusion into a two-dimensional (2-D) bleached region and the fluorescence recovery as observed by the fluorescence microscope [22, 23, 24, 25, 26, 27]. Nowadays, however, bleaching experiments can be easily carried out on confocal *scanning* laser microscopes (CSLMs) as they are often equipped with the feature to bleach arbitrary regions in the sample. When the bleaching geometry is defined in the software, the microscope scans the laser beam over the sample in a raster pattern, pixel-by-pixel and line-by-line, while modulating the beam intensity according to the designed pattern. The ability to bleach arbitrary regions makes such CSLMs an excellent standard tool to perform FRAP experiments.

Few FRAP models exist, however, for use with a CSLM. A model based on a statistical evaluation of the fluorescence inside the bleached region has been reported, but the analysis was limited to 2-D samples [28]. Both two-dimensional and three-dimensional models have been developed as well, based on a numerical approach [29, 30, 31, 32], but due to the complicated and often time-consuming computations involved, the practical use

of this model seems limited. An approximate but very practical three-dimensional (3-D) model has been developed for use with objective lenses of low numerical aperture (NA) on a CSLM [33]. This method relies on a specially adapted CSLM and uses a stationary laser beam for bleaching and a line-scanning beam for recording the fluorescence recovery. This sequence of scanning modes appears not always to be possible on commercial CSLMs, which are rather equipped with the possibility to bleach 2-D geometries by a scanning beam. Therefore, it would be an advantage to have a FRAP model that can readily be applied on such standard CSLMs. Additionally, to allow general and widespread use of the model, it should be based on ‘simple’ mathematics that can be easily programmed in a standard fitting routine and with short computation times.

Here we present such a new FRAP model that can be easily applied on almost any modern CSLM equipped with the feature to bleach arbitrary regions. An outline of the general mathematical basis will be given first which describes the bleaching process for a geometry bleached by a scanning laser beam. Next, the analytical solution will be derived that describes 3-D fluorescence recovery as observed by the confocal microscope after bleaching of disk-shaped geometry. After extensive experimental evaluation, the new FRAP model will be used to characterize the diffusion of fluorescent dextrans in vitreous body isolated from bovine eyes and lung sputum expectorated by cystic fibrosis (CF) patients.

## **1.2 Theoretical framework: derivation of the FRAP model**

### **1.2.1 Bleaching a geometry with a scanning beam**

When a geometry is bleached by a CSLM, it is done sequentially, pixel-by-pixel and line-by-line, as is illustrated in Fig. 1.1. We will assume that the bleaching phase is very short so that the amount of fluorescence recovery that will take place during bleaching is negligible. Furthermore, it is assumed that the bleaching reaction can be described by an irreversible first-order reaction,

$$\frac{\partial}{\partial t}C(x, y, z, t) = -\alpha I_b(x, y, z)C(x, y, z, t), \quad (1.1)$$

where  $C(x, y, z, t)$  is the spatial concentration of fluorophores at a bleach time  $t$ ,  $\alpha$  is the bleach rate which is specific for a certain type of fluorophore in a particular medium,

and  $I_b(x, y, z)$  is the 3-D intensity distribution of the bleaching beam. In a CSLM, the light source is a laser beam focused down through an objective lens and the resulting 3-D intensity distribution is called the illumination intensity distribution (see Appendix B, section B.1). From now on we will therefore refer to  $I_b(x, y, z)$  as the bleaching intensity distribution. To describe the bleaching phase in the case of a CSLM, Eq. (1.1) has to be solved for the bleaching beam being scanned across the sample according to a certain 2-D geometry. Since a 2-D geometry is scanned sequentially line-by-line, it is instructive to first consider the case of the bleaching of a single line segment (see Appendix A, section A.2). These results can subsequently be extended to the general 2-D case as explained in section A.3, where it is found that the concentration of fluorophores after bleaching of a 2-D geometry  $B(x, y)$  by scanning of the bleaching intensity distribution  $I_b(x, y, z)$  can be calculated from:

$$C_b(x, y, z) = C_0(x, y, z)e^{-\frac{\alpha}{v\Delta y}K(\mathbf{r})}, \quad (1.2)$$

where  $v$  is the constant line scanning speed and  $\Delta y$  is the distance between two adjacent scanning lines (see Fig. A.2), and where it is understood that  $\Delta y$  is smaller than one-half the resolution of the bleaching intensity distribution.  $K(x, y, z)$  is the bleaching intensity distribution which results from scanning the bleaching geometry with  $I_b(x, y, z)$  and can be calculated from the convolution product of  $B(x, y)$  and  $I_b(x, y, z)$ :

$$\begin{aligned} K(\mathbf{r}) &= B(\mathbf{r}) \otimes I_b(\mathbf{r}) \\ &= \iiint_{\infty} B(x', y', z') I_b(x - x', y - y', z - z') dx' dy' dz'. \end{aligned} \quad (1.3)$$

From Eq. (1.2) it can be seen that the scanning speed  $v$  and the distance between the adjacent bleach lines  $\Delta y$  play an important role in the amount of bleaching. It is worth noting that on a CSLM instrument, both parameters can be varied by changing the electronic *zoom factor*. Zoom 1 corresponds to the full field of view, whereas, for example at zoom 2, only one-half the full distance in the  $x$ - and  $y$ -directions is scanned. This means that at zoom 2 the line-scanning speed  $v$  and the interline distance  $\Delta y$  will be only one-half their value at zoom 1. Therefore, if  $v_0$  and  $\Delta y_0$  are respectively the scanning speed and interline distance at zoom 1, then at zoom  $Z$  the scanning speed  $v = v_0/Z$ , and the interline distance  $\Delta y = \Delta y_0/Z$ , and Eq. (1.2) can be rewritten as:

$$C_b(x, y, z) = C_0(x, y, z)e^{-\frac{\alpha Z^2}{v_0 \Delta y_0}K(\mathbf{r})}, \quad (1.4)$$

explicitly showing the strong (power of 2) dependence of the amount of bleaching on the zoom setting.

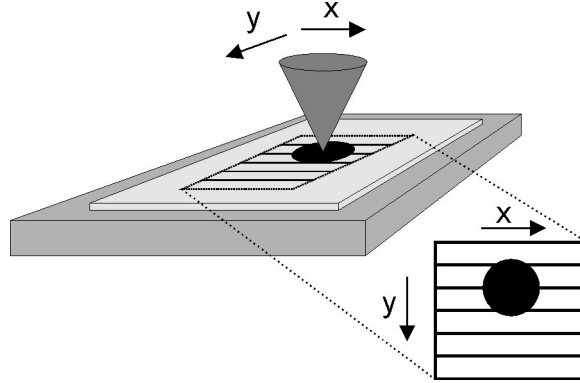


**Figure 1.1:** On a CSLM it is possible to photobleach user-defined regions. While scanning in a raster pattern, line by line, the intensity of the laser beam is modulated between a low and high intensity according to the user-defined region. *Image courtesy of Bart Huyck.*

## 1.2.2 Bleaching of a disk by a scanning beam

Now we will apply Eq. (1.2) for the bleaching of an arbitrary geometry to the special case of a disk with radius  $w$  and a constant bleaching intensity. In this case, the geometry  $B(r)$  in cylindrical coordinates is:

$$B(r) = \begin{cases} 1 & \text{if } r \leq w \\ 0 & \text{if } r > w. \end{cases} \quad (1.5)$$

Analogous to previous theoretical work on FRAP in three dimensions [33], we take the bleaching intensity distribution  $I_b(x, y, z)$  to be radially and axially Gaussian distributed, with respective resolutions  $r_0$  and  $z_0$ :

$$I_b(x, y, z) = I_{0b} e^{-2\frac{x^2+y^2}{r_0^2}} e^{-2\frac{z^2}{z_0^2}}. \quad (1.6)$$

It should be noted that the radial resolution  $r_0$  is considered to be independent of the axial coordinate  $z$  (compare, for example, with the intensity distributions discussed in Appendix B, sections B.2 and B.3). As a consequence, Eq. (1.6) is valid only for lenses of relatively low NA (which have a cylindrical illumination profile). Lenses of high NA have a distinct conical shape and the radial resolution will be a function of the axial coordinate  $z$ . However, a more complicated bleaching intensity distribution such as this will prevent us from finding an analytical solution for the recovery process, which is one of the objectives of this study. Therefore, we will continue with Eq. (1.6), realizing this derivation in 3-D is only valid for lenses of low NA. If the disk's radius  $w$  is much larger than the radial

resolution  $r_0$ , the bleaching intensity distribution may be considered to have a negligible radial resolution and can be approximated by:

$$I_b(x, y, z) = I_{0b} \delta(x, y) e^{-2\frac{z^2}{z_0^2}}, \quad (1.7)$$

where  $\delta(x, y)$  is the Dirac-Delta function. How small the radial resolution will have to be compared to the bleaching disk's radius for this assumption to be true, will have to be determined experimentally (see section 1.4.3). By substitution of Eqs. (1.5) and (1.7) into Eq. (1.3), it follows that the resulting bleaching light distribution  $K(r, z)$  in cylindrical coordinates is:

$$K(r, z) = \begin{cases} I_{0b} e^{-2\frac{z^2}{z_0^2}} & \text{if } r \leq w \\ 0 & \text{if } r > w, \end{cases} \quad (1.8)$$

which is a cylindrical illumination profile of radius  $w$  with a uniform radial and a Gaussian axial distribution. Eq. (1.8) leads to the important conclusion that, if a disk is scanned whose radius  $w$  is much larger than the radial resolution of the bleaching intensity distribution, the resulting bleaching illumination profile is equivalent to that of a stationary beam with a uniform radial and a Gaussian axial distribution, with respective resolutions  $w$  and  $z_0$ . Therefore, we will refer to the new FRAP model as the uniform disk model. The 3-D fluorophore concentration distribution after bleaching of a uniform disk by a scanning beam is finally found from Eqs. (1.2) and (1.8):

$$C_b(r, z) = \begin{cases} C_0(r, z) e^{-K_0 e^{-2\frac{z^2}{z_0^2}}} & \text{if } r \leq w \\ C_0(r, z) & \text{if } r > w, \end{cases} \quad (1.9)$$

where we have defined the bleaching parameter

$$K_0 = \frac{\alpha I_{0b}}{v \Delta y}, \quad (1.10)$$

which determines the amount of bleaching. From Eq. (1.4) it immediately follows that the bleaching parameter can be explicitly written in terms of the zoom setting  $Z$  of the CSLM as well:

$$K_0 = \frac{\alpha I_{0b} Z^2}{v_0 \Delta y_0}. \quad (1.11)$$

To have a good understanding of the assumption made in Eq. (1.7) and its implications, let us examine the difference between the discontinuous approximation Eq. (1.8) and the

exact solution for  $K(x, y, z)$ , which can be calculated from Eqs. (1.5) and (1.6)<sup>1</sup>:

$$K(r) = I_0 2\pi e^{-2\frac{r^2}{r_0^2}} e^{-2\frac{z^2}{z_0^2}} \int_{r'=0}^w r' e^{-2\frac{r'^2}{r_0^2}} I_0\left(\frac{4rr'}{r_0^2}\right) dr', \quad (1.12)$$

where  $I_0$  is the zero order modified Bessel function. Eq. (1.12) has to be solved numerically. Both the exact and approximate intensity distributions are plotted in Fig. 1.2A for three disks of radii,  $w = r_0$ ,  $w = 3r_0$ , and  $w = 5r_0$ . It is clear that, the larger the radius  $w$  compared to the bleaching resolution  $r_0$ , the better the approximation Eq. 1.8 will be valid. It is also important to note that, if the concentration after bleaching is calculated with the exact solution for  $K(x, y, z)$ , the radius of the disk (at full-width half-maximum, i.e., FWHM) tends to increase slightly with increasing bleaching parameter  $K_0$  because of the slope at the edges and the exponential process. Examples for a disk of radius  $w = 5r_0$  are shown in Fig. 1.2B for three different  $K_0$  values, together with their best discontinuous approximation at the FWHM position. Based on such simulations we have determined an approximate relation between the bleaching parameter  $K_0$  and the increase in length  $\Delta w$  of the bleaching disk's radius relative to the resolution  $r_0$  of the bleaching PSF. These results are shown in the inset of Fig. 1.2B, leading to the following relation (based on a best fit of a second-degree polynomial):

$$\frac{\Delta w}{r_0} = -0.0106K_0^2 + 0.163K_0 \quad (0 \leq K_0 \leq 6). \quad (1.13)$$

If one wants to obtain the diffusion coefficient with the highest possible accuracy, it will be necessary to take Eq. (1.13) into account. In 'Results and Discussion', section 1.4, we will demonstrate the effect of taking Eq. (1.13) into account or not.

### 1.2.3 Three-dimensional fluorescence recovery after bleaching of a uniform disk

After (the instantaneous) photobleaching of a uniform disk, the bleached molecules will start to diffuse out of the bleached volume and will be replaced by diffusion of unbleached fluorophores into the bleached volume. The fluorophore concentration distribution at a time  $t$  after bleaching can be calculated by solving Ficks second law in cylindrical

---

<sup>1</sup>and by transforming the convolution integral Eq. 1.3 to cylindrical coordinates first (see, e.g. <http://omlc.ogi.edu/pubs/prahl-pubs/prahl88/node23.html>) and making use of the identity  $\int_0^{2\pi} e^{4rr' \cos \theta / r_0^2} d\theta = 2\pi I_0\left(\frac{4rr'}{r_0^2}\right)$ .



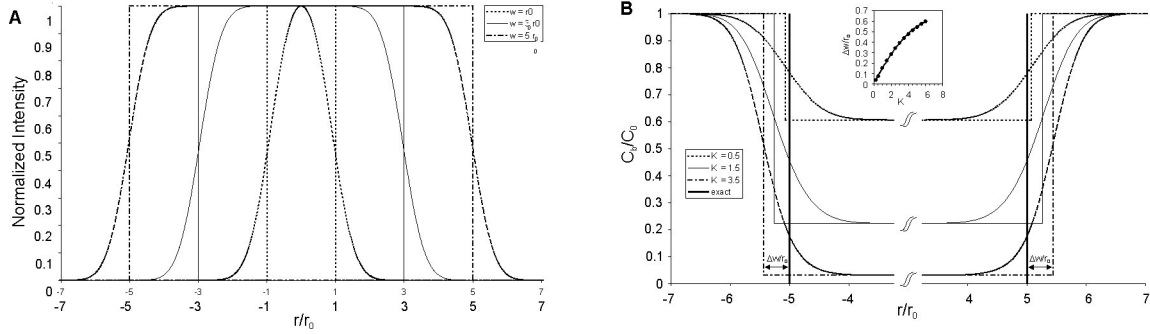


**Figure 1.2:** (A) When scanning a disk of radius  $w$ , the edges of the resulting light distribution show a slope that extend over a certain distance in space because of the radial Gaussian distribution of the bleaching intensity distribution. The larger the radius  $w$  compared to the radial resolution  $r_0$  of the bleaching intensity distribution, the better the radial intensity profile can be approximated by a discontinuous step function which is 1 inside the bleaching disk and zero outside. The exact radial illumination profile, according to Eq. 1.12 together with the discontinuous approximation Eq. 1.8 are plotted for three different radii:  $w = r_0$ ,  $w = 3r_0$ , and  $w = 5r_0$ . It is clear that, the larger the radius  $w$ , the better the discontinuous approximation will be valid. (B) The exact bleaching profile for a disk of radius  $w = 5r_0$  has been calculated for different values of the bleaching parameter:  $K_0 = 0.5$ ,  $1.5$ , and  $3.5$ . The bold lines at  $r = 5r_0$  and  $r = -5r_0$  indicate the bleaching disk's boundaries. For each of the bleaching profiles the best discontinuous approximation is drawn as well with edges at the FWHM. As can be seen, based on the positions of the FWHM, the effective radius of the bleached disk becomes larger with increasing bleaching depth. The increase in length  $\Delta w/r_0$  is indicated at each side of the profile for  $K_0 = 3.5$ . In the inset, the increase in length  $\Delta w/r_0$  of the bleaching disk's radius  $w$  is plotted as a function of the bleaching parameter  $K_0$ . A second-degree polynomial describes well this relationship for  $0 \leq K_0 \leq 6$ .

coordinates [34],

$$\frac{1}{D} \frac{\partial}{\partial t} C(r, z, t) = \left( \frac{\partial^2}{\partial r^2} + \frac{1}{r} \frac{\partial}{\partial r} \right) C(r, z, t) + \frac{\partial^2}{\partial z^2} C(r, z, t), \quad (1.14)$$

for the initial condition Eq. 1.9 (see Appendix C, section C.1). Next, the total fluorescence,  $F_{tot}(t)$ , inside the disk can be calculated as observed by the CSLM when using a strongly attenuated detection beam. The 3-D intensity distribution  $I_d(x, y, z)$  of the detection beam focused through the objective lens will be termed the confocal detection PSF (point spread function; see Appendix B, section B.1).  $I_d(x, y, z)$  is considered to be of the same form as the bleaching intensity distribution  $I_b(x, y, z)$ , except for the intensity which is  $A \times$  smaller than the bleaching intensity:

$$I_d(x, y, z) = I_b(x, y, z)/A. \quad (1.15)$$

Again, assuming that the resolution of the confocal detection PSF is much smaller than the radius of the bleaching disk, it is finally found (see Appendix C, section C.2)) that the total fluorescence inside the bleached disk can be calculated from:

$$\begin{aligned} \frac{F_{tot}(t)}{F_0} = & 1 + \frac{1}{\operatorname{erf}\left(\sqrt{2} \frac{\Delta z_0}{z_0}\right)} \sum_{n=1}^{+\infty} \left[ \frac{(-K_0)^n}{n!} \frac{1}{\sqrt{a_n}} \operatorname{erf}\left(\sqrt{\frac{2a_n}{a_n - n}} \frac{\Delta z_0}{z_0}\right) \right] \\ & \cdot \left( 1 - e^{-2\tau_r/t} \left[ I_0\left(2\frac{\tau_r}{t}\right) + I_1\left(2\frac{\tau_r}{t}\right) \right] \right), \end{aligned} \quad (1.16)$$

where  $F_0$  is the total fluorescence inside the disk before bleaching;  $\Delta z_0$  a parameter taking a finite confocal pinhole aperture into account by rejecting fluorescence light from planes above  $\Delta z_0$  and below  $-\Delta z_0$ ;  $I_0$  and  $I_1$  are the modified Bessel functions of zeroth and first order;  $K_0$  is the bleaching parameter;  $a_n = 1 + n \left(1 + \frac{2t}{\tau_z}\right)$ ;  $\tau_z = \frac{z_0^2}{4D}$  the axial characteristic diffusion time and  $\tau_r = \frac{w^2}{4D}$  the radial characteristic diffusion time. In the case of a fully opened confocal aperture ( $\Delta z_0 \rightarrow +\infty$ ), the error functions reach unity and Eq. (1.16) becomes:

$$\frac{F_{tot}(t)}{F_0} = 1 + \sum_{n=1}^{+\infty} \left[ \frac{(-K_0)^n}{n!} \frac{1}{\sqrt{a_n}} \right] \left( 1 - e^{-2\tau_r/t} \left[ I_0\left(2\frac{\tau_r}{t}\right) + I_1\left(2\frac{\tau_r}{t}\right) \right] \right), \quad (1.17)$$

and for  $z_0 \rightarrow +\infty$  (low NA) Eq. (1.17) reduces to:

$$\frac{F_{tot}(t)}{F_0} = 1 + \sum_{n=1}^{+\infty} \left[ \frac{(-K_0)^n}{n!} \frac{1}{\sqrt{1+n}} \right] \left( 1 - e^{-2\tau_r/t} \left[ I_0\left(2\frac{\tau_r}{t}\right) + I_1\left(2\frac{\tau_r}{t}\right) \right] \right). \quad (1.18)$$

In fact, it can be shown that Eq. (1.18) is true for any value of  $\Delta z_0$  (and not just for ( $\Delta z_0 \rightarrow +\infty$ )), and hence it is independent of the confocal aperture. It is important

to note that Eq. (1.18) is equivalent to the expression of Soumpasis (1983) [23] for 2-D diffusion in the case of a *stationary* bleaching beam with uniform radial intensity distribution, except that we have explicitly taken the bleaching depth into account. This leads to the important conclusion that, for objective lenses of low numerical aperture (for which  $(z_0 \rightarrow +\infty)$ ), the 3-D Eq. (1.16) for a disk bleached by a *scanning* beam reduces to the simpler 2-D formula for a uniform disk bleached by a *stationary* beam [23]. It also follows that Eq. (1.16) can be considered to be a 3-D expansion of the already known 2-D formula for a uniform disk bleached by a *stationary* beam.

In this work we will use relatively low NA lenses (NA  $\sim 0.2$ ) for which we have seen that the 3-D Eq. (1.16) does not give more accurate results than Eq. (1.18) for the 2-D case. For lenses of slightly higher NA (NA  $\sim 0.5$ ) it is expected that Eq. (1.16) will be needed instead. We also recall at this point that the 3-D expression Eq. (1.16) will not be valid for lenses of high NA. However, the 2-D expression Eq. (1.18) will be valid for lenses of high NA as well if the sample is thin compared to the axial resolution of the scanning beam. In that case there will be uniform bleaching along the z-axis throughout the sample and the diffusion is restricted to two dimensions.

Eqs. (1.16), 1.17 and (1.18) are valid if all molecules are mobile. In practice, however, there can be a mobile fraction  $k$  (and an immobile fraction  $1 - k$ ). To take such a mobile fraction  $k$  into account, these expressions have to be substituted into the right part of

$$F_{tot}(t) = F_{tot}(0) + k(F_{tot}(t) - F_{tot}(0)). \quad (1.19)$$

Let it be noted that for numerical computations, Eq. (1.18) cannot be used to calculate the fluorescence at  $t = 0$  (i.e. immediately after bleaching). Instead, the expression

$$\frac{F_{tot}(0)}{F_0} = 1 + \sum_{n=1}^{+\infty} \left[ \frac{(-K_0)^n}{n!} \frac{1}{\sqrt{1+n}} \right]. \quad (1.20)$$

should be used, as explained in Appendix B, section B.1.

It is worth recalling that we have made a number of assumptions in the derivation of the FRAP model that are to be met by the experimental conditions:

1. The fluorescent molecules in the sample have to be initially uniformly distributed. This means that there should be no concentration gradient present before bleaching which gives rise to net diffusion.

2. The diffusion process has been assumed to be isotropic and to take place in an infinite medium. In practice, the latter condition means that during the time period over which the recovery is observed, the diffusion front should not have reached any boundaries at which it will be reflected and influence the free diffusion process [34]. By examining the sample with the confocal microscope, the user can choose an area that fulfills these requirements.
3. An objective lens of low NA should be used for bleaching and observation of the fluorescence recovery in a 3-D sample. Lenses of high NA can be used in combination with the 2-D expressions if the thickness of the sample is small compared to the axial resolution of the lens, in which case the diffusion is restricted to two dimensions.
4. The bleaching phase has to be sufficiently short to avoid recovery during bleaching. As a rule of thumb, the total bleaching time should be at least  $15\times$  smaller than the characteristic recovery time [1].
5. Finally, there should be no flow present in the medium that can contribute to the fluorescence recovery, which can be checked by examining the position of the bleached disk in the recovery images.

## **1.3 Materials and methods**

### **1.3.1 FRAP equipment**

The FRAP experiments are performed on a CSLM (model MRC1024 UV, Bio-Rad, Hemel Hempstead, UK) modified to be able to bleach arbitrary regions [29]. All bleaching experiments have been performed with the 488-nm line of a 4 W Ar-ion laser (model Stabilite 2017; Spectra-Physics, Darmstadt, Germany). In general, the intensity of the bleaching beam is  $10^3\times$  to  $10^4\times$  higher than the detection beam. Typical bleaching powers in the sample range from 1 to 15 mW. A  $10\times$  objective lens (CFI Plan Apochromat; Nikon, Badhoevedorp, The Netherlands) with a numerical aperture (NA) of 0.45 was used. On the Bio-Rad MRC1024, however, the back aperture of this lens is only partially filled, resulting in a lower effective NA of  $\sim 0.2$  and an increased resolution radius of  $r_0 = 1\ \mu\text{m}$ .

### **1.3.2 Test solutions**

Before performing FRAP measurements on solutions of a fluorophore, the concentration range has to be determined in which a linear relation exists between the observed

fluorescence and the concentration of the fluorophore. Based on the outcome of such experiments on FITC-dextran (Sigma- Aldrich, Bornem, Belgium) solutions (prepared in HEPES buffer at pH 7.4), the following concentrations have been chosen: 2 mg/ml for FITC-dextran  $M = 2 \times 10^6$  g/mol, which will be referred to as FD2000; 1.5 mg/ml for FITC-dextran  $M = 4.64 \times 10^5$  g/mol, which will be referred to as FD464; 4 mg/ml for FITC-dextran  $M = 1.67 \times 10^5$  g/mol, which will be referred to as FD167. Next, FITC-dextran solutions were prepared in HEPES buffer containing varying amounts of glucose. The glucose was used to vary the dynamic viscosity of the FITC-dextran solutions. The dynamic viscosity  $\eta$  [Ns/m<sup>2</sup>] for each of the solutions was determined by measuring its density  $\rho$  [kg/m<sup>3</sup>] and kinematic viscosity  $\nu$  [m<sup>2</sup>/s] and making use of the relation  $\eta = \rho\nu$ . The kinematic viscosity was measured with a capillary viscosimeter (model PVS1; Lauda Dr. R. Wobser GmbH & CO. KG, Lauda-Königshofen, Germany). The density was determined with a picnometer.

FRAP experiments were performed on the FITC-dextran solutions in borosilicate microcapillaries (Vitrocom, Mountain Lakes, NJ) with square cross-section ( $300 \mu\text{m} \times 300 \mu\text{m}$  inner dimensions, 5 cm long, wall thickness of  $150 \mu\text{m}$ ) to eliminate any currents in the solution while retaining a 3-D environment for the diffusion to take place.

### **1.3.3 Bovine vitreous**

Vitreous gel was dissected from bovine eyes obtained from the local abattoir. For each FRAP experiment,  $\sim 200$  ml of vitreous from an individual eye was put in a cuvette with a glass bottom for use with an inverted microscope (Nalge Nunc International, Naperville, IL). 30 ml of the FITC-dextran solutions (described above) was injected at several locations near the center of the vitreous gel with a needle. The samples were stirred by hand with a plastic rod for at least  $10\times$ . The fluorescent solution was allowed to spread throughout the sample for 30-60 min before performing FRAP experiments. FRAP measurements were performed in those regions of the sample that showed the lowest fluorescence signal to make sure that measurements were performed in the vitreous gel and not in or near one of the injection sites.

### **1.3.4 Cystic fibrosis sputum**

Approval for the collection of cystic fibrosis (CF) sputum was obtained from the Ethics Committee of the University Hospital of Ghent. The sputum was expectorated by

CF patients during chest physiotherapy. Details on the collection and storage of the CF sputum have been described previously [7].

Fluorescent (yellow-green) polystyrene nanospheres of two different sizes, bearing carboxyl groups on their surface, were obtained from Molecular Probes (Leiden, The Netherlands). The weight-average hydrodynamic diameters, measured by dynamic light scattering, of the nanospheres diluted in distilled water were  $37 \text{ nm} \pm 2 \text{ nm}$ , and  $89 \text{ nm} \pm 2 \text{ nm}$ . The fluorescent nanospheres, diluted in ‘sputum buffer’ (85 mM  $\text{Na}^+$ , 75 mM  $\text{Cl}^-$ , 3 mM  $\text{Ca}^{2+}$ , and 20 mM HEPES pH 7.4), and the FITC-dextran solutions were gently mixed with the freshly collected CF sputa and incubated overnight at  $48^\circ\text{C}$ . The final concentration of the nanospheres in the CF sputum was  $4.02 \times 10^{12}$  particles/ml for the 37 nm particles and  $4.45 \times 10^{12}$  particles/ml for the 89 nm particles. The final concentration of the FITC-dextran in the CF sputum was 0.36, 0.14, and 0.18 mg/ml for FD167, FD464, and FD2000, respectively.

To perform FRAP experiments, the CF sputum containing the FITC-dextran or nanospheres was sandwiched between a microscope slide and a coverslip sealed by two adhesive spacers of  $120 \mu\text{m}$  thickness each (Secure-Seal Spacer; Molecular Probes, Leiden, The Netherlands) in between.

### 1.3.5 Experimental FRAP protocol

The sample is at first positioned on the microscope stage and the location of interest is brought into focus. Since Eq. (1.18) is independent of the confocal diaphragm setting, it is opened completely to detect as much fluorescence light as possible with a low power illumination beam and to minimize bleaching when recording the fluorescence recovery. After a disk of a particular diameter has been drawn in the bleaching software, a time-series is recorded with the CSLM resulting in a stack of images (see Fig. 1.3A). The first image of the series shows the sample before bleaching, the second one shows the disk at the time of bleaching, and the subsequent images show the recovery process after bleaching. The time interval between the images is user-defined, with a minimum of 2.13 s for our confocal microscope at  $512 \times 512$  pixels per image and ‘normal’ scanning speed<sup>2</sup>. The choice of this time period will depend on the recovery speed. Usually, we have recorded stacks of 30 images with a time interval between 2.5 s and 60 s.

---

<sup>2</sup>For a box size of  $128 \times 512$  pixels, the time interval can be reduced to 1.5 s.

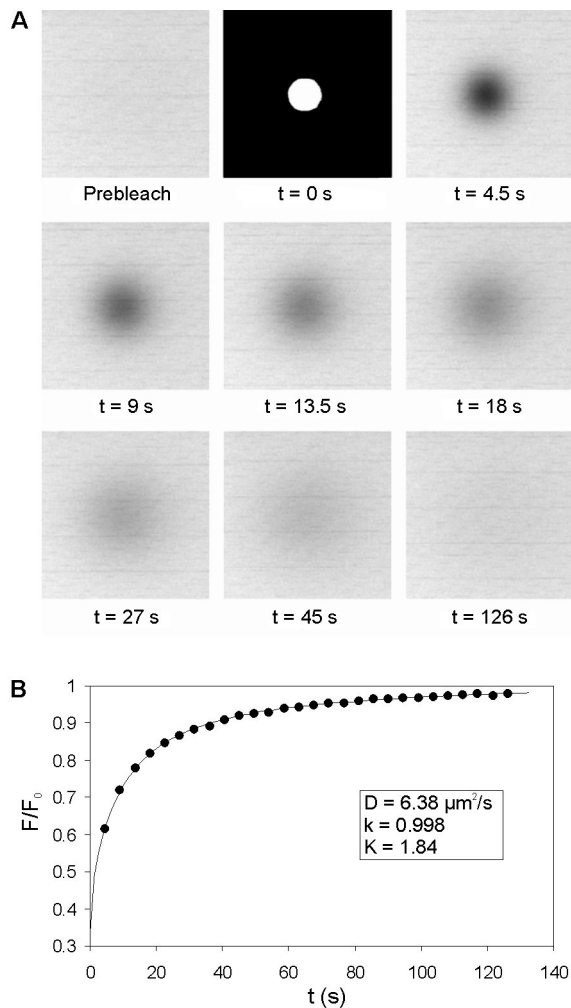


**Figure 1.3:** (A) A FRAP experiment is performed on the FD167 solution with 30% glucose (w/w). An image sequence is recorded of 30 images at regular time intervals of 4.5 s. The first image shows the sample before bleaching, the so-called prebleach image. When the second image is scanned, the bleaching software is activated and a user-defined disk is bleached. Next, the laser intensity is switched back to its previous level to record the recovery over multiple images at regular time intervals. (B) A dedicated image processing program extracts the recovery curve from the image sequence, as explained in the main text. The experimental data are indicated by black circles ( $\bullet$ ). A best fit of the model (solid line) finally yields the translational diffusion coefficient  $D$ , the mobile fraction  $k$ , and the bleaching parameter  $K_0$ .

### 1.3.6 Data extraction and fitting

An image processing program was written to extract the experimental recovery curve from the stack of images. The data extraction is based on the following calculations. First, the position of the bleached disk is analyzed by a center-of-mass algorithm that determines the center of the bleached disk for each of the images. This allows checking for any displacement by flow in the sample. Second, each of the recovery images is normalized to the first image, the prebleach image. To prevent an increase in noise due to this process, each of the images is first smoothed by a  $3 \times 3$  convolution mask. Next, the mean fluorescence intensity inside the disk is calculated for each image. To correct for any bleaching that might have occurred during the recording of the recovery phase, this value is normalized to the mean fluorescence intensity of one or more user-defined background regions. Finally, the experimental parameters are determined by a least-squares fit of Eqs. (1.13), (1.18), and (1.19) to the experimental recovery curve, as is shown in Fig. 1.3B. Let it be noted that the uniform disk model indeed accurately describes the experimental recovery curve. Because the recovery data results from integrating the fluorescence signal over the entire bleached disk, there is only a *very small level of noise* present in the experimental data.

## 1.4 Results and discussion

To fully examine and validate the new FRAP model, the influence of the different model parameters - the bleaching parameter  $K_0$ , the interline distance  $\Delta y$ , and the radius of the bleached disk  $w$  - on the measured diffusion coefficient  $D$  has to be examined.

### 1.4.1 The bleaching parameter $K_0$

#### $D$ vs. $K_0$

If the uniform disk model is correct, the measured diffusion coefficient  $D$  should not be dependent on the bleaching depth, which is directly related to the bleaching parameter  $K_0$  according to Eq. (1.9). Therefore, we have bleached in the FD167 solution with 30% (w/w) glucose, disks of constant radius  $w = 12.5 \mu\text{m}$  (which is a correct value as will be shown further on) but with different zoom settings to obtain a series of different  $K_0$  values (cfr. Eq. (1.11)). The measured diffusion coefficient versus the corresponding  $K_0$  value is shown in Fig. 1.4A. The experiments have been evaluated both with and without taking the broadening of the bleaching disk with increasing bleaching depth into account, as predicted by Eq. (1.13). Without the correction for the radius  $w$ , there is a slight



decrease of the measured diffusion coefficient  $D$  with increasing bleaching depth because of an underestimation of the radius  $w$ . Taking Eq. (1.13) into account for  $r_0 = 3.5 \mu\text{m}$  nicely eliminates this dependency, whereas a correction for  $r_0 = 1.4 \mu\text{m}$  is clearly insufficient. This result supports other observations from unrelated bleaching experiments that for fluorescein-labeled probes, the lateral resolution (and very likely the axial resolution as well) increases considerably at bleaching intensities compared to the resolution at imaging intensities. This increase in resolution is caused by the saturation of fluorescein at high bleaching intensities, as will be discussed in detail in Chapter 2. It is also important to note from the uncorrected values in Fig. 1.4A that, for  $0.5 \leq K_0 \leq 2$ , the variation of the diffusion coefficient is smaller than the experimental standard deviations (SDs). Therefore, we suggest that within the experimental accuracy, Eq. (1.13) can be neglected in practice for  $0.5 \leq K_0 \leq 2$ .

### First-order photobleaching kinetics

The experiments from this section can also be used to check if the bleaching kinetics can be described by a first-order reaction, as was assumed in the derivation of the model. According to Eq. (1.11), the bleaching parameter  $K_0$  can be written in terms of the zoom setting  $Z$ . If two disks of the same radius  $w$  are bleached in the same sample with identical bleaching intensity but with a different zoom setting  $Z_1$  and  $Z_2$ , it follows that, if first-order kinetics are valid, the ratio of the two fitted  $K_0$  values should be equal to:

$$\frac{K_{01}}{K_{02}} = \left( \frac{Z_1}{Z_2} \right)^2. \quad (1.21)$$

The  $K_0$  values from the experiments above can be used to verify Eq. (1.21) since the radius of the bleaching disk and bleaching intensity were held constant whereas the different bleaching depths were obtained by changing the zoom setting. The results are shown in Fig. 1.4B, where Eq. (1.21) was calculated for each measurement with regard to the measurement with lowest zoom setting and  $K_0$  value. A linear fit to these data shows there is a good correspondence to Eq. (1.21) because a slope is found of approximately 1 and an intercept of approximately 0.

### Influence of noise in relation to $K_0$

Inspection of the error flags in Fig. 1.4A reveals that the relative SD values of the measured diffusion coefficients increase with decreasing  $K_0$  values and become relatively

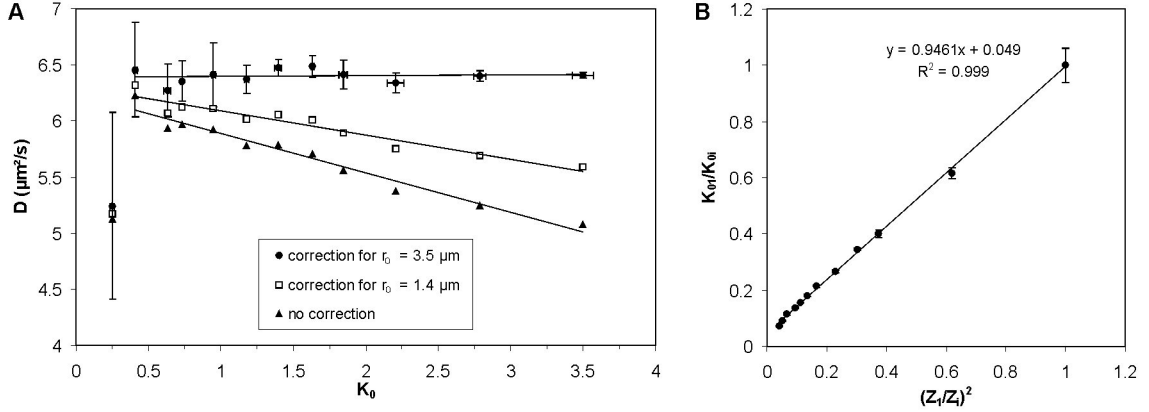


**Figure 1.4:** (A) FRAP measurements have been performed ( $w = 12.5 \mu\text{m}$ ) on the solution of FD167 in 30% (w/w) glucose, for different bleaching depths (i.e. different  $K_0$  values). All data are the result of 5-7 measurements and the error flags are the corresponding SD values. For clarity, the error flags are only shown for one of the data series, but are virtually the same for both other series. The black triangles are the results when Eq. (1.13) is not taken into account (no correction for the increasing radius with increasing bleaching depth). Because of an underestimation of the real bleaching radius, the measured diffusion coefficient decreases with increasing  $K_0$  value. The white squares are the results when Eq. (1.13) is taken into account for  $r_0 = 1.4 \mu\text{m}$  and the black circles for  $r_0 = 3.5 \mu\text{m}$ . The solid lines are linear fits to the different data series. It is clear that the ‘normal’ resolution  $r_0 = 1 \mu\text{m}$  (see section 1.3.1), is insufficient to correct for the dependency on  $K_0$ , confirming other observations that the effective radial resolution increases considerably at bleaching intensities for fluorescein-labeled probes. (B) As explained in the main text, the relationship  $K_{01}/K_{0i} = (Z_1/Z_i)^2$  should be valid in the case of first-order bleaching kinetics. A linear fit to the experimental data shows this to be true in good approximation (slope  $\approx 1$  and intercept  $\approx 0$ ).

large for  $K_0$  values below 0.5. Although not explicitly shown, the same observation is true for the SD values of the mobile fraction  $k$  and bleaching parameter  $K_0$ . In other words, the accuracy of the measurements tends to decrease with decreasing bleaching depth. We will now show this is due to the presence of noise, which will mainly depend on both the amplification of the light detector of the CSLM, also called the ‘gain’, and the number of pixels in the bleached disk over which the recovery data is integrated. Simulations were performed based on Eq. (1.18) to which a certain percentage of normally distributed noise was added. Then the fitting routine was applied to these data to examine the influence on the fitted parameters. For the simulations we have taken  $D = 5.5 \mu\text{m}^2/\text{s}$ ,  $k = 1$  and different values for  $K_0$  between 0.25 and 3.5. Ten simulations are performed for each  $K_0$  value and for two levels of noise, 0.5% and 1%. Some examples are shown in Fig. 1.5A, from which it is clear that the influence of noise increases with decreasing bleaching depth and it is to be expected that the fitted parameters become less accurate for smaller values of  $K_0$ . The results for the diffusion coefficient for both noise levels are shown in Fig. 1.5B. These simulations have shown that in all cases the exact values are found for all parameters within the standard deviation (SD). As expected, the relative SD for each of the parameters increases with decreasing  $K_0$  value (i.e. decreasing bleaching depth). Evidently, the SD values for the 1% noise level are larger compared to the 0.5% level. For  $K_0$  values below 0.5 the SD’s become relatively large compared to the other values and we conclude that, because of the presence of noise, as a rule of thumb the bleaching parameter should be preferably at least 0.5 to obtain accurate measurements.

### 1.4.2 The interline distance $\Delta y$

In the model it is assumed that the disk is uniformly bleached. As explained in Appendix A, section A.4, this condition is met for a scanning beam with Gaussian intensity distribution in the focal plane if  $\Delta y \leq 0.5r_0$ . The distance between the adjacent lines  $\Delta y$  when scanning an image with the CSLM is directly determined by the electronic zoom setting. For the  $10\times$  NA 0.45 objective lens used in this study,  $\Delta y = 2.115 \mu\text{m}$  at zoom 1, whereas at zoom setting  $Z$ , this becomes  $\Delta y = 2.115/Z \mu\text{m}$ . Hence, it is possible to verify experimentally to what extent the measurements are independent of the interline distance by performing FRAP experiments on the same solution with different zoom settings.

The results for  $D$  as a function of the zoom setting are shown in Fig. 1.6A. The radius of the bleached disk was held constant at  $15 \mu\text{m}$  (which is a correct value as will be shown in the next section). The horizontal line shows the mean value of all measurements. As

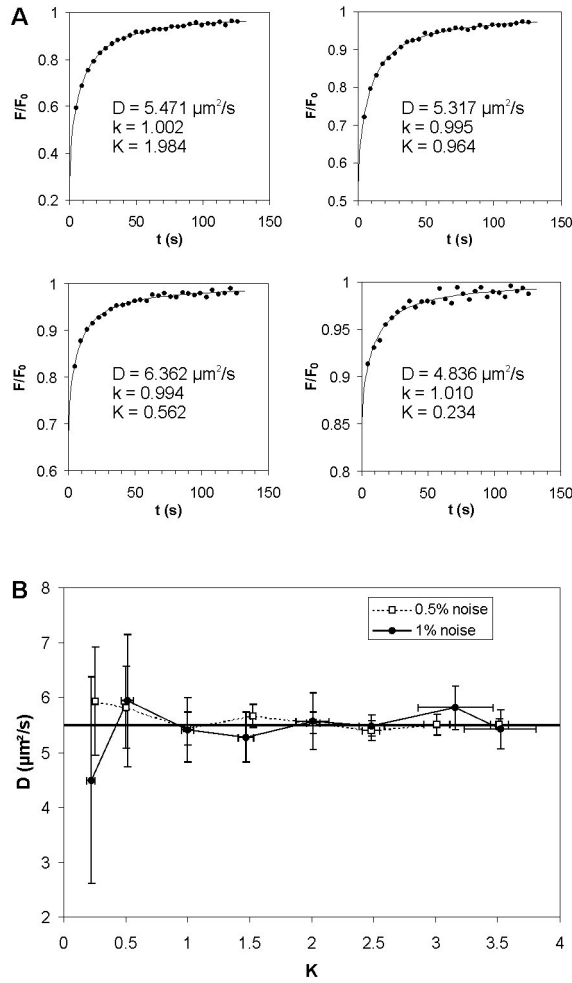


**Figure 1.5:** (A) Recovery curves have been simulated according to Eq. (1.18) for  $D = 5.5 \mu\text{m}^2/\text{s}$ ,  $k = 1$  and  $0.5 \leq K_0 \leq 3.5$  to which 0.5% and 1% normally distributed noise is added. To evaluate the influence of noise on the measured parameters, a fit of the model is applied to these data. Examples are shown for 0.5% noise and  $K_0 = 0.25, 0.5, 1$  and  $2$ . As can be seen, the noise will have a greater effect on the fitting of data with small bleaching depths. (B) Ten simulations have been calculated for each different  $K_0$  value of the model parameters and both noise levels to obtain the mean value and corresponding SD. The results for the diffusion coefficient are shown in the graph, where the error flags are the SD values. The horizontal line indicates the correct value of  $D = 5.5 \mu\text{m}^2/\text{s}$ , which in all cases is found within the SD. The SD's increase with decreasing  $K_0$  value (i.e. with decreasing bleaching depth) because the recovery interval becomes smaller. Evidently, the SD's also increase with increasing noise level.

can be seen, the measured diffusion coefficient is independent of the zoom setting for at least down to zoom 3, which corresponds to an interline distance of  $\Delta y = 0.705 \mu\text{m}$ . At lower zoom settings no sufficient bleaching could be obtained for meaningful measurements, even at maximum laser intensity. For the  $10\times$  objective lens, the radial resolution is  $1 \mu\text{m}$ , although at bleaching intensities the effective bleaching resolution seems to be rather  $3.5 \mu\text{m}$  as discussed in the previous section. Hence we have experimental proof that the measurements are independent of the interline distance for at least up to  $0.2r_0$ , which is in agreement with what is expected theoretically. Larger interline distances will, in practice, not occur very often because of insufficient bleaching at low zoom settings.

### 1.4.3 The radius $w$ of the bleached disk

As discussed in section 1.2.2, the radius  $w$  of the bleached disk should be sufficiently large compared to the radial resolution  $r_0$  of the bleaching beam. Therefore, we have performed FRAP experiments on the same solution, FD167 with 40% (w/w) glucose, with increasing values for the radius  $w$ , ranging from  $5.7 \mu\text{m}$  to  $20.8 \mu\text{m}$ . As can be seen from Fig. 1.6B, the measured  $D$  values are independent of the radius in the region  $w = 12.5 \mu\text{m}$  to  $21 \mu\text{m}$ . For smaller values of  $w$  it is clear that the discontinuous approximation is not valid any more<sup>3</sup>. Therefore, we have always bleached disks with a radius between  $12.5 \mu\text{m}$  and  $15 \mu\text{m}$ , which corresponds to  $\sim 4\times$  the bleaching resolution in fluorescein samples. For much larger values of the radius  $w$ , deviations from the 2-D approximation are likely to occur because of an increasing contribution to the fluorescence recovery by diffusion in the  $z$ -direction.

### 1.4.4 Validation of the disk model

Having determined the ranges in which the model parameters  $K_0$ ,  $\Delta y$ , and  $w$  may vary, it is now possible to test the ability of the new model to accurately measure diffusion coefficients. According to the Stokes-Einstein equation, a linear relation should be found between the translational diffusion coefficient  $D$  ( $\text{m}^2/\text{s}$ ) and the reciprocal value of the dynamic viscosity  $\eta$  ( $\text{Ns}/\text{m}^2$ ),

$$D = \frac{\kappa T}{6\pi\eta r_H}, \quad (1.22)$$

---

<sup>3</sup>As explained in Chapter 3, the effective bleaching resolution depends on the laser power in the sample. For lower laser intensities, the minimal radius will therefore be smaller than  $12.5 \mu\text{m}$ .

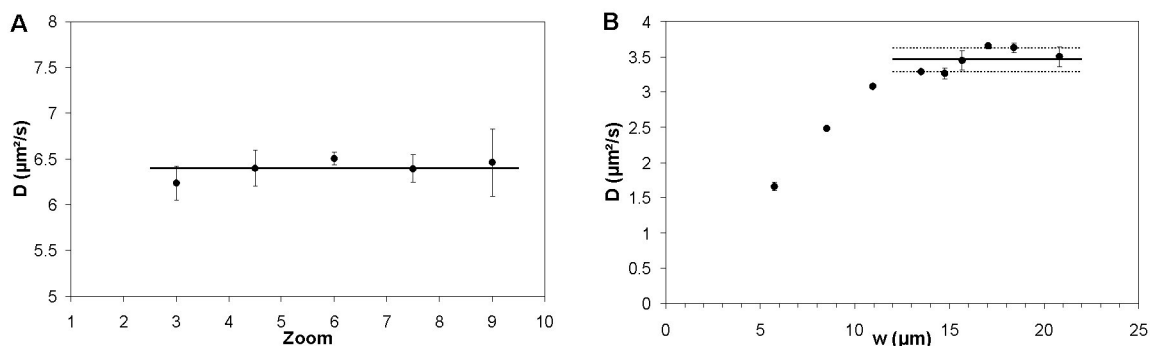


**Figure 1.6:** (A) The zoom setting on a CSLM determines the interline distance  $\Delta y$  for a given objective lens, which must be small enough for the uniform disk model to be valid. On our instrument,  $\Delta y$  is  $2.115 \mu\text{m}$  at zoom 1 for the  $10\times$  objective lens and becomes  $\Delta y/Z$  at zoom  $Z$ . Experiments have been performed on the FD167 solution with 30% (w/w) glucose, with a constant disk radius of  $15 \mu\text{m}$  and different zoom settings:  $Z = 3, 4.5, 6, 7.5,$  and  $9$ . The results are shown in the graph where each circle ( $\bullet$ ) is the mean result of 4-5 measurements and the error flags are the corresponding SD values. The horizontal line indicates the mean of all measurements. As can be seen, there is no dependency on the zoom setting within the experimental accuracy, for at least down to zoom 3. (B) For the uniform disk model to be valid, the radius  $w$  of the bleaching disk should be sufficiently large compared to the resolution  $r_0$  of the bleaching beam. FRAP measurements have been performed using different radii on the FD167 solution with 40% (w/w) glucose. The results for the diffusion coefficient  $D$  as a function of the radius  $w$  are shown in the graph. Each circle ( $\bullet$ ) is the mean of five measurements and the error flags are the corresponding SD values. The diffusion coefficient  $D$  becomes independent of  $w$  starting from approximately  $w = 12.5 \mu\text{m}$ . The solid horizontal line indicates the mean value of the six measurements with  $w \geq 12.5 \mu\text{m}$  and the dashed lines indicate the corresponding SD value.

where  $r_H$  is the hydrodynamic radius (m) of the diffusing molecules,  $\kappa$  the Boltzmann constant ( $1.38 \times 10^{-23}$  J/K), and  $T$  the absolute temperature (K). Fig. (1.7)A shows the measured diffusion coefficient as a function of the reciprocal dynamic viscosity of the FITC-dextran glucose solutions. A good linear relationship is found between  $D$  and  $1/\eta$ , as predicted by Eq. (1.22). Additionally, the ability of the uniform disk FRAP method to determine correctly absolute diffusion coefficients can be verified by comparing the measured values to their theoretical estimates. The hydrodynamic radius  $r_H$  of the FITC-dextrans can be estimated from a previously reported empirical relation [35, 36]:

$$r_H = 0.015M^{0.53 \pm 0.02}, \quad (1.23)$$

where the molecular weight  $M$  is expressed in g/mol and  $r_H$  in nm. Based on Eq. (1.23), the FITC-dextrans used in this study have a hydrodynamic radius of 32.8 nm (FD2000), 15.1 nm (FD464), and 8.8 nm (FD167). Knowing  $r_H$  and  $\eta$ , a theoretical estimate of the diffusion coefficient of the FITC-dextrans can be made with Eq. (1.22). A parity plot is presented in Fig. (1.7)B showing the theoretically estimated values of the diffusion coefficients versus those actually measured. The solid line corresponds to Eq. (1.23) using the exponent of 0.53, whereas the dashed lines are calculated for exponent values of 0.51 and 0.55. As can be seen, there is a good correspondence between the measured values and their theoretical estimates. Considering Eq. (1.23) was determined from unrelated FRAP experiments on FITC-dextrans using a different FRAP model and a different instrument, these results prove the model is able to accurately determine the absolute values of the translational diffusion coefficients.

In addition we have measured the diffusion coefficient values of three aqueous solutions (FD2000, 37 nm, and 89 nm polystyrene nanospheres) by dynamic light scattering. The results for the diffusion coefficients are  $6.16 \pm 0.68 \mu\text{m}^2/\text{s}$  for FD2000,  $12.46 \pm 0.70 \mu\text{m}^2/\text{s}$  for the 37-nm spheres, and  $5.19 \pm 0.12 \mu\text{m}^2/\text{s}$  for the 89-nm spheres. The diffusion coefficients of the same solutions were measured with the new FRAP technique as well:  $6.43 \pm 0.09 \mu\text{m}^2/\text{s}$  for FD2000,  $11.37 \pm 0.58 \mu\text{m}^2/\text{s}$  for the 37 nm spheres, and  $5.68 \pm 0.09 \mu\text{m}^2/\text{s}$  for the 89 nm spheres. It is clear that the results from both techniques are in close agreement, giving additional proof that the new FRAP model is able to accurately measure absolute translational diffusion coefficients.

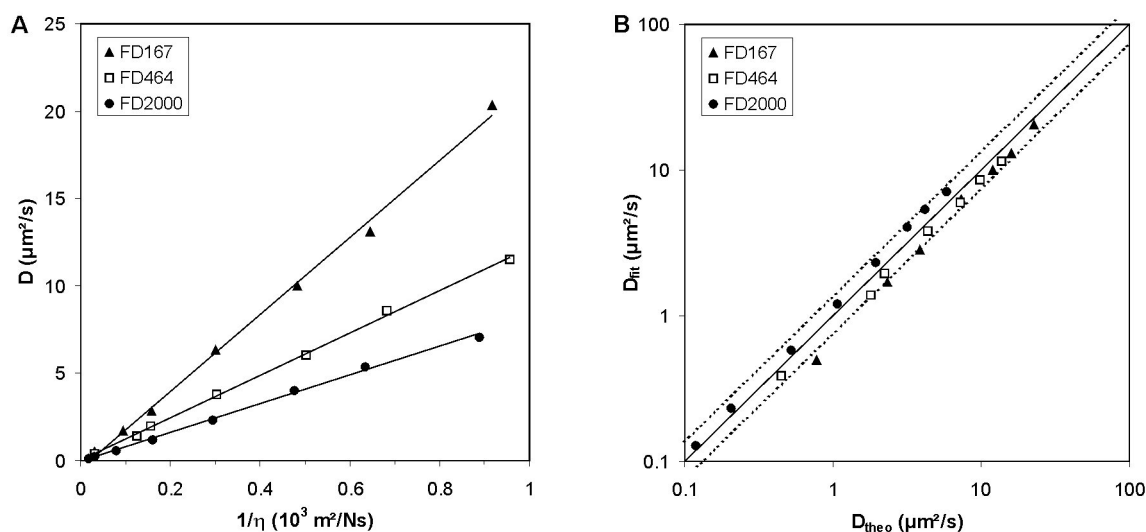


**Figure 1.7:** (A) The uniform disk model is verified with the Stokes-Einstein relation. FRAP measurements have been performed on FITC-dextran solutions. A linear relationship between the measured diffusion coefficient  $D$  and the reciprocal viscosity ( $\eta$ ) is found, as predicted by the Stokes-Einstein equation. (B) Using Eqs. (1.22) and (1.23), the diffusion coefficient values of the FITC-dextran solutions can be estimated. The parity graph shows the measured diffusion coefficients  $D_{\text{fit}}$  versus the estimated values  $D_{\text{theo}}$ . The solid line has been calculated from Eq. (1.23) with an exponent of 0.53 and the dashed lines correspond to the exponent values of 0.51 and 0.55. As almost all measured diffusion coefficients fall within these limits, this proves the model can be used to accurately measure absolute translational diffusion coefficients.



### 1.4.5 FRAP measurements with the CSLM in bovine vitreous and cystic fibrosis sputum

The eye is an ideal target for DNA therapy because it is easy to reach for treatment. DNA packed in viruses or non-viral nanoparticles can be administered by intravitreal injection. However, as the retinal epithelial cells are situated at the back of the eye, it has to be examined whether large molecules and nanoparticles can diffuse through the vitreous toward the target cells. A similar question arises when one wants to deliver drugs to the lungs, such as for treatment of CF, where the mucus may hinder the transport of therapeutics to the underlying lung cells.

As a first application, the new FRAP model, which is well-suited for measurements in bulk 3-D samples, was used to evaluate the effect of the size of macromolecules on their diffusion through both bovine vitreous and CF sputum. FITC-dextran solutions were injected into the vitreous gel and were observed to spread freely throughout the sample, resulting in a rather homogeneous fluorophore distribution. When mixing the CF sputum with FITC-dextran, however, a more heterogeneous distribution was obtained (see Fig. 1.8A). For comparison, the CF sputum was also mixed with fluorescent nanospheres (see Fig. 1.8B). While the FITC-dextran seemed to be located between the biopolymers of the sputum, the polystyrene nanospheres did rather adsorb to the biopolymers, probably due to hydrophobic interactions. A similar observation has already been reported for polystyrene nanospheres mixed with cervical mucus [21]. The FRAP measurements did indeed reveal substantial immobile fractions of 38% for the 37 nm spheres and 56% for the 89 nm spheres (see Fig. 1.8C and D).

The results of the FRAP measurements are shown in Table 1.1. A complete fluorescence recovery in vitreous for all FITC-dextran ( $k \approx 1$ ) was observed, suggesting that the molecules did not strongly chemically interact with the biopolymers. The diffusion coefficient values of FD167, FD464, and FD2000 in vitreous decreased, respectively, to  $81 \pm 3\%$ ,  $74 \pm 6\%$ , and  $65 \pm 8\%$ , compared to the value in buffer. In CF sputum, the diffusion coefficient values of FD167, FD464, and FD2000 decreased, respectively, to  $34 \pm 3\%$ ,  $37 \pm 3\%$ , and  $32 \pm 2\%$ . These results show that, in vitreous, increasing the size of the diffusing molecules induces a stronger sterical retardation by the meshwork. In CF sputum, on the other hand, the decrease in diffusion coefficient values of the FITC-dextran seems to be rather independent of their size, indicating that the CF mucus does not impose a sterical hindrance on these molecules. These observations might be explained by the following hypothesis. The interfibrillar spaces of vitreous contain hyaluronic acid, which is a very

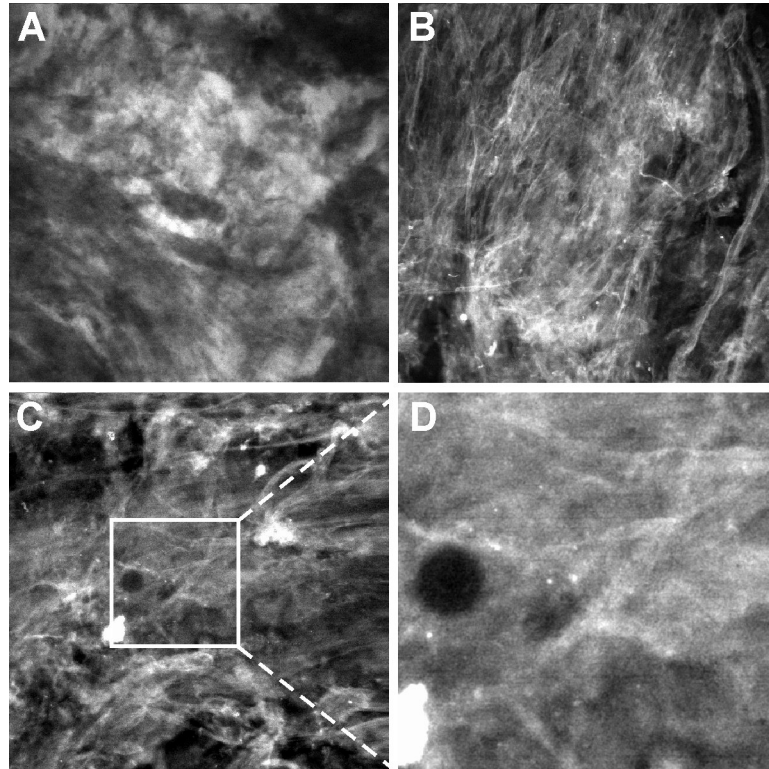


**Figure 1.8:** (A) Confocal image of cystic fibrosis sputum mixed with a FITC-dextran solution of 464 kDa molecular weight. The field of view (FOV) is  $1047 \mu\text{m} \times 1047 \mu\text{m}$ . (B) Confocal image of cystic fibrosis sputum mixed with 89 nm polystyrene nanospheres. The nanospheres tend to adsorb to the biopolymers of the CF sputum. The FOV is  $1047 \mu\text{m} \times 1047 \mu\text{m}$ . (C) Confocal image of cystic fibrosis sputum mixed with 89 nm spheres, recorded after the completion of a FRAP experiment in which a disk of radius  $15 \mu\text{m}$  was bleached. Because of the presence of an immobile fraction, the recovery is incomplete and the bleached disk remains visible. The FOV is  $524 \mu\text{m} \times 524 \mu\text{m}$ . (D) Enlargement of the central part of image C. This image is the last image of the time-series recorded in the FRAP experiment. The FOV is  $175 \mu\text{m} \times 175 \mu\text{m}$ .

efficient network-forming polymer [35, 37, 38] having a mesh size of tens of nanometers [35]. The hyaluronic acid network sterically hinders the diffusion of the FITC-dextrans: the larger the molecule, the stronger the sterical hindrance. In contrast, the aqueous pores of the CF sputum network have a diameter of 100-400 nm [7] and are filled with free (not entangled) biopolymers. This diluted biopolymer solution does not sterically hinder the diffusion of FITC-dextrans through the pores, but slows down the diffusion of the FITC-dextrans by a viscous drag, which is independent of the size of the diffusing FITCdextrans.

	HEPES buffer		CF sputum		Bovine vitreous	
	$D \pm SD$	$k \pm SD$	$D \pm SD$	$k \pm SD$	$D \pm SD$	$k \pm SD$
FD167	$18.80 \pm 0.17$	$1.003 \pm 0.002$	$6.43 \pm 0.64$	$0.977 \pm 0.014$	$15.23 \pm 0.62$	$0.995 \pm 0.018$
FD464	$10.97 \pm 0.50$	$1.005 \pm 0.003$	$4.09 \pm 0.24$	$0.971 \pm 0.016$	$8.07 \pm 0.53$	$1.010 \pm 0.003$
FD2000	$6.43 \pm 0.09$	$1.000 \pm 0.003$	$2.05 \pm 0.11$	$0.900 \pm 0.020$	$4.18 \pm 0.53$	$0.984 \pm 0.022$

**Table 1.1:** Measurement ( $n = 5$ ) of the diffusion coefficient  $D$  ( $\mu\text{m}^2/\text{s}$ ) and mobile fraction  $k$  by FRAP of FITC-dextrans in bulk 3-D samples: HEPES buffer, cystic fibrosis sputum, and bovine vitreous

## 1.5 Conclusions

We have presented a new 3-D FRAP model based on the bleaching of a uniform disk by the scanning beam of a confocal scanning laser microscope. Although the 3-D model has been derived for lenses of low numerical aperture, the corresponding 2-D expressions will be valid for high numerical aperture lenses as well if the sample thickness is small enough compared to the axial resolution of the bleaching beam. In addition, it has been shown that the model is equally valid for a stationary beam with a uniform radial intensity distribution.

Through a rigorous mathematical treatment of the bleaching process by a scanning beam, we have been able to show that the distance between two adjacent lines on the CSLM should be less than one-half the radial resolution of the scanning beam to obtain a uniformly bleached geometry. Additionally, the experiments have shown that the radius of the bleached disk should be  $\sim 4\times$  the resolution of the bleaching beam to avoid boundary effects. Therefore, the uniform disk approach in combination with low NA lenses is ideal for measurements on bulk samples such as biological or synthetic gels and solutions. In combination with high NA lenses, the corresponding 2-D expressions can be used for intracellular measurements as well if the cell thickness is small compared to the axial resolution

of the bleaching beam.

The new FRAP model has the advantage of not requiring extensive mathematical or programming skills because the mathematical expressions are straightforward and can easily be programmed in a standard fitting routine. As the method of bleaching a disk by a scanning beam is readily available on commercial CSLMs, it offers a versatile tool for FRAP measurements and can be applied by anyone familiar with the CSLM instrument.

## Chapter 2

# Implications of anomalous photobleaching behaviour of fluorescein on FRAP measurements

### Summary

In the evaluation of the FRAP disk model which has been presented in Chapter 1, we have indirectly observed that the resolution radius of the bleaching beam seems to be larger than expected theoretically (see section 1.4.3). We have studied this effect separately and report our findings in this chapter. We will present both experimental and theoretical evidence that fluorescein, one of the most frequently used fluorophores in fluorescence recovery after photobleaching (FRAP) experiments, does not always comply with the basic assumptions that are made in many FRAP models: an invariant bleaching intensity distribution (BID) in combination with first order photobleaching kinetics. We show that at high light intensity levels which are typical for the photobleaching phase of FRAP experiments, the higher order diffraction maxima of the BID substantially contribute to the photobleaching process and can no longer be neglected. As a result, the bleaching profiles are larger than expected theoretically from the FRAP models, as if being bleached by an expanded BID. Although this effect is not always directly evident from the FRAP experiments, neglecting it may shift the calculated diffusion coefficient by as much as over one order of magnitude. FRAP models that do not require the actual knowledge of the BID are insensitive to this effect. Others will require the experimental determination of the actual bleaching profile for each experiment in combination with an adjustment of the theory to take a variable apparent BID into account.

## 2.1 Introduction

The diffusion coefficient can be calculated from a FRAP experiment by fitting of an appropriate FRAP model to the experimental recovery curve. In many FRAP models - the so-called discontinuous photobleaching techniques - the bleaching phase is assumed to be very short compared to the recovery time [22, 23, 24, 27, 30, 33, 39, 40, 41, 42]<sup>1</sup>. Consequently, diffusion during bleaching can be neglected and the bleaching phase can be solely described by the photochemical bleaching process. In addition, the assumption is usually made that the bleaching process can be described by an irreversible first order reaction [22, 23, 27, 30, 31, 33, 39, 42, 43, 44]:

$$\frac{\partial}{\partial t}C(x, y, z, t) = -\alpha I_b(x, y, z)C(x, y, z, t), \quad (2.1)$$

where  $C(x, y, z, t)$  is the spatial concentration of fluorophores at a bleach time  $t$ ,  $\alpha$  is the bleach rate which is specific for a certain type of fluorophore in a particular medium, and  $I_b(x, y, z)$  is the 3D intensity distribution of the bleaching beam, the ‘bleaching intensity distribution’ (BID) in short. If the bleaching beam is stationary, Eq. (2.1) immediately leads to:

$$C_b(x, y, z) = C_0(x, y, z)e^{-\alpha I_b(x, y, z)t}, \quad (2.2)$$

where  $C_0(x, y, z)$  is the fluorophore concentration distribution before bleaching and  $C_b(x, y, z)$  the fluorophore concentration distribution after bleaching during a time  $t$ . In case of a geometry bleached by a scanning beam, which is mostly the case for FRAP experiments on a CSLM, Eq. (2.1) leads to (see Chapter 1 and Appendix A):

$$C_b(x, y, z) = C_0(x, y, z)e^{-\frac{\alpha}{v\Delta y}K(x, y, z)}, \quad (2.3)$$

where  $v$  is the line scanning speed and  $\Delta y$  the distance between two adjacent scanning lines and where it is understood that  $\Delta y$  is smaller than half the resolution of the BID.  $K(x, y, z)$  is the bleaching intensity distribution which results from scanning the bleaching geometry  $B(x, y)$  with the BID  $I_d(x, y, z)$  and can be calculated from their convolution product (see Eq. (1.3)). In both cases we find a simple exponential decay of the concentration of fluorophores during bleaching.

After the ‘instantaneous’ bleaching phase, the fluorescence inside the bleached region will gradually recover due to diffusion of the bleached fluorophores out of the bleached

---

<sup>1</sup>Reference [42] corresponds to Chapter 1 of this thesis.

region and diffusion of unbleached fluorophores from the surroundings into the bleached region. The diffusion process is described by Fick's second law [34]:

$$\frac{\partial}{\partial t}C(x, y, z, t) = D\nabla^2C(x, y, z, t), \quad (2.4)$$

where  $D$  ( $\text{m}^2/\text{s}$ ) is the diffusion coefficient and  $C(x, y, z, t)$  the spatial concentration distribution of the diffusing substance at a time  $t$  *after* bleaching. To model the recovery phase, this differential equation has to be solved for the concentration distribution right after bleaching as calculated from Eq. (2.2) or (2.3). Hence, the correctness of the FRAP model depends directly on the validity of assuming first order kinetics for the photobleaching process. In case first order kinetics are not valid, the concentration distribution after bleaching will be different from the one calculated from Eq. (2.2) or (2.3). Consequently, the FRAP model will no longer be valid and the calculated values for the diffusion coefficient will be erroneous.

A very popular fluorophore for FRAP is fluorescein [1, 45] because it photobleaches fairly easily and therefore complies with the assumption of a very short bleaching phase. It has been shown, however, that the bleaching process of fluorescein is not a simple first order reaction and in microscopy, in general, it does not follow a single exponential decay [46]. It is therefore to be expected that the concentration distribution after bleaching is no longer accurately predicted by Eq. (2.2) or (2.3) when using fluorescein. One observation of this kind is reported in Chapter 1 where it was found that bleaching profiles in fluorescein samples are larger than expected theoretically as if bleaching was induced by an expanded BID.

The study presented here aims to evaluate the effect of the deviation of the bleaching process of fluorescein from first order kinetics on the spatial concentration distribution after photobleaching in a FRAP experiment. First we will repeat in short the photochemical processes leading to the photobleaching of fluorescein. Then, we will evaluate, both experimentally and theoretically, the concentration distribution of fluorescein after photobleaching with the confocal microscope by comparison with the bleaching profiles expected from the FRAP models. Finally, a discussion will be given on the implications of the anomalous photobleaching behaviour of fluorescein on various FRAP models.

## 2.2 Theoretical background: photobleaching of fluorescein in microscopy

### 2.2.1 The photobleaching process of fluorescein

A detailed description of the photobleaching kinetics of fluorescein has been published by Song et al. [46]. As our theoretical analysis is based on their work, we will repeat the main conclusions here. A fluorophore can make an electronic transition from the ground state S to the excited singlet state S\* (see Fig. 2.1) by absorbing a photon of wavelength  $\lambda$  (m) and corresponding energy  $hc/\lambda_{ex}$ , where  $h$  is Planck's constant and  $c$  is the speed of light. If the excitation light has an irradiance  $H$  (W/m<sup>2</sup>) and the fluorophore has an absorption cross section  $\sigma_a$  (m<sup>2</sup>/molecule), the rate of photon absorption  $k_a$  (s<sup>-1</sup>) is:

$$k_a = \sigma_a \left( H \cdot \frac{\lambda_{ex}}{hc} \right). \quad (2.5)$$

The absorption cross-section for fluorescein at 488 nm and pH > 7 is  $3.06 \cdot 10^{-20}$  m<sup>2</sup>/molecule [47]. The number of fluorophores in the excited singlet state S\* will be depopulated via fluorescence emission (rate  $k_f$ ), radiationless internal conversion (rate  $k_{ic}$ ) and radiationless intersystem crossing to the excited triplet state T\* (rate  $k_{isc}$ ). The spin-forbidden transition from T\* to S will happen at a (usually very low) rate  $k_1$ . While being in the excited singlet or triplet state, irreversible photochemical destruction can occur of the fluorophores, a process which is termed photobleaching. Those fluorophores that are photobleached can no longer take part in the fluorescence excitation-emission cycle.

For fluorescein it has been demonstrated that the short-lived excited singlet state does ordinarily not contribute to the photobleaching mechanism. The long-lived triplet excited state, at the other hand, becomes depopulated via two major pathways: (1) the reaction between a triplet and another triplet or a ground state fluorescein molecule, and (2) the reaction between a triplet fluorescein molecule and an oxygen molecule. These two mechanisms are termed the dye-to-dye (D-D) and dye-to-oxygen (D-O) mechanisms and can lead to either reduced (R) or semi-oxidized (X) radical forms. These radicals can again react with triplet state molecules and revert either to stable non-fluorescent photoproducts or back to the ground state. Song et al. [46] have incorporated all relevant photochemical reactions into a theoretical model comprising the following six coupled differential



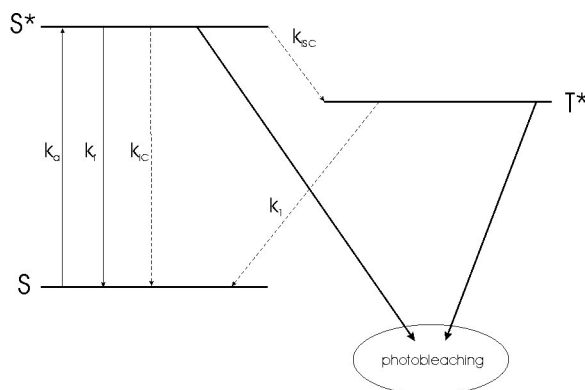


**Figure 2.1:** A simplified Jablonski energy diagram for a typical fluorophore showing possible transitions between the ground state  $S$ , the excited singlet state  $S^*$  and the excited triplet state  $T^*$ , as explained in the main text.

equations:

$$\begin{aligned} \frac{d}{dt} [N_S(t)] &= [k_d N_{S^*}(t) + k_1 N_{T^*}(t) + k_2 N_{T^*}^2(t) + k_3 N_{T^*}(t) N_S(t) \\ &\quad + k_6 N_{T^*}(t) N_X(t) + k_7 N_{T^*}(t) N_R(t) + k_8 N_{T^*}(t) N_{O_2}(t)] \\ &\quad - [k_a N_S(t) + k_5 N_{T^*}(t) N_S(t)] \end{aligned} \quad (2.6a)$$

$$\frac{d}{dt} [N_{S^*}(t)] = k_a N_S(t) - [k_d N_{S^*}(t) + k_{isc} N_{S^*}(t)] \quad (2.6b)$$

$$\begin{aligned} \frac{d}{dt} [N_{T^*}(t)] &= k_{isc} N_{S^*}(t) - [k_1 N_{T^*}(t) + k_2 N_{T^*}^2(t) + k_3 N_{T^*}(t) N_S(t) \\ &\quad + 2k_4 N_{T^*}^2(t) + k_5 N_{T^*}(t) N_S(t) + k_6 N_{T^*}(t) N_X(t) \\ &\quad + k_7 N_{T^*}(t) N_R(t) + k_8 N_{T^*}(t) N_{O_2}(t) + k_9 N_{T^*}(t) N_{O_2}(t)] \end{aligned} \quad (2.6c)$$

$$\frac{d}{dt} [N_X(t)] = k_4 N_{T^*}^2(t) + k_5 N_{T^*}(t) N_S(t) + k_9 N_{T^*}(t) N_{O_2}(t) \quad (2.6d)$$

$$\frac{d}{dt} [N_R(t)] = k_4 N_{T^*}^2(t) + k_5 N_{T^*}(t) N_S(t) \quad (2.6e)$$

$$\frac{d}{dt} [N_{O_2}(t)] = k_9 N_{T^*}(t) N_{O_2}(t). \quad (2.6f)$$

The individual photochemical reactions and the corresponding rate constants as reported in Song et al. [46] are shown in Table 2.1. This set of differential equations has to be solved numerically for a given rate of photon absorption  $k_a$  and initial values for the concentrations  $N_S$ ,  $N_{S^*}$ ,  $N_{T^*}$ ,  $N_X$ ,  $N_R$  and  $N_{O_2}$ . The rate of photon absorption  $k_a$  can be calculated from Eq. (2.6) for a given irradiance  $H$ .

Reaction	Description	Rate constants
$S + h\nu \rightarrow S^*$	Photon absorption	$k_a$
$S^* \rightarrow S + h\nu'$	Fluorescence emission	$k_d = k_f + k_{IC} = 2.134 \cdot 10^8 \text{ s}^{-1}$
$S^* \rightarrow S$	Internal conversion	
$S^* \rightarrow T^*$	Intersystem crossing	$k_{isc} = 6.6 \cdot 10^6 \text{ s}^{-1}$
$T^* \rightarrow S$	Radiationless deactivation	$k_1 = 50 \text{ s}^{-1}$
$T^* + T^* \rightarrow T^* + S$	Triplet quenching	$k_2 = 5 \cdot 10^8 \text{ M}^{-1}\text{s}^{-1}$
$T^* + S \rightarrow S + S$	Triplet quenching	$k_3 = 5 \cdot 10^7 \text{ M}^{-1}\text{s}^{-1}$
$T^* + T^* \rightarrow R + X$	Electron transfer	$k_4 = 6 \cdot 10^8 \text{ M}^{-1}\text{s}^{-1}$
$T^* + S \rightarrow R + X$	Electron transfer	$k_5 = 5 \cdot 10^7 \text{ M}^{-1}\text{s}^{-1}$
$T^* + X \rightarrow S + X$	$T^*$ quenching by X	$k_6 + k_7 = 5 \cdot 10^8 \text{ M}^{-1}\text{s}^{-1}$
$T^* + R \rightarrow S + R$	$T^*$ quenching by R	
$T^* + O_2 \rightarrow S + O_2$	Physical quenching by $O_2$	$k_8 = 1.56 \cdot 10^9 \text{ M}^{-1}\text{s}^{-1}$
$T^* + O_2 \rightarrow X + HO_2$ (or $O_2^-$ )	Chemical quenching by $O_2$	$k_9 = 1.4 \cdot 10^8 \text{ M}^{-1}\text{s}^{-1}$

**Table 2.1:** Photochemical reactions of fluorescein (*reproduced from [46]*)

## 2.2.2 Photobleaching of fluorescein by a focused laser beam

When a laser beam is focused down through an objective lens, a complex 3-D intensity distribution results around the focal point (see Appendix B, section B.1). For clarity and because most FRAP models are limited to diffusion in 2 dimensions, the study presented here will be restricted to 2 dimensions as well (focal plane). When an objective lens is uniformly illuminated by incoherent light propagating from a theoretical point, the radial irradiance distribution in the focal plane is given by the Fraunhofer-Airy formula (see Eq. (B.10)), which is valid for small diffraction angles:

$$H(r) = \pi P \left( \frac{0.61}{w} \right)^2 \left[ \frac{2J_1(1.22\pi r/w)}{1.22\pi r/w} \right]^2, \quad (2.7)$$

where  $P$  is the power (W) of the light emerging from the objective lens,  $J_1$  is the first-order Bessel function of the first kind and  $w$  the resolution of the lens, which is defined as the position of the first minimum. For an objective lens of numerical aperture NA, the resolution can be calculated from the Rayleigh criterion:  $w = 0.61\lambda/\text{NA}$  [48]. Fig. 2.2 shows the actual diffraction pattern in the focal plane of the objective lens that will be used in this study (see section 2.3.1), which is recorded by imaging a small fluorescent nanosphere with

a completely opened confocal diaphragm. A logarithmic colourmap was applied to make the first and second order diffraction ring visible. Unfortunately, the diffraction pattern is not perfectly radially symmetric. Therefore we will discuss the intensity distributions along one direction only ( $y$ -direction) throughout this study. The intensity distribution along the  $y$ -direction is shown in Fig. 2.2A as well. By analysing the position of the first minimum, we find that the resolution  $w$  is approximately  $1.5 \mu\text{m}$ . For comparison, the theoretical irradiance distribution according to Eq. (2.7) is shown in Fig. 2.2B for  $w = 1.5 \mu\text{m}$ . One might argue that the Fraunhofer-Airy formula theoretically does not apply to the situation where the objective lens is illuminated by a coherent Gaussian laser beam, as is the case for the  $10\times$  lens on the Bio-Rad MRC1024 used in this study. We will nevertheless use Eq. (2.7) because it adequately describes the real diffraction pattern, as can be seen by comparing Figs. 2.2 A and B. Eq. (2.7) will therefore be used in the simulations further on as it provides for sufficient accuracy for the (qualitative) purposes of this study.

For most fluorescence applications it is sufficient to take the central part of the diffraction pattern into account. For example, the central maximum of the Fraunhofer-Airy distribution contains 84% of the total amount of light in the diffraction pattern, while the subsequent higher order maxima have a relative intensity of only 1.7%, 0.4%, 0.1% etc. Hence, a more simple Gaussian distribution is ordinarily used to approximate the BID:

$$H(r) = H(0)e^{-2r^2/r_0^2}, \quad (2.8)$$

which accurately describes the central peak as is shown by the best fit of Eq. (2.8) in Figs. 2.2 A and B. In that context, the parameter  $r_0$  is usually referred to as the resolution of the BID as well, but differs slightly from  $w$  because it has a different definition ( $r_0 \approx 0.69w$ ).

FRAP models that explicitly take the BID into account never use the relatively complicated Eq. (2.7) but rather the simplified Gaussian intensity distribution Eq. (2.8) [22, 43, 27, 30, 39] or possibly a 3-D extension with an additional axial (modified) Gaussian distribution [33, 31, 42]. However, as we will show further on, the higher order diffraction maxima cannot be neglected any longer in case of fluorescein being bleached by a high intensity laser beam. Under the extreme illumination conditions of the bleaching phase, even the higher order diffraction maxima will be able to populate the excited triplet state  $T^*$  significantly, resulting in a complex expanded bleaching profile which can no longer be explained by a simple Gaussian intensity distribution.

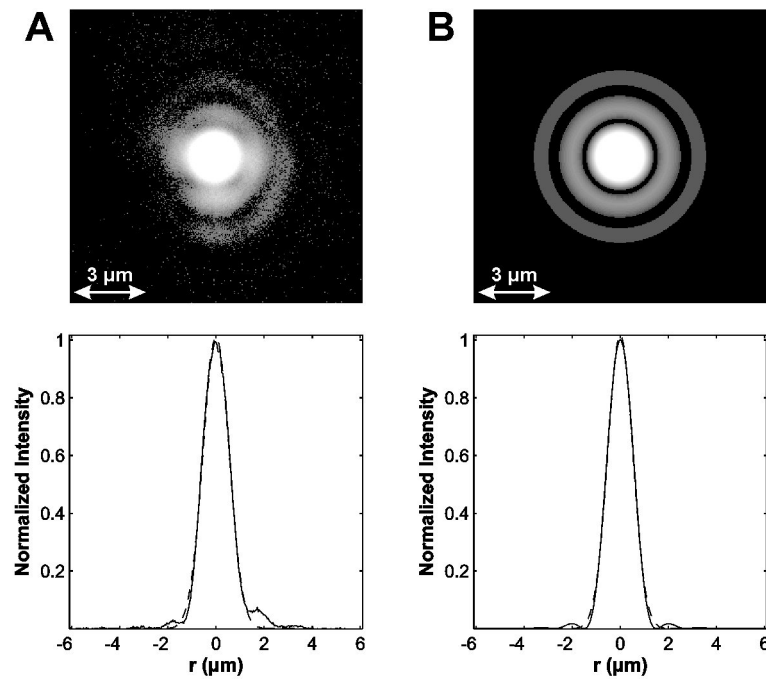


**Figure 2.2:** The illumination intensity distribution in the focal plane. **(A)** The diffraction pattern in the focal plane of the  $10\times$  objective lens has been recorded by imaging a 190 nm fluorescent nanosphere with the confocal microscope. The confocal diaphragm was opened completely to allow the light coming from higher order diffraction rings to enter the detector. Besides the central maximum, the first and second order diffraction ring are visible as well after applying a logarithmic colourmap. The intensity distribution along the vertical direction in the image is also shown (solid line). The central peak can be very well approximated by a Gaussian intensity distribution (dashed line). **(B)** For comparison, the diffraction pattern according to the Fraunhofer-Airy formula is shown as well using the same colourmap. Again the central peak of the theoretical curve (solid line) can be very well approximated by a Gaussian intensity distribution (dashed lines).

## 2.3 Materials and methods

### 2.3.1 The bleaching and imaging apparatus

The FRAP experiments are performed on a CSLM (model MRC1024 UV, Bio-Rad, Hemel Hempstead, UK) equipped with the SCAMPER module [29]. The module consists of a 4 W Ar-ion laser (model Stabilite 2017; Spectra-Physics, Darmstadt, Germany) and an acousto optical modulator (AOM) (Brimrose, Campbell, Baltimore, MD, USA), controlled by a computer and dedicated software. The AOM controls the intensity of the laser beam that is sent to the CSLM. A high-power laser beam ('bleaching beam') is used for photobleaching, while a low power beam ('detection beam') is used for the recording of the confocal images. Bleaching masks can be designed in the software that controls the AOM. While recording an image with the CSLM, low and high power laser light is sent to the sample according to the selected bleaching mask.

All bleaching experiments have been performed with the 488 nm line from the Ar-ion laser. The intensity of the laser beam at the sample can be controlled over a range of 0 to 10 mW. A 10 $\times$  objective lens (CFI Plan Apochromat; Nikon, Badhoevedorp, The Netherlands) with a numerical aperture (NA) of 0.45 was used for bleaching. On the Bio-Rad MRC1024 the back aperture of this lens is only partially filled, however, resulting in a lower effective NA of about 0.2 and a resolution  $w$  of 1.5  $\mu\text{m}$ . The resolution was determined by directly imaging 190 nm fluorescent nanospheres (Molecular Probes, Leiden, The Netherlands) with a completely opened confocal diaphragm. Imaging of the bleached profiles was done with a high resolution 60 $\times$  water immersion lens of 1.2 NA (CFI Plan Apochromat; Nikon, Badhoevedorp, The Netherlands) having a resolution  $w$  of approximately 0.2  $\mu\text{m}$  (also see Fig. 7.5).

### 2.3.2 Photobleaching experiments

Fluorescein isothiocyanate dextrans (Sigma-Aldrich, Bornem, Belgium) of 2000 kDa molecular weight (FD2000) were incorporated in an acrylamide gel. The acrylamide gel was prepared by radical polymerisation of an aqueous acrylamide solution (30% w/w). The solution was prepared by dissolving acrylamide in deoxygenated phosphate buffer (10 mM  $\text{Na}_2\text{HPO}_4$ , 0.02% sodium-azide, adjusted with 1 N hydrochloric acid to pH 7.0). Prior to addition of the gelation reagents, 3.915 mg/g gel of FD2000 was added. The polymerisation reagents were N,N,N',N'-tetramethylene-ethylenediamine (TEMED; Fluka, Buchs,

Switzerland) and ammonium persulphate (10% w/v) (APS; VWR International, Leuven, Belgium). The procedure involves adding 0.5  $\mu\text{L}$  TEMED solution to 1 gram hydrogel. After mixing, 2.5  $\mu\text{L}$  APS solution was added to initiate gelation. The gelating mixture was transferred into in a cuvette with a glass bottom for use with an inverted microscope (Nalge Nunc International, Naperville, IL, USA). The gelation required 1 hour at room temperature. FRAP measurements using the FRAP disk model described in Chapter 1 revealed a diffusion coefficient of  $0.020 \pm 0.005 \mu\text{m}^2/\text{s}$  and a large fraction of immobile fluorescent FITC-dextran of  $90 \pm 5\%$ .

Bleaching experiments were performed with a stationary laser beam ('beam parked') or a line scanning beam. The laser power at the sample was between 1  $\mu\text{W}$  and 10 mW. The time between the bleaching phase and imaging of the bleached profiles was between 10 to 30 min to allow diffusion of the mobile fraction to complete. After that time, any remaining bleaching is due to the immobile fraction and reflects directly the bleaching profile immediately after bleaching. Confocal images were recorded of the bleaching profiles with the  $60\times$  1.2 NA objective lens to obtain the best possible resolution. Before normalizing the confocal images to the background fluorescence, they were convolved with a smoothing mask to reduce the noise.

### 2.3.3 Photobleaching simulations

To study the bleaching of fluorescein at the focal plane, a program was written in Matlab to solve the six coupled differential equations (2.6) numerically. For the simulation of the spot photobleaching experiments, the absorption rate  $k_a(r)$  is calculated from Eqs. (2.5) and (2.7). A GUI<sup>2</sup> was designed as well (see Fig. 2.3) to allow easy input of all parameters. At first a set of radial coordinates  $r$  is defined together with the initial concentrations of  $N_S$ ,  $N_{S^*}$ ,  $N_{T^*}$ ,  $N_X$ ,  $N_R$  and  $N_{O_2}$ . In the simulations reported here, it is always assumed that all fluorescein molecules are initially in the ground state ( $N_{S^*} = N_{T^*} = N_X = N_R = 0$ ). Next, the differential equations are solved for each of the radial coordinates and the corresponding value of  $k_a(r)$ . When the illumination time  $t$  has passed, in general there still will be a number of fluorescein molecules in the excited singlet and triplet state:  $N_{S^*} \& N_{T^*} > 0$ . Therefore, even when the illumination is switched off, the photobleaching reactions still can go on for some time until all the molecules are either bleached or back in the ground state. This has been taken into account in the simulation program by setting  $k_a$  to zero after the bleaching time  $t$  and continue to solve the differential equations until the number

---

<sup>2</sup>Graphical User Interface

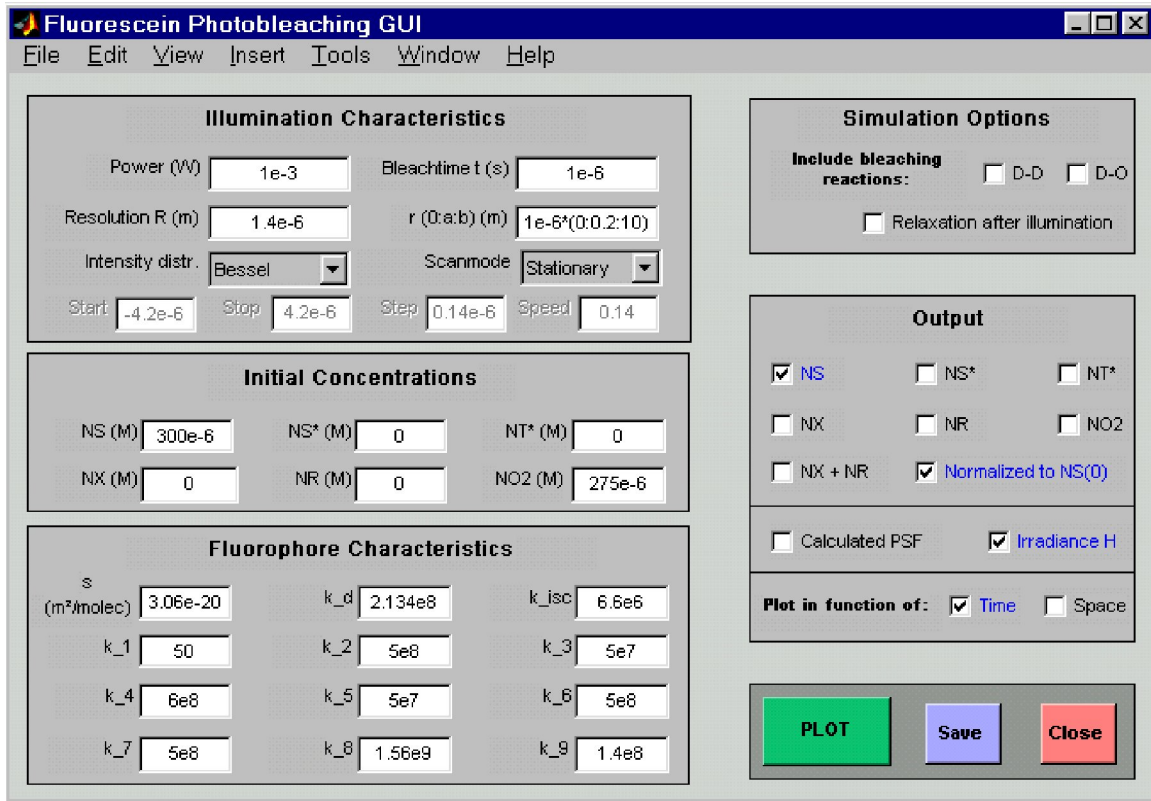


**Figure 2.3:** A Matlab GUI to allow easy input of all simulation parameters.

of bleached molecules ( $N_X + N_R$ ) together with the number of ground state molecules  $N_S$  are equal to the initial number of molecules.

In FRAP experiments on the CSLM, a scanning beam is often used for bleaching rather than a stationary beam [28, 29, 30, 31, 40, 41, 42, 49]. Therefore, the program for the simulation of the photobleaching of fluorescein was extended for a line-scanning beam as well. When bleaching a line segment, the bleaching will be uniform along the scanning direction (except at the boundaries). Only in the direction perpendicular to the scanning direction a bleaching gradient will exist. It is therefore sufficient to calculate the bleaching profile perpendicular to the scanning direction for one position on the bleached line segment only. In the simulation algorithm, the line scanning is taken into account by first defining a start and end position of the laser beam ( $x_s$  and  $x_e$ ) relative to the position on the line at which the bleaching profile is calculated ( $x_0$ ): the laser beam starts at position  $x_s$  and is moved at a scanning speed  $v$  in discrete steps  $\Delta_x$  towards the position  $x_e$ . At each step the laser beam is stationary for a time  $\Delta t = \Delta x/v$  and the effect is calculated at

position  $x_0$ . The smaller the step size  $\Delta x$ , the better the continuous movement of the laser scanning beam will be approximated (at the cost of an increased calculation time). All line scanning simulations reported here were calculated with a step size that is one fifth of the resolution of the bleaching beam ( $\Delta x = w/5$ ) because no appreciable differences in the calculated bleaching profiles were observed for smaller step sizes. The start and ending position of the bleaching beam were always taken symmetrically at 10 times the resolution of the bleaching beam:  $x_s = x_0 - 10w$  and  $x_e = x_0 + 10w$ .

## 2.4 Results

### 2.4.1 Photobleaching of immobilized FD2000

To visualize the bleaching profiles at different bleaching conditions, FITC-dextran of molecular weight 2000 kDa were incorporated into an acrylamide gel. Using a stationary laser beam, spots were photobleached in the gel with a low NA objective lens for different bleaching times. Confocal images were subsequently recorded using a high NA objective lens to obtain the best possible resolution. Some examples are shown in Fig. 2.4. The shape of the illumination beam for a low NA lens is virtually cylindrical (cfr. Fig. 7.2, and in literature e.g. [33, 42, 43]) and the diffraction pattern does virtually not change along the optical axis near the focal plane. Hence, by using a high NA lens for imaging in combination with a small confocal aperture, it is possible to observe the bleaching profile in the focal plane alone, although the gel is a 3-D system.

To be able to relate the results of this study directly to the existing FRAP models (see section 2.5), we will now define the ‘apparent BID’ as the intensity distribution one would have to take into account to explain the experimentally observed bleaching profile if the bleaching process would follow first order kinetics. In other words, the ‘apparent BID’ is the intensity distribution  $I_{app}$  that has to be used in Eq. 2.2 to correctly calculate the observed bleaching profile. If  $C_b$  denotes the fluorescence concentration distribution after photobleaching, the normalized ‘apparent BID’  $I_{app}(r)/I_{app}(0)$  can be calculated from:

$$\frac{I_{app}(r)}{I_{app}(0)} = \frac{\ln(C_b(r)/C_0)}{\ln(C_b(0)/C_0)}. \quad (2.9)$$

The first spot (Fig. 2.4A) was bleached at a low intensity of  $2 \mu\text{W}$ , which is typical for confocal imaging conditions, and a bleaching time of 125 ms. The apparent BID calculated



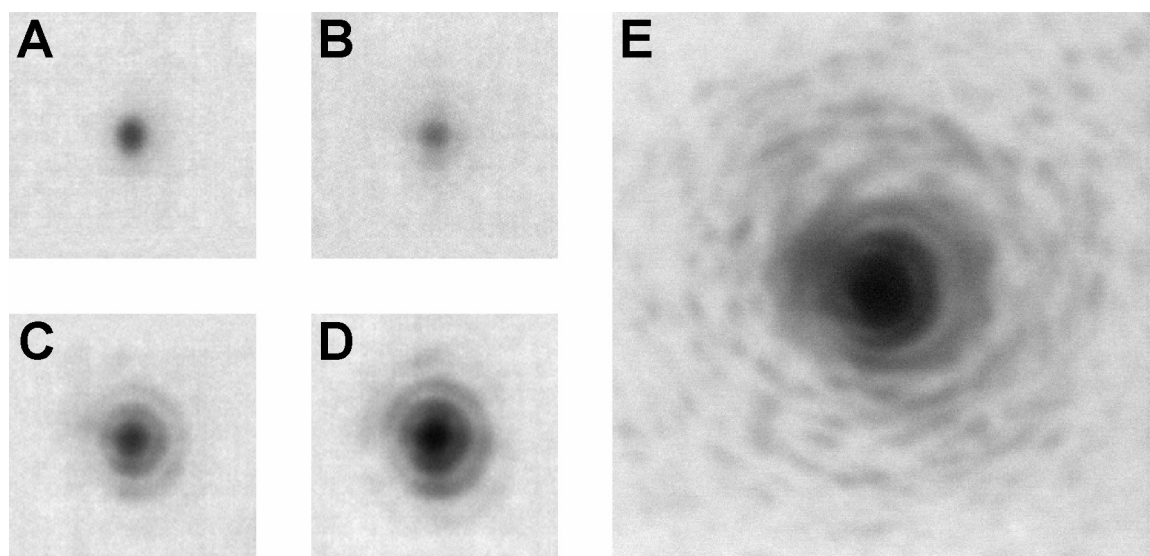


**Figure 2.4:** Using a stationary laser beam, spots are photobleached in an acrylamide gel loaded with FITC-dextran. All images are shown to the same scale. **(A)** At a low intensity of  $2 \mu\text{W}$  and a bleaching time of 125 ms, only the central peak of the BID contributes to the bleaching process. **(B)** At a high bleaching intensity of 10 mW and a bleaching time of  $100 \mu\text{s}$ , also the first order diffraction ring is able to cause photobleaching. **(C)** For a bleaching time of  $500 \mu\text{s}$  and **(D)**  $1000 \mu\text{s}$  at 10 mW, the contribution of the first and second diffraction ring is becoming even more pronounced. **(E)** When increasing the illumination time to 100 ms, the fourth diffraction ring is clearly showing up as well, together with various diffraction spots. The square root of the original image is displayed here to make all features visible.

from Fig. 2.4A using Eq. (2.9) is shown in Fig. 2.5A. A best fit of Eq. (2.8) shows there is a very good correspondence of the apparent BID with a Gaussian intensity profile, in accordance with what is assumed theoretically in the FRAP models. We note that the bleached spot was not perfectly circular but was stretched along the  $y$ -direction resulting in a slightly increased Gaussian radius. The same observation has already been reported in literature for a similar CSLM [43] and is probably due to one of the scanning mirrors not being completely stationary in the ‘beam parked’ mode. To check the validity of a Gaussian BID for high intensity laser beams, spots were bleached at 10 mW and different bleaching times: 25  $\mu\text{s}$  (image not shown), 50  $\mu\text{s}$  (image not shown), 100  $\mu\text{s}$  (Fig. Fig. 2.4B), 500  $\mu\text{s}$  (C), 1000  $\mu\text{s}$  (D) and 100 ms (E). A Gaussian apparent BID is still found for very short bleaching pulses of 25  $\mu\text{s}$  (Fig. 2.5B) and 50  $\mu\text{s}$  (C), although a slight broadening of the profile is already observed compared to Fig. 2.5A. When bleaching for 100  $\mu\text{s}$  (D), the higher order diffraction rings are already starting to show up as indicated by the arrows and the corresponding apparent BID starts to deviate from a pure Gaussian distribution. For bleaching times of 500  $\mu\text{s}$  (E) and 1000  $\mu\text{s}$  (F) the higher order diffraction rings become much more pronounced, expanding the apparent BID even more. Although the apparent BIDs do no longer correspond to a simple Gaussian distribution, it is worth noting it is still possible to approximate the apparent BIDs by an (expanded) Gaussian intensity distribution. Fig. 2.4E, finally, shows the situation if the bleaching time is increased even more to 100 ms. Besides the fourth order diffraction ring, all kinds of diffraction spots take part in the bleaching process. Fitting of a Gaussian intensity distribution to the apparent BID in this case (data not shown) yielded a highly increased Gaussian resolution of  $r_0 = 7.59 \mu\text{m}$ .

Besides being dependent on the bleaching time, the apparent BID also depends on the bleaching intensity. Since many FRAP techniques make use of a scanning beam for bleaching, a line photobleaching experiment instead of spot photobleaching was chosen here to explicitly show that the results from this study equally apply to a scanning beam as well. Three line segments of 80  $\mu\text{m}$  are bleached at different bleaching powers, but with an equal total amount of light received. A first line is bleached by scanning two times at 10 mW. A second one is bleached at 1 mW by scanning 20 times. A third one is bleached at 75  $\mu\text{W}$  by scanning 267 times. A confocal image of the right part of each of the line segments is shown in Fig. 2.6. The fluorescence intensity profile (along the  $y$ -direction) and the corresponding apparent BID are shown for each line in Fig. 2.6A, B and C. Assuming first order bleaching kinetics, the bleaching profile of a single line segment  $[a, b]$  can be calculated from Eq. (2.3) with  $\Delta y = 1$  and  $K(x, y, z) = \int_a^b I_b(x - x', y, z) dx'$  (see Appendix

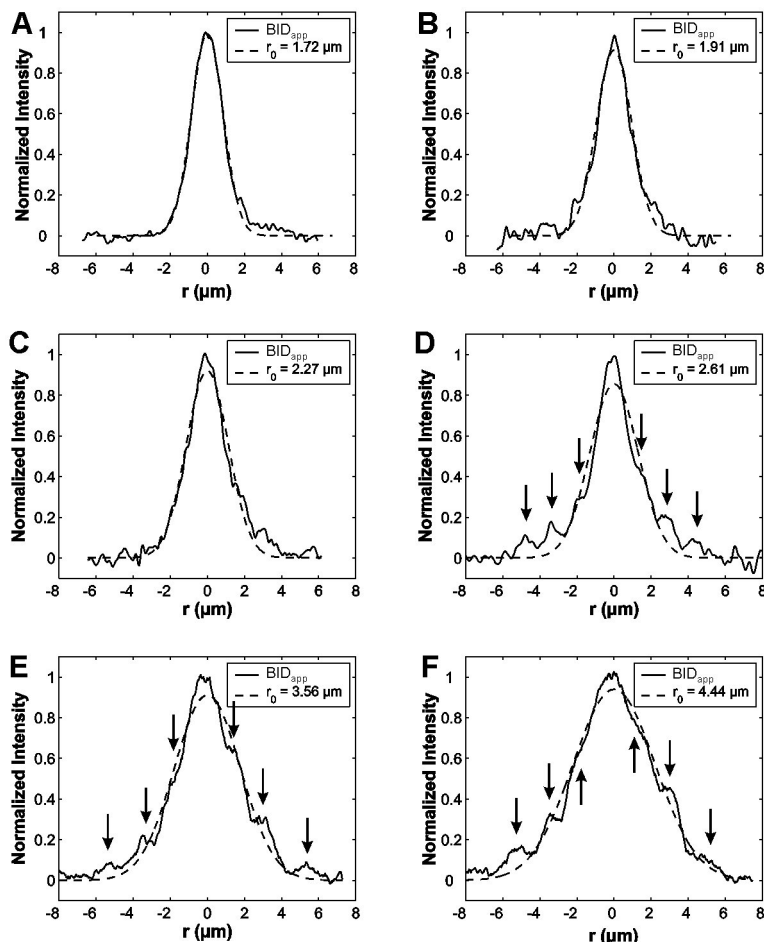


**Figure 2.5:** The apparent BID in case of fluorescein depends on the specific bleaching conditions. (A) At a low bleaching intensity of  $2 \mu\text{W}$ , only the central peak of the diffraction pattern takes part in the bleaching process. Hence, the apparent BID corresponds to a Gaussian distribution. (B) At  $10 \text{ mW}$  and  $25 \mu\text{s}$  bleach time, the apparent BID can still be approximated by a Gaussian distribution, although an expansion is already observed. (C) For a bleaching time of  $50 \mu\text{s}$  the apparent BID expands even more and (D) for  $100 \mu\text{s}$  the individual diffraction rings are becoming visible as indicated by the arrows. (E) Bleaching for  $500 \mu\text{s}$  and (F)  $1000 \mu\text{s}$  increases the relative contribution of the higher order diffraction rings even more, causing a substantial expansion of the original BID.

A, section A.1). For a Gaussian BID according to Eq. (2.8) and a line segment which is much longer than the resolution  $r_0$ , the resulting bleaching intensity distribution finally becomes (cfr. section 3.2.2):

$$K(x, y, z) = \sqrt{\frac{\pi}{2}} I_{0b} r_0 e^{-2y^2/r_0^2}. \quad (2.10)$$

Eq. (2.10) expresses that, when scanning a Gaussian intensity beam along the  $x$ -direction, the Gaussian intensity distribution is preserved along the  $y$ -direction. Hence, if the bleaching process follows first order kinetics, the apparent BID calculated from Eq. (2.9) should still be Gaussian distributed. At a low bleaching intensity, the apparent BID is indeed Gaussian distributed (Fig. 2.6C), while a deviation from a pure Gaussian distribution occurs for increasing bleaching intensities (Fig. 2.6B and A). Fitting of a Gaussian intensity distribution in Fig. 2.6 explicitly shows the expansion of the apparent BIDs with increasing bleaching intensity. Again the expansion is due to the participation of the higher order diffraction rings in the bleaching process. The individual diffraction maxima are difficult to distinguish, however, because of the scanning process along the  $x$ -direction. Additionally it is clear from Fig. 2.6 that the amount of bleaching is different for each of the three situations as well, although all lines did receive an equal amount of light. Bleaching at high intensities for a short time appears to be less efficient than bleaching at lower intensities for a longer time.

## 2.4.2 Simulation of photobleaching immobilized fluorescein

The photochemical reactions according to Table 2.1 and the corresponding mathematical model Eq. (2.6) can be used to explain the observations of the previous section. It should be noted it is not the intention to find an exact quantitative agreement between the simulations and the experimental data because the reaction scheme by Song et al. [46] was presented for free fluorescein in solution. As most of the FITC-dextran are immobilized in the acrylamide gel, the contribution of the D-D interactions to the bleaching of fluorescein is expected to be very small and virtually all bleaching will be due to the D-O reactions. This can be taken into account in the simulations by setting the rate constants  $k_2$ ,  $k_3$ ,  $k_4$ ,  $k_5$ ,  $k_6$  and  $k_7$  to zero. It is very likely that the values of the other rate constants will have changed as well for FD2000 immobilized in the acrylamide gel compared to the values for free fluorescein in solution. It is, however, beyond the scope of this study to assess the exact values (if at all it is possible). Instead the same values as reported in 2.1 have been used. The initial concentration of fluorescein in the gel was approximately  $250 \mu\text{M}$  (which

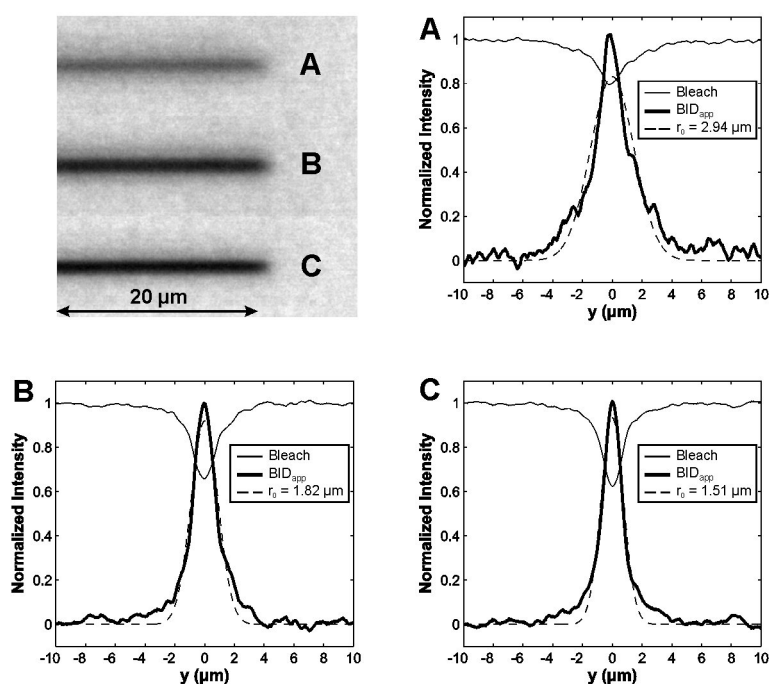


**Figure 2.6:** Three line segments are photobleached at different bleaching intensities but with an equal total amount of light received. (A) Scanning twice at 10 mW, (B) 20 times at 1 mW and (C) 267 times at 0.075 mW results each time in a different bleaching profile. Although all lines have received the same amount of light, bleaching is most efficient when scanning multiple times at a lower laser intensity. Bleaching at low intensities has the additional advantage of preserving a Gaussian distribution for the apparent BID, while an expansion is observed at high intensity levels.

can be calculated from the concentration of FD2000 in the gel and the loading degree of fluorescein on the dextran chains). The initial oxygen concentration is taken to be  $250 \mu\text{M}$  as well [46]. Assuming that all fluorescein molecules are initially in the ground state, the simulations therefore always start from the initial condition:  $N_S = 250 \mu\text{M}$ ,  $N_{O_2} = 250 \mu\text{M}$  and  $N_{S^*} = N_{T^*} = N_X = N_R = 0$ .

We simulated the photobleaching of immobilized fluorescein as a function of time first to examine the course of the photobleaching process. The solid lines in Fig. 2.7 are calculated for a bleaching intensity of 10 mW and a bleaching time of 1 ms. After  $10^{-11}$  s the ground state S is being depleted to the advantage of the excited singlet state  $S^*$  which peaks at around  $10^{-8}$  s. After  $10^{-8}$  s the excited singlet state  $S^*$  starts to decay to both the ground state S and the long-lived excited triplet state  $T^*$ . Between  $10^{-8}$  and  $10^{-6}$  s almost all fluorescein molecules are gradually getting trapped in the long-lived excited triplet state  $T^*$ . Once the triplet state molecules arise, the D-O reactions can start producing the photobleaching products X and R, which are formed from  $10^{-7}$  s on. The formation of the photobleaching products X and R cause the triplet state to be depleted, together with the number of oxygen molecules. At  $10^{-4}$  s almost no molecules are left in the ground state because all are either photobleached or in the triplet state. At  $10^{-3}$  s the illumination is switched off ( $k_a = 0$ ) and the reactions are allowed to continue until all molecules are either photobleached, or back in the ground state.

The first order maximum of the BID has a relative intensity of 1.7% (see Fig. 2.2). To see what happens at this intensity level, the same calculations were repeated at a bleaching power of 0.17 mW (Fig. 2.7, dashed lines). Essentially the same processes are taking place, albeit somewhat delayed because of the reduced illumination intensity. It is important to note that the triplet state still becomes significantly populated, despite the very much reduced illumination intensity. As a result, about the same level of bleaching is reached after  $10^{-3}$  s, which explains why the higher order diffraction rings are showing up in the bleaching experiments.

To see this more clearly, calculations have been performed for a BID according to Eq. (2.7) at a bleaching power of 10 mW and for different bleaching times. Fig. 2.8A shows the result for  $t = 25 \mu\text{s}$ . The apparent BID is calculated from the calculated bleaching profile using Eq. (2.9). For comparison with the experimental data (Fig. 2.5), it should be realized that the simulated bleaching profile is not what is observed directly through a microscope. When observing an object through a microscope, the object is modulated

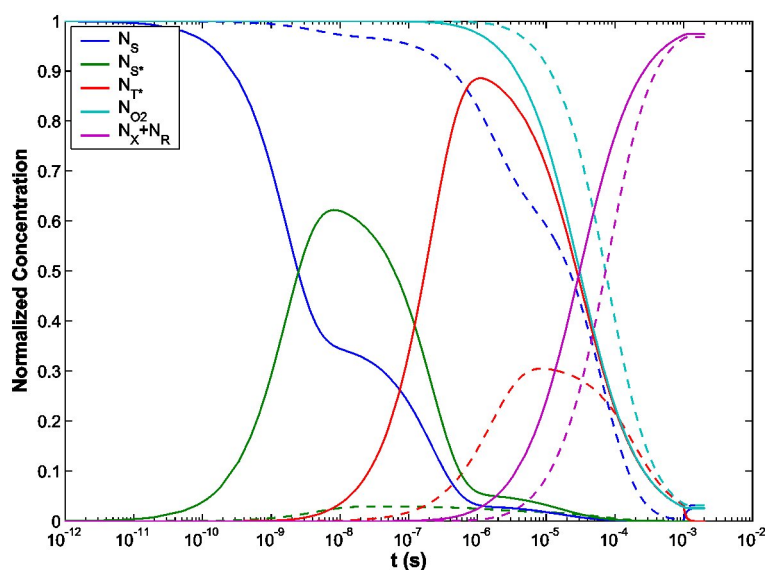


**Figure 2.7:** The evolution over time of fluorescein molecules in the various energy levels is simulated for an illumination intensity of 10 mW (solid lines) and 0.17 mW (dashed lines). The evolution of the number of oxygen molecules and the photobleaching products is shown as well. All populations are normalized by the initial fluorophore population at the ground state. The bleaching time is 1 ms, after which the illumination is switched off ( $k_a = 0$ ) and the reactions are allowed to continue until all fluorescein molecules are photobleached or back in the ground state.

by the detection point spread function (PSF), which depends directly on the objective lens being used (see Appendix B, section B.1). The detection PSF of an objective lens in the focal plane of a confocal microscope can be approximated by a Gaussian intensity distribution corresponding to the central diffraction peak. This is because the higher order diffraction rings only have a small contribution to the collected fluorescence compared to the central peak and because the higher order diffraction rings are largely blocked by the small confocal aperture (see Fig. B.2). The 60 $\times$  objective lens that was used to image the bleaching profiles in section 2.4.1 has a Gaussian resolution of approximately 0.2  $\mu\text{m}$ . To obtain a more direct comparison between the simulated and experimental data, the simulated bleaching profile is therefore convolved with the corresponding Gaussian mask. The result is shown in Fig. 2.8B. The individual maxima seem less pronounced because of the limited resolving power of the objective lens. Together with the presence of experimental noise, this explains why the individual maxima are not always easy to discern in the experimental apparent BIDs (compare with Fig. 2.5). The same calculations have been performed for:  $t = 50 \mu\text{s}$  (Fig. 2.8C), 100  $\mu\text{s}$  (D), 500  $\mu\text{s}$  (E) and 1000  $\mu\text{s}$  (F). Only the convolved apparent BIDs together with a Gaussian fit are shown for clarity. Comparing Figs. 2.5)B-F with Figs. 2.8B-F shows that the theory corresponds well with what is observed experimentally: an apparent BID that expands with increasing bleaching time due to the increasing contribution to the bleaching process of the higher order diffraction rings. Again we find that each of the expanded apparent BIDs can be approximated by a Gaussian distribution. The corresponding Gaussian radii are in close agreement with the experimental values.

The line photobleaching experiments have been simulated as well for bleaching powers of 10 mW, 1 mW and 0.075 mW. The simulation program does not allow to calculate repeated line scans, however, because of the substantial computation times involved. Alternatively we have simulated line profiles using those three intensities but with different scanning speeds. The scanning speed at 1 mW was 1/10 of the scanning speed at 10 mW, and 1/133 at 0.075 mW. Hence, the same amount of light will be received in all three cases. The resulting bleaching profiles are shown in Fig. 2.9A. In correspondence with the experimental observations, a better bleaching efficiency is obtained when using a low bleaching intensity with an increased bleaching time. This effect can be explained by the limited rate at which the photobleaching reactions (D-D and/or D-O) can proceed. Although a high intensity level can cause very quickly a high population of the excited triplet state, the D-D and D-O reactions will not have much time to proceed if the bleaching time is short. A lower intensity level at the other hand induces only a limited population of the



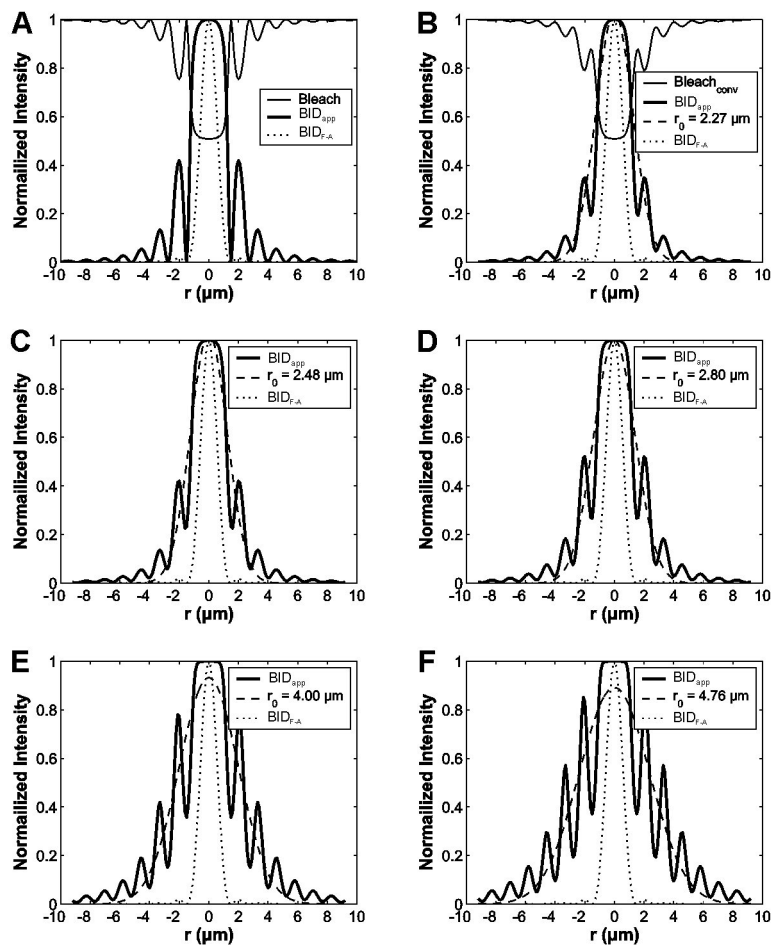


**Figure 2.8:** The bleaching of immobilized fluorescein by a stationary laser beam is simulated for a laser power of 10 mW and different bleaching times. The dotted line shows the intensity distribution of the illumination BID according to the Fraunhofer-Airy formula (Eq. (2.7)) for a resolution of  $w = 1.5 \mu\text{m}$ . **(A)** The solid line shows the bleaching profile for  $t = 25 \mu\text{s}$ . The bold line is the corresponding apparent BID. **(B)** When an object is observed by a microscope, it is modulated by the detection PSF, which depends primarily on the objective lens that is used. The results of figure A are therefore convolved with a Gaussian mask having a resolution radius of  $0.2 \mu\text{m}$  in accordance with the properties of the  $60\times$  objective lens used for imaging the experimental bleach profiles in section 2.4.1. As a result, the individual maxima appear less pronounced. The dashed line is a best fit of a Gaussian intensity distribution to the apparent BID. The fitted Gaussian resolution is specified in the legend. **(C - F)** The same calculations are repeated for bleaching times of  $50 \mu\text{s}$ ,  $100 \mu\text{s}$ ,  $500 \mu\text{s}$  and  $1000 \mu\text{s}$ . The longer the bleaching time, the more the higher order diffraction maxima contribute to the apparent BID. As a result, the apparent BID expands with increasing bleaching time.

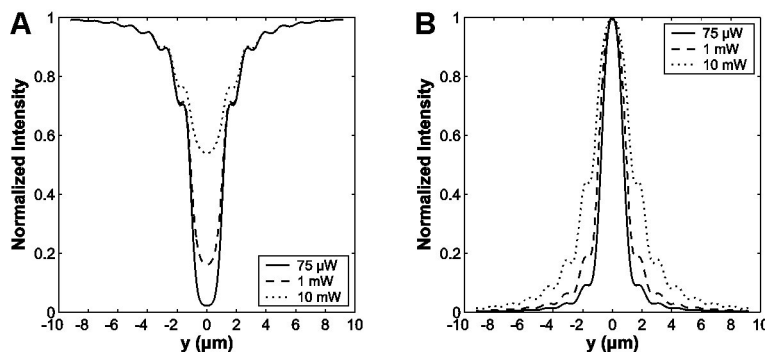


**Figure 2.9:** The bleaching of three lines is simulated for three different intensities:  $75 \mu\text{W}$ ,  $1 \text{ mW}$  and  $10 \text{ mW}$ . To obtain the same total amount of light for each of the lines, the scanning speed is changed accordingly. **(A)** The bleaching profiles show that a better bleaching efficiency is obtained when using a low power beam in combination with a reduced scanning speed. **(B)** From the corresponding apparent BIDs it is clear that at high intensities the higher order diffraction maxima are able to contribute significantly to the bleaching process. As a result, the apparent BID expands with increasing bleaching intensity.

triplet state, but in combination with an extended bleaching time, more bleaching can be obtained because the photobleaching reactions now have more time to convert the triplet state molecules to the photobleaching products. The apparent BIDs are shown in Fig. 2.9B. Again we find an expansion of the apparent BID with increasing bleaching intensities. A best fit of a Gaussian intensity distribution (not shown) yields a resolution  $r_0$  of  $1.32 \mu\text{m}$  ( $0.075 \text{ mW}$ ),  $1.73 \mu\text{m}$  ( $1 \text{ mW}$ ) and  $2.95 \mu\text{m}$  ( $10 \text{ mW}$ ). These values are in good correspondence with the experimental results (cfr. Fig. 2.6).

## 2.5 Discussion

Both theory and experiments confirm that the photobleaching of fluorescein, in general, does not follow a simple exponential decay, especially not under typical bleaching conditions of a FRAP experiment where high intensity light levels are used to obtain very fast photobleaching. We have demonstrated that, in general, for fluorescein it is no longer sufficient to solely take the central diffraction spot into account as is assumed in the derivation of many FRAP models. Instead it has become clear that the higher order diffraction rings can induce a significant amount of photobleaching. The net result is an apparent bleaching illumination profile that is expanded with regard to the actual bleaching illumination profile. In addition, not only does the apparent BID depend on the bleaching

intensity, it also depends on the bleaching time or scanning speed in case of a stationary or scanning beam respectively.

The theory shows that the actual situation is even more complicated. Besides being dependent on the different illumination parameters, the photobleaching of fluorescein is dependent on multiple photochemical reactions, as summarized in Table 2.1. The individual reaction rates of the D-D and D-O reactions will depend on the mobility of the respective molecules in the system. The values reported in Table 2.1 are for free fluorescein in solution. In general, however, the mobility of the molecules in actual samples, such as cells or biopolymer gels, will differ from the situation in water. As a result, the various reaction rates will depend on the sample under study. It is even very likely that in complex chemical systems, such as intracellular media, additional reactions will take part in the photobleaching process of fluorescein. In addition, free fluorescein is rarely used in FRAP experiments. Instead, fluorescein, or rather fluorescein isothiocyanate (FITC), is used as a marker for the actual macromolecules under study, such as proteins or strands of DNA. This in turn will affect the rate constants of the electronic transitions of fluorescein. And finally, the bleaching process also depends on the molar concentrations of both fluorescein and oxygen in the system. Considering those various variable parameters, whose exact values are unknown in most cases, it becomes clear that the apparent BID cannot be accurately predicted in actual practice. The experimental and simulated data as presented in section 2.4 are therefore only indicative of what can happen. To illustrate the many possibilities, we have simulated three spot photobleaching experiments where all parameters are kept the same, except for the reactions that take part in the photobleaching process. In the first simulation both D-D and D-O reactions were allowed, in the second one only the D-O reactions, and in the third only the D-D reactions. A laser beam of 10 mW was used with a bleaching time of 10  $\mu$ s. The values from Table 2.1 were used for the reaction rates. The results are shown in Fig. 2.10, from which it is clear that, besides the amount of bleaching (Fig. 2.10A), also the shape of the apparent BID (Fig. 2.10B) is significantly effected by the reactions that take part.

FRAP models almost always assume first order photobleaching kinetics. Hence the concentration distribution after bleaching can be calculated directly from a single exponential function (Eq. (2.2) or (2.3)) and an invariant Gaussian BID (Eq. (2.8)) which is solely determined by the microscope optics. For fluorescein we have demonstrated that, when assuming first order kinetics, the BID can no longer be considered to be invariant. Instead an ‘apparent BID’ had to be defined whose shape and intensity depends on many param-

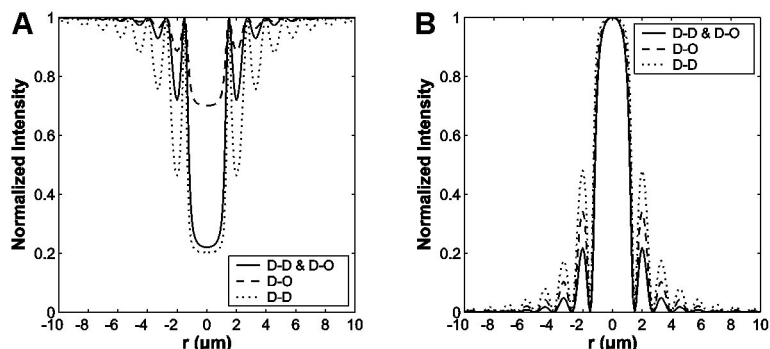


**Figure 2.10:** The bleaching profile and corresponding apparent BID in fluorescein depends strongly on the various parameters that take part in the photobleaching process. As an example, the results of three simulations are shown, calculated for identical parameters (see main text for details), except for the reactions that are allowed to take part in the photobleaching process: D-D and D-O (solid line), D-O (dashed line) and D-D (dotted line). **(A)** The bleaching profiles and **(B)** the corresponding apparent BIDs are very different in each case.

eters. It was also demonstrated that the apparent BID can be roughly approximated by a Gaussian intensity distribution whose resolution will depend on the specific experimental conditions. It is therefore to be expected that existing FRAP models are still able to calculate valid diffusion coefficients from experiments using fluorescein, on condition that the correct apparent Gaussian resolution can be determined for every single experiment. If not, serious errors will result. For example, in the FRAP equation for spot photobleaching with a Gaussian beam in the fundamental work of Axelrod et al. [22], the diffusion coefficient  $D$  is calculated from fitting the parameter  $D/r_0^2$  to the experimental recovery curve, where  $r_0$  is the Gaussian resolution of the bleaching beam. Hence the resolution  $r_0$  has to be known with great precision to obtain an accurate diffusion coefficient. Our experiments have shown that an expansion of the apparent Gaussian radius with a factor 2 to 5 is very well possible. If one does not take this effect into account, the calculated diffusion coefficient would consequently be erroneous by a factor 4 to 25!

There are a few possibilities to deal with a variable apparent BID. For FRAP models that explicitly require the knowledge of the Gaussian resolution  $r_0$ , the only solution in this case is to extract  $r_0$  directly from the experiments, which can be done by acquiring an image of the bleaching profile immediately after the bleaching phase (which is independent of  $D$ ) and using the FRAP formula to extract  $r_0$ . In practice it is difficult, however, to obtain an image immediately after bleaching because of limited image acquisition rates.

One FRAP technique having the possibility to assess the bleaching profile immediately after bleaching has been presented by Blonk et al. [33]. A stationary beam is used for bleaching and is immediately followed by a line scanning phase to record the recovery. Because the time between the bleaching phase and the first recovery line scan is in the order of 1 ms,  $r_0$  can be extracted from the first recovery line scan. But even then Blonk's formula would need adaptation in case of fluorescein to take a different bleaching and imaging illumination profile into account. Alternatively, a pragmatic approach to FRAP, suggested by Koppel [50], that does not require the actual knowledge of the bleaching kinetics or bleaching illumination profile could be used. The method does depend on a Gaussian shape of the initial bleaching profile (line or spot), though, whose size has to be determined from the first recovery image as well.

A workaround in case of fluorescein is to use FRAP models that do not require the precise knowledge of the BID or the concentration distribution after bleaching. An example is the model of Tsay and Jacobson [25] or Berk et al. [26] that uses the Fourier transform of the recovery images. They have shown that the diffusion coefficient can be calculated without determining the BID of the microscope by measuring the decay of the spatial Fourier transform of the recovery images. Also recently a FRAP method making use of Fourier transforms has been published [51]. An other example is the model of Kubitscheck et al. [28] who have derived a moments analysis of the fluorescence recovery images that does not require the knowledge of the initial concentration distribution after bleaching. A disadvantage is the inability to determine the immobile fraction independently. We note that methods that use a relative determination of the diffusion coefficient [45, 52] should be used with care. Such a method relies on two series of FRAP experiments, one in the actual sample and one in a series of standard solutions of known viscosity. If both FRAP experiments are performed under exactly the same conditions, the diffusion coefficient in the sample can be calculated relative to the calibration reference solutions without knowing the actual bleaching profile. This approach can possibly yield invalid results because the apparent BID depends directly on the mobility of the molecules that take part in the bleaching process, as we have shown in this study. Therefore, even under the exact same illumination conditions, the bleaching profile in the sample will, in general, be different from the one in solution (different viscosity and/or bleaching reactions), and consequently a general relation between the two recovery curves may not be possible any more.

Another alternative is to use a FRAP model where geometries are uniformly bleached that are much larger than the characteristic dimensions of the BID. An example is the

FRAP model presented in Chapter 1 which is based on the bleaching of a uniform disk having a radius of at least 4 times the Gaussian resolution of the apparent BID. In that case, a change of the shape of the BID will only be ‘felt’ at the boundaries of the bleached geometry. As was shown in section 1.4.3, neglecting the expansion of the BID usually will not cause errors larger than 10% in the determination of the diffusion coefficient. Hence this method can be used with great confidence and does not require to take special measures.

The most straightforward solution is, of course, to avoid fluorescein in FRAP experiments and to use a fluorophore that shows a more favourable photobleaching behaviour. From experience we know that one such a fluorophore is NODD (N-(7-Nitrobenz-2-oxa-1,3-diazol-4-yl)diethyl amine). NODD is incorporated in polystyrene microspheres that are encoded by photobleaching (see Chapter 7). In this application it is essential to have the best possible resolution (i.e. a non-expanded BID) to write as much information as possible per unit area. It needs to be examined, though, which other fluorophores for FRAP meet this condition as well. This could be done, for example, by performing FRAP experiments on a series of samples with a known diffusion coefficient. If the diffusion coefficient is known, the apparent Gaussian resolution  $r_0$  for each of the solutions can be calculated from the corresponding FRAP formula. If  $r_0$  remains constant for all samples, the apparent BID is invariant for that particular fluorophore and is suitable for use with the existing FRAP models. In the FRAP model that will be presented in Chapter 3, which is based on the bleaching of a line segment, both an independent bleaching and imaging illumination profile is taken into account. This model will be very well suited to look for a suitable fluorophore or alternatively to take an expanded BID explicitly into account.

Finally we note that our bleaching experiments and simulations have shown that the change in shape of the BID is small when bleaching at a lower laser power (in combination with an extended bleaching time). In actual practice, however, one may be forced to use a higher bleaching power to obtain sufficient bleaching in a short time because most FRAP models assume a very short bleaching phase compared to the characteristic recovery time. A FRAP model which takes both a bleaching and imaging resolution into account, such as the line model in Chapter 3, will be very well suited to examine for different fluorophores the expansion of the BID as a function of the bleaching power.

## **2.6 Conclusions**

In this study we have presented both experimental and theoretical evidence that one of the most popular fluorophores for use with FRAP, fluorescein, does not unconditionally comply with the basic assumptions that are made in many FRAP models: an invariant bleaching illumination distribution in combination with first order photobleaching kinetics. Instead, the bleaching behaviour of fluorescein appears to be dependent on many parameters, leading to a dramatically variable apparent BID. This effect is not always evident from the experiments, but neglecting it can induce errors of more than one order of magnitude in the calculation of the diffusion coefficient. Therefore it seems advisable to look for fluorophores that do not show anomalous photobleaching behaviour, or to use/develop FRAP models that are insensitive to the actual shape of the bleaching illumination profile, or to perform FRAP experiments at sufficiently low bleaching powers.

# Chapter 3

## A line model for fluorescence recovery after photobleaching with the confocal laser scanning microscope.

### Summary

A FRAP model will be presented in this chapter for use with the CSLM based on the photobleaching of a long line segment. The line method is developed to complement the disk method from Chapter 1. Although being more subject to the influence of noise, the line model has the advantage of a smaller bleach region, thus allowing faster and more localized measurements of the diffusion coefficient and mobile fraction. An outline of the mathematical derivation will be given first, leading to a final analytical expression to calculate the fluorescence recovery. By incorporating an independent bleaching and imaging resolution, the line model is also very well suited to examine directly the influence of the bleaching power on the effective bleaching resolution (cfr. Chapter 2). The influence of noise on the accuracy of the measured model parameters will be examined separately by computer simulations. Next, the influence of the confocal aperture and the bleaching power will be examined on the measured diffusion coefficient of 3-D samples in order to find the optimal experimental conditions for the line method. This will be done for R-phycoerythrin and FITC-dextrans of various molecular weights. Finally, the ability of the line method to measure correctly absolute diffusion coefficients and mobile fractions in 3-D samples will be evaluated extensively by comparison with measurements with the disk method from Chapter 1.



## 3.1 Introduction

A new FRAP model was presented in Chapter 1 for mobility measurements in 3-D samples based on the photobleaching of a disk by a CSLM. One of the assumptions in its derivation was that the radius of the bleached disk is ‘much larger’ than the (Gaussian) resolution of the bleaching beam. The experiments have shown this condition is fulfilled when the disk’s radius is at least 4 to 5 times the bleaching resolution. An other assumption was that the photobleaching is done by a low NA objective lens. Such a lens has a resolution of  $\sim 1 \mu\text{m}$ , which means that the bleached disk should have a diameter of at least  $8 \mu\text{m}$ . In reality, however, the minimal diameter is rather between 10 and  $15 \mu\text{m}$  due to an expansion of the bleaching illumination distribution at photobleaching intensities, as discussed in Chapter 2. Bleaching of such a large disk has the advantage that the recovery signal in a FRAP experiment can be calculated over a large area consisting of many individual pixels<sup>1</sup>. As a result, the amount of noise in the experimental recovery curve is very low (cfr. Fig. 1.3). A disadvantage, at the other hand, is that its application to cellular research will be limited due to the limited size of many cells and cell compartments. The disk diameter could be made smaller for ‘flat’ samples for which it is possible to use the disk model in combination with high NA lenses, as discussed at the end of section 1.2. For example, a disk of 2 to  $3 \mu\text{m}$  should be feasible in combination with a NA 1.2 lens which has a resolution of  $\sim 0.25 \mu\text{m}$ . But even then, because of the requirement of free diffusion (i.e. no boundaries), there will be many cases where the disk is still too large.

Therefore, we have developed another FRAP model for use with the CSLM that uses a smaller photobleaching geometry: a single long line segment. A FRAP method that uses short line segments has already been reported for 2-D [30] and 3-D measurements [31]. The practical use of this model is limited, though, because no analytical solutions can be found for such short line segments and time-consuming numerical computations have to be used instead. Additionally, the 3-D FRAP model make use of the modified Gaussian intensity distribution (cfr. Appendix B section B.2), the use of which is questionable in single-photon photobleaching experiments (see section 7.4.3 for experimental evidence). To overcome these problems, we have therefore chosen for the bleaching by a low NA lens of a line segment which is ‘much longer’ than the resolution of the writing beam. As will be explained in section 3.2, under these conditions the problem is reduced to 1-D diffusion,

---

<sup>1</sup>For example, a typical pixel size for the disk-photobleaching experiments is  $\sim 0.3 \mu\text{m}$ . When bleaching a disk of e.g.  $15 \mu\text{m}$  diameter, this means that the recovery signal is integrated over approximately 2000 individual pixels.

although the method is still suited for measurements in 3-D samples. This approach has the important advantage of finding an analytical solution to the problem, which allows fast and easy fitting of the experimental recovery curves. Additionally, by incorporating an independent bleaching and imaging resolution, the line model will also be very well suited to test the findings of Chapter 2 directly on fluorescent solutions. In particular it has the possibility to determine the (radial) effective bleaching resolution quantitatively as a function of the bleaching power.

In this chapter, we aim to evaluate the ability of the line model to accurately measure the diffusion coefficient and mobile fraction of 3-D test solutions. First, an outline of the mathematical derivation will be given which leads to the final analytical solution. The assumptions that were made in the derivation will be discussed as well, especially how they relate to the experimental conditions. In the experimental section, we will test the influence of noise, confocal aperture and bleaching power separately in order to assess the instrumental settings which are needed for optimal results. Finally, the ability of the line method to accurately measure absolute diffusion coefficients and mobile fractions in 3-D samples will be evaluated extensively by comparison with measurements with the disk method from Chapter 1.

## 3.2 Theoretical framework: derivation of the FRAP line model

### 3.2.1 Photobleaching of a long line segment

Again we will assume that the photobleaching process can be described by first-order reaction kinetics (see Appendix A, section A.1). As discussed in section A.2, on condition of a short bleaching phase<sup>2</sup>, the fluorophore concentration after bleaching,  $C_b(x, y, z)$ , of a single line segment along the  $x$ -direction can be calculated from (cfr. Eq. (A.2)):

$$C_b(x, y, z) = C_0(x, y, z) e^{-\frac{\alpha}{v} \int_a^b L(x') I_b(x-x', y-Y, z) dx'}, \quad (3.1)$$

where  $\alpha$  is the photobleaching rate of the fluorophore,  $v$  the scanning speed of the bleaching beam and  $L(x)$  is the function that describes the modulation of the light intensity along the line segment  $[a, b]$  and has values between 0 and 1, where 0 means light switched off

---

<sup>2</sup>in order for any recovery during bleaching to be negligible

and 1 means maximum bleaching intensity. In a FRAP experiment, the bleaching intensity remains constant:  $L(x) = 1$ . If we take the origin at the centre of a line segment of length  $l$  ( $a = -l/2$ ,  $b = l/2$ ,  $Y = 0$ ), Eq. (3.1) becomes:

$$C_b(x, y, z) = C_0(x, y, z)e^{-\frac{\alpha}{v}K(x, y, z)}, \quad (3.2)$$

where

$$K(x, y, z) = \int_{-l/2}^{l/2} I_b(x - x', y, z) dx'. \quad (3.3)$$

We further assume that the bleaching intensity distribution  $I_b(x, y, z)$  has a radial and axial Gaussian distribution:

$$I_b(x, y, z) = I_{0b} e^{-\frac{x^2+y^2}{r_{0e}^2}} e^{-\frac{z^2}{z_{0e}^2}},$$

which, for very low NA lenses ( $z_{0e} \rightarrow +\infty$ ), reduces to:

$$I_b(x, y) = I_{0b} e^{-\frac{x^2+y^2}{r_{0e}^2}}. \quad (3.4)$$

In other words, since for low NA lenses the radial resolution  $r_{0e}$  is much smaller than the axial resolution  $z_{0e}$ , the bleaching intensity distribution is nearly cylindrical and there will be virtually no contribution to the recovery from diffusion along the axial direction. It will have to be examined experimentally under which conditions this assumption is valid (see section 3.4.2). Combining Eqs. (3.4) and (3.3) we obtain:

$$K(x, y) = \sqrt{\frac{\pi}{8}} I_{b,0} r_{0e} e^{-\frac{y^2}{r_{0e}^2}} \left[ \operatorname{erf} \left( \sqrt{2} \frac{x + l/2}{r_{0e}} \right) - \operatorname{erf} \left( \sqrt{2} \frac{x - l/2}{r_{0e}} \right) \right]. \quad (3.5)$$

To allow us to find an analytical solution for the FRAP model, we will now make the assumption that the bleached line segment is much longer than the resolution of the bleaching beam, i.e.  $l \gg r_{0e}$ . Then, at sufficient distance from both ends, i.e.  $-l/2 \ll x \ll l/2$ , Eq. (3.5) simplifies to:

$$K(y) = \sqrt{\frac{\pi}{2}} I_{0b} r_{0e} e^{-2y^2/r_{0e}^2}. \quad (3.6)$$

The last assumption implies that the fluorescence recovery will have to be analyzed at sufficient distance from the ends of the bleached line segment to avoid a contribution from diffusion along the  $x$ -direction. Combining Eqs. (3.6) and (3.2), we finally find that the fluorophore concentration after bleaching of a long line segment can be calculated from:

$$C_b(x, y, z) = C_0(x, y, z)e^{-K_0 e^{-2y^2/r_{0e}^2}}, \quad (3.7)$$

where  $K_0 = \sqrt{\frac{\pi}{2}} I_{0b} r_{0e} \alpha/v$  is called the bleaching parameter since it determines directly the amount of bleaching.

### 3.2.2 Fluorescence recovery after photobleaching of a long line segment

Similar to the derivation of the disk model in section 1.2.3, Fick's second law has to be solved for the initial condition Eq. (3.7) to calculate the fluorophore concentration  $C$  at a time  $t$  after bleaching. Assuming a uniform fluorophore concentration distribution before bleaching, the diffusion equation has to be solved in the  $y$ -direction only, according to the assumptions made in the previous paragraph:

$$\frac{\partial}{\partial t} C(y, t) = D \frac{\partial^2}{\partial y^2} C(y, t).$$

The diffusion equation can be solved by applying a Fourier transform to the  $y$  coordinate, finally leading to:

$$C(y, t) = \frac{C_0}{2\sqrt{\pi Dt}} \int_{-\infty}^{+\infty} e^{-K_0 e^{-\frac{2y'^2}{r_0^2}}} e^{-\frac{(y-y')^2}{4Dt}} dy'.$$

Analogous to Appendix C, section C.1 (cfr. Eq. (C.5) to (C.9)), we finally obtain:

$$C(y, t) = C_0 \sum_{n=0}^{+\infty} \frac{(-K_0)^n}{n!} \frac{e^{-\frac{2ny^2}{r_0^2(a_n-n)}}}{\sqrt{a_n-n}}, \quad (3.8)$$

where we have defined  $a_n = 1 + n(1 + 2t/\tau_r)$  and  $\tau_r = r_0^2/4D$ .  $\tau_r$  is called the *radial characteristic diffusion time*.

As explained in section C.2, the fluorescence  $F$  as observed by a CSLM is calculated from the convolution of the fluorophore concentration distribution  $C$  and the confocal detection PSF  $I_d$  according to Eq. (C.11). As usual we will take the confocal detection PSF to be a Gaussian distribution in both radial and axial directions, but this time with its own independent resolution parameters  $r_{0d}$  and  $z_{0d}$ :

$$I_d(x, y, z) = I_{0d} e^{-\frac{x^2+y^2}{r_{0d}^2}} e^{-\frac{z^2}{z_{0d}^2}}. \quad (3.9)$$

Introducing detection resolutions which are independent from the bleaching resolutions will allow us to take a finite confocal aperture into account, as well as a possible increase of the effective bleaching intensity distribution (see Chapter 2). The convolution of  $C(y, t)$  according to Eq. (3.8) and  $I_d(x, y, z)$  according to Eq. (3.9) leads to:

$$F(y, t) = C_0 I_{0d} \sum_{n=0}^{+\infty} \frac{(-K_0)^n}{n!} \frac{1}{\sqrt{a_n-n}} \int_{-\infty}^{+\infty} e^{-\frac{x'^2}{r_{0d}^2}} dx' \int_{-\infty}^{+\infty} e^{-\frac{z'^2}{z_{0d}^2}} dz' \int_{-\infty}^{+\infty} e^{-\frac{y'^2}{r_{0d}^2}} e^{-\frac{2n(y-y')^2}{r_0^2(a_n-n)}} dy'.$$

Similarly, the observed fluorescence before bleaching,  $F_0$ , is calculated from:

$$\begin{aligned} F_0 &= C_0 I_{0d} \int_{-\infty}^{+\infty} e^{-2\frac{x'^2}{r_{0d}^2}} dx' \int_{-\infty}^{+\infty} e^{-2\frac{z'^2}{z_{0d}^2}} dz' \int_{-\infty}^{+\infty} e^{-2\frac{y'^2}{r_{0d}^2}} dy' \\ &= C_0 I_{0d} \int_{-\infty}^{+\infty} e^{-2\frac{x'^2}{r_{0d}^2}} dx' \int_{-\infty}^{+\infty} e^{-2\frac{z'^2}{z_{0d}^2}} dz' \sqrt{\frac{\pi}{2}} r_{0d}, \end{aligned}$$

and the observed fluorescence after bleaching becomes:

$$F(y, t) = \frac{F_0}{r_{0d}} \sqrt{\frac{2}{\pi}} \sum_{n=0}^{+\infty} \frac{(-K_0)^n}{n!} \frac{1}{\sqrt{a_n - n}} \int_{-\infty}^{+\infty} e^{-2\frac{y'^2}{r_{0d}^2}} e^{-\frac{2n(y-y')^2}{r_{0e}^2(a_n-n)}} dy'.$$

The integral to be solved is of the same type as the one in Eq. (C.6) for  $a = \frac{2n}{(a_n-n)r_{0e}}$ ,  $b = \frac{2}{r_{0d}^2}$  and  $c = +\infty$ . Using its solution according to Eq. (C.8), the observed fluorescence finally becomes:

$$\frac{F(y, t)}{F_0} = \sum_{n=0}^{+\infty} \frac{(-K_0)^n}{n!} \frac{e^{-\frac{2ny^2}{nr_{0d}^2 + r_{0e}^2(a_n-n)}}}{\sqrt{n\frac{r_{0d}^2}{r_{0e}^2} + (a_n - n)}}. \quad (3.10)$$

To take a mobile fraction  $k$  into account, Eq. (3.10) has to be substituted into the right part of

$$F(y, t) = F(y, 0) + k(F(y, t) - F(y, 0)), \quad (3.11)$$

where  $F(y, 0)$  is the fluorescence at  $t = 0$ , which is immediately after bleaching.

Let it be noted that the dependency on the spacial coordinate  $y$  is preserved in Eq. (3.10)<sup>3</sup>. This means that the FRAP analysis can be done in two different ways. First it is possible to record confocal  $xy$ -images of the fluorescence recovery after bleaching of the line. From each of the  $xy$ -images, the fluorescence intensity profile along  $y$  can be extracted and fitted directly by Eq. (3.10) to obtain  $D$ . Although this method is the most accurate one since the entire fluorescence distribution is used to calculate  $D$ , its use in actual practice will be limited because of limited frame rates of CSLMs. In other words, the CSLM will generally not be fast enough to image the recovery process at a sufficient

---

<sup>3</sup>For the disk model of Chapter 1, at the other hand, it was necessary to sacrifice the dependency on the radial coordinate to find an analytical solution. In the disk method it is rather the total (or average) intensity inside the bleached disk which is used for analysis.

sampling rate. Instead it will be much more likely to use the CSLM in  $xt$ -mode, where the laser beam is repeatedly scanned along a single line. The image that results from an  $xt$ -experiment consists of the same line that is displayed over time, as is illustrated in Fig. 3.1. The FRAP protocol in  $xt$ -mode is as follows:

1. Record a number of line-scans at a low intensity to obtain the pre-bleach fluorescence signal  $F_0$ .
2. Activate the bleaching protocol to bleach a long line segment. The bleaching of the line segment may be repeated a number of times to increase the amount of bleaching. However, the overall bleach time should be small enough to avoid any significant recovery during bleaching.
3. Record the fluorescence recovery by continuing the  $xt$ -scan at a low intensity.

This method has the advantage that the recovery process is sampled at the CSLM's line-scanning rate. Its disadvantage is that only a part of the available information is used. The expression that should be used for fitting the recovery curve from an  $xt$ -experiment is Eq. (3.10) for  $y = 0$ :

$$\frac{F(0, t)}{F_0} = \sum_{n=0}^{+\infty} \frac{(-K_0)^n}{n!} \left( n \frac{r_{0d}^2}{r_{0e}^2} + (a_n - n) \right)^{-\frac{1}{2}}. \quad (3.12)$$

It is worth recalling that we have made a number of assumptions in the derivation of the FRAP line model that are to be met by the experimental conditions:

1. The fluorescent molecules in the sample have to be initially uniformly distributed. This means that there should be no concentration gradient present before bleaching which gives rise to net diffusion.
2. The diffusion process takes place in an infinite medium. In practice, the latter condition means that during the time period over which the recovery is observed, the diffusion front should not have reached any boundaries at which it will be reflected and influence the free diffusion process (Crank, 1975). By examining the sample with the confocal microscope, the user can choose an area that fulfills these requirements.
3. An objective lens of low NA should be used for bleaching and observation of the fluorescence recovery in a 3-D sample. Lenses of high NA can be used as well in combination with 'flat' samples as long as:

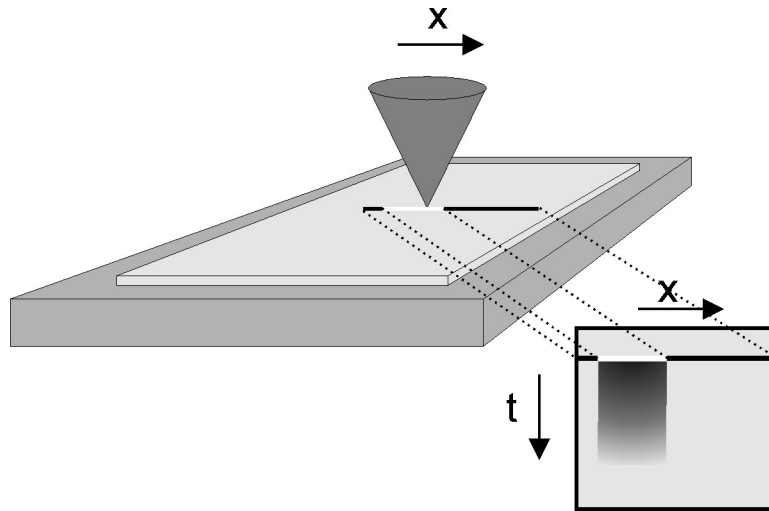


**Figure 3.1:** If the CSLM is working in  $xt$ -mode, the same line is scanned repeatedly, resulting in an  $xt$ -image consisting of the same line which is displayed over time. The  $xt$ -mode can be used for the FRAP line model. First a number of pre-bleach scans are recorded at a low laser intensity to determine the fluorescence intensity before bleaching. Next, a user-defined line segment is bleached at a high laser intensity. Finally, the laser beam is switched back to its low intensity to record the fluorescence recovery after photobleaching. *Image courtesy of Bart Huyck.*

- the bleaching profile along the axial direction stretches throughout the entire sample to avoid diffusion along the axial direction;
- the part of the bleaching intensity distribution inside the sample is nearly cylindrical.

The latter condition implies that, the higher the NA, the smaller the sample's thickness will have to be.

4. The fluorescence recovery should be analysed sufficiently far from the line ends.
5. The bleaching phase has to be sufficiently short to avoid recovery during bleaching. As a rule of thumb, the total bleaching time should be at least  $15\times$  smaller than the characteristic recovery time [1].
6. Finally, there should be no flow present in the medium that can contribute to the fluorescence recovery.

## 3.3 Materials and methods

### 3.3.1 FRAP equipment

The FRAP experiments are performed on a CSLM (model MRC1024 UV, Bio-Rad, Hemel Hempstead, UK) modified to be able to bleach arbitrary regions [29] and equipped with a 4 W Ar-ion laser (model Stabilite 2017; Spectra-Physics, Darmstadt, Germany). A 10× objective lens (CFI Plan Apochromat; Nikon, Badhoevedorp, The Netherlands) with a numerical aperture (NA) of 0.45 was used. On the Bio-Rad MRC1024, however, the back aperture of this lens is only partially filled, resulting in a lower effective NA of  $\sim 0.2$  and an increased resolution radius of  $r_0 = 1 \mu\text{m}$ .

### 3.3.2 Test solutions

Two different fluorophores have been used for the evaluation of the FRAP line model: R-phycoerythrin (Molecular probes, Leiden, The Netherlands) and FITC-dextran (Sigma-Aldrich, Bornem, Belgium) of different molecular weights:  $M = 2 \times 10^6$  g/mol, which will be referred to as FD2000;  $M = 4.64 \times 10^5$  g/mol, which will be referred to as FD464;  $M = 1.67 \times 10^5$  g/mol, which will be referred to as FD167;  $M = 71.6 \times 10^3$  g/mol, which will be referred to as FD71. R-phycoerythrin was supplied as a suspension of 4 mg/ml in 60% saturated ammonium sulfate and 50 mM potassium phosphate, pH 7.0. Following the supplier's instructions, the suspension centrifuged at 5000 rpm for 10 minutes, after which the pellet was dissolved in PBS buffer, pH 7.4. This suspension was brought into a semi-permeable membrane and dialyzed against the same buffer for 24 hours. The final suspension volume in the membrane was approximately 1.8 ml which was further diluted by adding PBS buffer to obtain a final concentration of approximately 1 mg/ml.

Before performing FRAP measurements on solutions of a fluorophore, the concentration range has to be determined in which a linear relation exists between the observed fluorescence and the concentration of the fluorophore. Based on the outcome of such experiments, the following concentrations have been chosen: 1 mg/ml for R-phycoerythrin, 10 mg/ml for FD2000, 2 mg/ml for FD464, 6 mg/ml for FD167 and 6 mg/ml FD71. Next, solutions were prepared in HEPES buffer containing varying amounts of glucose. The glucose was used to vary the dynamic viscosity of the solutions, and hence the diffusion coefficient of the fluorescent molecules.

To perform FRAP experiments, the fluorescent solutions were 'sandwiched' between



a microscope slide and a coverslip sealed by an adhesive spacer of 120  $\mu\text{m}$  thickness (Secure-Seal Spacer; Molecular Probes, Leiden, The Netherlands) in between. Such a microscopic chamber is small enough to eliminate any currents in the solution while retaining a 3-D sample environment. The 496.5 nm line of the Ar-ion laser was used for excitation of R-phycoerythrin and the 488 nm line for the FITC-dextran.

### 3.3.3 Experimental FRAP protocol

The sample is at first positioned on the microscope stage and the location of interest is brought into focus. As will be shown in the experiments, the confocal diaphragm should be set to a small value to obtain valid results. For the 10 $\times$  objective lens used in this study on the Bio-Rad MRC1024, the iris should be  $\leq 1.2$ . The CSLM is set to *xt*-mode and a suitable ‘zoom’ setting is chosen. Next, the length of the bleach line is defined in the photobleaching software, as well as the number of prebleach lines and the number of times the bleaching scan should be repeated. Then, the FRAP experiment is started and the *xt*-images are recorded. Two examples of *xt*-FRAP-images are shown in Fig. 3.2. On the Bio-Rad MRC1024, at ‘normal’ scanning speed, the pixel dwell-time is 2.4  $\mu\text{s}$  and the time period between two line-scans is 2.048 ms. The images usually consist of 512  $\times$  512 pixels. In case of slow recovery, multiple post-bleach *xt*-images may be recorded.

### 3.3.4 Data extraction and fitting

An image processing program was written to extract the experimental recovery curve from the *xt*-images. As indicated by the yellow rectangle in Fig. 3.2, a rectangular ROI (Region Of Interest) can be defined of a certain length and width to calculate the fluorescence intensity as a function of time. The width of the ROI determines the number of pixels over which the fluorescence signal will be averaged for each line in the image. To correct for possible laser intensity fluctuations or possible bleaching while imaging the fluorescence recovery, a reference back-ground ROI (BG) can be chosen as well (green rectangle in Fig. 3.2). To obtain the final recovery curve, the following calculations are performed: first, the ROI fluorescence curve is normalized against the BG curve; next, the average pre-bleach fluorescence is calculated from the pre-bleach lines; and finally, the fluorescence curve is normalized to the pre-bleach fluorescence. Two examples of such a final FRAP recovery curves are shown in Fig. 3.2 as well. The experimental parameters are finally determined by a least-squares fit of Eqs. (3.12) and (3.11) to the experimental recovery curve, as is shown by the red curve in Fig. 3.2.

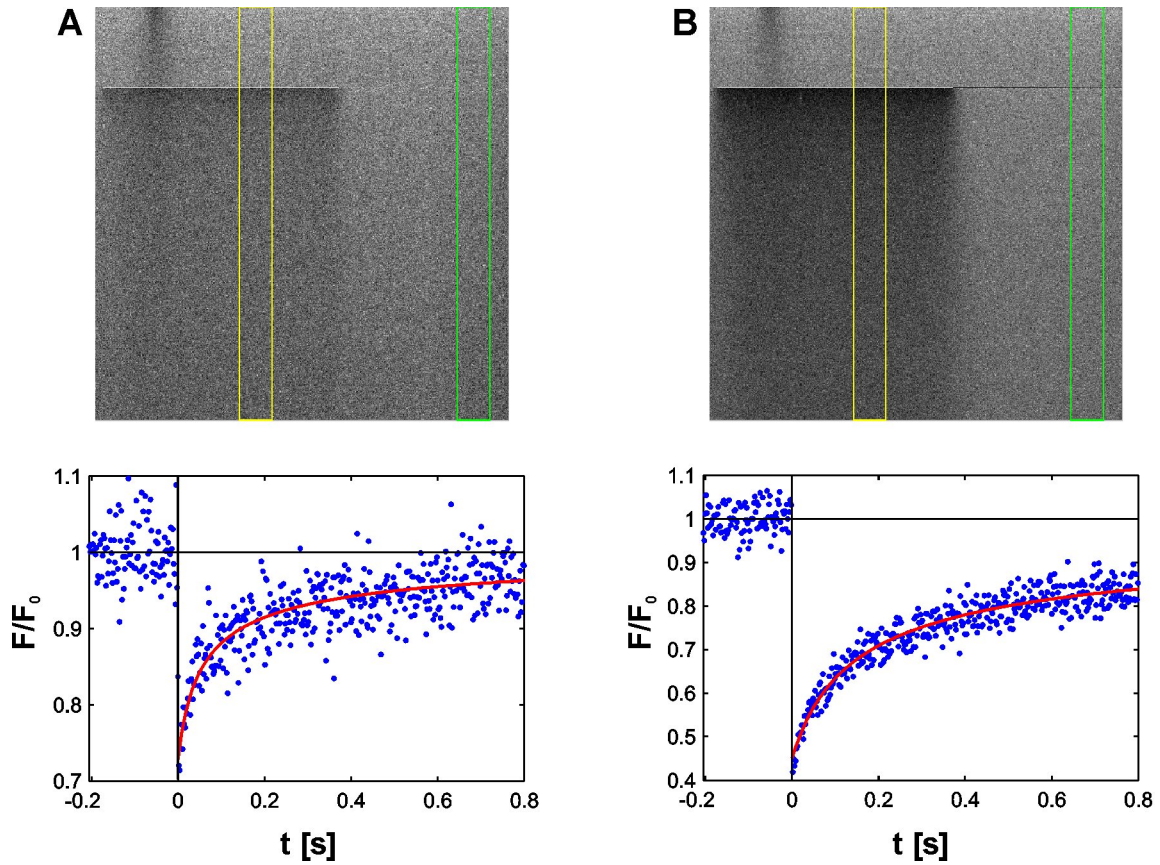


**Figure 3.2:** Two examples of  $xt$ -images are shown of a FRAP line experiment on a fluorescent solution (R-phycoerythrin with 36% (w/w) glucose). First, 100 lines are recorded at a low laser intensity to determine the fluorescence before bleaching. Next, a line segment of  $50\ \mu\text{m}$  long is bleached with the  $10\times$  lens at  $1\ \text{mW}$  for image *A* and  $4\ \text{mW}$  for image *B*. After bleaching, the laser intensity is switched back to its previous (low) level to record the fluorescence recovery. As explained in the main text, the FRAP curve is extracted from the  $xt$ -images by defining a main ROI (yellow rectangle) and a back-ground ROI (green rectangle). The final recovery curves (blue) are shown below image *A* and *B*. At the start of an image, the scanning beam of the Bio-Rad MRC1024 is stationary for a short period of time before actually starting the scanning movement. As a result, the fluorescence becomes bleached at the position where the laser beam is stationary. This is the reason why all  $xt$ -images have a bleach spot at the upper left corner which also recovers over time. This unwanted and very annoying artifact causes the first 150 pixels of the images to be unusable. For that reason the main ROI is chosen towards the right end of the bleach line rather than at the centre.

## 3.4 Results and discussion

### 3.4.1 Influence of noise

Because there is a lot more noise present in the line-experiments compared to the disk-experiments from Chapter 1, it is worth looking separately at the influence of noise on the accuracy of the measured model parameters ( $D$ ,  $k$  and  $K$ ). Based on Eq. (3.12), a FRAP curve was first calculated for  $D = 10 \mu\text{m}^2/\text{s}$ ,  $k = 1$  and  $K = 0.25$ . Next, a certain percentage of normally distributed noise was added to this ideal FRAP curve. This was repeated for 20 times from which the average recovery curve was calculated to simulate an ROI of 20 pixels wide. A best fit by Eq. (3.12) was subsequently performed to calculate  $D$ ,  $k$  and  $K$ . The fitting to the same curve was done for  $k = 1$  fixed as well, to see if the accuracy to calculate  $D$  increases when the mobile fraction is known. The results are shown in Fig. 3.3 for noise levels of 1%, 5%, 10%, 15%, 20% and 25%. The result for each noise level is the mean value from 10 simulations. The error bars are the corresponding standard deviations (SDs). The results for  $D$  and  $k$  when  $k$  was a free fitting parameter are shown in Fig. 3.3A and B. The result for  $D$  when  $k$  was held fixed to 1 is shown in Fig. 3.3C. As could be expected, the SDs increase with increasing percentage of noise. It is worth noting that in all cases the correct value is found within the SD. Interestingly, the accuracy (in terms of the SD) of  $D$  is not much better when the mobile fraction is held fixed to its correct value in the fitting algorithm. We therefore conclude that in the fitting of the experimental recovery curves, the mobile fraction can be one of the fitting parameters without affecting the accuracy to determine  $D$ .

### 3.4.2 Influence of the confocal aperture

In the derivation of the line model, we made the assumption of a cylindrical bleaching beam whose intensity distribution does not change along the optical axis (cfr. Eq. (3.4)). In 3-D samples, this situation will be best approximated by a low NA lens. In reality, however, the illumination intensity distribution is not perfectly cylindrical, but has a slight conical shape (cfr. Appendix B, section B.3). This means that the illumination beam becomes wider at larger distances from the focal plane. Therefore, when bleaching a single line, the width of the line will also gradually increase at increasing distance from the focal plane. The fluorescence recovery after bleaching will be different along the optical axis as well since it depends directly on the width (squared!) of the line (cfr. Eq. (3.8)). When imaging with a large confocal aperture, the detected fluorescence recovery will therefore be an average of the recoveries at the different planes along the optical axis. When fitting

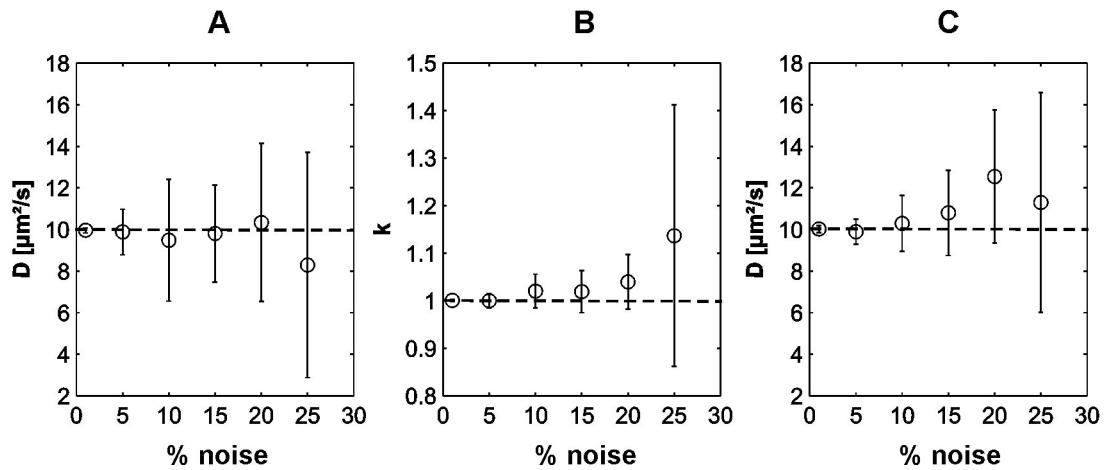


**Figure 3.3:** A recovery curve was simulated according to Eq. (1.18) for  $D = 10 \mu\text{m}^2/\text{s}$ ,  $k = 1$  and  $K = 0.25$  to which different percentages of normally distributed noise have been added. To evaluate the influence of noise on the measured parameters, a fit of Eq. (1.18) is subsequently applied to these data. Ten simulations have been calculated for each different noise level from which the average value is calculated. The results for the diffusion coefficient  $D$  when the mobile fraction  $k$  was one of the free fitting parameters are shown in figure A. The corresponding result for the mobile fraction  $k$  is shown in figure B. The results for the diffusion coefficient  $D$  when the mobile fraction  $k$  was kept fixed to its correct value of 1 is shown in figure C. The error flags are the SD values. Although the SDs increase for increasing noise levels, the correct value is found in all cases within the SD. Comparing the results from figure A with figure C shows that the diffusion coefficient is not more accurately determined when  $k$  is held fixed in the fittings.

the recovery curve with Eq. (3.12), it is therefore to be expected that the measured diffusion coefficient will be lower than the actual value. However, by choosing a small confocal aperture, the detected fluorescence will mainly come from the focal plane and it is to be expected that the diffusion coefficient will be measured correctly.

To determine the dependency of the measured diffusion coefficient on the confocal aperture, we have therefore performed FRAP experiments on the same solution (R-phycoerythrin with 36% (w/w) glucose) for different settings of the confocal aperture. The results are shown in Fig. 3.4A where the measured diffusion coefficient is plotted as a function of the iris setting of the CSLM. Each value of  $D$  is the mean value of 10 measurements. The error bars are the corresponding SDs. Bleaching was done at 500  $\mu\text{W}$ . A value of 1.25  $\mu\text{m}$  for  $r_0$  was used in the fittings, which is a correct value for R-phycoerythrin at this bleaching intensity as will be shown further on. As expected, the measured diffusion coefficient decreases for large confocal apertures. Within the experimental accuracy, no difference is found for  $D$  at iris settings smaller than 2. The diffusion coefficient of the same solution was measured with the disk model as well, yielding  $D = 11.83 \pm 0.49 \mu\text{m}^2/\text{s}$ . This is indicated in Fig. 3.4A by the horizontal lines. A good correspondence is found with the values measured with the line model at iris settings smaller than 2.

The same experiment was repeated for a solution of FD167 with 20% (w/w) glucose. Bleaching was done at 2000  $\mu\text{W}$ . A value of 2.1  $\mu\text{m}$  was taken for  $r_0$ , which is a correct value for FD167 at this bleaching intensity, as will be shown further on. The results are shown in Fig. 3.4B. In agreement with the results for R-phycoerythrin, we find that  $D$  becomes independent of the confocal aperture for iris settings smaller than 2. The diffusion coefficient obtained with the disk model was  $D = 9.95 \pm 0.80 \mu\text{m}^2/\text{s}$ . Again there is a good correspondence with the line model if the iris is set at a value smaller than 2.

From these experiments we conclude that, within the experimental accuracy, the measured diffusion coefficient becomes independent of the confocal aperture for iris settings smaller than 2 on the Bio-Rad MRC1024 and the 10 $\times$  objective lens. The measured diffusion coefficient decreases for larger confocal apertures, as expected. To be on the safe side, all following experiments have been performed at an iris setting of 1.2.

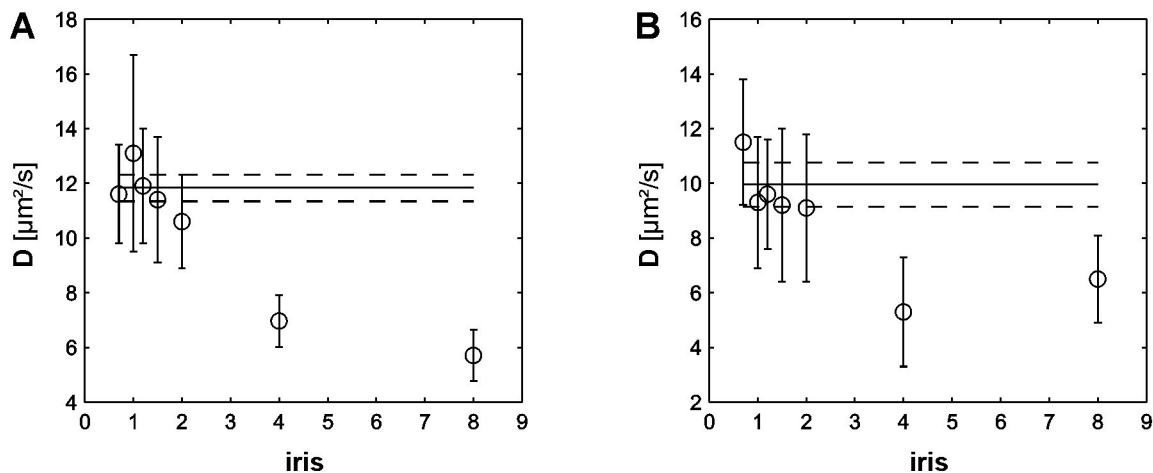


**Figure 3.4:** Frap experiments were performed for varying iris settings on **(A)** a solution of R-phycoerythrin with 36% (w/w) glucose and **(B)** a solution of FD167 with 20% (w/w) glucose. Each value for  $D$  is the mean of 10 measurements. The error bars are the corresponding SDs. The diffusion coefficient of the same solutions was measured by the disk model as well, as indicated by the horizontal solid line. The dashed lines indicate the corresponding SD value.

### 3.4.3 Influence of the bleaching power

It has been shown in Chapter 2 that the effective resolution of the bleaching beam depends on the bleaching power. For this very reason, an independent bleaching and imaging resolution was taken into account in the derivation of the line model. We will now examine directly the influence of the bleaching power  $P$  on the effective bleaching resolution  $r_0$  for both R-phycoerythrin and FD167. We are especially interested in finding a region of bleaching powers where  $r_0$  is independent of  $P$ . This can be done by performing line experiments for different bleaching powers on a solution of a known diffusion coefficient. The effective bleaching resolution  $r_0$  can be determined by fitting of the recovery curves with Eq. (3.12) for a known value of  $D$ .

First, the diffusion coefficient of a solution of R-phycoerythrin with 36% (w/w) glucose was measured with the disk model:  $D = 11.83 \pm 0.51 \mu\text{m}^2/\text{s}$ . Next, line experiments were performed on the same solution for different bleaching powers ranging from 0.32 mW to 4 mW. The effective bleaching resolution was determined by fitting of Eq. (3.12) to the recovery curves for  $D = 11.83 \mu\text{m}^2/\text{s}$ . The results are shown in Fig. 3.5A, where each value is the mean of ten measurements. The error bars are the corresponding SDs. These experiments support directly the results from Chapter 2: the effective bleaching resolution

increases with increasing bleach power. For low bleaching powers,  $r_0$  approaches a value of  $1 \mu\text{m}$ , which is the real resolution of the illumination intensity distribution (cfr. 3.3.1). As can be seen from Fig. 3.5A,  $r_0$  reaches a constant value within the experimental accuracy for bleaching powers below 1 mW. The mean of all  $r_0$  values below 1 mW bleaching power is indicated by the black horizontal line. The dashed lines indicate the corresponding SD levels. Since the experimental accuracy decreases for lower bleaching powers, we suggest to use a power between 0.5 mW and 1 mW for bleaching of R-phycoerythrin and an  $r_0$  value of  $1.25 \mu\text{m}$ .

The same experiment was repeated for a solution of FD167 with 20% (w/w) glucose. A diffusion coefficient of  $D = 9.95 \pm 0.80 \mu\text{m}^2/\text{s}$  was found with the disk model. Line experiments were performed on the same solution for bleaching powers between 1 mW and 5 mW. We note at this instance that fluorescein photobleaches less easily compared to R-phycoerythrin. Therefore it was not possible to obtain sufficient bleaching for powers below 1 mW. The results are shown in Fig. 3.5B. Each value is again the mean of ten measurements and the error bars are the corresponding SDs. Although somewhat less striking as compared to the result for R-phycoerythrin, the same tendency is found of an increasing bleaching resolution with increasing bleaching power. We note that, in contrast with R-phycoerythrin, the bleaching resolution does not tend to approach the value of  $1 \mu\text{m}$ . Instead it seems to level off at a value of  $\sim 2 \mu\text{m}$ . For FITC-dextran we therefore suggest to use a bleaching power between 1 and 2 mW with an  $r_0$  value of  $2.1 \mu\text{m}$ .

As a corollary of these findings, it is interesting to repeat the experiment from section 1.4.3, where the minimal radius  $w$  is determined for the disk model to give valid results. At the time the experiments of Chapter 1 were performed, the influence of the bleaching power on the bleaching resolution was not known, although there was already a suspicion from indirect evidence (cfr. section 1.4.1). The bleaching power used for the experiments of Chapter 1 was usually around 10 mW, which, as we know now for sure, results in an increase of the bleaching resolution radius for FITC-dextran. At this bleaching power it was found that the minimal radius  $w$  is  $\sim 12.5 \mu\text{m}$  (see Fig. 1.6B). The effective bleaching resolution was estimated at  $\sim 3.5 \mu\text{m}$ , from which it was concluded that the disk's diameter should be at least  $\sim 4\times$  the effective bleaching resolution. It is therefore interesting to see if the same result is found for R-phycoerythrin when bleaching is done at a modest 1 mW bleaching power for which we have found an effective bleaching resolution of  $\sim 1.25 \mu\text{m}$ . The results are shown in Fig. 3.6 for a solution of R-phycoerythrin with 50% (w/w) glucose. Note that this result is qualitatively very similar to Fig. 1.6B. The solid horizontal

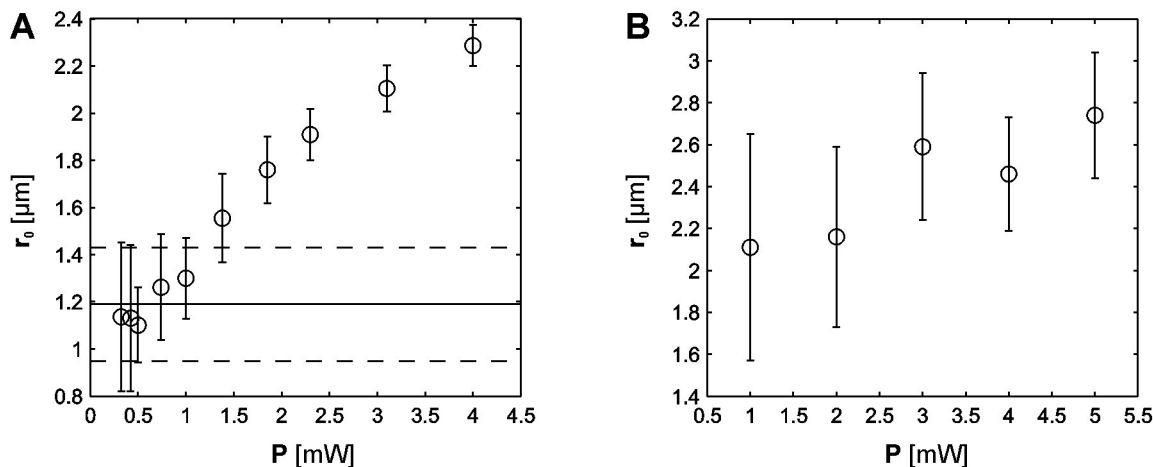


**Figure 3.5:** Frap experiments were performed for different bleaching powers on (A) a solution of R-phycoerythrin with 36% (w/w) glucose and (B) a solution of FD167 with 20% (w/w) glucose. The effective bleaching resolution radius was determined by fitting of the line model to the recovery curves. Each value for  $r_0$  is the mean of 10 measurements. The error bars are the corresponding SDs. The horizontal line in figure A indicates the mean of all  $r_0$  values that correspond to a bleaching power  $\leq 1$  mW. The dashed lines indicate the corresponding SD levels.

line indicates the mean of all values for which  $w \geq 6 \mu\text{m}$  and the dashed lines indicate the corresponding SD levels. As expected, we now find a much smaller minimal radius of  $w \approx 6 \mu\text{m}$ , which is  $\sim 5\times$  the effective bleaching resolution. This result is in good agreement with what was concluded in Chapter 1 considering that the bleaching resolution in Chapter 1 was only estimated indirectly. Being able to use smaller bleaching disks is an important asset because it reduces the recovery times significantly (which are proportional to  $w^2$ ).

### 3.4.4 Validation of the line model

Having determined the correct settings for the confocal aperture and the bleaching power, the ability of the line model to accurately measure absolute diffusion coefficients can be evaluated. This can be done by comparing the diffusion coefficient as determined from line experiments with the diffusion coefficient obtained with the disk model. This is a valid approach since the disk model has already been proven to be able to accurately measure absolute diffusion coefficients (see section 1.4.4).

A series of R-phycoerythrin solutions have been made with different amounts of glucose to obtain a range of diffusion coefficients. The diffusion coefficient of each of the



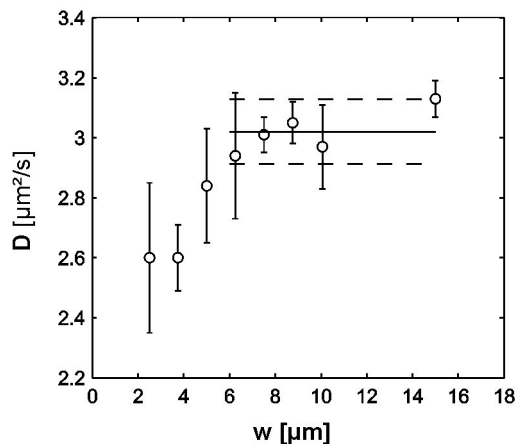


**Figure 3.6:** The experiment from section 1.4.3 is repeated for an R-phycoerythrin solution with 50% (w/w) glucose at a reduced bleaching power of 1 mW. The results for the diffusion coefficient  $D$  as a function of the radius  $w$  are shown in the graph. Each circle is the mean of five measurements and the error flags are the corresponding SD values. The diffusion coefficient  $D$  becomes independent of  $w$  starting from approximately  $w = 6 \mu\text{m}$ . The solid horizontal line indicates the mean value of the six measurements for which  $w \geq 6 \mu\text{m}$  and the dashed lines indicate the corresponding SD levels.

solutions was measured with the disk model first, the results of which are shown in Table 3.1. The same solutions were subsequently measured with the line model as well, the results of which are shown in Table 3.2. The bleaching power was 1 mW for both the disk and line experiments. A corresponding bleaching resolution  $r_0$  of  $1.25 \mu\text{m}$  was used to calculate the diffusion coefficients. The diffusion coefficients obtained with the line model are plotted against the diffusion coefficients obtained with the disk model in Fig. 3.7. Ideally, the data points should be spread along the diagonal, which is true within the experimental error. It is also worth noting that the mobile fraction was calculated correctly as well, as can be seen in Table 3.2.

The same experiments were repeated for 4 series of FITC-dextran solutions with different amounts of glucose. The bleaching power was 2 mW and a corresponding bleaching resolution  $r_0$  of  $2.1 \mu\text{m}$  was used to calculate the diffusion coefficients. As an example, the results for FD167 are shown in Table 3.3 and 3.4 for the disk and line model, respectively. The results for all FITC-dextran solutions are shown in Fig. 3.8, where the diffusion coefficient obtained with the line model is plotted against the diffusion coefficient obtained with the disk model. Again we find a good correspondence between the line and disk model within

**Table 3.1:** The diffusion coefficients  $D$  of R-phycoerythrin solutions with different concentrations of glucose as measured ( $n = 5$ ) with the disk model. The mobile fraction  $k$  and bleaching parameter  $K_0$  are shown as well.

% (w/w) glucose	$D \pm \text{SD}$	$k \pm \text{SD}$	$K_0 \pm \text{SD}$
30	$15.15 \pm 0.45$	$1.009 \pm 0.004$	$2.23 \pm 0.12$
36	$10.59 \pm 0.62$	$1.010 \pm 0.003$	$1.715 \pm 0.043$
40	$7.40 \pm 0.35$	$1.008 \pm 0.007$	$1.909 \pm 0.086$
44	$3.911 \pm 0.039$	$1.010 \pm 0.007$	$1.848 \pm 0.021$
48	$3.18 \pm 0.14$	$1.010 \pm 0.011$	$1.803 \pm 0.084$
56	$1.586 \pm 0.077$	$1.010 \pm 0.010$	$1.576 \pm 0.052$

**Table 3.2:** The diffusion coefficients  $D$  of R-phycoerythrin solutions with different concentrations of glucose as measured ( $n = 10$ ) with the line model. The mobile fraction  $k$  and bleaching parameter  $K_0$  are shown as well.

% (w/w) glucose	$D \pm \text{SD}$	$k \pm \text{SD}$	$K_0 \pm \text{SD}$
30	$12.9 \pm 2.6$	$1.004 \pm 0.015$	$0.504 \pm 0.020$
36	$9.1 \pm 1.8$	$0.994 \pm 0.024$	$0.514 \pm 0.052$
40	$7.4 \pm 1.3$	$0.995 \pm 0.024$	$0.504 \pm 0.026$
44	$4.45 \pm 0.66$	$0.984 \pm 0.031$	$0.510 \pm 0.025$
48	$3.48 \pm 0.63$	$0.983 \pm 0.035$	$0.370 \pm 0.020$
56	$1.66 \pm 0.21$	$1.013 \pm 0.026$	$0.423 \pm 0.017$

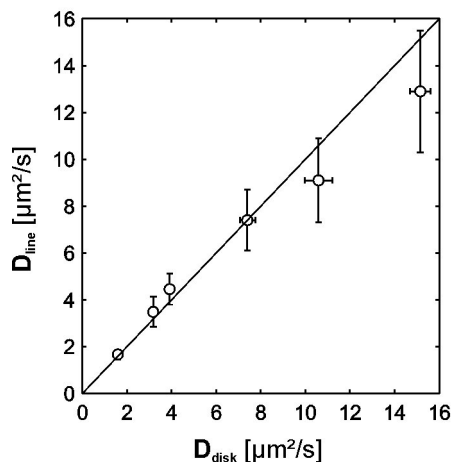


**Figure 3.7:** The diffusion coefficient of a series of R-phycoerythrin solutions of different viscosities is measured with both the disk and line FRAP method. The diffusion coefficients measured with the line model are in good agreement with the values from the disk model within the experimental accuracy.

the experimental accuracy. We note that, for reasons unknown as yet, the values of the FD71 solutions are lower than expected theoretically based on the size of the molecules. Since both the disk and line model give very similar results (see Fig. 3.8D), it is not likely to be an artifact of the FRAP measurements, but rather of the FD71 molecules which were rather old and may have degraded. To be sure, the experiments will have to be repeated for a new batch of FD71.

These experiments show that absolute diffusion coefficients can be measured correctly in 3-D samples with the line model on condition that the effective bleaching resolution is known and the confocal aperture is correctly set. The experiments also show that the bleaching resolution as determined from one solution is valid for all other solutions of the same fluorophore regardless of their viscosity. Comparing the SD values of the disk model with the SD values of the line model it is clear that, as expected, the accuracy of the disk model is superior to the line model. While the relative SD error of  $D$  measured with the disk model is typically around 5%, it is rather 20 to 25% for the line model. The same holds true for the mobile fraction: the mobile fraction is measured correctly with the line model, but with a reduced accuracy as compared to the disk model.

**Table 3.3:** The diffusion coefficients  $D$  of FD167 solutions with different concentrations of glucose as measured ( $n = 5$ ) with the disk model. The mobile fraction  $k$  and bleaching parameter  $K_0$  are shown as well.

% (w/w) glucose	$D \pm \text{SD}$	$k \pm \text{SD}$	$K_0 \pm \text{SD}$
0	$17.9 \pm 1.4$	$0.996 \pm 0.008$	$0.98 \pm 0.13$
10	$16.21 \pm 0.69$	$0.993 \pm 0.012$	$0.730 \pm 0.033$
20	$10.22 \pm 0.80$	$0.984 \pm 0.007$	$0.750 \pm 0.024$
30	$5.49 \pm 0.41$	$0.994 \pm 0.014$	$0.533 \pm 0.024$
40	$1.91 \pm 0.31$	$0.973 \pm 0.006$	$0.640 \pm 0.203$
46	$1.90 \pm 0.12$	$0.978 \pm 0.010$	$0.459 \pm 0.023$
56	$0.473 \pm 0.050$	$0.972 \pm 0.020$	$0.394 \pm 0.084$

**Table 3.4:** The diffusion coefficients  $D$  of FD167 solutions with different concentrations of glucose as measured ( $n = 10$ ) with the line model. The mobile fraction  $k$  and bleaching parameter  $K_0$  are shown as well.

% (w/w) glucose	$D \pm \text{SD}$	$k \pm \text{SD}$	$K_0 \pm \text{SD}$
0	$21.0 \pm 1.5$	$1.038 \pm 0.027$	$0.202 \pm 0.012$
10	$19.0 \pm 4.2$	$1.018 \pm 0.041$	$0.154 \pm 0.012$
20	$10.7 \pm 1.5$	$0.997 \pm 0.033$	$0.171 \pm 0.010$
30	$6.11 \pm 1.0$	$1.008 \pm 0.042$	$0.122 \pm 0.009$
40	$2.13 \pm 0.51$	$1.056 \pm 0.065$	$0.107 \pm 0.009$
46	$1.56 \pm 0.38$	$0.938 \pm 0.078$	$0.186 \pm 0.044$
56	$0.50 \pm 0.17$	$1.16 \pm 0.11$	$0.107 \pm 0.036$

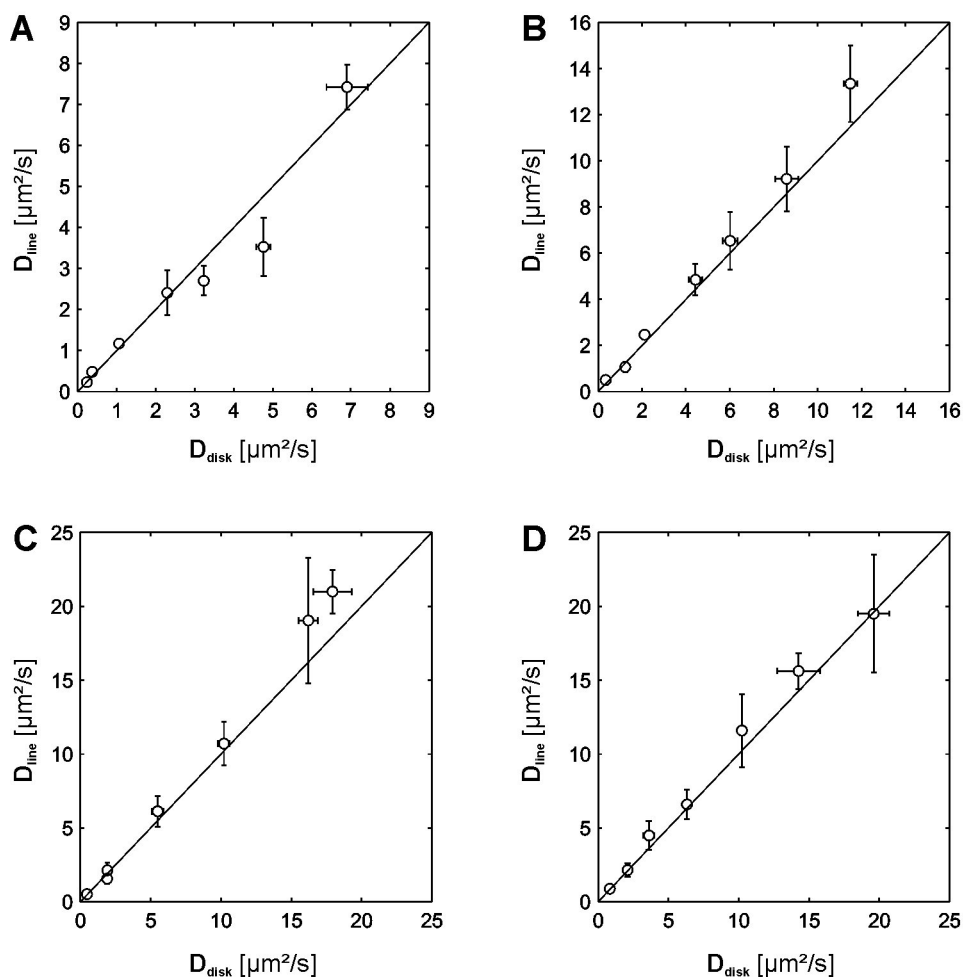


**Figure 3.8:** The diffusion coefficients of 4 series of FITC-dextran solutions of different viscosities is measured with both the disk and line FRAP method: **(A)** FD2000, **(B)** FD464, **(C)** FD167 and **(D)** FD71. The diffusion coefficients measured with the line model are in good agreement with the values from the disk model within the experimental accuracy.

## 3.5 Conclusions

A new FRAP method has been presented in this chapter based on the photobleaching of a line segment which is much longer than the effective resolution of the bleaching beam. By additionally excluding diffusion along the optical axis, the recovery process is reduced to a one-dimension problem for which we have been able to find an analytical solution. We have shown that the latter condition is fulfilled for measurements in 3-D samples if the bleaching is done with a low NA objective lens in combination with a small confocal aperture. In particular we have found that an iris setting smaller than 2.0 should be used for the 10× objective lens used in this study on the Bio-Rad MRC1024. The line method is expected to work fine in combination with objective lenses of higher NA as well, if the sample is sufficiently thin in order to avoid side effects from the conical shape of the bleaching beam. This will be examined experimentally in the near future.

By incorporating an independent bleaching and imaging resolution into the model, the line method could be used to evaluate quantitatively the findings of Chapter 2 for actual fluorophore solutions. For R-phycoerythrin, a strong dependency was found of the effective bleaching resolution  $r_0$  on the bleaching power  $P$ . The experiments have shown that  $r_0$  becomes independent of  $P$  for bleaching powers  $\leq 1$  mW within the experimental accuracy. In particular we suggest to use a bleaching power between 0.5 and 1 mW (at  $\lambda = 496.5$  nm) for R-phycoerythrin with a value for the effective bleaching resolution of  $r_0 = 1.25 \mu\text{m}$ . Although somewhat less striking, a similar dependency of  $r_0$  on  $P$  was found for FD167. Because FITC-dextran bleach less easily as compared to R-phycoerythrin, a bleaching power between 1 and 2 mW (at  $\lambda = 488$  nm) was necessary to obtain sufficient photobleaching with the line method. The corresponding effective bleaching resolution was found to be  $r_0 = 2.1 \mu\text{m}$ . It is noteworthy that the  $r_0$  value, as determined from a single solution, is valid for all other solutions of the same fluorophore, regardless of their viscosity (or molecular weight of the dextran chains in case of the FITC-dextran).

Under these conditions, we have shown that the line method is able to measure absolute diffusion coefficients and mobile fractions correctly. Compared to the disk method, the line method has the disadvantage of being less accurate due to a lower signal to noise ratio. This is because the recovery signal is integrated from typically 20 to 40 pixels, whereas 1000 to 2000 pixels are used for the disk method. The diffusion coefficients measured with the line method have a relative SD error of typically 20 to 25%, while this is only about 5% for the disk method. The line method has the advantage of a smaller bleaching region

compared to the disk model, allowing more localized measurements. A related advantage is that the line method is much faster than the disk model because the characteristic diffusion time is proportional to the square of the bleaching geometry's dimensions.

We conclude that the line model offers a straightforward and fast way to measure diffusion coefficients and mobile fractions on a microscopic scale in 3-D samples. Because of its small dimensions it has the potential for intra-cellular measurements as well, which will be evaluated in the near future. Since the bleaching of a line can be easily accomplished by commercial CSLMs, it can be applied by anyone familiar with the CSLM instrument. Additionally, no extensive mathematical or programming skills are required because the final FRAP expressions are very straightforward.

## Part II

# Encoding of microbeads



# Chapter 4

## Introduction to the encoding of microcarriers

### Summary

In answer to the ever-increasing need to carry out many assays simultaneously in drug screening and drug discovery, several microcarrier-based multiplex technologies have arisen in the past few years. The compounds to be screened are attached to the surface of microcarriers, which can be mixed simultaneously in a vessel that contains the target analyte. Each microcarrier has to be encoded to know which compound is attached to its surface. In this introductory chapter, the methods that have been developed for the encoding of microcarriers are reviewed and discussed.

### 4.1 The necessity of encoding microcarriers

Drug discovery, drug screening and diagnostics commonly involve carrying out assays on large numbers of molecules. These assays typically include screening chemical libraries for compounds of interest and screening for particular target molecules, such as antigens, antibodies, nucleotides and peptides, in test samples. The thousands of individual reactions that are required for these purposes are preferably carried out all at once. Promising tools for this purpose are the ‘multiplex technologies’, which allow multiple discrete assays to be carried out simultaneously in the same microvolume sample.

Perhaps one of the most important challenges in developing multiplex assays is the necessity to track each reaction. For example, if only one reaction of interest occurs in

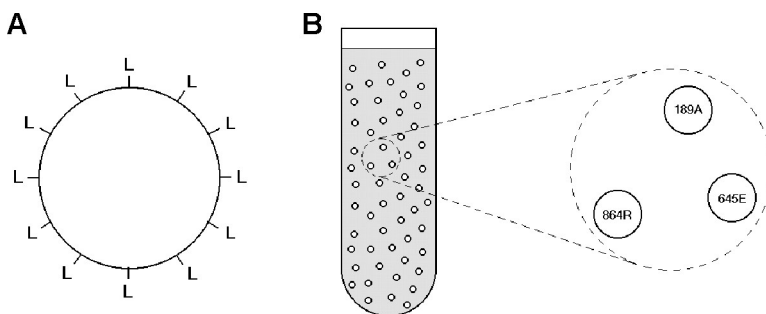


**Figure 4.1:** The need to encode microcarriers. **(A)** Schematic representation of a microcarrier that has a particular ligand or compound bound to its surface. **(B)** In microcarrier-based assays, many molecules – attached to the microcarriers – can be tested at the same time by mixing the microcarriers in the same vial that contains the target analyte. The code on each microcarrier allows the ligand or compound attached to its surface to be identified.

a group of thousands of molecules that are screened against a certain target analyte, it must be possible to determine which molecule produced that reaction. There are two main strategies for doing this. In the first method, each of the molecules is physically separated in the wells of a microtitre plate or by applying them at a particular place in an array – as is done in so-called ‘high-density’ DNA arrays or microchips [53, 54, 55, 56]. In the second strategy, the reactions are carried out on individual microcarriers each carrier having a particular molecule bound to its surface. In the first approach, it is the exact location (x,y coordinate) on the microtitre plate or microarray that allows the identification of the molecule that is analysed at that place. This method of tracking a reaction is usually referred to as positional (or spatial) encoding. The second approach requires each of the microcarriers to be labelled to allow the identification of molecules bound to their surface (see Figure 4.1). This method allows uniquely encoded microcarriers to be mixed and subjected to an assay simultaneously. Those microcarriers that show a favourable reaction between the attached molecule and the target analyte – which can be registered, for example, by a resulting fluorescent signal – can then have their codes read, thereby revealing the identity of the molecule that produced the favourable reaction.

The need for encoding microparticles also arises in the field of combinatorial chemistry [57, 58, 59, 60], especially in the ‘split-and-mix’ method, in which multiple products are synthesized simultaneously on synthesis beads within the same reaction vessel by combining sets of building blocks in just a few steps [61, 62]. The output of the split synthesis is a large number of compounds attached to the synthesis beads, each bead having one

type of compound bound to its surface. To know which compound is bound to a particular bead, either the compound itself has to be identified by analytical tools, or the bead has to be encoded.

The microparticles can be encoded before the synthesis, in which case the particles need to be decoded at each cycle to keep track of their reaction pathways. Alternatively, the microparticles can be encoded during the synthesis by adding a detectable chemical tag at each cycle that encodes for that particular step. In this strategy, which is termed *chemical encoding*, separation from the microcarriers and chemical analysis of the tags is needed to identify the code. Common molecular identification tags are, for example, halo-aryl tags [63], secondary amines [64], peptides [65, 66], oligonucleotides [67] and dialkylamine tags [68, 69]. The detection methods for the elucidation of the codes are generally laborious, expensive and not very amenable to automation [70]. Moreover, the encoding chemistries can interfere with the compound synthesis, resulting in artifacts. Therefore, alternative encoding strategies that overcome these limitations are desirable.

This review focuses on such encoding strategies for microcarriers that are used in combinatorial synthesis, drug screening and diagnostic applications. We discuss encoding technologies that are commercially available today, as well as those that are being developed that hold much promise for the future. Spectrometric encoding technologies are presented in the first section. The second section deals with electronic encoding, and an overview of graphical and physical encoding methods is given in the last two sections.

## 4.2 Methods for encoding microcarriers

### 4.2.1 Spectrometric encoding

Encoding methods have been developed in which the microcarriers can be decoded by placing them directly into a spectrometer. Cleavage of the encoding tags is therefore avoided.

#### **Spectrometric chemical tags**

Spectrometric encoding methods have been developed that make use of chemical tags, most of which have already been reviewed [70]. Therefore, only a short summary will be given here. A first spectrometric encoding method that makes use of chemical

tags is mass encoding. The synthesized compound is identified by mass spectroscopy of the chemical encoding tags [71, 72, 73, 74, 75, 76, 77, 78]. A second method that has been explored is NMR encoding, in which the compounds themselves, which are synthesized on the microcarriers, are analysed by  $^{13}\text{C}$ -NMR spectroscopy [79]. Fluorine nuclear magnetic resonance (FNMR) spectroscopy has recently been used as well, in which fluorine-containing molecules are used as encoding tags [80]. In addition, energy-dispersive X-ray spectroscopy has been reported [81], although the synthesis beads need to be flattened to allow correct identification. Infra-red (IR) encoding has also been described, in which molecules that have a clearly distinguishable IR absorption are used to tag a combinatorial library. However, the number of available tags is limited [82].

### Optical encoding

An important spectrometric strategy that has been substantially developed over the past few years is optical encoding, in which the compound that is attached to a microcarrier is identified by the absorption or emission spectrum of the microcarrier. For example, microcarriers can be optically encoded by chromophores or fluorophores that are covalently bound to the surface [83, 84]

An alternative optical encoding approach, which is applied in combinatorial chemistry, is colloidal encoding [85, 86, 87]. As shown in Figure 4.2, two types of beads are used: large ‘support’ beads ( $\sim 100\ \mu\text{m}$  diameter) and smaller, silica ‘encoding’ beads ( $0.2\text{--}5.0\ \mu\text{m}$  diameter). A fluorescent code is generated on each support bead during the split-and-mix synthesis through the physical attachment of the encoding beads, which contain specific combinations of fluorescent dyes. At first, several batches of encoding beads are synthesized. Each batch consists of one type of encoding beads, so that all beads in a particular batch have identical spectral properties. At each step of the split-and-mix process, the support beads are split into several portions, and each portion is mixed with a different suspension of encoding beads that encode for that particular step. The encoding beads will be physically attached to the surface of the support beads (between 50 and 400 per bead) by means of colloidal forces. To achieve this, before their use, multilayers of positively and negatively charged polyelectrolytes are built onto the surface of the encoding beads to enhance their electrostatic attraction to the support beads [88]. At the end of the split-and-mix process, each support bead carries several different encoding beads that record the reaction history. By viewing the microbead in a fluorescence microscope through different optical filters, both the location of each encoding bead and the combination of

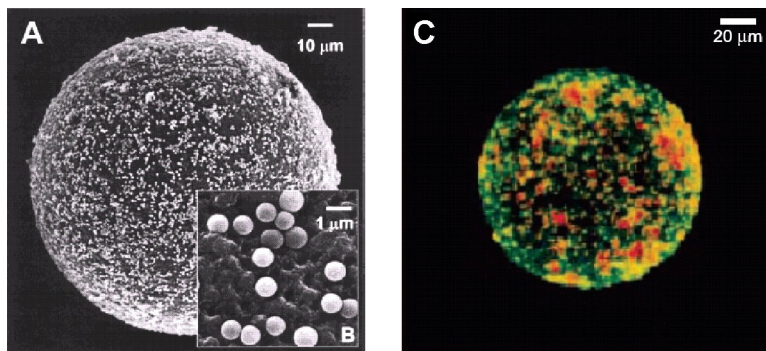


**Figure 4.2:** Colloidal encoding. (A, B) Transmission electron microscopic images of small reporter beads attached to a large support bead by colloidal forces. (C) Fluorescence microscope image of fluorescent encoding beads non-covalently attached to the surface of a large support bead. Images were taken from [87].

fluorescent dyes in the encoding beads can be detected. As each type of encoding bead codes for a known building block in the split-and-mix synthesis, the structure of the synthesized compound on the support bead can be identified. The colloidal encoding method has been used for a 100-member tripeptide library [87]. Twenty types of encoding bead were used, which contained one, two or three fluorescent dyes. Because chemical tags are avoided, the colloidal encoding method has the advantage of eliminating possible interference of the encoding tags with the synthesis reaction steps. Moreover, the silica encoding beads can withstand the harsh chemical conditions of the combinatorial split-and-mix process. A possible drawback of the technique with regard to automation is the need for two-dimensional image analysis to decode each microbead. The more dyes that are used in the encoding scheme, the more images that need to be recorded and analysed. This will take a far longer decoding time compared with optical encoding methods, for which the information is stored in the overall fluorescence spectrum of the beads (see below). A clear advantage of the technique is the numerous uniquely encoded microbeads that can be generated. In theory, more than ten billion compounds could be encoded if seven or more fluorescent dyes were used. However, it remains to be seen if this will be achievable in practice, because some difficulties arise when using multiple fluorescent dyes, as discussed below.

Alternatively, microcarriers can be optically encoded by incorporating distinct proportions of different fluorescent dyes. This colour encoding strategy is used in the *x*MAP technology of Luminex Corporation, in which 5.5 μm polystyrene beads are internally loaded with precise proportions of red (emission wavelength,  $\lambda_{em} = 650$  nm) and orange (

$\lambda_{em} \sim 585$  nm) dyes [89]. A green fluorescent reporter molecule ( $\lambda_{em} \sim 530$  nm) is used to quantify the target analyte in screening applications. The number of colour codes that can be generated depends on the number of dyes and the ratios that are used. In theory, numerous unique codes should be possible, but in practice, there are some limitations. Clearly, the dyes that are to be mixed have to be compatible, and the loading of the beads with the different ratios of dyes that are used in the encoding scheme has to be reproducible. The more ratios that are used, the more difficult this will be. Furthermore, to detect correctly the different fluorescent dyes, their spectra have to be clearly distinguishable, with a minimal spectral overlap to minimize the process of fluorescence resonance energy transfer. Therefore, the ideal dyes should have both coinciding excitation spectra and clearly separated emission bands. If the excitation spectra are not overlapping, multiple lasers or laser lines have to be used to excite the different dyes, which creates the added need for the laser lines to be stable, and therefore considerably increases the cost of the detection instruments. Other reported difficulties are that small differences in bead size or composition alter the relative dyeing efficiency, and that the spectrum of the combined dyes depends on the dye content [90]. Finally, in addition to the encoding fluorophores, a reporter fluorophore that has its own spectrum is needed, which restricts the choice of encoding fluorophores even further. Because of these practical difficulties and limitations, the number of colour codes in the Luminex system seems to be limited to 100 at present (see Figure 4.3). Nevertheless, even with the relatively limited degree of multiplexing, the technique has proved to be of great use in many applications [91, 92, 93, 94, 95, 96, 97, 98, 99, 100, 101, 102, 103], including genotyping, measuring cytokine and thyroid levels, cystic-fibrosis screening, genetic human lymphocyte antigen (HLA) typing, kinase testing and allergy testing.

The bead-based, fibre-optic array is another system that makes use of colour-encoded beads that are prepared by incorporating of multiple fluorescent dyes. In an optical imaging fibre, which consists of thousands of hexagonally packed, micrometre-sized individual optical fibres, the cores of the individual fibres are selectively etched by taking advantage of the difference in etch rates between the core and cladding materials. By controlling the etching time, a high-density, ordered microwell array of known shape and volume is obtained [104]. As shown in Fig. 4.4, each well is ideally filled with one bead by dipping the etched end in a solution of colour-coded microspheres that have a size and volume slightly smaller than the etched microwells [105, 106, 107]. The other end of the fibre bundle is coupled to an imaging fluorescence system that independently resolves each fibre, while simultaneously viewing the entire array. By sending excitation light of appropriate wavelengths through the imaging fibre, each microsphere will fluoresce isotropically. The

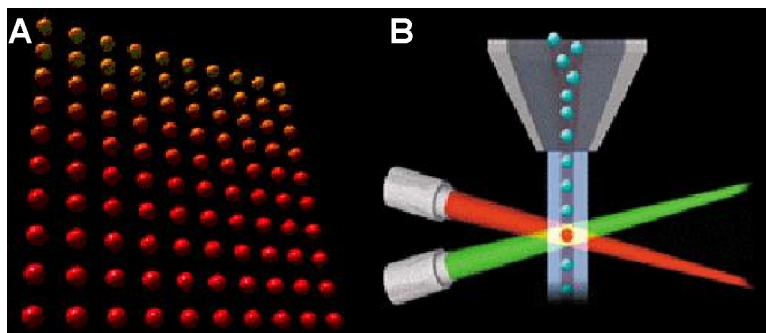


**Figure 4.3:** The Luminex *x*MAP system. **A** A set of 100 microspheres, each microsphere having a unique ratio of two fluorescent dyes. **B** The microspheres are identified individually in a rapidly flowing fluid stream that passes by two laser beams: one reveals the colour code of the bead, and one quantifies the biomolecular reaction by measuring the fluorescence intensity of the reporter. ©Luminex Corporation.

fluorescence is captured by the same fibre, and is sent back to the detection system. Using a charge-coupled device (CCD) camera and optical filters, an image is captured of the fluorescence that emerges from the fibre bundle. Two dyes are used to encode the beads, and a third fluorophore is used as a reporter. The bead-based fibre-optic array can be considered to be a hybrid of the microarray and the encoded-bead technology. Although the probes are positioned in a two-dimensional array, their identities are not known from their positions in the array but from their spectral properties. The BeadArray has the advantage over microarrays of being small and flexible, which allows the sensor to be placed directly into sample solutions rather than bringing the samples to the surface of the sensor. The same limitations, as discussed above, of using multiple fluorescent dyes in the encoding scheme apply here, which results in a limited multiplexing degree of 100 uniquely encoded microsphere sets. This technology has been applied to genotyping, gene-expression profiling, proteomics and diagnostics [108, 109, 110, 111, 112].

Another encoding method that makes use of multiple fluorescent dyes has recently been presented [85, 86], in which several alternating fluorescent and non-fluorescent concentric silica layers are synthesized around a silica core particle (see Fig. 4.5). In this technology, the split-and-mix method is used to synthesize different sets of particles. A collection of core particles is split into several portions, and a different fluorescent layer is synthesized onto the particles of each portion by using silane coupling agents labelled with fluorescent dyes. Next, the particles are recombined, and the process is repeated for several cycles. At the end of the process, a mixture of all possible combinations is obtained

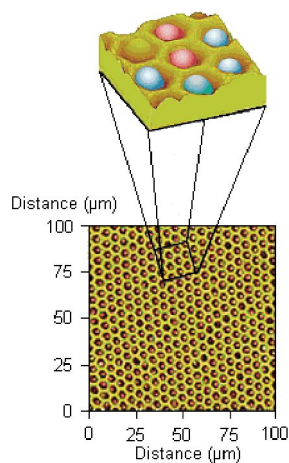


**Figure 4.4:** Bead-based fibre-optic array. Atomic-force micrograph of  $\sim 3.6 \mu\text{m}$  diameter microwells that contain a single  $3.1 \mu\text{m}$  diameter microsphere in each microwell. Each microsphere is encoded by a combination of fluorescent dyes. *Image taken from [107].*

that has to be run through a flow cytometer to separate physically the uniquely encoded bead sets according to their fluorescent signature. This technique avoids the difficulties that are related to the mixing of organic fluorescent dyes by physically separating them into different layers. But the same limitations of spectral requirements as the previous techniques apply.

Many of the problems related to organic dyes are largely overcome by using fluorescent semiconductor nanocrystals, which are also known as ‘quantum dots’ [113]. Conventional dye molecules have a narrow excitation spectrum, which makes simultaneous

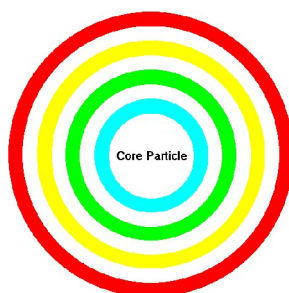


**Figure 4.5:** A microcarrier that consists of different fluorescent layers. The microcarrier is prepared by covalently binding various fluorescent dyes in silica layers (coloured areas) that are applied around a core silica particle. Non-fluorescent silica layers (white areas) are synthesized between the fluorescent layers. *Image taken from [85].*



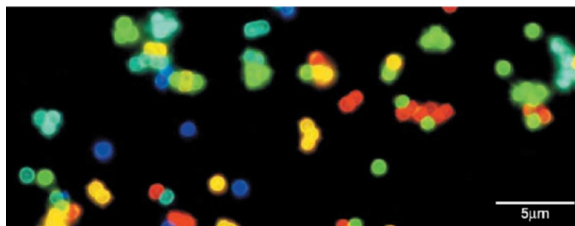


**Figure 4.6:** Nanocrystals in microspheres. Fluorescence micrograph of a mixture of cadmium selenide (CdSe)-zinc sulphide (ZnS) quantum-dot-tagged beads that are emitting single-colour signals at wavelengths of 484, 508, 547, 575 and 611 nm. (*Image taken from [114].*)

excitation of different dyes difficult, and their broad emission spectrum with a long tail at red wavelengths introduces spectral crosstalk between different detection channels. This makes quantification of the relative amounts of the dyes difficult. By contrast, semiconductor nanocrystals have a continuous excitation spectrum, and an emission spectrum that can be continuously tuned by changing the particle size. Their emission spectrum is very narrow (typical widths of 20 – 30 nm) in the visible region. Therefore, many sizes of nanocrystal can be excited simultaneously with only one wavelength of light, which results in many emission colours with minimal spectral overlap. Moreover, the quantum dots are more photochemically stable in comparison to conventional fluorophores.

The use of quantum dots for multicolour optical encoding of microcarrier-based biological assays has already been reported [114, 115]. As shown in Fig. 4.6, quantum dots (zinc-sulphide-capped cadmium-selenide nanocrystals) of different sizes are embedded into polymeric microbeads at different ratios. By using six colours at ten intensity levels, about one million codes can be generated. Nevertheless, it is acknowledged that the actual encoding capabilities are likely to be substantially lower, because of spectral overlapping, fluorescence-intensity variations and signal-to-noise requirements. It has been suggested that it would be better to use more colours, rather than more intensity levels. A realistic scheme would comprise five to six colours with six intensity levels, which could yield  $\sim 10,000 - 40,000$  recognizable codes. Furthermore, a fluorescent signal will be needed for the detection of the target. To keep the spectral interference with the encoding spectra to a minimum, it will be necessary to separate the encoding and reporter signals as far as possible. The technique has been put into practice for triple-colour-encoded beads in DNA-hybridization studies.

As an alternative for the two dyes that are used in the Luminex beads, it has been

suggested to replace one of the encoding colours – for example, orange – with a dye that has the same spectrum as the other encoding dye (red), but with a substantially different fluorescence decay time [116]. This would increase the multiplexing capabilities of the system, because the part of the spectrum that becomes available (around the orange wavelengths) can be used by a second reporter fluorophore for the biological probes. The dyes can be incorporated at different ratios, and time-resolved fluorescence measurements will reveal the identity of the microcarrier. Although the approach was shown to be valid, it is acknowledged that the implementation of lifetime optics and electronics – the hardware needed to measure fluorescence decay-times – to existing flow cytometers would be more expensive and complex compared with new flow cytometers that allow for the direct analysis of the binding of two probes by using multiple lasers and detectors.

Recently, another time-resolved, multiplexed bioassay has been proposed that makes use of phosphorescent nanospheres [117]. The spheres can be distinguished by their individual decay time and spectral distribution of their emission light. Two dyes are incorporated into the nanospheres: a phosphorescent ruthenium metal-ligand complex (MLC) and a strongly fluorescent cyanine dye. As the two dyes are in close spatial proximity, and because the emission spectrum of the MLC (the donor) overlaps the absorption spectrum of the cyanine (the acceptor), efficient resonance energy transfer (RET) occurs. It has been shown that, by varying the concentration of the acceptor dye, the luminescence decay time of the donor is changed, which causes a change in the decay behaviour of the stimulated fluorescence of the acceptor dye. By using different acceptor dyes at several concentrations, a two-dimensional encoding scheme results: the emission maximum reflects the type of acceptor dye, and the decay time reflects its concentration. With ten different acceptor dyes, 400 uniquely encoded beads should be possible. Despite the still relatively limited number of codes that can be generated, this technique has some important assets. First, only one laser line is needed for excitation of the beads, because the same donor is used for a whole series of multiplexing labels. Second, the beads show characteristics of phosphorescence, because the fluorescence of the acceptor dye is induced by RET in the particle that comes from the slow-decaying donor dye. Hence, time-resolved methods of phosphorescence detection can distinguish between background fluorescence (nanosecond timescale) and encoding phosphorescence (microsecond timescale).

## 4.2.2 Electronic encoding

The use of radio frequency (rf) memory tags for the encoding of combinatorial libraries was originally described independently by two groups [118, 119, 120]. As shown in Fig. 4.7, an rf memory tag consists of essentially two components: an antenna and a microelectronic chip with a unique, non-volatile 40-bit identity (ID) code laser etched onto it [70]. This means that  $2^{40}$  ( $\sim 10^{12}$ ) unique codes are possible. The electronic components are enclosed in a glass capsule that measures  $8 \text{ mm} \times 1 \text{ mm} \times 1 \text{ mm}$ . When placing the rf tag near a computer-interfaced transceiver, the antenna absorbs the rf signal of the transceiver, which is converted into electrical energy, thereby activating the chip. On activation, the chip sends its ID-code in an rf pulse to the transceiver, which allows the code to be read and the tag to be identified. Despite the numerous unique codes that can be generated, the technique could not be used for the encoding of individual microcarriers because of the large dimensions of the rf tag. In combinatorial chemistry, the directed sorting technique, which is a strategy that is a hybrid of parallel synthesis and the split-and-mix method is used [121, 122]. The tags are placed in porous vessels, one for each vessel. In addition, each vessel contains several beads on which the compounds will be synthesized. Before the synthesis, a computer assigns a compound that is to be synthesized to each ID-code. A dedicated instrument automatically distributes the different vessels over the different solutions at each synthesis step according to their ID-codes to obtain the desired compound. At the end of the process, each vessel has one particular compound synthesized onto its beads. This technique has been applied in the synthesis of a diverse range of compounds, including the synthesis of a library of Taxol and Epothilone analogues [121], among other examples [122].

Recently, however, small rf tags have been reported that are used as individual microcarriers [123, 124]. The reusable ‘microtransponders’ from PharmaSeq, which measure  $250 \mu\text{m} \times 250 \mu\text{m} \times 100 \mu\text{m}$ , are integrated circuits that comprise photocells, electronic circuitry and an antenna (see Fig. 4.8). A serial number is stored electronically to identify the DNA probes that are attached to the surface of the transponder. During an assay, the transponders are placed in a solution that contains DNA sequences tagged with a fluorescent reporter molecule. When flowing through a dedicated scanner, a laser beam causes the fluorescent molecules of complementary sequences that are hybridized to the probe on the microtransponder to glow, and prompts each chip to transmit its code by an rf signal. In addition to DNA assays, this technology can be applied to single-nucleotide polymorphism (SNP) analyses, gene-expression analyses and drug discovery. Although

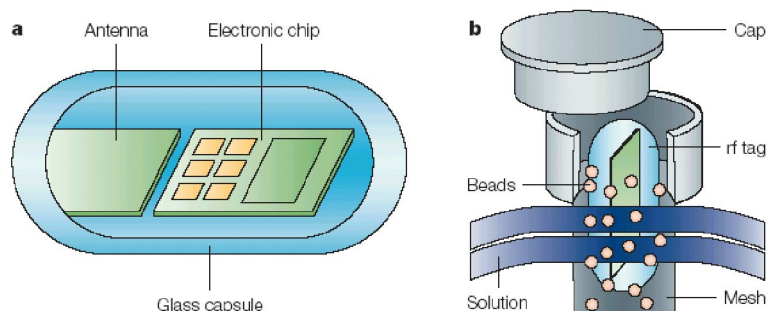


**Figure 4.7:** (a) Schematic illustration of the essential components of a radio frequency (rf) tag: an electronic chip and an antenna enclosed in a glass capsule. (b) An rf tag in a porous vessel with synthesis beads to be used in the directed sorting technique. Image taken from [122].

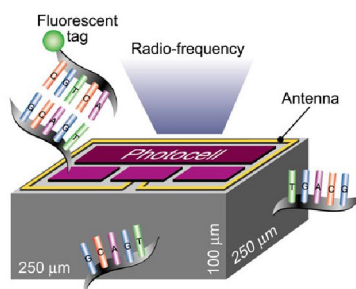


**Figure 4.8:** The small dimensions of the PharmaSeq Microtransponder allow it to be used as an individual microcarrier for screening applications. The reusable transponder comprises photocells, electronic circuitry, and an antenna. ©PharmaSeq

the microtransponder dimensions are still large compared with typical microcarriers (1-50  $\mu\text{m}$ ), the technique is promising because of the virtually unlimited number of unique codes. Moreover, as no fluorescence is needed to encode the particles, an increased multiplexing level is obtained, as several probes can be used simultaneously, each probe having its own reporter fluorophore.

### 4.2.3 Graphical Encoding

It is possible to store information by spatial modulation of a material or its properties, which will be termed graphical encoding in this article. For example, printed text can be read owing to the spatial modulation of black ink on a white background (for a high differential contrast) according to certain patterns that are known to us as alphanumeric

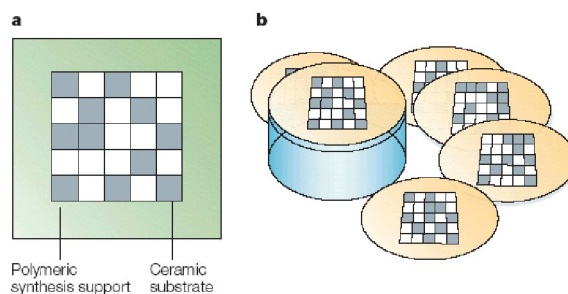


**Figure 4.9:** (a) A two-dimensional, laser-etched barcode on a ceramic substrate is embedded in a plastic synthesis support. (b) Two-dimensional barcodes that are used for the labelling of individual vessels for the directed sorting technique. *Images reproduced from [126].*

characters. Other examples are barcodes or the encoding of compact discs. Graphical encoding methods have been applied to combinatorial chemistry and drug discovery as well, starting with the ‘tea-bag’ method [125], in which microbeads are placed in a set of mesh enclosures. Each tea bag is labelled with a unique code, but the labels are not designed to be machine readable, which makes them unsuited to automated handling.

Two-dimensional barcodes, laser-etched onto a chemically inert alumina ceramic plate, have been described as a practical application of a graphical encoding strategy that is suited to combinatorial chemistry [126]. As shown in Fig. 4.9, the barcoded plate (3 mm × 3 mm) is surrounded by a stable plastic square (10 mm × 10 mm × 2 mm) on which the compounds are synthesized. The two-dimensional barcodes are read by a CCD camera and pattern-recognition software. Two-dimensional barcodes have a large spatial encoding density, which allows a substantial amount of information to be stored in a small area. Because of their large dimensions, it is unlikely that these tags will be used as individual synthesis supports. Instead, they are used as an alternative to the rf tags to label the reaction vessels in the directed sorting strategy (see above).

Two promising graphical-encoded metal particles have recently been reported. In the first method, which was developed by SmartBead Technologies, optical barcoded aluminium rods are produced [127], as shown in Fig. 4.10. The aluminium is sputtered on a 3-inch-diameter substrate, such as a silicon wafer, and patterned into separate encoded rods by optical lithography and dry etching. On a 3-inch-diameter substrate, more than 100,000 aluminium rods can be produced. The rod dimensions are typically 100 μm × 10 μm × 1 μm. They are encoded by a series of etched holes that form a miniature bar-

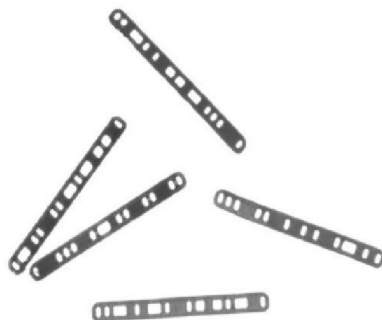


**Figure 4.10:** Aluminium rods with barcode. The particles and their codes are produced by optical lithography and dry etching of an aluminium layer sputtered on a substrate. The particle dimensions are  $100\ \mu\text{m} \times 10\ \mu\text{m} \times 1\ \mu\text{m}$ . ©SmartBead Technologies.

code. More than 100,000 codes can be generated using encoding schemes that are used for standard barcodes. A practical difficulty of this method is that the ligands or compounds have to be bound to the aluminium surface. For example, it is acknowledged that proteins bind only weakly to untreated aluminium when incubated in an aqueous solution [127]. Therefore, a further step needs to be developed to modify the particle surface chemically.

In the second method, metal cylindrical rods are fabricated (as shown in Fig. 4.11), which consist of adjacent (submicrometre) stripes of alternating metals [128]. The particles are prepared by the sequential electrochemical reduction of different metal ions into the pores of membrane templates, followed by particle release. The length of each of the stripes can be adjusted by controlling the amount of current that is passed in each electroplating step [129]. The differential optical reflectivity patterns of the adjacent stripes identify the rods. For example, the reflectivity characteristics of gold are different to those of silver or platinum. The number of uniquely encoded rods is virtually unlimited, as many parameters can be varied: the width and overall length of the rods; the number and type of the metals; and the number, length and order of the stripes. The codes can be identified by conventional light microscopy and image analysis. However, the detection can be automated by sending the particles through a cytometer-like apparatus. The minimal useful stripe length will be determined by the optical detection resolution and is estimated to be  $\sim 500\ \text{nm}$ . The diameter of the rods is determined by the diameter of the pores of the membrane template, which is between  $15\ \text{nm}$  and  $12\ \mu\text{m}$ , whereas the overall length of the particles will be  $1\text{-}50\ \mu\text{m}$ . Although, in theory, many different metals can be used, this number will be limited in practice because the reflectivity characteristics are wavelength dependent, and a spectral overlap might occur, which would cause a situation similar to

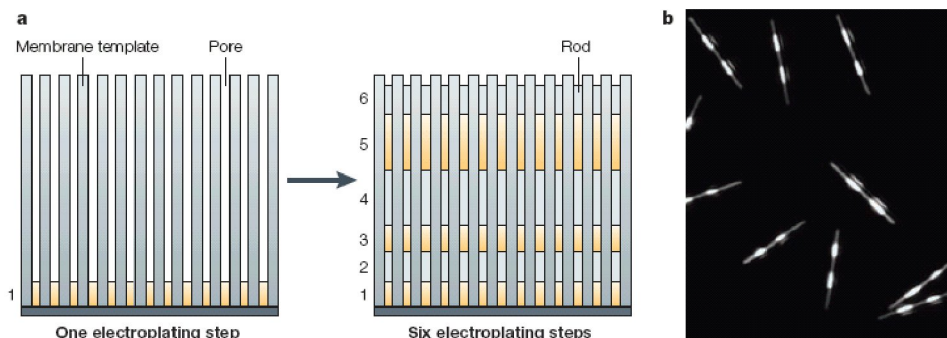


**Figure 4.11:** Metallic nanorods. **(a)** Vertical cross section of the template membrane. The rods are synthesized in the pores of the template membrane by sequential electrodeposition of different metals, which results in different metallic segments on top of each other. The length of the segments can be varied. **(b)** Alternating gold and silver stripes create the ‘barcode’ pattern on these  $4.5\ \mu\text{m}$  long particles. When viewed in blue light under a microscope (reflectance mode), silver is much more reflective than gold, which makes it possible to discriminate between the segments. (*Images reproduced from [131].*)

the spectral overlap of different fluorophores. For example, nickel (Ni) and palladium (Pd) have similar reflectivity spectra at wavelengths above 600 nm, and will be nearly indistinguishable if placed next to each other. Therefore, the metals used in the encoding scheme have to be selected carefully, depending on the wavelength of the detection beam. This technique has some clear advantages, including a virtually unlimited number of unique codes and a small particle length and volume. Moreover, many particles can be fabricated simultaneously – as many as there are pores in the membrane template. However, all particles produced in the same process will have identical codes because they were created by the same electrochemical reduction steps. So, to create 1,000 different codes, the process must be repeated 1,000 times. It has been shown that depositing a  $2\text{-}\mu\text{m}$ -thick segment takes  $\sim 30$  minutes to complete [130]. Therefore, an important factor for the feasibility of this technique will be the time needed to create one set of rods. Again, special chemistries are needed to bind the probes to the metal surface. Nevertheless, the particles have been shown to be valid solid supports for both a ‘sandwich’ hybridization assay and a double simultaneous sandwich immunoassay [131].

Similar to the rf tags, both techniques that use metal particles have the extra advantage of an increased degree of multiplexing, because no fluorescence is used in the encoding scheme. A practical disadvantage is the rapid settling of the particles owing to their large

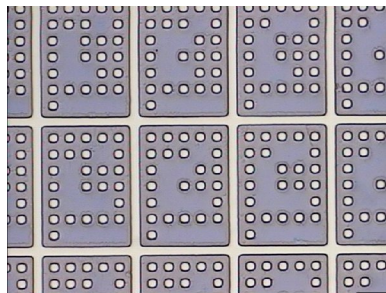


**Figure 4.12:** TEM image of polymeric particles from 3D Molecular Sciences. The particles are made using microelectronic machine systems photolithography technology. *Image courtesy of 3D Molecular Sciences, Ltd.*

mass density, which makes continuous agitation necessary to keep the particles in suspension.

3D Molecular Sciences created graphically encoded polymeric particles that are made using microelectronic machine systems photolithography technology. The particles can be encoded by their shape (see Fig. 4.12) or pattern of holes and are typically 50-500  $\mu\text{m}$  in size. Using the current masking system, 1000 codes can be produced, but more than 1 million unique codes are theoretically possible. Because the particles are polymeric, many chemical functionalizations for biomolecule attachment are possible.

Yet another new way of graphically encoding microcarriers has recently been developed, in which a pattern is written inside homogeneous, fluorescently dyed microspheres by ‘spatial selective photobleaching’ of the fluorescence (see Chapter 5 and [132, 133, 134]), as is shown in Fig. 4.13. Photobleaching is a photo-induced process by which fluorescent molecules lose their fluorescent properties, which results in a fading of the fluorescent colour. By using a specially adapted laser scanning confocal microscope [30], patterns can be photobleached at any depth inside the fluorescently dyed microsphere. Any geometry can be bleached – such as a symbol, an alphanumeric code or a barcode – and even three-dimensional structures can be generated. Furthermore, different bleaching levels can be obtained, which makes it possible to use ‘grey values’ in the encoding scheme. For example, barcodes can be bleached to have bars of different widths and intensity levels. The minimal width is determined by the optical resolution of the objective lens of the microscope that is used for writing. A useful minimal width is estimated to be between 0.5 and 1.5  $\mu\text{m}$ . This technique has several advantages. First, a virtually unlimited number of unique codes can be generated. A second important advantage is the low-cost commercial availability





**Figure 4.13:** Spatial selective photobleaching. Confocal image of a 28  $\mu\text{m}$  diameter fluorescent microsphere with a bleached barcode and an alphanumeric code.

of the microspheres that are used in this technique; for example, fluorescent polystyrene microspheres. Moreover, as the encoding technique is readily applicable to microspheres that are common to combinatorial chemistry and screening applications, good use can be made of the current extensive knowledge on creating bead-based libraries or carrying out bead-based assays, thereby eliminating the need for the development of special chemistries. A third asset is the possibility of encoding the beads at any time in the reaction process. Yet another advantage is the need for only one fluorescent dye in the encoding scheme, which allows at least two fluorophores to be used for probing, therefore increasing the multiplex capabilities. A practical disadvantage of the technique is the need for accurate positioning of the beads at readout time to ensure the correct identification of the encoded pattern. For example, if a barcode is written at the central plane of a microsphere, the sphere has to be presented to the reading beam in a well-defined position and orientation for the barcode to be entirely visible. If not, a time-consuming, three-dimensional confocal scan would be necessary to detect the complete barcode. It will therefore be a technical challenge to develop an apparatus that enables fast and automatic correct positioning and orienting of the beads.

Alternatively, the process of photochroming can be used instead of photobleaching. A microsphere that is loaded with a photochromic dye is, for example, initially colourless and transparent, but will carry a coloured (for example, blue) pattern after ultraviolet illumination of selected regions. This method has the added advantage that the encoded pattern can be detected by conventional light microscopy, which eliminates the need for a confocal microscope for detection. Moreover, no fluorescence is needed for the encoding scheme, which further increases the multiplexing capabilities.

#### 4.2.4 Physical encoding

Encoding strategies that make use of the ability to discriminate between microcarriers that have different detectable physical properties ‘as a whole’ are termed ‘physical encoding schemes’. It has been suggested many times that microcarriers can be distinguished by their differences in size [135, 136], density, refractive index [137], shape [138], composition [139, 140, 141] and so on. The number of uniquely encoded microcarriers that can be fabricated by physical encoding will be rather limited compared with previously mentioned techniques, because it would be difficult to manufacture, for example, thousands of beads that can be identified on the basis of differences in refractive index. Physical encoding is more likely to be used in addition to one of the previously mentioned techniques. For example, Trau and Battersby [85] have used eight parameters, such as size and refractive index, that can be detected by modern flow cytometers in addition to their fluorescent optical signatures.

### 4.3 Conclusions

Many strategies for encoding microcarriers have arisen in the past couple of years, which have tried to provide a solution to the multiplexing needs in the fields of drug discovery, drug screening and diagnostics, or solve the need to encode compound libraries that are synthesized in combinatorial chemistry. Not only the number of beads that can be uniquely encoded is important, but also the ability to rapidly and automatically encode and decode the microcarriers. These requirements, in addition to the cost of the techniques, will probably determine which one of the discussed methods will be broadly used for commercial applications. In terms of the number of codes, the graphical and electronic encoding strategies are the most promising. Conversely, optical encoding strategies have the advantage of being easier to decode, as only the overall optical properties of the particles need to be detected. The next few years will show if the speed and operating costs of graphical encoding methods can be optimized to enable their use in industrial applications.

# Chapter 5

## Encoding microbeads by spatial selective photobleaching

### Summary

Bead-based assays on very large numbers of molecules in gene expression studies, drug screening and clinical diagnostics, require the encoding of each of the microspheres according to the particular ligand bound to its surface. This allows mixing the uniquely encoded microspheres and subjecting them to an assay simultaneously. When a particular microsphere gives a positive reaction, the substance on its surface can be identified by reading the code. Previously reported techniques for colour encoding polymer microspheres only allow for a limited number of unique codes. Graphical encoding methods use metallic particles, which are rather uncommon in screening applications. Here, we demonstrate a new approach to encode polymer microspheres that are commonly used in screening applications, such as polystyrene microspheres, with a method that provides a virtually unlimited number of unique codes. Patterns can be written in fluorescently dyed microspheres by ‘spatial selective photobleaching’ and can be identified by confocal microscopy. Such encoded microparticles can find broad application in the collection and analysis of genetic information, high-throughput screening, medical diagnostics and combinatorial chemistry, and can also be used for labelling of consumer goods or as security labels to prevent counterfeiting.

## 5.1 Introduction

Tagging items by attaching or incorporating encoded labels has become a common technique in almost every imaginable area, from the consumer market to scientific research. Imagine, if you will, the well-known barcodes in supermarkets, or security labels – such as holograms on bank notes and credit cards – that assure an item is genuine and deter counterfeiting. Nowadays the use of encoded labels has found its way into chemical, biological and medical research as well. Indeed, the so-called ‘multiplex technologies’ - platforms that allow us to carry out many reactions simultaneously - have already made substantial contributions to progress in the biomedical fields of gene expression profiling, drug discovery, drug screening and clinical diagnostics. Because the amount of sequence data produced in current genomics and proteomics research is ever increasing, the need to rapidly screen large numbers of nucleic acids and proteins is addressed by these multiplex technologies. Two main approaches have been developed, the first being the high-density arrays, where the molecules to be screened are deposited on a glass or silicon substrate as a 2-D array and whose identity is known from their position in the array. However, aside from the cost of these devices that has remained relatively high, this technique also suffers from some disadvantages that are largely overcome by a second type of multiplex strategy: ‘bead-based assays’ [134, 142, 143]. The molecules to be screened are attached to the surface of a microsphere, usually one compound for each microsphere. The different microspheres can be subsequently suspended in a solution containing the target analyte, resulting in many reactions at the same time. If a particular microsphere is observed to give a positive reaction, the trick is to find out which compound is attached to the surface of that microsphere. Therefore, the spheres must have a code that allows identifying the molecules attached to their surface. The efficiency of the bead-based assay is directly related to the number of unique codes that are available. Indeed, the more spheres that can be uniquely encoded, the more reactions that can be carried out simultaneously.

Many researchers have recognized the importance of bead-based assays, and quite a few different encoding strategies have been developed (see Chapter 4). For example, microspheres can be colour-encoded by different chromophores, fluorophores or fluorescent semiconductor nanocrystals inside the microspheres. Although these microspheres have proven to be very suitable carriers in screening applications, the number of unique codes that can be generated in practice is rather limited (in the order of  $10^2$  to  $10^4$ ) because it becomes increasingly more difficult to distinguish between the different spectra the higher the number of colours used. Recently two alternatives have been reported that provide for

an unlimited number of uniquely encoded microparticles. The first technique uses metal strips in which a barcode is etched consisting of holes of different lengths. The second uses metal rod-shaped particles consisting of adjacent stripes of alternating metals with different reflectivity characteristics. Although both techniques yield many possible unique codes, the use of metal particles is quite uncommon to biological assays and may require specialized chemistry.

In this chapter a new type of encoded microparticles will be discussed that combines the advantages of providing for an unlimited number of unique codes and employing microparticles that have been common to screening applications for many years and are commercially available at low cost, such as polystyrene microspheres. Such encoded microparticles can find broad application in the collection and analysis of genetic information, high-throughput screening medical diagnostics and combinatorial chemistry. However, let it be noted that these encoded particles can equally find application in many other fields as well, such as tracking and labelling of consumer goods or as security labels to prevent counterfeiting. Therefore, first a description will be given of the new encoding technology followed by a section covering its many potential applications.

## 5.2 Encoding by ‘Spatial Selective Photobleaching’

As shown in Fig. 5.1, a pattern can be written inside a homogeneously fluorescently dyed microsphere by ‘spatial selective photobleaching’ of the fluorescence. Photobleaching is a photo-induced process where fluorescent molecules lose their fluorescent properties, resulting in a fading of the fluorescent colour. The term ‘spatial selective photobleaching’ refers to the photobleaching of certain regions in e.g. a fluorescent microsphere.

Any geometry can be bleached, such as a symbol or a barcode, at a certain depth in the microsphere by using a confocal scanning laser microscope (CSLM) modified to this purpose by adding the ‘SCAMPER’ module. The module, first developed by Wedekind et al. [30], consists of a powerful 1W Ar-ion laser and a fast optical switch, an acousto optical modulator (AOM), controlled by a computer and dedicated software. As schematically shown in Fig. 5.2, the laser light emerging from the Ar-ion laser is directed to the AOM, which diffracts a high or low power laser beam according to the signal it receives from the computer towards an optical fiber. Finally, the laser beam is transported to the CSLM

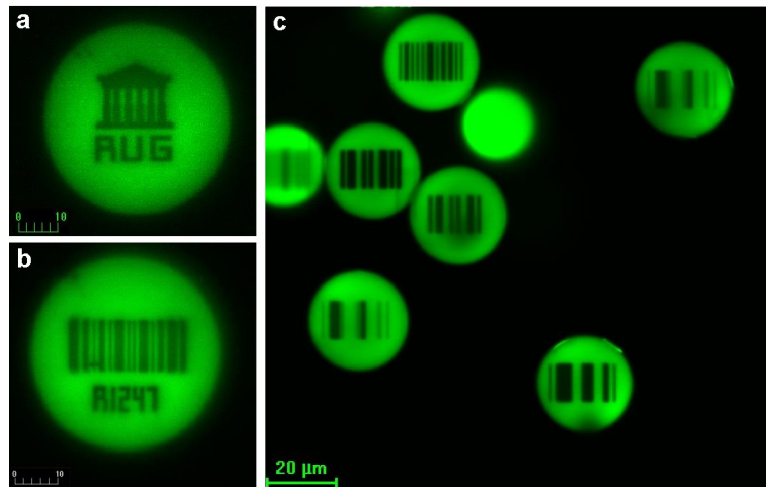


**Figure 5.1:** Encoding by spatial selective photobleaching. (a) A logo was bleached at the central plane of a  $45\ \mu\text{m}$  green-fluorescent microsphere. (b) A barcode was bleached at the central plane of a  $45\ \mu\text{m}$  microsphere. Bars of four different widths were used and each code-element (bar) is separated from the next one by an unbleached region of  $1\ \mu\text{m}$ . To illustrate the versatility of possible geometries, an alpha-numeric code was added as well. (c) Confocal image of green-fluorescent  $28\ \mu\text{m}$  microspheres encoded with various barcodes.

(Bio-Rad MRC1024 UV), where it is focused through the microscope's objective lens into the fluorescent microsphere. The high-power laser beam is used for photobleaching, while the low power beam excites the fluorescent molecules without significant bleaching and is used for mere imaging. Bleaching patterns can be designed in dedicated software that controls the AOM. While taking an image with the CSLM - which is done by scanning the laser beam in a raster pattern, pixel by pixel, line by line - the software controls the AOM in such a way that low and high power laser light reaches the sample according to the designed pattern. The regions in the sample that were hit by the high power laser light will be bleached to an extent depending on the amount of light received.

There are two main requirements for the microsphere material to be workable. First, the material has to be sufficiently transparent for the laser light to get inside the microsphere. Second, most of the fluorescent molecules should be fixed in the material, either by chemical bonds, or by physically entrapping them in the meshes of the material's matrix. Else the bleached code would fade away over time because of the random movement - a process that is called 'diffusion' - of the fluorescent and bleached molecules. At this moment the method of spatial selective photobleaching has successfully been applied to

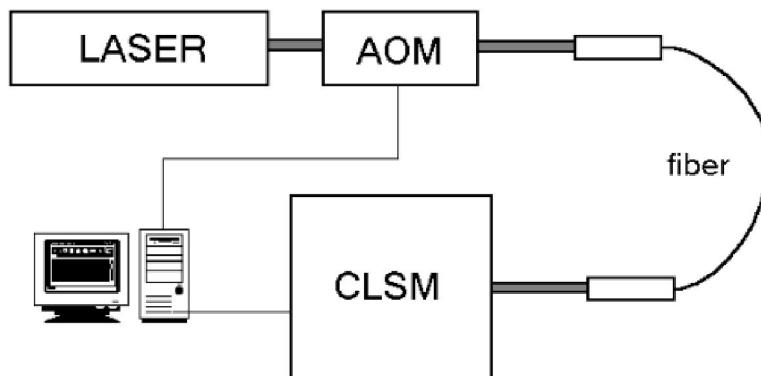


**Figure 5.2:** Diagram of the instrumental set up. The encoding instrument is a CSLM modified with the SCAMPER module consisting of a powerful laser, a computer controlled AOM to rapidly switch between a low and high laser intensity and an optical fiber to transport the laser light to the CSLM where it is focused into the fluorescent microspheres.

polystyrene, argogel (polyethylene glycol grafted polystyrene) and dextran beads. Other common polymer bead materials are expected to work fine as well.

### 5.3 Code design

The bleaching pattern can be of any geometry, one-, two- or even three-dimensional. But as the pattern is bleached pixel by pixel, the time needed for the writing process will depend on the complexity of the pattern. In applications such as high-throughput screening, the codes should be written and read as fast as possible. Therefore, in this study we will focus mainly on the design of one-dimensional codes, such as barcodes. An example is shown in figure Fig. 5.1b.

Information can be stored in width as well as in intensity of the code elements, as will be discussed in section 6.3. Fig. 5.3a shows a bleached barcode consisting of eight bars of equal width, but using eight different bleaching levels. The graph shows the intensity profile across the barcode. Indeed, eight different intensities can be distinguished, thus proving the feasibility of intensity encoding. However, one must be careful not to place the bars too close as this will cause the intensity profiles of the bars to overlap, making it more difficult to distinguish between the different levels. The reader is referred to Chapter 7 for a more in depth treatment of the different aspects that are important

for the photobleaching of a code. In Fig. 5.3b a combination of double width ( $1.06 \mu\text{m}$  and  $2.12 \mu\text{m}$ ) and double intensity encoding (bleached and unbleached) is shown. For Fig. 5.3c double width ( $1.6 \mu\text{m}$  and  $3.2 \mu\text{m}$ ) and triple intensity encoding was used. The first and last bars were added as a simple start and stop sign but do not belong to the actual code. These examples demonstrate the feasibility of multiple width and intensity encoding.

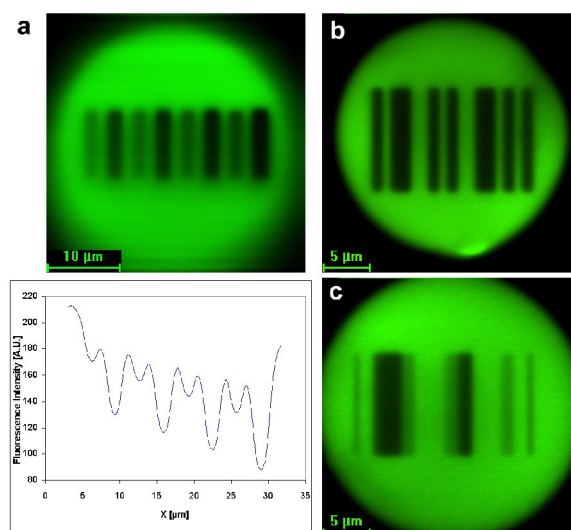


**Figure 5.3:** Intensity and width encoding. **(a)** To demonstrate the possibility of intensity encoding, a barcode was bleached at the central plane of a  $45 \mu\text{m}$  microsphere using eight different bleaching levels. The intensity profile across the barcode shows indeed eight bleaching intensities.  $x$  is the direction perpendicular to the bars. **(b)** A barcode was bleached at the central plane of a  $28 \mu\text{m}$  microsphere using two intensities (bleached and unbleached) and two widths ( $1.06 \mu\text{m}$  and  $2.12 \mu\text{m}$ ). **(c)** A combination of three widths and two intensities was used in this barcode, which was bleached at the central plane of a  $28 \mu\text{m}$  microsphere. The first and last bars were added as a simple start and stop sign and are not part of the code itself.

The number of unique codes that can be generated depends on three aspects, the first obviously being the space available inside the microsphere. Empirically we have seen that at the central plane of a microsphere, as a rule of thumb, about 70% of the diameter can be used for the writing of a code. Bleaching near the edges becomes less efficient because of the spherical shape and should be avoided. For example, at the central plane of a  $50 \mu\text{m}$  sphere, the central  $35 \mu\text{m}$  is available for writing a code. The second aspect is the resolution of the writing beam, primarily depending on the characteristics of the objective lens and the wavelength of the light used [48]. But inside a microsphere, the real resolution will be



less than theoretically predicted because of a mismatch between the refractive index of the microsphere material and its surrounding medium [144, 145]. For example, the refractive index of polystyrene and water is respectively 1.59 and 1.33. This mismatch of refractive indices causes spherical aberrations that result in a decrease in resolution. These issues are discussed in detail in Chapters 6 and 7. Finally, the number of codes is determined by the number of different widths and intensities that are employed in the encoding scheme, as will be discussed in section 6.3. If only two intensities are used, the experiments show it is possible to make a readable code with bars having a minimal width of  $1 \mu\text{m}$ . More intensities will probably require a larger minimal width of the bars in order for the different levels to remain clearly distinguishable. The experiments show that a minimal width of  $1.5 \mu\text{m}$  is feasible in this case. To give an idea of the number of different codes that can be generated in actual practice, consider for example a  $50 \mu\text{m}$  diameter microsphere in which  $30 \mu\text{m}$  is available at the central plane for writing a code. Using 3 widths ( $1.5 \mu\text{m}$ ,  $3 \mu\text{m}$  and  $4.5 \mu\text{m}$ ) and 3 intensities, an incredible number of  $179 \times 10^6$  codes can be generated. Employing only two intensities allows the use of smaller code elements. Therefore the combination of two intensities and three widths ( $1 \mu\text{m}$ ,  $2 \mu\text{m}$  and  $3 \mu\text{m}$ ) still yields  $4.23 \times 10^6$  different codes. From this it is clear that the number of unique codes that can be generated using the spatial selective photobleaching technique is virtually unlimited.

A barcode like the one in the example above, is a one-dimensional code in that its spatial information is stored in only one direction: the width of the bars. The code geometry however is two-dimensional: the bars have a certain length for facile reading. If one wants to encode the microspheres as fast as possible, it is worth considering writing ‘barcodes’ consisting of bars of minimal length, what could be termed ‘dotcodes’. An example is shown in Fig. 5.4 where the same barcode as in 5.3c is bleached by scanning only one line across the central plane of the microsphere. The time it takes to perform a single line scan depends on the maximum scan speed of the CSLM, which in this case was limited to 1.2 ms. Let it be noted this minimal time is not a fundamental limit to the bleaching process but an instrument dependent parameter. Therefore, an encoding rate of  $10^2$  to  $10^3$  microspheres per second seems feasible.

Although in our experiments the microspheres were stationary while being encoded by the scanning laser beam, it is very well possible to use a stationary laser beam while the microspheres are moved appropriately past the beam. This is especially attractive in case of the aforementioned ‘dot code’, where the microspheres would have to pass the stationary laser beam only once for writing or reading the code. The microspheres could be

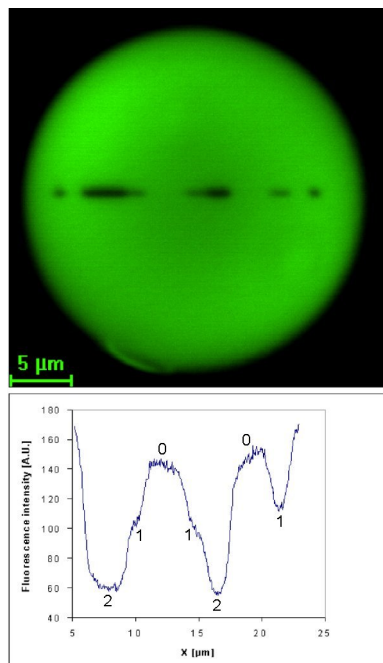


**Figure 5.4:** A ‘dot code’. The same barcode as shown in 5.3c was bleached at the central plane of a 28  $\mu\text{m}$  microsphere. The bleaching was done by scanning only once across the central line. The first and last ‘dots’ were added as a simple start and stop sign and are not part of the actual code. The graph shows the intensity profile across the bleached ‘dot code’, leaving out the first and last dot.  $x$  is the direction of the dot code. The three intensity levels can be distinguished, and the numbers on the graph indicate the bleaching levels: 0 = unbleached, 1 = medium bleached, 2 = fully bleached.

transported by a fluid flow in a capillary or flow-cell or by fixing the spheres to a platform that can be mechanically positioned.

## 5.4 Position and orientation of the microspheres

Although at this moment only one microsphere at a time can be encoded, the technique is amenable to automation. In screening and diagnostics applications, the encoded microspheres will be subjected to chemical or biological assays in which they are free to move and rotate. In general, after recollection, the microspheres will have an orientation different from when they were encoded. To correctly identify a code, a major challenge in the reading process will be to obtain the same position and orientation of the microspheres as when they were encoded in order for the pattern to be clearly visible. By providing

the microspheres with orientation information it is possible to automatically position the spheres correctly for readout. For example it would be possible to use elliptical spheres instead of spherical ones. Or alternatively apply a ferromagnetic coating to the microspheres that allows them to be oriented in a magnetic field.

To evaluate the latter possibility, a batch of green-fluorescent 38  $\mu\text{m}$  polymer microspheres was coated with chromiumdioxide particles. Similar ferromagnetic microspheres have previously been used for studying mechanotransduction across the cell surface and through the cytoskeleton [146]. Fig. 5.5 shows a microscopic fluorescence image of ferromagnetic-coated microspheres. To visualise the chromiumdioxide particles, the microscope was focused on the surface of the microspheres. At first, the microspheres were suspended in distilled water and magnetized by a strong magnetic field. Next, to show that the magnetized ferromagnetic microspheres can be oriented in an external magnetic field, an arrow was bleached at the central plane of a magnetic microsphere while being exposed to and oriented by a weak external magnetic field (Fig. 5.6, image A). Subsequently, confocal images were taken (1-2 seconds interval) to record the movement of the microsphere while being subjected to a randomly rotating magnetic field (Fig. 5.6, images B–H). During the movement the arrow was observed to follow the magnetic field and return to its exact original orientation together with the magnetic field (compare images A and H of Fig. 5.6). This experiment demonstrates the possibility to orient a magnetized ferromagnetic-coated microsphere at the encoding step and retrieve the same orientation at the decoding step by applying a weak external magnetic field, thus bringing the code to the correct readout position. Let it be noted that after deposition of the ferromagnetic coating on the microsphere's surface, it is certainly possible to apply a final coating of bead material, e.g. polystyrene, in order to protect the assay environment from the ferromagnetic particles.

## 5.5 Photochroming

Instead of photobleaching, the process of photochroming might be used as well for the encoding of microcarriers. Upon illumination of a photochromic compound with light of the appropriate wavelength, its absorption spectrum changes, which is observed as a change in colour. For example, the compound may be initially colourless, but turns blue after UV-illumination. Microspheres that are loaded with this photochromic compound are initially colourless and transparent, but will carry a coloured pattern inside at a certain

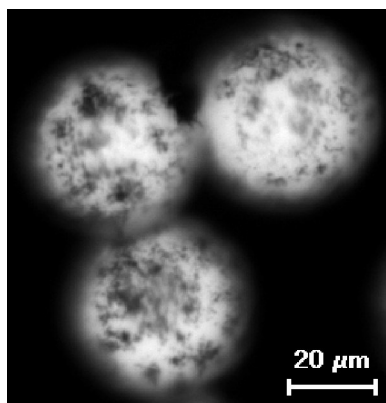


**Figure 5.5:** Fluorescence microscope image of green-fluorescent  $38 \mu\text{m}$  microspheres coated with ferromagnetic chromium dioxide particles. The microscope was focused at the top surface of the microspheres to visualise the ferromagnetic particles.

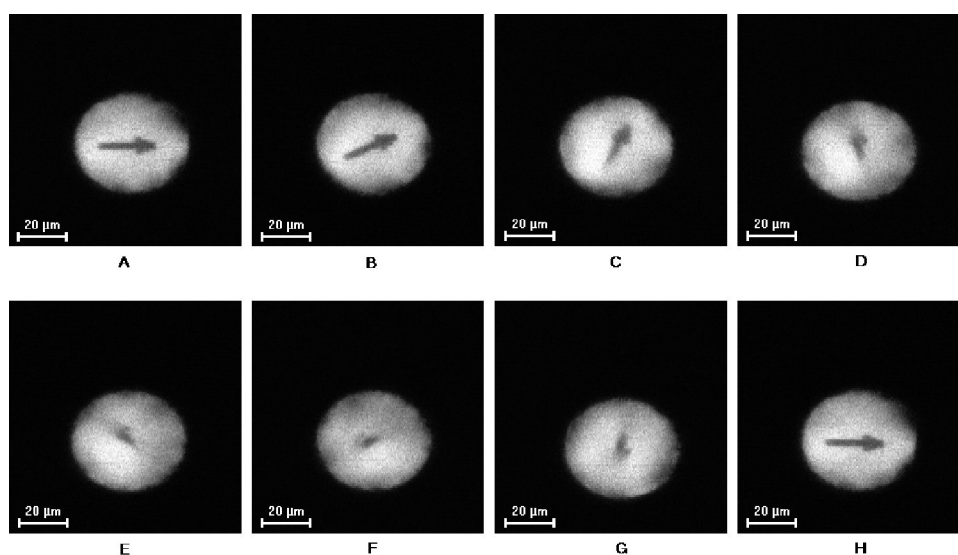


**Figure 5.6:** Magnetic orientation of a magnetized ferromagnetic microsphere. (A) An arrow was bleached at the central plane of a magnetized ferromagnetic microsphere to visualize its orientation. (B-H) Subsequently, a sequence of confocal images (1 image every 2 seconds) was taken to record the movement of the microsphere while being subjected to an external randomly moving magnetic field. The microsphere follows precisely the movement of the external magnetic field. When the magnetic field returns to its original orientation, the microsphere is observed to do the same (compare images A and H). Images B to G represent the situation of the microsphere being subjected to an assay during which it will be randomly oriented. Image H demonstrates the possibility at readout time to correctly reorient the microsphere such that the encoded pattern becomes clearly visible again.

depth.

To show the feasibility of this approach, 28  $\mu\text{m}$  polystyrene microspheres were loaded with the photochromic compound 1,2-Bis(2-methoxy-5-phenyl-3-thienyl)perfluorocyclopentene, as described in [147], which has initially no absorption in the visible range, but develops an absorption band extending from about 450 nm to 750 nm after UV illumination, with an absorption maximum near 600 nm. Consequently, the photochromic compound is initially transparent to visible light, but turns blue upon UV illumination. The loading was done by suspending 5mg of dry microspheres in a 2% (w/v) solution of the photochromic compound in  $\text{CH}_2\text{Cl}_2$  and overnight incubation. Then the suspension was centrifuged for 5 minutes at 12000 rpm. Finally the spheres were separated and resuspended in de-ionised water. Fig. 5.7 shows such a photochromic microsphere prior to and after the photochroming step. Because the UV Ar-ion laser is not equipped with the SCAMPER module, it was not possible to create complex codes. Instead, a small square region of the microsphere was illuminated with the 357 nm line of the UV Ar-ion laser by temporarily increasing the zoom factor of the CSLM. The red 647 nm laser line from a Kr/Ar laser was subsequently used to record the transmission images. As expected from the photochromic properties, in the transmission mode the microsphere is transparent to the red light, except for the UV-illuminated area. This experiment demonstrates the possibility of encoding microcarriers by photochroming as an alternative to photobleaching<sup>1</sup>.

In both techniques the codes can be written at any internal depth of the microsphere. Imaging of a photobleached code has to be done by a confocal microscope in order to distinguish between fluorescence coming from the plane in which the code is written and fluorescence coming from other depths. Encoding by photochroming might have an advantage over photobleaching because of increased photosensitivity. Moreover, a regular light microscope is sufficient to image the photochromic codes, because the spheres are completely transparent and colourless except for the code, while a confocal microscope is needed to detect the bleached pattern inside the fluorescent microspheres. It seems advisable, though, that a multi-photon microscope should be used for writing the photochromic codes. Else the code will be obscured by photochroming at other depths than the focal plane because of the conical shape of the writing beam. Further experiments are needed to fully compare the pros and cons of encoding by photobleaching and photochroming.

---

<sup>1</sup>The interested reader can find additional information on the use of photochromic compounds for optical data storage in [148]

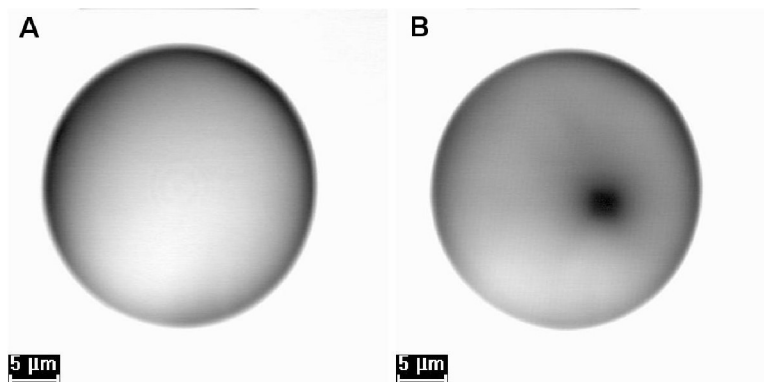


**Figure 5.7:** Encoding by photochroming. (A) Transmission image of a photochromic microsphere prior to the photochroming step. (B) Transmission image after photochroming of a  $2\ \mu\text{m} \times 2\ \mu\text{m}$  square by the 357 nm UV line from an Ar-ion laser. The red 647 nm line from a Kr/Ar laser was used for the recording of both transmission images.

## 5.6 Putting the code to work

Microspheres have been successfully used in screening and diagnostic applications for many years, despite restrictions by current technologies in terms of numbers of unique codes (in the order of  $10^2$  to  $10^4$ ). Now, with the new technology described herein, clearly, numerous applications are possible. For example, microspheres have been successfully applied to genotyping, measuring cytokine and thyroid levels, cystic-fibrosis screening, genetic human lymphocyte antigen (HLA) typing, kinase testing, allergy testing, DNA-hybridisation studies, proteomics and immunoassays (see Chapter 4). As the number of codes that can be generated is almost unlimited (in the order of  $10^6$  to  $10^8$ ), this spatial selective encoding technique can boost the well-established bead-based screening techniques to a new level of efficiency, reducing time and cost.

Additionally, many other applications are possible as well. We suggest the encoded microparticles be used as security labels to prevent brand piracy, product diversion and counterfeiting. These crimes not only cause brand owners to lose billions of dollars annually, but legitimate jobs are often lost and government agencies lose considerable sales tax and income tax revenues. Encoded microspheres could be incorporated into the packaging or may even be mixed with a coating spray. The encoded particles could also be incorporated into bank notes to provide for an unmistakable final level of secure identification or be mixed with inks and paints to print shares, entrance tickets, credit cards, etc. Yet

another field of application is ‘tracking and tracing’ of goods to control quality, security and efficiency in manufacturing processes. Tracking means knowing where a product is at any given moment, while tracing means knowing where a product has been before. This is very important for food safety as the recent dioxine crisis in animal feed and the outbreaks of mad cow disease in Europe have shown. Furthermore, the particles could also be incorporated into explosives and guns to trace their origin when used in crimes.

## 5.7 Conclusions

We have presented a novel way of encoding microspheres that holds much promise for use in biomedical and biotechnological research. As the encoding method is applicable to regular microspheres common to screening applications for many years, it has a major advantage in that users can benefit from the current extensive knowledge on performing bead-based assays, eliminating the need for the development of new special chemistries. Moreover this technique provides for a virtually unlimited number of unique codes, hence overcoming current limits of existing bead-based encoding strategies and increasing cost and time efficiency. Therefore, this new approach to the encoding of microspheres is very promising in overcoming many of the restrictions of current screening techniques and is expected to open new horizons in gene expression research, high-throughput drug screening, drug discovery and medical diagnostics. Moreover, many other applications of the encoded particles can be found, such as safety labels to prevent counterfeiting and for tracking and tracing of goods to assure their name brand quality to the consumers.

# Chapter 6

## Theoretic considerations on the encoding by photobleaching of fluorescent microcarriers

### Summary

It is important to gain insight in the process of writing codes in microcarriers by photobleaching in order to establish the parameters that play an important role in the bleaching of a code. In the first section of this document a first-order theory of photobleaching and its application in the writing of a barcode will be presented. Imaging of the photobleached code with a confocal microscope will be discussed as well. Based on these theoretic calculations, a computer program was written to simulate the writing by photobleaching and confocal imaging of a barcode and will be discussed in the second section. This simulation program provides for an easy and fast way to evaluate the effect of the different parameters – such as the type of objective lens that is used for writing and/or reading, the amount of noise, etc. – on the readability of the code.

### 6.1 Theory of first-order photobleaching by a scanning beam applied to the writing of a barcode

#### 6.1.1 First-order photobleaching

For simplicity we make the assumption that the kinetics of the photobleaching process can be described by an irreversible first-order reaction with rate constant  $\alpha$ . The value



of the bleach constant  $\alpha$  depends on the material characteristics (i.e. fluorophore and sample matrix). Let  $I_b(\mathbf{r})$  denote the 3-D intensity distribution of the bleaching laser beam focused through the objective lens of the microscope in the sample and  $B(\mathbf{r})$  the bleaching pattern. The three-dimensional light-distribution  $K(\mathbf{r})$  that results from scanning  $I_b(\mathbf{r})$  in the sample according to  $B(\mathbf{r})$  is given by the convolution product of  $B(\mathbf{r})$  and  $I_b(\mathbf{r})$  (see Appendix A):

$$\begin{aligned} K(\mathbf{r}) &= B(\mathbf{r}) \otimes I_b(\mathbf{r}) \\ &= \iiint_{\infty} B(x', y', z') I_b(x - x', y - y', z - z') dx' dy' dz'. \end{aligned} \quad (6.1)$$

After bleaching of a 1-D bleaching pattern  $B(x)$  with a scanning beam, the concentration of unbleached fluorophores  $C(\mathbf{r})$  at position  $\mathbf{r}$  can be calculated from (see Appendix A, Eq. (A.2)):

$$C(\mathbf{r}) = C_0(\mathbf{r}) e^{-\frac{\alpha}{v} K(\mathbf{r})}, \quad (6.2)$$

where  $C_0(\mathbf{r})$  is the initial distribution of unbleached fluorophores and  $v$  the constant scanning speed. For a 2-D bleaching pattern  $B(x, y)$ , the concentration of unbleached fluorophores can be calculated from (see Appendix A, Eq. (A.4)):

$$C(\mathbf{r}) = C_0(\mathbf{r}) e^{-\frac{\alpha}{v \Delta y} K(\mathbf{r})}, \quad (6.3)$$

where  $\Delta y$  is the distance between two adjacent scanlines. Eqs. (6.2) and (6.3) are valid only in the case of 100% immobile fluorescent molecules. The more general case of a mobile and immobile fraction will be discussed further on in section 6.1.4.

Eqs. (6.1) and (6.2) or (6.3) provide the general mathematical basis for the (first-order) photobleaching of a pattern  $B(\mathbf{r})$  by scanning the intensity distribution  $I_b(\mathbf{r})$  with speed  $v$  inside the sample matrix loaded with fluorescent molecules. We will now proceed by calculating the 3-D light distribution  $K(\mathbf{r})$ , according to Eq. (6.1), for the bleaching of a barcode.

### 6.1.2 Bleaching of a 2-D barcode

In case of a 2-D bleaching pattern, Eq. (6.1) becomes:

$$K(\mathbf{r}) = \int_{-\infty}^{+\infty} \int_{-\infty}^{+\infty} B(x', y') I_b(x - x', y - y', z) dx' dy'. \quad (6.4)$$

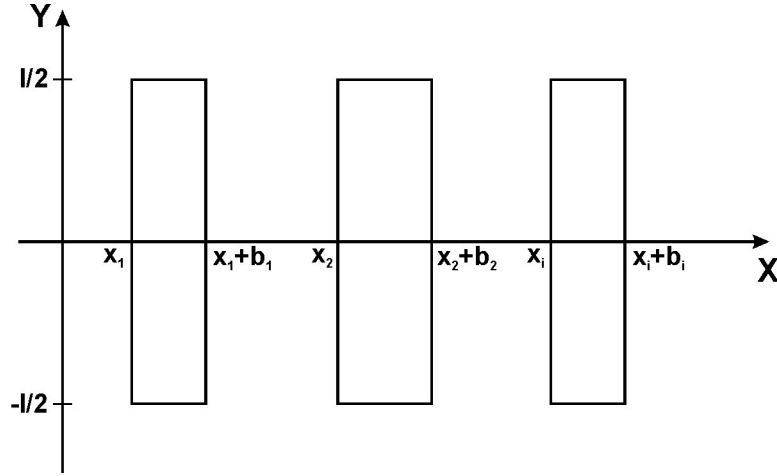


**Figure 6.1:** Bleaching pattern consisting of rectangles in parallel.

Let us now assume that the bleaching pattern consists of rectangles in parallel, as is the case for a barcode (see Figure 6.1). Rectangle  $i$  starts at position  $x_i$ , has a width  $b_i$  and will be bleached with laser intensity  $B_i$  relative to the maximum bleaching intensity ( $0 \leq B_i \leq 1$ ). All rectangles have the same length  $l$ .

For a pattern consisting of  $N$  rectangles, Eq. (6.4) becomes:

$$K(\mathbf{r}) = \int_{-l/2}^{+l/2} \sum_{i=1}^N \left( B_i \int_{x_i}^{x_i+b_i} I_b(x-x', y-y', z) dx' \right) dy'. \quad (6.5)$$

Next, a choice has to be made for the illumination intensity distribution. As explained in Appendix B, one of the distributions that will be evaluated is the modified Gaussian intensity distribution (see section B.2):

$$I_b(\mathbf{r}) = I_{b,0} e^{-2\frac{x^2+y^2}{w_e^2(z)}} e^{-2\frac{z^2}{z_{r,e}^2}}, \quad (6.6a)$$

where

$$w_e^2(z) = w_{0,e}^2 \left( 1 + \left( \frac{z}{z_{r,e}} \right)^2 \right) \quad (6.6b)$$

and

$$z_{r,e} = \frac{n\pi w_{0,e}^2}{\lambda_e}, \quad (6.6c)$$

on condition that

$$w_{z,e} \leq \sqrt{2} \frac{n\pi}{\lambda_e} w_{0,e}^2. \quad (6.6d)$$

The other illumination distribution that will be evaluated is the fundamental Gaussian-beam solution (see section B.3):

$$I_b(\mathbf{r}) = I_{b,0} \left( \frac{w_{0,e}}{w_e(z)} \right)^2 e^{-2 \frac{x^2+y^2}{w_e^2(z)}}, \quad (6.7)$$

where  $w_e(z)$  and  $z_{r,e}$  are defined as in Eq. (6.6b) and (6.6c) respectively.  $I_{b,0}$  is the light intensity at the origin, which can be expressed in terms of the total light power in the sample  $P$  (see sections B.2 and B.3):

$$I_{b,0} = \frac{2P}{\pi w_{0,e}^2}. \quad (6.8)$$

Eq. (6.8) applies to both Eq. (6.6) and (6.7). Let it be noted that, according to Eq. (6.6), the modified Gaussian intensity distribution is uniquely determined by the Gaussian radius in the focal plane  $w_{0,e}$  and the Gaussian radius along the optical axis  $w_{z,e}$ . The fundamental Gaussian beam solution, at the other hand, is uniquely determined by the Gaussian radius in the focal plane  $w_{0,e}$  alone, according to Eq. (6.7).

The 3-D bleaching intensity distribution  $K(\mathbf{r})$  for the modified Gaussian distribution is finally found by substituting Eq. (6.6) into Eq. (6.5), which leads to:

$$K(\mathbf{r}) = \frac{\pi}{8} I_{b,0} w_e^2(z) \sum_{i=1}^N \left[ B_i \left( \operatorname{erf} \left( \sqrt{2} \frac{x - x_i}{w_e(z)} \right) - \operatorname{erf} \left( \sqrt{2} \frac{x - (x_i + b_i)}{w_e(z)} \right) \right) \right] \cdot \left[ \operatorname{erf} \left( \sqrt{2} \frac{y + l/2}{w_e(z)} \right) - \operatorname{erf} \left( \sqrt{2} \frac{y - l/2}{w_e(z)} \right) \right] e^{-2 \frac{z^2}{w_{z,e}^2}}. \quad (6.9)$$

In case of the fundamental distribution we find  $K(\mathbf{r})$  by substituting Eq. (6.7) into Eq. (6.5):

$$K(\mathbf{r}) = \frac{\pi}{8} I_{b,0} w_{0,e}^2 \sum_{i=1}^N \left[ B_i \left( \operatorname{erf} \left( \sqrt{2} \frac{x - x_i}{w_e(z)} \right) - \operatorname{erf} \left( \sqrt{2} \frac{x - (x_i + b_i)}{w_e(z)} \right) \right) \right] \cdot \left[ \operatorname{erf} \left( \sqrt{2} \frac{y + l/2}{w_e(z)} \right) - \operatorname{erf} \left( \sqrt{2} \frac{y - l/2}{w_e(z)} \right) \right]. \quad (6.10)$$

The function ‘erf’ denotes the ‘error function’, which is defined as:

$$\operatorname{erf}(z) = \frac{2}{\sqrt{\pi}} \int_0^z e^{-z^2} dz. \quad (6.11)$$

Eqs. (6.9) and (6.10) describe the three-dimensional light distribution  $K(\mathbf{r})$  during bleaching of a pattern consisting of  $N$  rectangles of length  $l$ , where rectangle  $i$  starts at position  $x_i$ , has width  $b_i$  and is bleached with a bleaching intensity  $B_i$  relative to the maximum bleaching intensity. From Eq. (6.9) or (6.10) together with Eq. (6.8) and (6.3) the concentration of unbleached fluorophores  $C(\mathbf{r})$  after a bleaching time  $t$  can be calculated at any point in three-dimensional space.

### 6.1.3 Bleaching of a 1-D barcode or ‘dotcode’

As discussed in section 5.3, in order to increase the writing speed, one could bleach a 1-D barcode or ‘dotcode’, for which only one linescan is needed. Using the same notations as in the previous sections, it follows from Eq. (6.1) that the bleaching light distribution  $K(\mathbf{r})$  in this case is:

$$\begin{aligned} K(\mathbf{r}) &= \int_{-\infty}^{+\infty} B(x') I_b(x - x', y, z) dx' \\ &= \sum_{i=1}^N \left( B_i \int_{x_i}^{x_i+b_i} I_b(x - x', y, z) dx' \right). \end{aligned}$$

Using the modified Gaussian distribution Eq. (6.6), this finally leads to:

$$\begin{aligned} K(\mathbf{r}) &= \sqrt{\frac{\pi}{8}} I_{b,0} w_e(z) \cdot e^{-2\left(\frac{y^2}{w_e^2(z)} + \frac{z^2}{w_{z,e}^2}\right)} \\ &\cdot \sum_{i=1}^N \left[ B_i \left( \operatorname{erf} \left( \sqrt{2} \frac{x - x_i}{w_e(z)} \right) - \operatorname{erf} \left( \sqrt{2} \frac{x - (x_i + b_i)}{w_e(z)} \right) \right) \right]. \end{aligned} \quad (6.12)$$

And in case of the fundamental Gaussian distribution Eq. (6.7), this leads to:

$$\begin{aligned} K(\mathbf{r}) &= \sqrt{\frac{\pi}{8}} I_{b,0} \frac{w_{0,e}^2}{w_e(z)} \cdot e^{-2\frac{y^2}{w_e^2(z)}} \\ &\cdot \sum_{i=1}^N \left[ B_i \left( \operatorname{erf} \left( \sqrt{2} \frac{x - x_i}{w_e(z)} \right) - \operatorname{erf} \left( \sqrt{2} \frac{x - (x_i + b_i)}{w_e(z)} \right) \right) \right]. \end{aligned} \quad (6.13)$$

Substitution of Eq. (6.12) or (6.13) into (6.2) again allows to calculate at any point in three-dimensional space the concentration of unbleached fluorophores  $C(\mathbf{r})$  after bleaching.

### 6.1.4 Mobile fraction and multiple illumination scans

The above equations need slight modification if a mobile fraction is present in the encoding medium. Let  $C_0$  be the initial fluorophore concentration of which a fraction  $k$  is mobile (and a fraction  $1 - k$  immobile):

$$C_0 = (1 - k)C_0 + kC_0.$$

After instantaneous photobleaching, the mobile molecules will start to diffuse out of the photobleached area and will be replaced over time by unbleached fluorophores from the surroundings<sup>1</sup>. In case of a mobile fraction  $k$ , Eq. (6.2) or (6.3) should be replaced by:

$$C(\mathbf{r}) = (1 - k)C_0(\mathbf{r})e^{-\kappa K(\mathbf{r})} + kC_0(\mathbf{r}), \quad (6.14)$$

where  $\kappa = \frac{\alpha}{v}$  or  $\kappa = \frac{\alpha}{v\Delta y}$  for a 1-D or 2-D bleaching pattern respectively. Let it be noted that Eq. (6.14) is only valid after completion of the diffusion of the mobile fraction.

Depending on the photobleaching rate  $\alpha$  of the system and the available laser power for bleaching, it can be necessary sometimes to repeat the photobleaching scan a couple of times to obtain sufficient bleaching. Again assuming no diffusion during the photobleaching phase which consists of  $n$  sequential scans, the final concentration is thus given by:

$$C(\mathbf{r}) = ((1 - k)e^{-n\kappa K(\mathbf{r})} + k) C_0(\mathbf{r}), \quad (6.15)$$

where  $\kappa = \frac{\alpha}{v}$  or  $\kappa = \frac{\alpha}{v\Delta y}$  for a 1-D or 2-D bleaching pattern respectively.

### 6.1.5 Relation between two systems with different bleaching efficiencies

In order to select a suitable encoding material for the microcarriers, one should be able to compare the bleaching efficiencies of different types of microcarrier materials. Based on the results of the previous sections, we will therefore now try to find a way to do so experimentally.

Consider two different encoding materials with respective bleaching efficiencies  $\alpha_1$  and  $\alpha_2$ , and mobile fractions  $k_1$  and  $k_2$ <sup>2</sup>. If the same pattern is bleached in both materials,

---

<sup>1</sup>We will assume an infinite medium, i.e. a medium whose volume is much larger than the photobleached subvolume.

<sup>2</sup>The mobile fraction of a system can be experimentally determined by a FRAP experiment.

it follows from Eq. (6.15) that:

$$C_1(\mathbf{r}) = \left( (1 - k_1) e^{-n_1 \frac{\alpha_1}{v\Delta y} I_{01} K(\mathbf{r})} + k_1 \right) C_{01}(\mathbf{r}) \quad (6.16a)$$

$$C_2(\mathbf{r}) = \left( (1 - k_2) e^{-n_2 \frac{\alpha_2}{v\Delta y} I_{02} K(\mathbf{r})} + k_2 \right) C_{02}(\mathbf{r}), \quad (6.16b)$$

where the bleaching intensities  $I_{01}$  and  $I_{02}$  have been explicitly written ‘outside’  $K(\mathbf{r})$ . Eqs. (6.16a) and (6.16b) can be rewritten as:

$$\alpha_1 = -\frac{v\Delta y}{n_1 I_{01} K(\mathbf{r})} \ln \left( \frac{C_1(\mathbf{r})/C_{01}(\mathbf{r}) - k_1}{1 - k_1} \right)$$

$$\alpha_2 = -\frac{v\Delta y}{n_2 I_{02} K(\mathbf{r})} \ln \left( \frac{C_2(\mathbf{r})/C_{02}(\mathbf{r}) - k_2}{1 - k_2} \right),$$

from which it immediately follows that the ratio of the bleaching efficiencies  $A = \alpha_1/\alpha_2$  can be calculated from:

$$A = \frac{\alpha_1}{\alpha_2} = \frac{n_2 I_{02}}{n_1 I_{01}} \frac{\ln \left( \frac{C_1(\mathbf{r})/C_{01}(\mathbf{r}) - k_1}{1 - k_1} \right)}{\ln \left( \frac{C_2(\mathbf{r})/C_{02}(\mathbf{r}) - k_2}{1 - k_2} \right)}. \quad (6.18)$$

According to Eq. (6.18), the ratio of the bleaching efficiencies  $A$  can be determined directly from the normalized fluorescence levels after bleaching of an identical bleaching pattern in both materials, if the mobile fractions are known, as well as the number of scans and the ratio of bleaching intensities that were used. Note that  $I_{02}/I_{01} = P2/P1$ , according to Eq. (6.8).

Another question that may arise is: if a certain bleaching level is obtained in one material, then how many scans or which laser intensity is needed to obtain a certain bleaching level in another type of material? This question is answered by the following expression, which follows immediately from Eq. (6.18):

$$\frac{n_2 I_{02}}{n_1 I_{01}} = A \frac{\ln \left( \frac{C_2(\mathbf{r})/C_{02}(\mathbf{r}) - k_2}{1 - k_2} \right)}{\ln \left( \frac{C_1(\mathbf{r})/C_{01}(\mathbf{r}) - k_1}{1 - k_1} \right)}. \quad (6.19)$$

Eq. (6.19) says that, if  $A$ ,  $k_1$  and  $k_2$  are known, and if  $n_1$  scans at intensity  $I_1$  are needed to obtain a normalized bleaching level  $C_1(\mathbf{r})/C_{01}(\mathbf{r})$  in the first material, then  $n_2$  scans at intensity  $I_2$  will be needed to obtain a normalized bleaching level  $C_2(\mathbf{r})/C_{02}(\mathbf{r})$  in the second material.

**Example:**

Two types of microspheres have been used in this study: NODD loaded microspheres from SINTEF and Green-fluorescent microspheres from Duke Scientific (DS). FRAP experiments have shown that  $k_{NODD} = 0.05$  and  $k_{DS} = 0.35$ , while  $A = \frac{\alpha_{NODD}}{\alpha_{DS}} = 6.6$ . If, for example, one bleaching scan yields 50% bleaching for the NODD spheres (i.e.  $C_1(\mathbf{r})/C_{01}(\mathbf{r}) = 0.5$ ), then, according to Eq. (6.19),  $n_{DS}I_{DS}/I_{NODD} \approx 13$  to obtain 50% bleaching in the DS spheres. This means that the laser intensity has to be increased 13 fold to obtain 50% bleaching in the DS spheres, or 13 scans are needed at the same intensity, etc. In the same way we find that, for a bleaching level of 0.4:  $n_{DS}I_{DS}/I_{NODD} \approx 17$  and for a bleaching level of 0.36:  $n_{DS}I_{DS}/I_{NODD} \approx 25$ . These examples explain why it can be much more difficult to bleach a code in the DS spheres compared to the NODD spheres.

### 6.1.6 The imaging process

The concentration  $C(\mathbf{r})$  after photobleaching as calculated by Eq. (6.15) is not equal to the fluorescence intensity that will be observed by a (confocal) microscope. Any object that is observed by a lens-based system, such as a microscope, will be ‘deformed’ by that system’s detection point-spread function:  $I_d(\mathbf{r})$ . The detection PSF expresses how the light from a point source will be observed. For a more detailed discussion about the confocal detection PSF, the reader is referred to Appendix B, section B.1. The fluorescence image  $F(\mathbf{r})$  of the real concentration distribution  $C(\mathbf{r})$  will therefore be the result of the convolution product of  $C(\mathbf{r})$  and  $I_d(\mathbf{r})$ :

$$\begin{aligned}
 F(\mathbf{r}) &= \int_{-\infty}^{+\infty} \int_{-\infty}^{+\infty} \int_{-\infty}^{+\infty} C(x', y', z') I_d(x - x', y - y', z - z') dx' dy' dz'. \\
 &= C(\mathbf{r}) \otimes I_d(\mathbf{r}).
 \end{aligned}
 \tag{6.20}$$

We will approximate the confocal detection PSF by a Gaussian distribution:

$$I_d(\mathbf{r}) = e^{-2\left(\frac{x^2+y^2}{w_d} + \frac{z^2}{z_d}\right)},
 \tag{6.21}$$

where  $w_d$  and  $z_d$  in Eq. (6.21) are the radial and axial  $e^{-2}$  radii, which we will refer to as *the radial and axial (Gaussian) detection resolution*.

No analytical solution could be found for Eq. (6.20) in combination with Eq. (6.15) for the photobleaching of a barcode. Therefore, Eq. (6.20) will be calculated by numerical computations making use of the ‘convolution theorem’, which states that the Fourier

transform of a convolution product of two functions is equal to the regular product of the Fourier transforms of those functions:

$$\begin{aligned}\mathcal{F}(F(\mathbf{r})) &= \mathcal{F}(C(\mathbf{r}) \otimes I_d(\mathbf{r})) \\ &= \mathcal{F}(C(\mathbf{r})) \times \mathcal{F}(I_d(\mathbf{r})),\end{aligned}\tag{6.22}$$

from which it immediately follows that the observed fluorescence  $F(\mathbf{r})$  can be calculated from:

$$F(\mathbf{r}) = \mathcal{F}^{-1}(\mathcal{F}(C(\mathbf{r})) \times \mathcal{F}(I_d(\mathbf{r}))),\tag{6.23}$$

where  $\mathcal{F}$  denotes the Fourier transform and  $\mathcal{F}^{-1}$  the inverse Fourier transform.

## 6.2 Code simulation program

The theory as presented in section 6.1 can be used for simulating the photobleaching of barcodes or dotcodes in 3-D space. Such a computer simulation program can be a handy tool to study the writing and reading of the codes under different circumstances, experiments which can be difficult to set-up in practice.

The program was written in Matlab and allows the input of all parameters mentioned in section 6.1. First, the user has to define the ‘simulation space’, which is a 3-D grid (or matrix) of spacial coordinates. Based on this grid, the barcode can be designed by specifying the location, width and relative bleaching intensity of the individual bars. The result of the simulation is shown in a new window displaying both the actual and observed fluorescence concentration distribution, i.e.  $C(x, y, z)$  and  $F(x, y, z)$  respectively. The 3-D simulation result can be examined in different ways. First it is possible to display a vertical cross-section of the simulated code. It is also possible to view the different planes ( $xy$ ) along the  $z$ -axis. This allows to examine what the code will look like when it is a certain distance out of focus. And finally, the option is included to rotate the simulation result over any angle in 3-D space to see how a rotated code will be observed by the CSLM. If desired, the result can be stored as a ‘.mat’ file which can be opened in an image processing program which was written in Matlab as well.

To allow easy input of all simulation parameters and manipulation of the simulation result, a GUI<sup>3</sup> was developed, named ‘Code Simulation Parameters’ (see Fig. 6.2). The input parameters and GUI functionalities have been divided into different subsections:

---

<sup>3</sup>GUI: Graphical User Interface



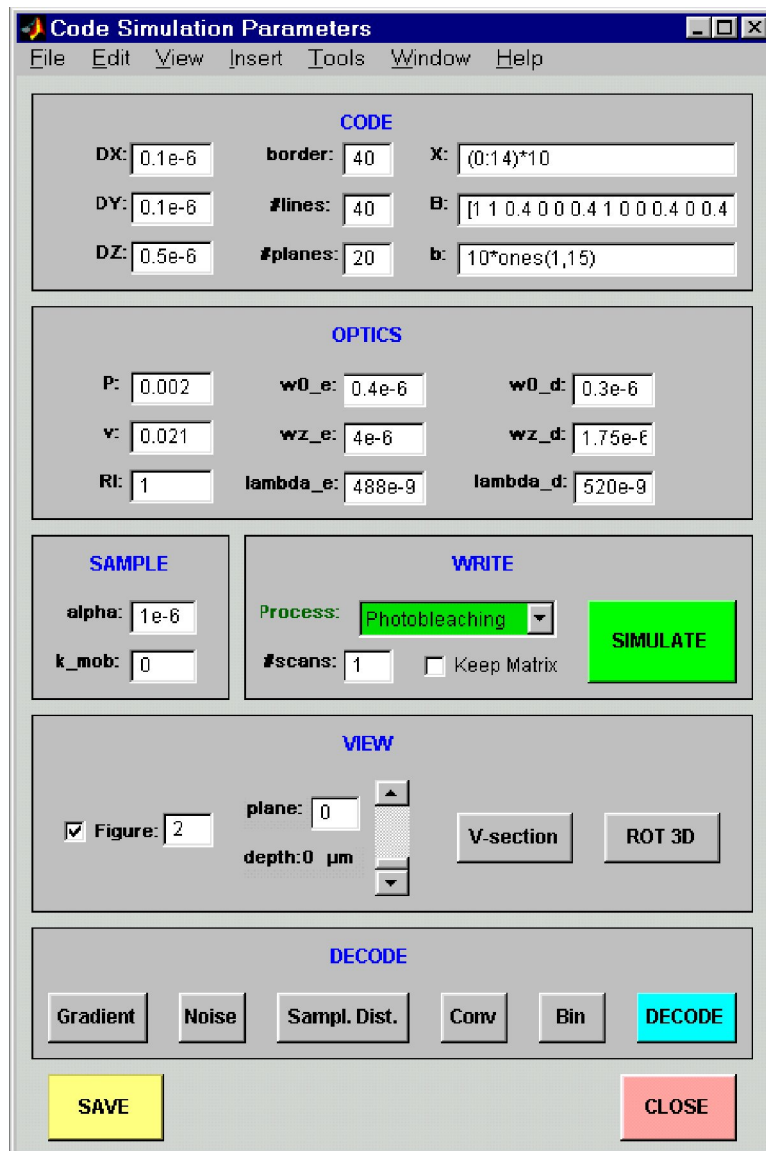


Figure 6.2: Matlab GUI for the simulation of photobleached barcodes.

## CODE

In the CODE section, the code layout and the 3-D grid representing the simulation space are defined.

- **DX, DY, DZ**: the distance [m] between two points of the grid in the respective directions.
- **X**: a (Matlab) array that defines the beginning location of all individual code-elements along the  $x$ -axis of the simulation matrix.
- **B**: a (Matlab) array that defines the relative bleaching intensities of the individual code-elements.
- **b**: a (Matlab) array containing the width of the individual code-elements<sup>4</sup>.
- **#lines**: the number of scanning lines along the  $y$ -direction<sup>5</sup>.
- **border**: the number of rows and columns that will be added to the simulation matrix, left and right ( $x$ -direction), above and under ( $y$ -direction) the barcode. In other words, ‘border’ is the space surrounding the barcode.
- **#planes**: determines the extent of the simulation matrix along the  $z$ -axis.

In conclusion, the parameters of the CODE section determine the 3-D simulation grid and the code layout. A fine simulation grid will yield accurate and smooth results, but evidently, the length of the computations will be proportional to the number of elements in the grid. We suggest that the values of DX, DY and DZ are chosen according to the Nyquist theorem<sup>6</sup>:  $DX, DY < \min(w0\_e, w0\_d)/2.3$  and  $DZ < \min(wz\_e, wz\_d)/2.3$ .

## OPTICS

In the OPTICS section, the user can fill out the parameters defining the illumination and detection optics.

- **P**: the bleaching laser power [W] in the sample.

---

<sup>4</sup>Let it be noted that all three arrays X, B and b should have the same number of elements.

<sup>5</sup>The physical length of the code-elements is:  $DY \times \#lines$ .

<sup>6</sup>Simply put, the Nyquist theorem says that a sampling distance of 2.3 times smaller than the system’s resolution is necessary to obtain all information.

- **v**: the scanning speed [m/s] of the bleaching beam<sup>7</sup>.
- **RI**: the refractive index of the objective lens immersion medium (air:  $n = 1$ ; water:  $n = 1.33$ ; oil:  $n = 1.52$ ).
- **w0\_e**: the radial Gaussian illumination resolution [m].
- **wz\_e**: the axial Gaussian illumination resolution [m].
- **lambda\_e**: the (vacuum) wavelength of the bleaching beam [m].
- **w0\_d**: the radial Gaussian detection resolution [m].
- **wz\_d**: the axial Gaussian detection resolution [m].
- **lambda\_d**: the (vacuum) fluorescence emission wavelength [m] (currently not used).

## SAMPLE

Two sample-dependent parameters:

- **alpha**: the photobleaching efficiency [ $\text{m}^2/\text{J}$ ].
- **k\_mob**: the mobile fraction.

## WRITE

- **Process**: the writing process (currently limited to photobleaching).
- **#scans**: the number of sequential photobleaching scans.
- **Keep Matrix**: After simulation of the photobleached code, the same process can be repeated a second time on the same matrix (containing the photobleached code) by checking this option and running the simulation again. Note that, if  $k_{\text{mob}} > 0$ , this is not the same as increasing **#scans**.
- **SIMULATE**: pressing this button will start the computations.

---

<sup>7</sup>On the Bio-Rad MRC1024, it takes approximately 1.23 ms to perform one line scan (from left to right). If  $L$  is the length [m] of the scanning line, which depends on the magnification of the objective lens and the zoom setting, the scanning speed  $v = L/0.00123$  [m/s].

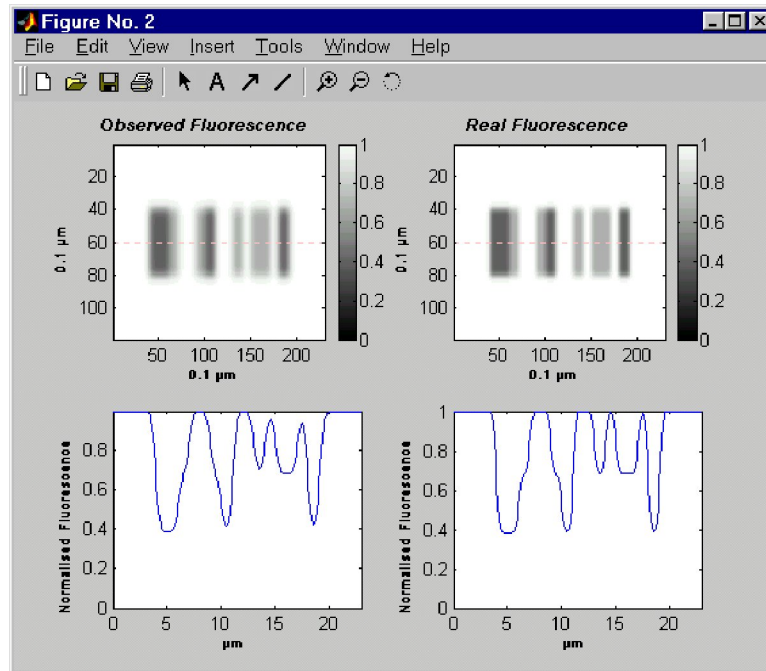


**Figure 6.3:** The simulation result is displayed in a separate window. An image is shown of the real concentration matrix  $C(x, y, z)$  and the fluorescence matrix  $F(x, y, z)$  as it is observed by the confocal microscope. The corresponding intensity profiles are shown as well.

## VIEW

When the simulation of the photobleaching process is ready, a figure window will be displayed (see Fig. 6.3) showing the focal plane of both the real concentration matrix  $C(x, y, z)$  and the fluorescence matrix  $F(x, y, z)$  as it is observed by the confocal microscope. Underneath both images, the central intensity profile is shown as well. The VIEW section allows to study the photobleached code from different points of view.

- The vertical slider allows to view different planes along the  $z$ -axis. The number of planes that can be viewed is determined by the parameter `#planes` from the CODE section. This feature can be used to study what a photobleached code will look like when it is viewed a certain distance out of focus. An example is shown in Fig. 6.4.
- **plane:** displays the plane number that is currently being viewed (0 = focal plane). The physical depth is also shown, which is calculated according to  $DZ$ .
- **Figure:** this is a Matlab specific option. When checked, each new drawing (for example when selecting a different plane) will be made in that Matlab figure window.

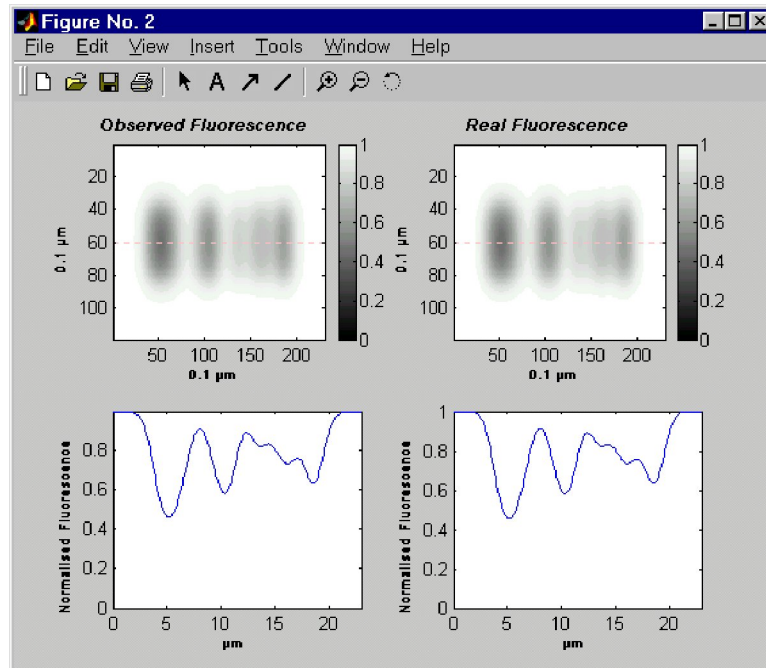


**Figure 6.4:** The same code is shown as in Fig. 6.3, but viewed at  $4 \mu\text{m}$  out-of-focus.

When unchecked, each new drawing command will open a new Matlab figure window. This can be convenient when comparing different views.

- **V-section:** generates a vertical section along the optical axis.
- **ROT 3D:** allows the simulated concentration matrix  $C(x, y, z)$  to be rotated in space. After rotation of  $C(x, y, z)$  the new fluorescence matrix  $F(x, y, z)$  is calculated. This option is included to study what a photobleached code will look like when the original encoding plane is tilted with respect to the focal plane of observation. Such a situation might happen when an encoded microsphere is collected again at the microscope for read-out after manipulation.

## DECODE

The DECODE section allows to examine the current intensity profile.

- **Gradient:** plots the first order derivative of the observed fluorescence intensity profile (see, for example, Fig. 7.9), which may be useful for automatic decoding.
- **Noise:** allows to add a certain percentage of normally distributed noise. This option is added to simulate experimental noise.

- **Sampl. Dist.:** allows to define a new sampling distance for the fluorescence intensity profile along the  $x$ -axis. Linear interpolation is used to calculate the resampled intensity profile. This option can be used to reduce the noise in the gradient.
- **Conv:** allows to convolve the fluorescence intensity profile with a uniform array of length  $n$ .  $n$  should be an odd number. If, for example,  $n = 3$ , then each fluorescence value will be replaced by its mean with its two neighbouring values. This is a filtering method that rejects high frequency components and is an other way to reduce the noise.
- **Bin:** allows ‘binning’ of the fluorescence intensity values (currently not active).
- **DECODE:** for automatic decoding of the current fluorescence profile based on its first derivative.

The **SAVE** button allows to save the simulated concentration and fluorescence matrix as a Matlab ‘.mat’ file. These files can be opened in an image processing tool which was written in Matlab as well.

### 6.3 Codes for microcarriers

There are a lot of possibilities of how the code can be designed. As was already pointed out in section 5.3, the codes in this particular application should be written and read as fast as possible. Therefore, in this study we will focus mainly on the design of one-dimensional codes, such as barcodes.

There exist, of course, already a lot of barcodes that are used for retail products, postal services, library systems etc.<sup>8</sup> These types of barcodes have been developed to be as little amenable to errors as possible, making their structure quite complicated. As a consequence, they take up a relatively large amount of space. This is not a problem for the applications mentioned above, but writing barcodes in small microcarriers at the optical resolution limit is something else though. In this application we are rather interested in a code that is as dense as possible. As already pointed out in section 5.3, to this end we may use multiple photobleaching levels in the encoding scheme in combination with length-encoding. Some of the possibilities are discussed below, although it is realized that other approaches may be suggested as well.

---

<sup>8</sup>The interested reader can find information about the different types of common barcodes on <http://www.makebarcode.com>, amongst many other websites.

### 6.3.1 ‘Black And White’ codes

#### Colour encoded binary

In this encoding scheme, two intensities are used: bleached (‘black’) and unbleached (‘white’). For example, when using 8 bits, the number 53 would be encoded as the binary 00110101, where 0 stands for unbleached and 1 for bleached. Although this is a very straightforward approach, the obvious disadvantage is the lack of a separation between the bits. An advantage is that the code has a fixed total length. A code consisting of 16 elements, for example, will yield  $2^{16} = 65536$  unique possibilities.

#### Length encoded binary

As an alternative, it is possible to encode 1 as a wide bar (two units) and 0 as a small bar (1 unit), while changing colour for every bit. Thus, 53 or 00110101 becomes: 010011011011. Note, however, that 101100100100 is equally possible, depending on the intensity of the first bit. Therefore, it would be possible to define two subsets, one starting with 0 and one starting with 1, thus doubling the number of possibilities. A disadvantage of this approach is that the codes will have a variable length. For example, the binary number 00000000 will take up 8 spacial units, while the binary number 11111111 will require 16 spacial units. This encoding scheme is therefore less dense than the colour encoded binary.

#### Code $M$ of $N$

In analogy with some of the existing types of barcodes, we could use a ‘ $M$  of  $N$ ’ pattern, which also uses two lengths and a different colour for each neighbouring element.  $N$  is the total number of bars (black) and spaces (white) in the code.  $M$  is the number of wide bars and spaces, and  $N - M$  the number of small bars and spaces. Thus, this type of barcode has a fixed length. The number of possibilities is given by the number of combinations<sup>9</sup>:

$$C_N^M = \frac{N!}{M!(N-M)!}$$

---

<sup>9</sup>Actually, the number of possibilities has to be calculated by the number of ‘permutations with repetition’. Consider an ensemble of  $N$  elements, consisting of  $a_1$  times the first element,  $a_2$  times the second element,  $\dots$ ,  $a_n$  times the  $n^{\text{th}}$  element. The number of unique rows that can be made using those elements is:  $\bar{P}_{a_1+a_2+\dots+a_n} = \frac{(a_1+a_2+\dots+a_n)!}{a_1!a_2!\dots a_n!}$ . In the special case of an ensemble of  $M$  times the first element and  $N - M$  times the second element, this is equal to the number of combinations of  $M$  elements out of  $N$ :  $\bar{P}_{M+N-M} = \frac{N!}{M!(N-M)!} = C_N^M$ .

‘Interleaved 2 of 5’ is a type of barcode that makes use of this encoding scheme.  $C_5^2 = 10$ , which is just enough to represent all ten digits. Larger numbers are created by combining the digits. ‘Code 39’ is an other example that encodes 43 unique characters. The mapping to characters and using the characters to build the code is not very space-efficient. Rather we could use the  $M$  of  $N$  code directly. For example, a ‘7 of 14’ code yields 3432 possibilities. If the wide element consists of 2 spacial units and the small element of 1 unit, such a code has a total length of 21 units. Three ‘digits’ of the ‘Interleaved 2 of 5’ code also need 21 units, but giving only 1000 possibilities.

### Multiple length encoding

As an extension of the code  $M$  of  $N$ , it is possible to construct codes consisting of three or more different lengths. Consider a code consisting of  $a_1$  bars of length 1,  $a_2$  bars of length 2,  $\dots$ ,  $a_n$  bars of length  $n$ , having a total of  $N = \sum_{i=1}^n a_i$  elements. The total number of unique possibilities can be calculated from the ‘permutations with repetition’:

$$\bar{P}_{a_1+a_2+\dots+a_n} = \frac{(a_1 + a_2 + \dots + a_n)!}{a_1!a_2!\dots a_n!}. \quad (6.24)$$

Such a code still has a fixed total length, while neighbouring elements can be distinguished from each other by their difference in colour (black or white). Note that two subsets can again be defined depending on the colour of the first element, hence doubling the number of possibilities. As an example, consider a code consisting of 1 element of three spatial units, 3 elements of two spatial units and 7 elements of 1 unit. This gives  $11!/(1!3!7!) = 1320$  possibilities for a total length of 16 spatial units.

### 6.3.2 Intensity codes

#### ‘Base $G$ ’ gray level encoding

One can also think of using only intensity encoding, excluding length encoding. The most straightforward way of constructing intensity codes is by using the different gray levels directly without further restrictions. The ‘colour encoded binary’ mentioned above is such an example for two intensities: ‘Base 2’ gray level encoding. The same principle can be extended to a ‘Base  $G$ ’ gray level encoding scheme for  $G$  intensities, yielding  $G^N$  unique possibilities. For example, a code consisting of 16 elements using 4 gray levels yields  $4^{16} = 4.2 \times 10^{12}$  unique possibilities. Such an encoding scheme has the same disadvantage as the ‘colour encoded binary’ of having no separation between the individual elements.



### ‘Exclusive Base $G$ ’ gray level encoding

As a refinement of the ‘Base  $G$ ’ gray level encoding, it is possible to introduce a separation between the individual elements by excluding the gray level of the previous element from the set of possible gray levels for the next element. Hence the name ‘Exclusive Base  $G$ ’ gray level encoding. This means that for each element following the first one, there are  $G - 1$  possible gray levels. For a code consisting of  $N$  elements this results in:

$$g(G - 1)^{N-1} \tag{6.25}$$

unique possibilities, where  $g$  is the number of gray levels ( $\leq G$ ) the first element is allowed to have. For example, a code consisting of 16 elements using 4 gray levels yields  $4 \times 3^{15} = 57 \times 10^6$  unique possibilities. Evidently, this is less than for the equivalent ‘Base 4’ encoding scheme, but a lot more than for a 16 element colour encoded binary:  $2^{16} = 65536$ .

### 6.3.3 Length and intensity encoding

As a natural extension of the multiple length and multiple intensity barcodes, it is possible to make a combination of both. From Eqs. (6.24) and (6.25) it follows that the number of unique possibilities can be calculated from:

$$g(G - 1)^{N-1} \cdot \frac{a_1 + a_2 + \dots + a_n}{a_1! a_2! \dots a_n!} \tag{6.26}$$

Such a code has a double encoding scheme. It has the advantage of having a fixed total length while the neighbouring elements can be distinguished from each other based on a difference in gray level. Note that Eq. (6.26) reduces to (6.24) for  $G = 2$  (black and white), and to Eq. (6.25) for  $n = 1$  (one length). Consider, for example, a code consisting of bars of three different lengths: 1 bar of 3 spatial units, 3 bars of 2 units and 7 bars of 1 unit. This code has a total length of 16 spatial units. In combination with two intensities this gives 2640 possibilities ( $g = 2$ ), according to Eq. (6.26). In combination with three gray levels, the number of possibilities increases to  $8.1 \times 10^6$  ( $g = 3$ ). And for 4 gray levels there are  $935 \times 10^6$  possibilities ( $g = 4$ ).

In reality, a start and stop sequence will have to be added to the actual code to distinguish when a code is being read from left to right or visa versa. In addition it might be preferable to add a controll sequence to the actual code to check for correct decoding. We will not, however, discuss these sequences here as they will strongly depend on the type of code that will be chosen in the end.

We finally note that the minimum physical length the smallest code element will mainly depend on the resolution of the writing beam, which itself will depend on the objective lens used for writing. As the theoretical diameter of the writing beam for a NA1.2 lens is 500 nm, it is to be expected that the minimum length will be approximately 1  $\mu\text{m}$ . This has to be experimentally evaluated, however, which will be done in the next section.

# Chapter 7

## Encoding and decoding of fluorescent microspheres: experiments and simulations

### Summary

In this chapter, the encoding of microspheres by photobleaching will be examined experimentally in detail, as well as imaging of the encoded beads with a CSLM. The different aspects that play a role in the writing and reading processes will be considered first separately. We will start with verifying if the bleaching process in the microbeads can be described by first order kinetics. Next, because the illumination and detection intensity distributions play a crucial role, as explained in the previous chapter, they will be examined experimentally for three different lenses and different confocal settings. The polystyrene microbeads are far from ideal microscopic objects. Because of their high refractive index and spherical shape, deviations from the ideal situation are expected to play a significant role, such as a focal shift and spherical aberrations. These effects are therefore examined separately first in the third section. The chapter is concluded with encoding and decoding experiments for different kinds of codes and optical configurations. Particularly, the readability of the code for different out-of-focus positions will be examined for different objective lens combinations. The theory of the previous chapter will be verified in detail by comparing simulated and experimental codes.

## 7.1 Experimental verification of first-order photobleaching in fluorescent microspheres

### 7.1.1 Aim and objectives

In the derivation of the formula's that describe the photobleaching of barcodes in section 6.1, we started from the assumption that the photobleaching process can be described by first-order reaction kinetics. Therefore, we will now verify if this is true for the type of microspheres that will be used in the encoding experiments. We will also try to determine the value of the photobleaching rate constant  $\alpha$ , which has to be known for the simulations.

### 7.1.2 Materials and methods

Polystyrene microspheres of 28  $\mu\text{m}$  diameter loaded with NODD (N-(7-Nitrobenz-2-oxa-1,3-diazol-4-yl)diethyl amine) were purchased from SINTEF Applied Chemistry (Trondheim, Norway). NODD is a fast bleaching green-fluorescent dye which is excitable with the blue 488 nm line from an Ar-ion laser and yields green fluorescence. Bleaching will be done using the 10 $\times$  objective lens on a single microsphere that is brought into focus. The zoom setting will be adjusted for the microsphere to fill almost the entire field of view. This is done to obtain sufficient photobleaching while the photobleaching mask still can be considered to be much larger than the microsphere. For such a photobleaching mask it can be calculated from Eq. (6.10)<sup>1</sup> that  $K = \pi w_{0e}^2/2$ , a constant independent from the spacial coordinates, which means homogeneous photobleaching throughout the entire microsphere. Together with Eqs. (6.8) and (6.15) this leads to:

$$C = C_0 e^{-\frac{n\alpha P}{v\Delta y}}, \quad (7.1)$$

where we have put the mobile fraction  $k = 0$  because the microsphere is homogeneously bleached and hence no net diffusion can occur. Moreover, FRAP experiments on the NODD spheres have revealed a very low mobile fraction of only 5% anyway. The microsphere will be gradually photobleached by sequential scans at a constant laser power  $P$ . It then follows from Eq. (7.1) that the photobleaching rate  $\alpha$  can be calculated by fitting of an exponential function to  $C$  vs. the number of sequential photobleaching scans  $n$ . To obtain  $C$  vs.  $n$ , an image will be recorded after each photobleaching scan. A 520 nm long pass filter and the smallest possible confocal pinhole setting are used for detection of the fluorescence.  $C$

<sup>1</sup>for a single rectangle and  $x_1 \ll x \ll x_1 + b_1$  and  $|y| \ll l$

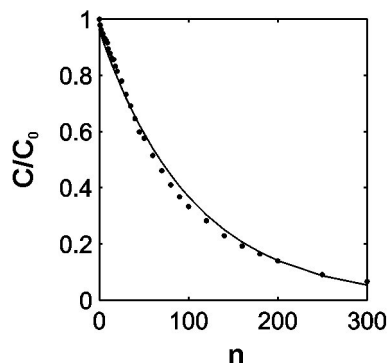


**Figure 7.1:** The normalized concentration is plotted as a function of the photobleaching scans. The black circles are the experimental data points and the solid line is the best exponential fit.

is then calculated from the mean fluorescence intensity of a central region of the microsphere.  $C_0$  is the calculated in the same way from the initial image that precedes the first photobleaching scan.

### 7.1.3 Experiment and discussion

A total of 300 photobleaching scans were performed on a single NODD microsphere. The bleaching power in the sample was  $50 \mu\text{W}$ . The zoom setting was 20, which corresponds to a pixel size  $\Delta y = 0.106 \mu\text{m}$  and a scanning speed  $v = 0.0441 \text{ m/s}$ . The results are shown in Fig. 7.1. An exponential fit yields  $C = 0.9601e^{-0.0096n}$  and a correlation coefficient  $R^2 = 0.9936$ . From Eq. (7.1) we calculate the approximate photobleaching rate for the NODD microspheres (at a photobleaching wavelength of 488 nm):  $\alpha \approx 1.0 \cdot 10^{-6} \text{ m}^2/\text{J}$ .

### 7.1.4 Conclusions

The experiment clearly shows an exponential decay of the fluorescence concentration as a function of the number of photobleaching scans. This demonstrates the validity of assuming first-order reaction kinetics to describe the photobleaching process in the NODD microspheres. We have also calculated the photobleaching rate for this type of microspheres:  $\alpha \approx 1.0 \cdot 10^{-6} \text{ m}^2/\text{J}$ . This value can be used for the simulations.

## 7.2 The experimental illumination and detection intensity distribution

### 7.2.1 Aim and objectives

As discussed in Chapter 6, the illumination intensity distribution plays a crucial role in the encoding of microcarriers by spatial selective photobleaching. In particular we have suggested two types of illumination intensity distributions: the ‘modified Gaussian intensity distribution’ and the ‘fundamental Gaussian-beam solution’. Both functions are discussed in Appendix B. Similarly, the confocal detection intensity distribution plays an equal important role in the decoding of the encoded microcarriers. In section 6.1.6 we have suggested to use a Gaussian intensity distribution, the use of which is motivated in Appendix B, section B.1. We will now verify if the experimental illumination and detection distributions can be approximated by the suggested functions. We will do this for the three main objective lenses of our CSLM.

### 7.2.2 Materials and methods

On a CSLM, the illumination detection distribution can be experimentally determined by imaging a fluorescent point source with a completely opened confocal diaphragm (iris setting 8.0 on the Bio-Rad MRC1024). In actual practice, subresolution fluorescent nanospheres are generally used for this purpose (see, for example, [149]). The confocal detection distribution can be obtained in the same way by closing down the confocal diaphragm. We have applied a drop of latex nanospheres of 190 nm diameter (Fluores-Brite, Polysciences, Warrington, U.S.A.) diluted in distilled water to a cover slip. The nanospheres adhered to the cover slip after drying in air. After rinsing, the cover slip was sealed on a microscope slide with water between the two glasses. The 488 nm line of an Ar-ion laser will be used for excitation and an 520 nm long pass filter for detection of the fluorescence.

Images are recorded of single nanospheres for different confocal diaphragm settings and for three different Nikon CFI objective lenses: Plan Apochromat 10× NA0.45, Plan Fluor 40× NA0.75, Plan Apochromat 60× NA1.2 WI (water immersion). As will be shown by the experiments, because the back aperture of the 10× lens is being underfilled by the laser beam, this lens rather behaves like a NA0.2 lens. For each setting an  $xz$ -image through the center of the nanosphere is recorded with 2× Kalman filtering. The pixel size

was matched to the  $z$ -step of the focus motor to obtain square pixel sizes in the final  $xz$ -image. The following pixel sizes (and  $z$ -steps) have been used for the  $xz$ -images: 200 nm for the 10 $\times$  lens and 100 nm for the 40 $\times$  and 60 $\times$  lenses. There is a *caveat*, however, for the  $z$ -step of the 10 $\times$  and the 40 $\times$  lens. In general, if there is a mismatch in refractive index between the lens immersion medium and the sample, there will be a difference between the nominal focus position (NFP) and the actual focus position (AFP) (see, for example, [149]). If  $n_1$  is the refractive index of the immersion medium,  $n_2$  the refractive index of the sample and NA the numerical aperture of the objective lens, the NFP and the AFP are related by:

$$\frac{\text{AFP}}{\text{NFP}} = \sqrt{\frac{n_2^2 - \text{NA}^2}{n_1^2 - \text{NA}^2}}, \quad (7.2)$$

which can easily be derived from geometrical considerations and Snel's law. Note that for a low NA Eq. (7.2) reduces to  $\text{AFP} = \text{NFP} \times n_2/n_1$ . As expected, it follows from Eq. (7.2) that for a perfectly matched system ( $n_1 = n_2$ ):  $\text{NFP} = \text{AFP}$ . It also follows from Eq. (7.2) that a displacement  $\Delta z$  of the sample relative to the objective lens along the optical axis causes an actual displacement

$$\Delta z_{\text{AFP}} = \Delta z \sqrt{\frac{n_2^2 - \text{NA}^2}{n_1^2 - \text{NA}^2}} \quad (7.3)$$

of the AFP in the sample. Both the 10 $\times$  and the 40 $\times$  lens have  $n_1 = 1$  (air), while the sample's refractive index  $n_2 = 1.33$  (water). It therefore follows for the 10 $\times$  lens (which has an effective NA of approximately 0.3) that the step size of 200 nm of the focus motor translates to a real step size of 272 nm in the sample. The 100 nm step size for the 40 $\times$  lens similarly translates to a step size of 166 nm in the sample. Those values will be used when measuring distances along the  $z$ -direction in the  $xz$ -images.

The raw images are processed in an image processing program which was written in Matlab. First, the  $xz$ -images are normalized against their background along the  $z$ -direction to correct for an inhomogeneous background. Next, the background fluorescence is calculated in a region far from the nanosphere and this value is subtracted from the whole image. Next, the radial and axial intensity profiles of the nanosphere are obtained. Fitting of a Gaussian distribution finally leads to the radial and axial Gaussian resolution.

## 7.2.3 Results and discussion

### 10× objective lens

The results for the 10× lens are shown in Fig. 7.2. An  $xz$ -image of the nanosphere for a completely opened confocal pinhole is shown in Fig. 7.2A. This is the illumination intensity distribution for the 10× objective lens. By fitting of a Gaussian function to the radial and axial intensity profile, it is found that the radial resolution  $w_{0e} = 0.98 \mu\text{m}$  and the axial resolution  $w_{ze} = 8.76 \mu\text{m}$ . The axial intensity profile is shown in Fig. 7.2E, ‘solid’ line. The fundamental Gaussian-beam solution was calculated for  $w_{0e} = 0.98 \mu\text{m}$  and is shown in Fig. 7.2B. The corresponding axial profile is shown in Fig. 7.2E, ‘dash-dotted’ line. According to Eq. (6.6d), the maximum axial resolution for the modified Gaussian intensity distribution is  $8.21 \mu\text{m}$ , which is slightly smaller than the measured value of  $8.76 \mu\text{m}$ . The modified Gaussian intensity distribution was therefore calculated for this maximum value and is shown in Fig. 7.2C. The corresponding axial profile is shown in Fig. 7.2E, ‘dashed’ line. As can be seen from Fig. 7.2E, both the fundamental and modified intensity distributions are close to the real intensity distribution, although the modified distribution gives a slightly better fit.

The  $xz$ -image of the nanosphere for a completely closed confocal pinhole (setting 0.7) is shown in Fig. 7.2D. The corresponding radial and axial profiles are shown in Fig. 7.2F. Both profiles can be very well fitted by a Gaussian intensity distribution, which supports the decision to use a normal Gaussian distribution in both radial and axial directions to represent the confocal detection intensity distribution. For a completely closed confocal pinhole we find that  $w_{0d} = 0.82 \mu\text{m}$  and  $w_{zd} = 6.01 \mu\text{m}$ . All measured radial and axial resolutions as a function of the confocal pinhole setting, which varies between 0.7 and 8 on the Bio-Rad MRC1024, are shown in Fig. 7.5. As expected, the resolution becomes better for smaller confocal pinhole diameters.

### 40× objective lens

The results for the 40× lens are shown in Fig. 7.3. An  $xz$ -image of the nanosphere for a completely opened confocal pinhole is shown in Fig. 7.3A. This is the illumination intensity distribution for the 40× objective lens. The radial resolution  $w_{0e} = 0.386 \mu\text{m}$  and the axial resolution  $w_{ze} = 1.93 \mu\text{m}$ . The axial intensity profile is shown in Fig. 7.3E, ‘solid’ line. The fundamental Gaussian-beam solution was calculated for  $w_{0e} = 0.386 \mu\text{m}$  and is shown in Fig. 7.3B. The corresponding axial profile is shown in Fig. 7.3E, ‘dash-dotted’



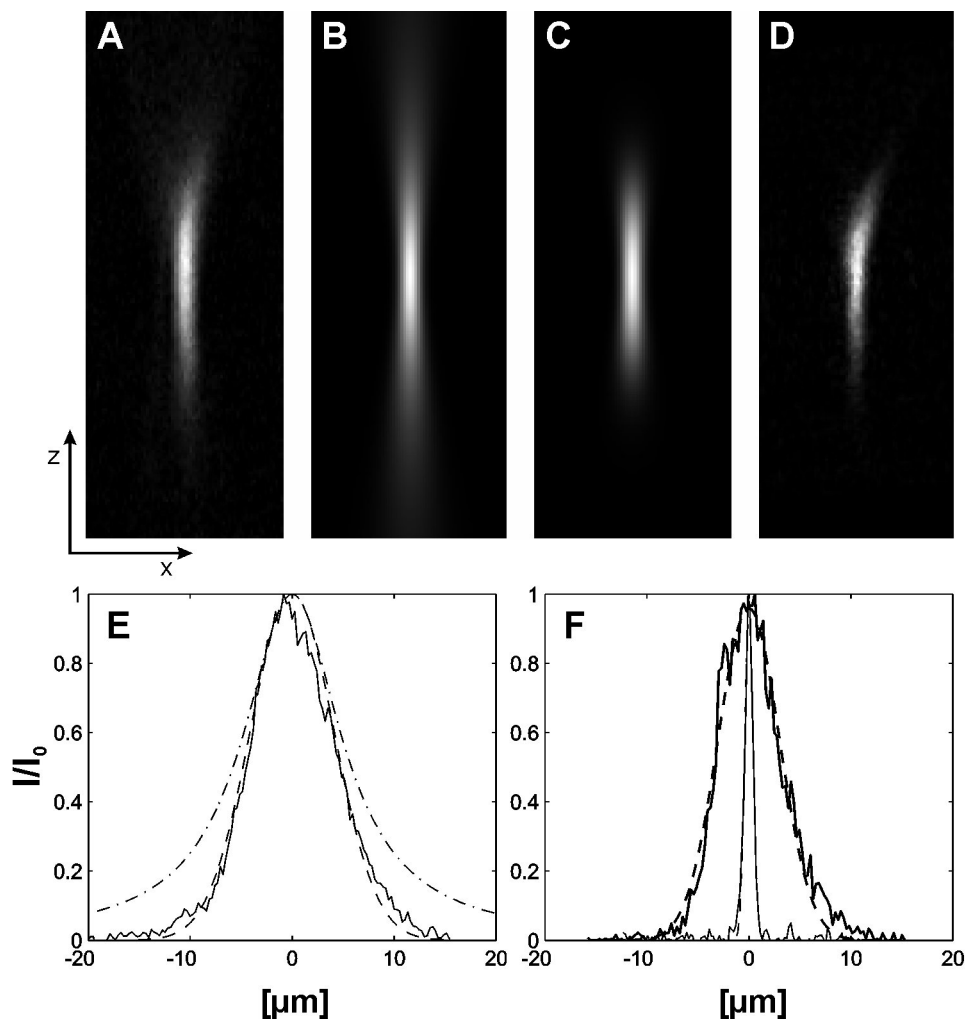


**Figure 7.2:** (A) An  $xz$ -image of a subresolution fluorescent nanosphere recorded by the  $10\times$  objective lens for a completely opened confocal pinhole. This image represents the illumination intensity distribution of the  $10\times$  objective lens. (B) The intensity profile according to the fundamental Gaussian-beam solution is calculated for the measured radial resolution  $w_{0e} = 0.98 \mu\text{m}$ . (C) The modified Gaussian distribution was calculated for the measured radial resolution  $w_{0e} = 0.98 \mu\text{m}$  and corresponding maximum axial resolution of  $w_{ze} = 8.2 \mu\text{m}$ . (D) An  $xz$ -image of the subresolution nanosphere for a completely closed confocal pinhole. This image shows the confocal detection distribution. (E) The axial intensity profiles are shown of the experimental (solid line), the fundamental Gaussian (dash-dotted line) and the modified Gaussian (dashed line) intensity distribution. Although the modified distribution corresponds best to the experimental profile, the fundamental distribution is not far off. (F) The radial (normal line) and axial (bold line) intensity profile when the confocal pinhole is closed completely. Both profiles are very well fitted by a Gaussian intensity distribution (dashed lines). Images A–D have dimensions of  $14.2 \mu\text{m} \times 38.2 \mu\text{m}$ .

line. According to Eq. (6.6d), the maximum axial resolution for the modified Gaussian intensity distribution is  $1.27 \mu\text{m}$ , which is substantially smaller than the measured value of  $1.93 \mu\text{m}$ . The modified Gaussian intensity distribution was therefore calculated for this maximum value and is shown in Fig. 7.3C. The corresponding axial profile is shown in Fig. 7.3E, ‘dashed’ line. As can be seen from Fig. 7.3E, the fundamental intensity distribution clearly gives a better fit in this case.

The  $xz$ -image for a completely closed confocal pinhole is shown in Fig. 7.3D. The corresponding radial and axial profiles are shown in Fig. 7.3F. Again, both profiles can be very well fitted by a Gaussian intensity distribution. For a completely closed confocal pinhole we find that  $w_{0d} = 0.334 \mu\text{m}$  and  $w_{zd} = 1.53 \mu\text{m}$ . All measured radial and axial resolutions as a function of the confocal pinhole setting are shown in Fig. 7.5. We find again that the resolution becomes better for smaller confocal pinhole diameters.

### 60× objective lens

The results for the 60× lens are shown in Fig. 7.4. An  $xz$ -image for a completely opened confocal pinhole is shown in Fig. 7.4A. This is the illumination intensity distribution for the 60× objective lens. The radial resolution  $w_{0e} = 0.254 \mu\text{m}$  and the axial resolution  $w_{ze} = 0.648 \mu\text{m}$ . The axial intensity profile is shown in Fig. 7.4E, ‘solid’ line. The fundamental Gaussian-beam solution was calculated for  $w_{0e} = 0.254 \mu\text{m}$  and is shown in Fig. 7.4B. The corresponding axial profile is shown in Fig. 7.4E, ‘dash-dotted’ line. According to Eq. (6.6d), the maximum axial resolution for the modified Gaussian intensity distribution is  $0.733 \mu\text{m}$ , which is larger than the measured value of  $0.648 \mu\text{m}$ . The modified Gaussian intensity distribution was therefore calculated for this measured value and is shown in Fig. 7.4C. The corresponding axial profile is shown in Fig. 7.4E, ‘dashed’ line. As can be seen from Fig. 7.4E, both the fundamental and modified intensity distributions are in good correspondence with the experimental profile.

The  $xz$ -image for a completely closed confocal pinhole is shown in Fig. 7.4D. The corresponding radial and axial profiles are shown in Fig. 7.4F. Again, both profiles can be very well fitted by a Gaussian intensity distribution. For a completely closed confocal pinhole we find that  $w_{0d} = 0.190 \mu\text{m}$  and  $w_{zd} = 0.348 \mu\text{m}$ . All measured radial and axial resolutions as a function of the confocal pinhole setting are shown in Fig. 7.5. We find again that the resolution becomes better for smaller confocal pinhole diameters.

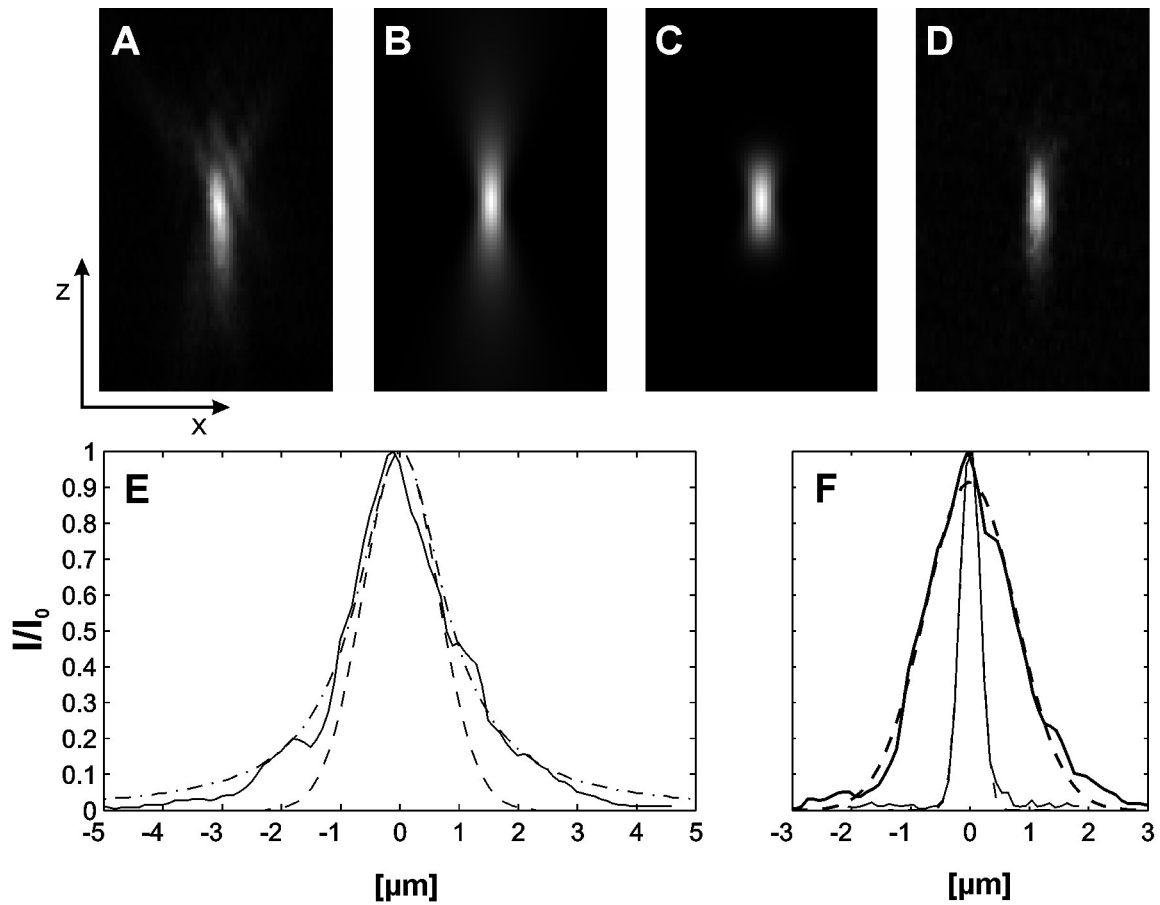


**Figure 7.3:** (A) An  $xz$ -image of a subresolution fluorescent nanosphere recorded by the  $40\times$  objective lens for a completely opened confocal pinhole. This image represents the illumination intensity distribution. (B) The intensity profile according to the fundamental Gaussian-beam solution is calculated for the measured radial resolution  $w_{0e} = 0.386 \mu\text{m}$ . (C) The modified Gaussian distribution was calculated for the measured radial resolution  $w_{0e} = 0.386 \mu\text{m}$  and corresponding maximum axial resolution of  $w_{ze} = 1.27 \mu\text{m}$ . (D) An  $xz$ -image of the subresolution nanosphere for a completely closed confocal pinhole. This image represents the confocal detection distribution. (E) The axial intensity profiles are shown of the experimental (solid line), the fundamental Gaussian (dash-dotted line) and the modified Gaussian (dashed line) intensity distribution. The fundamental Gaussian-beam solution corresponds best to the experimental intensity profile. (F) The radial (normal line) and axial (bold line) intensity profile when the confocal pinhole is closed completely. Both profiles are very well fitted by a Gaussian intensity distribution (dashed curves). Images A–D have dimensions of  $6.1 \mu\text{m} \times 10.0 \mu\text{m}$ .

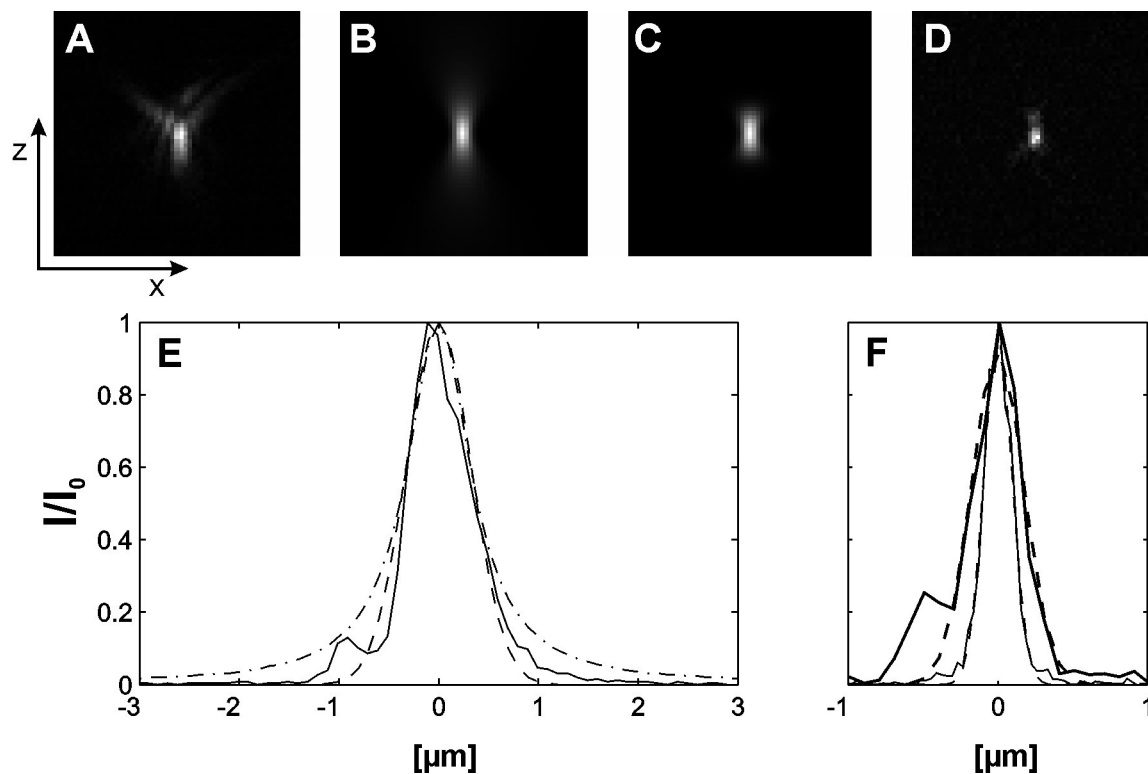


**Figure 7.4:** (A) An  $xz$ -image of a subresolution fluorescent nanosphere recorded by the  $60\times$  objective lens for a completely opened confocal pinhole. This image represents the illumination intensity distribution. (B) The intensity profile according to the fundamental Gaussian-beam solution is calculated for the measured radial resolution  $w_{0e} = 0.254 \mu\text{m}$ . (C) The modified Gaussian distribution was calculated for the measured radial and axial resolution:  $w_{0e} = 0.254 \mu\text{m}$  and  $w_{ze} = 0.648 \mu\text{m}$ . (D) An  $xz$ -image of the subresolution nanosphere for a completely closed confocal pinhole. This image represents the confocal detection distribution. (E) The axial intensity profile are shown of the experimental (solid line), the fundamental Gaussian (dash-dotted line) and the modified Gaussian (dashed line) intensity distribution. Both types of Gaussian distributions correspond well to the experimental intensity profile. (F) The radial (normal line) and axial (bold line) intensity profile when the confocal pinhole is closed completely. Both profiles are very well fitted by a Gaussian intensity distribution (dashed curves). Images A–D have dimensions of  $6.1 \mu\text{m} \times 6.1 \mu\text{m}$ .

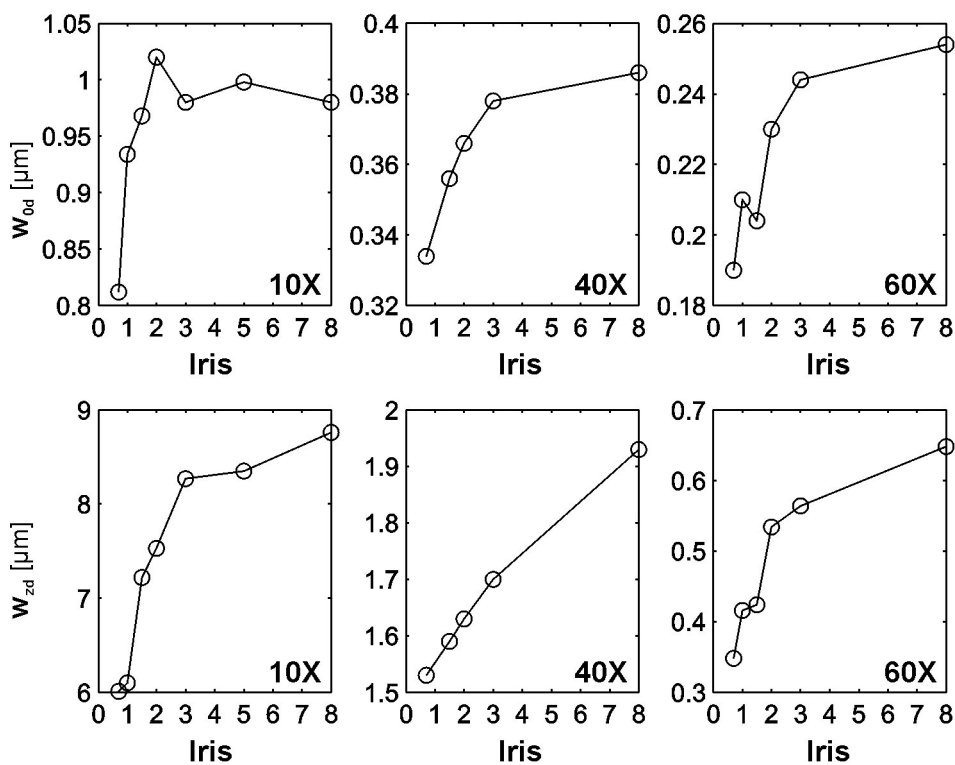


**Figure 7.5:** The radial and axial confocal detection resolutions,  $w_{od}$  and  $w_{zd}$ , are plotted as a function of the confocal iris setting on the Bio-Rad MRC1024 microscope for the 10×, the 40× and the 60× objective lens.

## 7.2.4 Conclusions

The experiments show that the fundamental and modified Gaussian distributions are both possible representations of the illumination intensity distribution of all three lenses. The modified Gaussian intensity distribution gave a slightly better correspondence for the 10× and 60× objective lenses, while the fundamental Gaussian distribution was best for the 40× lens. Comparison of real photobleached codes with simulated ones will have to show in the end which distribution represents best the illumination profile for each of the lenses.

When the confocal pinhole is closed down completely, the confocal detection intensity profile can be approximated by a normal Gaussian distribution in both radial and axial directions for all lenses. When opening the confocal pinhole, the detection distribution will gradually approach the illumination intensity distribution. The resolutions shown in Fig. 7.5 can be used as a reference to simulate different optical configurations.

## 7.3 Focal shift and spherical aberrations in microspheres

### 7.3.1 Aims and objectives

Analogous to the situation in section 7.2.2, inside the microbeads there will be a difference in the actual focus position (AFP) and the nominal focus position (NFP) because of a mismatch in refractive index between the lens immersion medium and the sample. The situation is a little more complicated in this case because the sample consists of two different materials. First there is the water in which the microsphere is suspended, and second there is the microsphere itself in which the laser beam is focused. One can easily show, however, that Eq. (7.3) is still valid regardless of the water being present in the sample:

$$\Delta z_{AFP} = \Delta z \sqrt{\frac{n_3^2 - \text{NA}^2}{n_1^2 - \text{NA}^2}}, \quad (7.4)$$

where  $n_1$  is the refractive index of the lens immersion medium and  $n_3$  the refractive index of the microsphere material. The microspheres are made of polystyrene, which has a refractive index  $n_3 = 1.59$ . Therefore, according to Eq. (7.4), the following correction factors have to be taken into account to determine the actual Z-step of the AFP inside

the microspheres: 1.64 for the 10 $\times$  lens, 2.12 for the 40 $\times$  lens and 1.82 for the 60 $\times$  lens. Eq. (7.4), however, does not take the spherical shape of the microspheres into account, nor spherical aberrations (see below). Therefore, we will determine the correction factors experimentally by measuring the apparent diameter of a microsphere of known size along the optical axis.

Apart from a focal shift, a mismatch in refractive indices will also cause spherical aberrations because the rays inside the illumination cone will be focused at different positions along the  $z$ -axis (for a detailed discussion, see [149]). As a result, the resolution of both the illumination and confocal intensity distributions will be deteriorate as a function of the penetration depth in the sample. Additionally, because of spreading of the focus, less light will penetrate the confocal pinhole and the observed intensity will decrease as well. It is beyond the scope of this work, however, to attempt to calculate the theoretic aberrated intensity distributions. The loss in resolution due to spherical aberrations will be determined experimentally in section 7.4 by comparison of experimental and simulated codes. In this section we will merely demonstrate the presence of spherical aberrations.

### 7.3.2 Materials and methods

A drop of a diluted suspension of the 28  $\mu\text{m}$  NODD microspheres, as described in section 7.1.2, is put into a chamber of a microscopic 96 well plate. A single microsphere is brought into the field of view. A 3 $\times$  Kalman filtered  $xz$ -image is acquired through the center of the microsphere with an iris setting of 0.7. The  $Z$ -step of the focus motor and the pixel size were set to 0.1  $\mu\text{m}$ . This experiment is repeated for the 10 $\times$ , the 40 $\times$  and the 60 $\times$  objective lenses. The ratio of the measured lateral and axial microsphere diameter will give the experimental  $z$ -correction factor. The edge steepness is calculated as the FWHM of the first derivative of the axial intensity profile through the top and bottom edges.

### 7.3.3 Experiments and discussion

The  $xz$ -images of the microspheres are shown in Fig. 7.6 together with their radial and axial profiles for all three lenses. As expected from Eq. (7.4), the microspheres look ‘squashed’ along the  $z$ -direction. However, because of the spherical shape of the microspheres, there is an asymmetry between the bottom and upper half in the images of the 40 $\times$  and 60 $\times$  lenses. The upper half appears to be elongated compared with the bottom half.

To measure the diameter of the microspheres along the radial and axial direction, the boundary of the microspheres has to be defined. This is not possible based on a certain intensity level because of the asymmetric axial intensity profiles. Instead, the boundary was defined as the location where the first derivative of the intensity profile reaches a local maximum. In other words, the boundary of the microsphere is defined as the location where the intensity profile at the edges is the steepest. These locations are indicated by circles in Fig. 7.6 for the radial and axial intensity profiles. This method did not work for the axial intensity profile of the 10 $\times$  lens because of the absence of a clear boundary. Instead, the radial boundary was calculated first according to the first derivative as described above. The intensity that corresponds to this location was taken as a measure to find the boundary in the axial direction.

The calculated  $z$ -correction factors are summarized in Table 7.1. For each type of lens the  $z$ -correction factor is calculated for the top and bottom half of the microspheres, as well as the average  $z$ -correction factor. For comparison, the theoretic value according to Eq. (7.4) is added as well. These results show there is a good correspondence between the ‘bottom’ and theoretic  $z$ -correction factor for the 10 $\times$  and 60 $\times$  lenses. The theoretic  $z$ -correction factor for the 40 $\times$  lens deviates from the ‘bottom’  $z$ -correction factor by 25%. The marked difference between the ‘top’ and ‘bottom’  $z$ -correction factors for the 40 $\times$  and 60 $\times$  lenses is probably because of spherical aberrations which blur the far side of the microbeads.

$z$ -correction Factors				
	BOTTOM	TOP	AVERAGE	THEORETIC
10 $\times$	1.66	1.56	1.61	1.64
40 $\times$	2.79	1.51	1.96	2.12
60 $\times$	1.82	1.28	1.50	1.82

**Table 7.1:**  $z$ -correction factors

The axial intensity profile of the 10 $\times$  lens is highly symmetrical. Therefore, spherical aberrations are not a primary issue for this low NA objective lens. There is a drop in intensity for increasing penetration depth for the 40 $\times$  and 60 $\times$  lenses because of spherical aberrations, as expected. It also clear that there is a substantial loss in resolution for increasing penetration depth, as can be seen by the difference in edge steepness of the



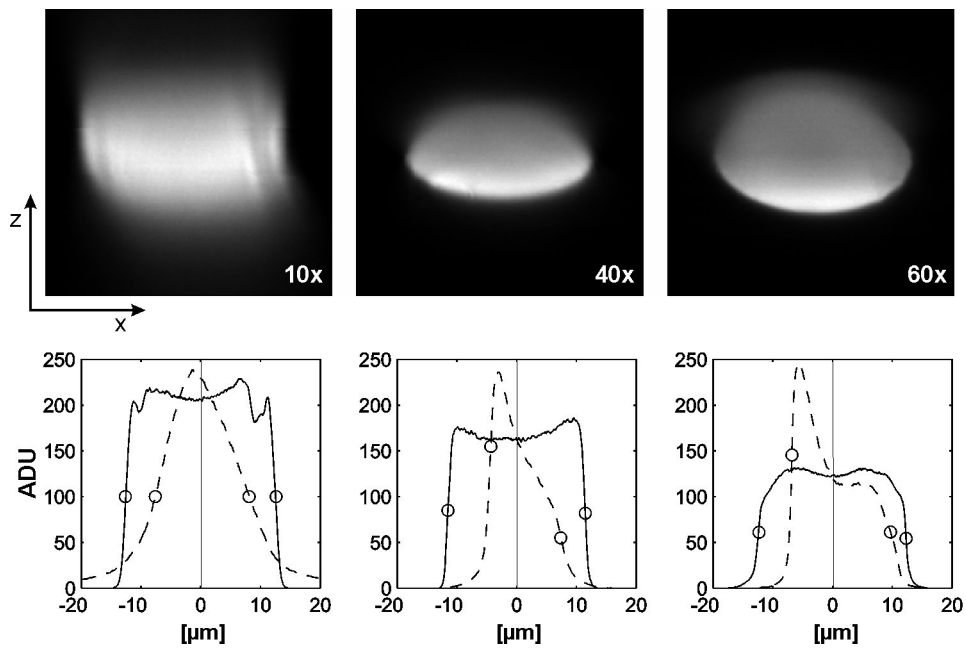


**Figure 7.6:** Confocal  $xz$ -images are recorded through the center of  $28\ \mu\text{m}$  NODD microspheres with the  $10\times$ , the  $40\times$  and  $60\times$  objective lenses. The images have dimensions of  $36\ \mu\text{m} \times 36\ \mu\text{m}$ . The corresponding radial (solid line) and axial (dashed line) intensity profiles are shown below each image. The circles denote the microsphere's edges. The difference between the refractive index of the lens immersion medium and the microsphere causes the microsphere to appear squashed along the  $z$ -axis. Spherical aberrations are markedly present for the  $40\times$  and the  $60\times$  lenses, as can be seen by the drop in intensity with increasing penetration depth and the difference in edge response for the bottom and top boundary of the microsphere.

bottom and top part of the microspheres.

### 7.3.4 Conclusions

As predicted by geometric optics, the experiments have shown there is a difference between the displacement of the NFP and the AFP because of a mismatch in refractive index between the lens immersion medium and the sample. Eq. (7.4) seems to predict the  $z$ -correction factor reasonably well, although it is clear that it is best to determine the  $z$ -correction factor experimentally.

Besides a focal shift, a mismatch in refractive indices also causes spherical aberrations, which results in a deterioration of the resolution of both the illumination and confocal detection distribution. Spherical aberrations were markedly present for the 40 $\times$  and 60 $\times$  lenses, which could be seen by blurring of the upper part of the microspheres and a corresponding drop in intensity. The loss in resolution will be estimated in the next section by comparison of experimental photobleached barcodes and simulated ones.

## 7.4 Encoding experiments and simulations

### 7.4.1 Aim and objectives

The final aim of this study is ideally to establish the optimal conditions for automated writing and reading of the codes in the fluorescent microspheres. In particular we want to examine which type of lens is best for writing and which one for reading. If at the read-out phase, the photobleached codes would always be perfectly aligned with the focal plane, the answer would be easy: look for the objective lens that gives the best writing resolution in the focal plane. In reality, however, the encoded microspheres will have rotated when they are collected at the microscope for read-out after being used in assays. In order to rotate them back to their original orientation, ferromagnetic microspheres and an external magnetic field will be used as was explained and demonstrated in section 5.4. But even then, certainly in an automated process, there will inevitably always be a certain amount of inaccuracy in the orientation (i.e. the angle of the encoded plane) and position (i.e. the out-of-focus distance) of the microspheres. We will therefore use different lenses for writing and reading of the barcodes and evaluate them in terms of resolution performance and out-of-focus tolerance.

The simulation program, as described in section 6.2, was developed to aid in this attempt to find the optimum optical configuration. To that end, it will therefore be necessary to evaluate if the simulated codes agree with the experimental ones. If the simulation program is able to accurately predict the real photobleached codes, it will be a convenient tool to quickly examine the effect in all three spacial dimension of changing certain optical parameters.

## 7.4.2 Materials and methods

The 28  $\mu\text{m}$  microspheres as described in section 7.1.2 will be used for the encoding experiments. Different types of codes will be photobleached in single microspheres using different lenses. A confocal ‘Z-stack’ will be recorded of each of these codes to examine their 3D structure. The ‘Z-step’ of the focus motor will depend on the imaging objective lens:  $\Delta z = 1 \mu\text{m}$  for the 10 $\times$  lens and  $\Delta z = 0.5 \mu\text{m}$  for the 40 $\times$  and 60 $\times$  lenses.

The readability of the codes will be examined as a function of the out-of-focus distance. As explained in section 6.3, the codes we are interested in consist of individual code elements, i.e. the ‘bars’ from the barcode, that are distinguishable based on a difference in ‘gray level’. In other words, neighbouring bars are to be distinguished from each other based on their contrast. The gray level transition between two bars should ideally be as sharp as possible. When plotting the first derivative of the code intensity profile, a transition between two neighbouring bars should therefore be visible by a ‘peak’. The magnitude of this local maximum of the first derivative reflects directly the contrast between two neighbouring bars. The ‘readability’ of the code will therefore be expressed in terms of peak heights of the first derivative of the code intensity profile.

## 7.4.3 Experiments and discussion

### ‘Black and white’ barcodes

First a barcode is bleached consisting of 4 small bars (two black and two white) and three wide bars (two black and one white). The small bars have a width of 1.5  $\mu\text{m}$  and the wide bars are 3  $\mu\text{m}$  wide. Bleaching was done with the 10 $\times$  (2.2 mW laser power), 40 $\times$  (1.4 mW laser power) and 60 $\times$  (1.0 mW laser power) lenses<sup>2</sup>. Z-stacks were subsequently acquired of each of the codes with all three lenses. The ‘in focus’ image of each

---

<sup>2</sup>Although the laser power was held constant for all three lenses, a different power in the sample results from different transmission efficiencies.

of the Z-stacks is shown in Fig. 7.7). Each row displays the same barcode, bleached by that particular lens, and imaged by each of the three lenses. Next, the Z-stacks were used to evaluate the readability of the codes as a function of out-of-focus position. This was done by taking the first derivative of the code intensity profile for each of the images and calculating the average ‘peak’ height. Some examples are shown in Fig. 7.9, third column. This peak height of the first derivative is a direct measure of the ability to discriminate two neighbouring bars. The results are summarized in the graphs of Fig. 7.7, where the average peak height is plotted against the NFP<sup>3</sup>. The solid line corresponds to imaging with the 60× lens, the dashed line with the 40× lens, and the dash-dotted line with the 10× lens. The results can be interpreted in the following way. The codes that were bleached with the 40× and 60× lenses are both best viewed by the 60× lens: the contrast in the focal plane decreases by about 40% when imaging with the 40× lens compared to the 60× lens. The graphs also show that the contrast of the codes rapidly deteriorates as a function of out-of-focus distance. However, the code bleached by the 40× lens has an extended out-of-focus readability as compared to the 60× lens. This is because of an elongated axial illumination profile of the 40× lens, as was shown in section 7.2. The graphs also show that the out-of-focus readability is better when imaged with the 60× lens compared to the 40× lens. This is because of a combination of a superior axial resolution of the 60× lens (see section 7.2) and a smaller  $z$ -correction factor (see section 7.3).

When the codes that are bleached by the 40× and 60× lenses are imaged by the 10× lens, we see that there is almost no contrast left. This is because the axial extent of the photobleached codes is small compared to the very elongated axial detection profile of the 10× lens. The actual code is thus ‘blurred’ by out-of-focus fluorescence. At the other hand, because of the very elongated axial detection profile, the contrast remains virtually the same as a function of the NFP.

A code consisting of five bars, three black and two white, was bleached with the 10× lens as well. Each bar has a width of 3  $\mu\text{m}$ . Because of the elongated, almost perfectly cylindrical, axial illumination profile, the bars are bleached throughout the entire microsphere. For that reason, the code is visible this time when imaged by the 10× lens with a reasonable contrast. Interestingly, when imaged in the central plane by the 40× and 60× lens, there is no gain in contrast. The graph shows that, for those two lenses, the code

---

<sup>3</sup>Let it again be noted that the NFP is equal to the distance moved by the focus motor. A correction is needed to obtain the the AFP, as was discussed in section 7.3

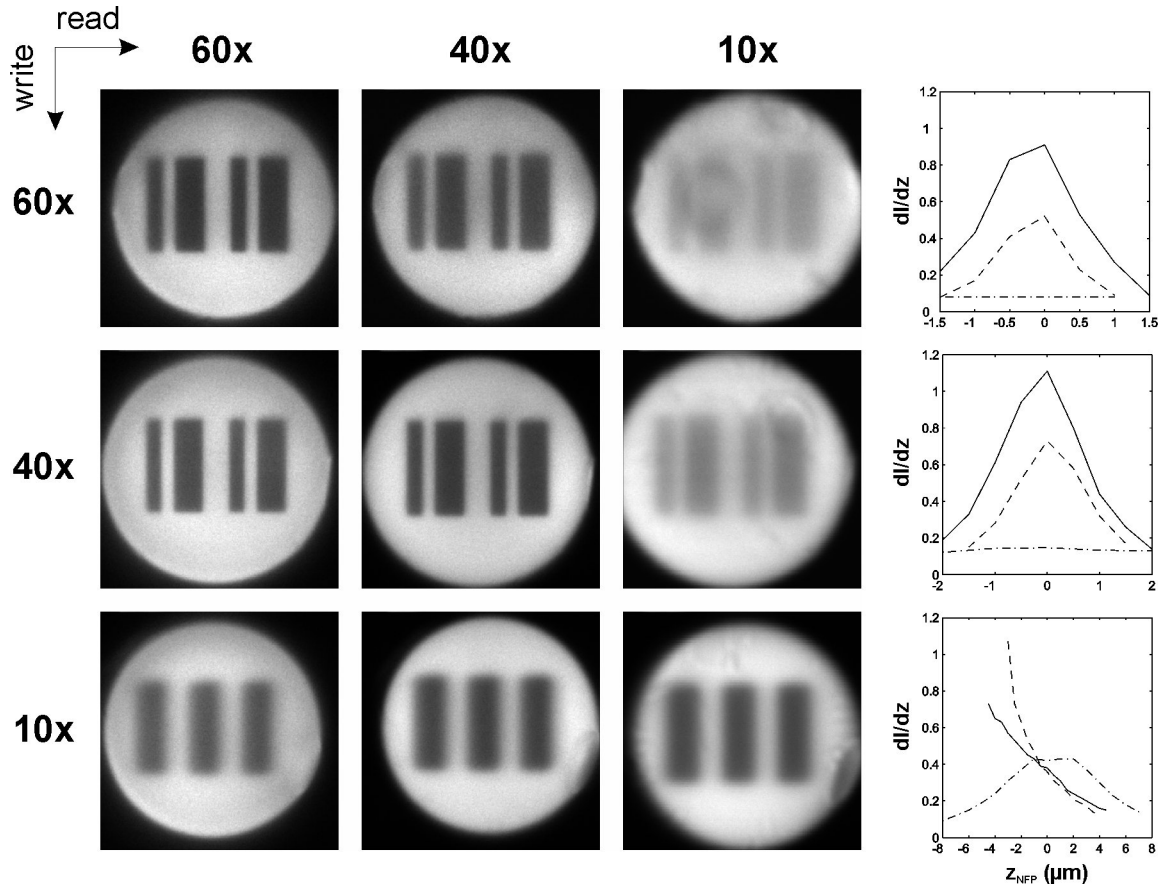


**Figure 7.7:** NODD microspheres are encoded with a black and white barcode by the 60 $\times$  (first row), the 40 $\times$  (second row) and the 10 $\times$  (third row) objective lenses. The small bars have a width of 1.5  $\mu\text{m}$  and the wide bars a width of 3  $\mu\text{m}$ . A confocal Z-stack is recorded of each of the encoded microspheres with the 60 $\times$  (first column), the 40 $\times$  (second column) and the 10 $\times$  (third column) objective lens. The ‘in-focus’ image is shown in each case. The image dimensions are 25.6  $\mu\text{m} \times 25.6 \mu\text{m}$ . The ‘readability’ graphs are shown in the fourth column (see main text for details). The solid line corresponds to imaging with the 60 $\times$  lens and the dashed line with the 40 $\times$  lens.

is much better visible near the bottom of the microsphere (close to the objective lens), but becomes almost unreadable near the far end. This is a striking manifestation of the spherical aberrations that were mentioned in section 7.3.

The same experiment was repeated with the  $40\times$  and  $60\times$  lenses for a slightly more complicated code consisting of 7 small bars (4 black and 3 white) and 4 wide bars (2 black and 2 wide). The small bars have a width of  $1\ \mu\text{m}$  and the wide bars a width of  $2\ \mu\text{m}$ . The results are shown in Fig. 7.8 and are almost identical to the previous ones. The readability deteriorates a little faster than in the previous case, indicating that wider bars give a little improvement in out-of-focus readability. Therefore, it can be concluded that bars of  $1\ \mu\text{m}$  are very well possible with excellent contrast in the focal plane, but the smaller the bars, the better the positioning accuracy will have to be. In particular, the results show that a positioning accuracy of better than  $\pm 1\ \mu\text{m}$  will be necessary. If the demand for the highest possible resolution is relaxed, the positioning accuracy can be relaxed as well by bleaching with lower NA lenses.

As a next step, we will now evaluate if the simulation program, as described in section 6.2, is able to generate codes that are in agreement with the experimental ones. As explained in section 7.3, the resolution of the writing and reading beam will be deteriorated compared to the values that have been measured in section 7.2. However, the actual resolution values inside the microspheres are not a priori known. In a process of trial and error, codes have therefore been simulated according to the experiments mentioned above with various resolution values until the best agreement with the experimental codes was obtained. Although it will be discussed in more detail below, we already note at this instance that it was not possible to find a good agreement with the experimental codes when using the modified Gaussian distribution. The fundamental Gaussian distribution, at the other hand, did yield good results. After extensive testing, the following resolution values have been obtained:

	$w_{0e}$	$w_{0d}$	$w_{zd}$
$10\times$	1.1	1.0	7.0
$40\times$	0.4	0.35	1.75
$60\times$	0.3	0.25	1.0

Those resolution values are very well possible considering the ‘ideal’ values mentioned in section 7.2 and the presence of spherical aberrations. In the simulations it was found

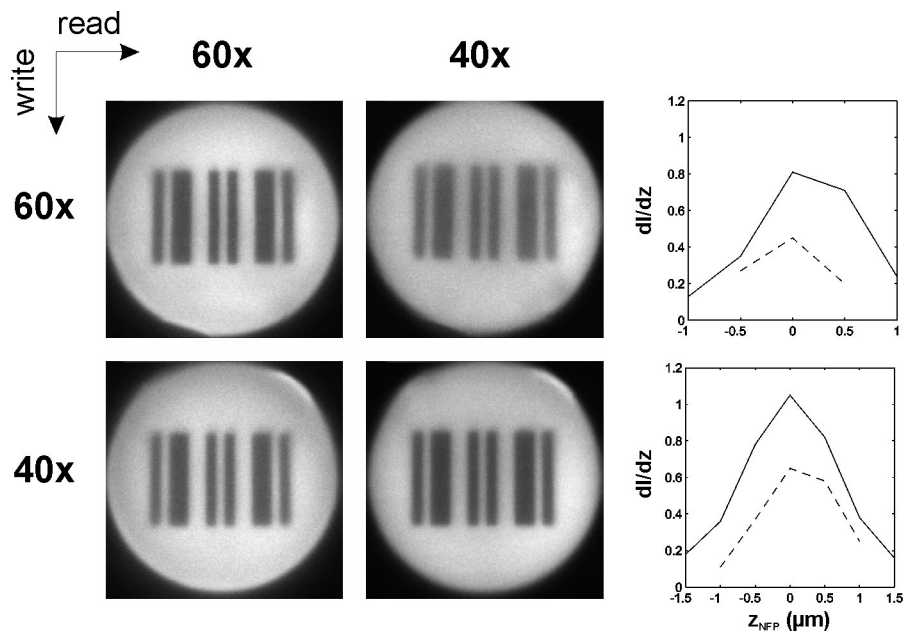


**Figure 7.8:** NODD microspheres are encoded with a black and white barcode by the 60 $\times$  (first row) and the 40 $\times$  (second row) objective lens. The small bars have a width of 1  $\mu\text{m}$  and the wide bars a width of 2  $\mu\text{m}$ . A confocal Z-stack is recorded of each of the encoded microspheres with the 60 $\times$  (first column) and the 40 $\times$  (second column) objective lens. The ‘in-focus’ image is shown in each case. The image dimensions are 25.6  $\mu\text{m}$   $\times$  25.6  $\mu\text{m}$ . The ‘readability’ graphs for each of the codes are shown in the third column (see main text for details). The solid line corresponds to imaging with the 60 $\times$  lens, the dashed line with the 40 $\times$  lens and the dash-dotted line with the 10 $\times$  lens.

that the value of the axial confocal resolution  $w_{zd}$  was not very critical. The values mentioned for  $w_{zd}$  have therefore an uncertainty of at least 25%.

An example is shown in Fig. 7.9 to demonstrate the very good correspondence between the simulated and experimental codes. The microsphere that is shown is the one from Fig. 7.7 which is bleached by the 40 $\times$  and imaged by the 60 $\times$  lens. The code is shown for different NFP's, from -2  $\mu\text{m}$  to +2  $\mu\text{m}$ , relative to the focal plane. Negative values are closer to the objective lens. The corresponding intensity profile and its first derivative are shown as well. The simulations that were performed are shown next to that: an image of the simulated code<sup>4</sup>, the corresponding intensity profile and its first derivative. At this instance it is important to recall that the  $z$ -scale of the simulated code corresponds to the AFP. As explained in section 7.3, the NFP and the AFP are related by a  $z$ -correction factor whose values are listed in Table 7.1 for the different lenses. Extensive comparisons between the experimental and simulated codes have shown that a good correspondence is found between both when the 'BOTTOM'  $z$ -correction factor from Table 7.1 is used. In this particular example, imaging was done by the 60 $\times$  lens, which has a correction factor of 2. This means that, for example, the image that was recorded at 1  $\mu\text{m}$  out-of-focus should be compared with the simulated image plane that is 2  $\mu\text{m}$  out of focus. Comparing the experimental and simulated intensity profiles and their first derivatives, shows they are almost identical! Note that, experimentally, there is a slight difference between the image planes above and below the focal plane. The code deteriorates a little faster when going deeper into the microsphere, which, again, is a manifestation of the spherical aberrations.

As already indicated above, simulations with the modified Gaussian distribution did not agree well with the experimental codes. In the focal plane, the results are almost identical with the fundamental Gaussian distribution, which is to be expected since both distributions are identical in the focal plane. However, when going out of focus, the bleaching profile obtained with the modified distribution quickly deviates from the one obtained with the fundamental distribution. This is illustrated in Fig. 7.10, where the intensity profile at  $z_{NFP} = -1 \mu\text{m}$  from Fig. 7.9 is repeated, together with the intensity profiles as calculated with the fundamental and modified Gaussian distributions. The modified Gaussian distribution clearly does not correspond to the experimental situation, whereas the fundamental Gaussian distribution gives a nearly perfect match. This is most likely because the modified Gaussian distribution does not comply with the law of conservation of

---

<sup>4</sup>The length of the bars was reduced compared to the real codes to limit the calculation times.



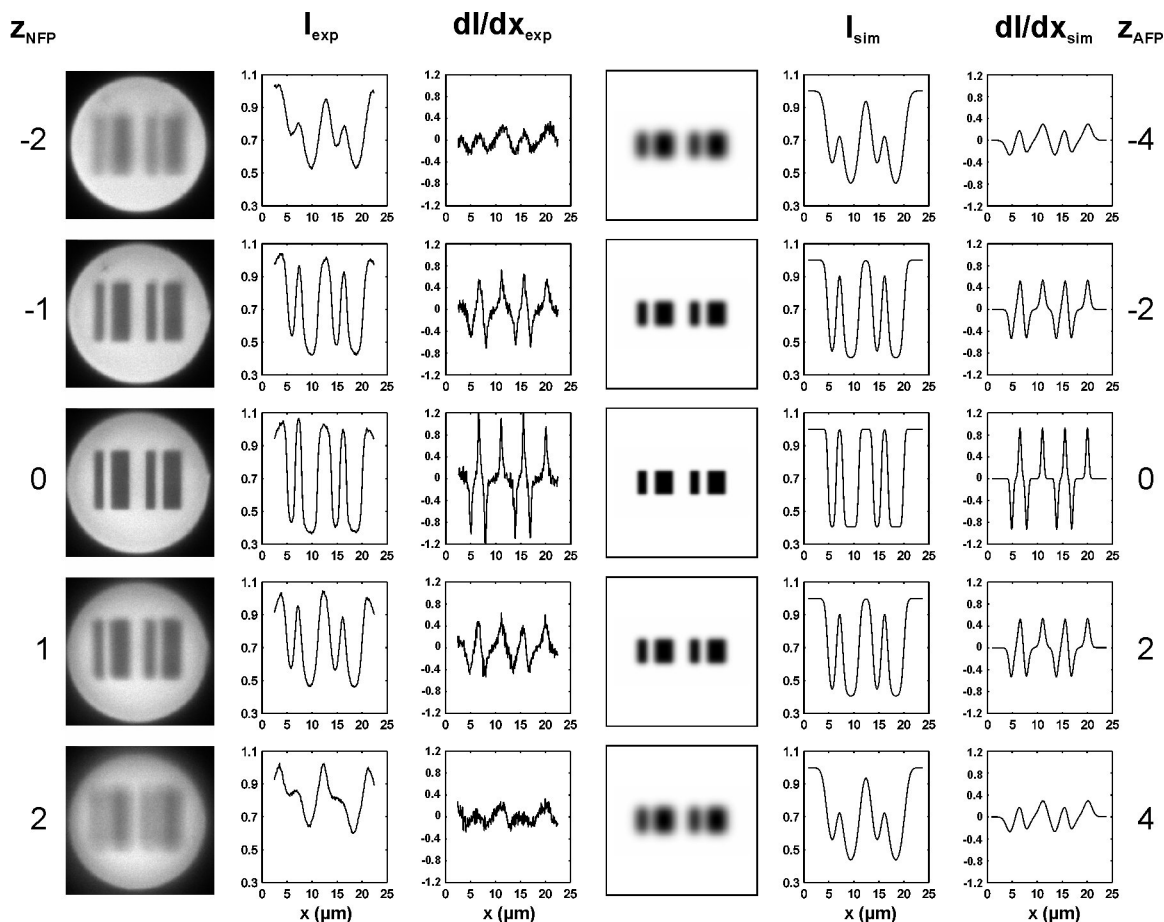


**Figure 7.9:** A black and white code bleached by the 40 $\times$  lens and imaged by the 60 $\times$  lens is shown at different positions along the optical axis. The image dimensions are 25.6  $\mu\text{m} \times 25.6 \mu\text{m}$ . The NFP position [ $\mu\text{m}$ ] is indicated relative to the plane in which the code was bleached. Negative values are closer to the objective lens. The intensity profile and its first derivative is shown for each image. The corresponding simulated code is shown to the right together with the intensity profile and its first derivative (see main text for details). The position of the AFP [ $\mu\text{m}$ ] is indicated as well.

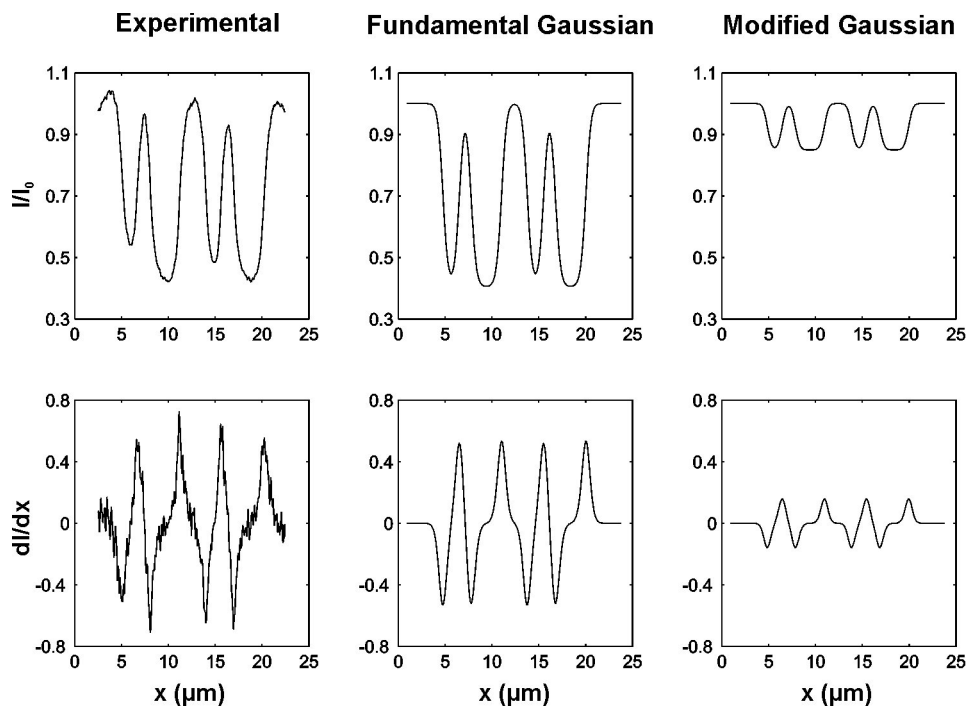


**Figure 7.10:** The intensity profile at  $z_{NFP} = -1 \mu\text{m}$  from Fig. 7.9 is shown again with its first derivative below. The code was simulated assuming a fundamental and modified Gaussian illumination intensity distribution. The corresponding intensity profiles and first derivatives are shown as well. While there is a very good correspondence for the fundamental Gaussian distribution, the modified Gaussian distribution is far off.

energy, as discussed in Appendix B, section B.2. We therefore conclude that the modified Gaussian intensity distribution should not be used any more in this context. The dramatic difference between both distributions can also be seen from Fig. 7.11 where the  $xz$ -images through the center of the simulated codes are shown. Because the fundamental distribution complies with the law of conservation of energy, the bleaching profile stretches throughout the entire space. The bleaching profile of the modified distribution, at the other hand, is limited to the vicinity of the focal plane<sup>5</sup>.

### Length and intensity encoding

To increase the number of unique codes, it is possible to use multiple intensity levels in combination with length encoding, as explained in section 6.3.3. This is evaluated by

<sup>5</sup>Because of this very property the modified Gaussian distribution might rather be a viable function to describe photobleaching by a two-photon process.

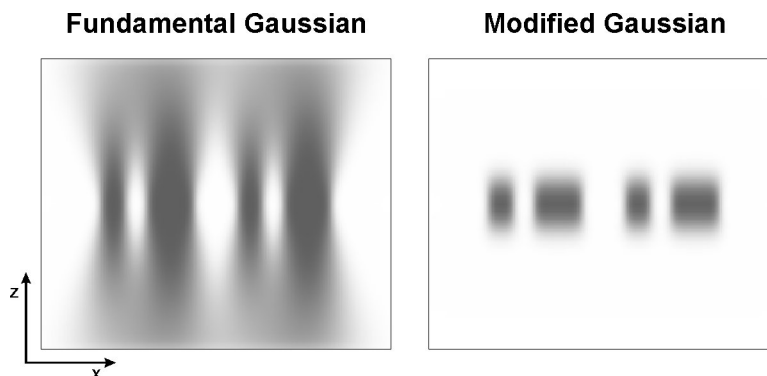


**Figure 7.11:** An  $xz$ -image through the center of the simulated code is shown in case of the fundamental and modified Gaussian illumination intensity distribution. The image dimensions are  $23.0 \mu\text{m} \times 19.1 \mu\text{m}$ .

photobleaching codes with three intensity levels and two widths. First a code has been photobleached by the  $40\times$  and  $60\times$  lenses consisting of three wide bars ( $3 \mu\text{m}$ ) and four small bars ( $1.5 \mu\text{m}$ ). The photobleaching power in the sample was  $1.9 \text{ mW}$  and  $0.63 \text{ mW}$  for the  $40\times$  lens, and  $1.35 \text{ mW}$  and  $0.45 \text{ mW}$  for the  $60\times$  lens. A confocal Z-stack was recorded of each of the codes with both the  $40\times$  and  $60\times$  lenses. The ‘in focus’ images are shown in Fig. 7.12 together with their intensity profile and corresponding first derivative. We note that, despite of a difference in photobleaching power, the bleaching depths are virtually the same for both lenses. This is very likely because of possible small variations in photobleaching rate  $\alpha$  between individual microspheres. In agreement with the results from the black and white codes, best contrast is obtained when imaging with the  $60\times$  lens. The loss in contrast (i.e. peak height) is the same for both codes when going from the  $60\times$  to the  $40\times$  lens. Although evident, it is important to note there is less contrast for the medium bleach level. In other words, the peak in the first derivative corresponding to a transition to an intermediate bleaching level is smaller than for a transition between ‘black and white’. As a consequence, the gray level code will become more rapidly unreadable when going out of focus compared to a black and white code. This also means that the positioning accuracy will have to be better in case of a gray level code.

Further evaluation of the confocal Z-stacks has also shown that there is an extended out-of-focus readability of the code when it is bleached by the  $40\times$  lens, compared to the  $60\times$  lens. This is illustrated in Fig. 7.13, where the code bleached by the  $60\times$  and  $40\times$  lens is shown at  $z_{NFP} = -1 \mu\text{m}$ . Both images are recorded with the  $60\times$  lens. As can be seen from the first derivative of the intensity profile, the transition to the intermediate

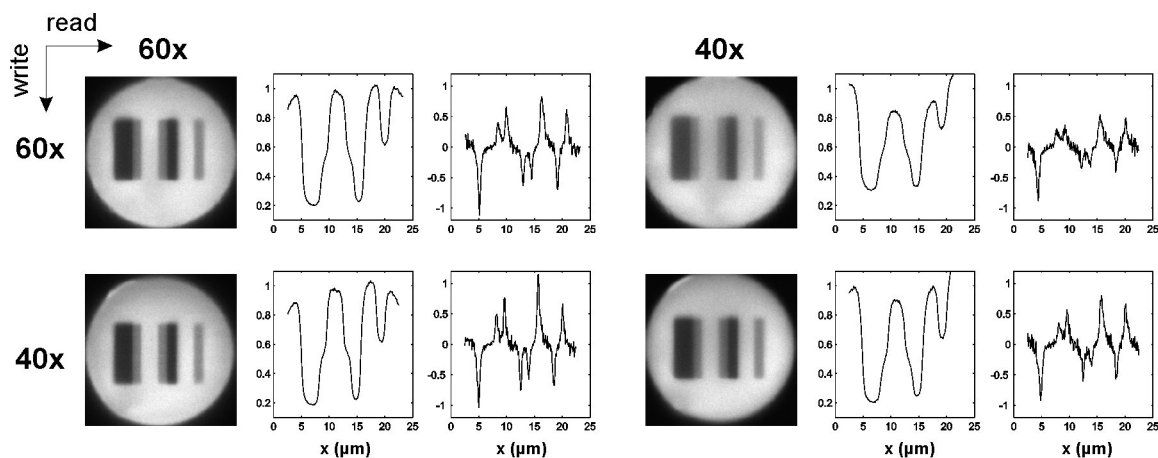


**Figure 7.12:** NODD microspheres are encoded with a barcode consisting of three intensities in combination with two bar widths. Encoding was done by the 60 $\times$  (first row) and the 40 $\times$  (second row) objective lens. The small bars have a width of 1.5  $\mu\text{m}$  and the wide bars a width of 3  $\mu\text{m}$ . A confocal Z-stack is recorded of each of the encoded microspheres with the 60 $\times$  (first column) and the 40 $\times$  (second column) objective lens. The ‘in-focus’ image is shown in each case. The image dimensions are 25.6  $\mu\text{m} \times 25.6 \mu\text{m}$ . The intensity profiles and their first derivative are shown for each image.

bleach level is only barely visible for the code bleached by the 60 $\times$  lens. However, the same transition is better visible for the code bleached by the 40 $\times$  lens. The reason for this is the elongated bleaching profile of the 40 $\times$  lens. Although, theoretically, the resolution in the focal plane will be a little less for the 40 $\times$  lens, this is compensated by an extended out-of-focus readability.

The situation as explained above was simulated to further examine the ability of the simulation program to accurately predict the photobleaching profiles. The same values as previously mentioned for the resolution parameters were used. The same photobleaching power was assumed for both lenses: 2 mW and 0.7 mW for the ‘black’ and ‘gray’ level respectively. Again a very good correspondence was found between the experiments and the simulations. The first derivative of the intensity profile for  $z_{NFP} = -1 \mu\text{m}$  (this is  $z_{AFP} = -2 \mu\text{m}$  in the simulation program) is shown in Fig. 7.13. In both cases there is an almost exact match between the simulation result and the experimental curve.

As a final experiment, a three-level intensity code was photobleached with smaller bars. The code consists of 4 wide bars (2  $\mu\text{m}$ ) and 7 small bars (1  $\mu\text{m}$ ). Bleaching was

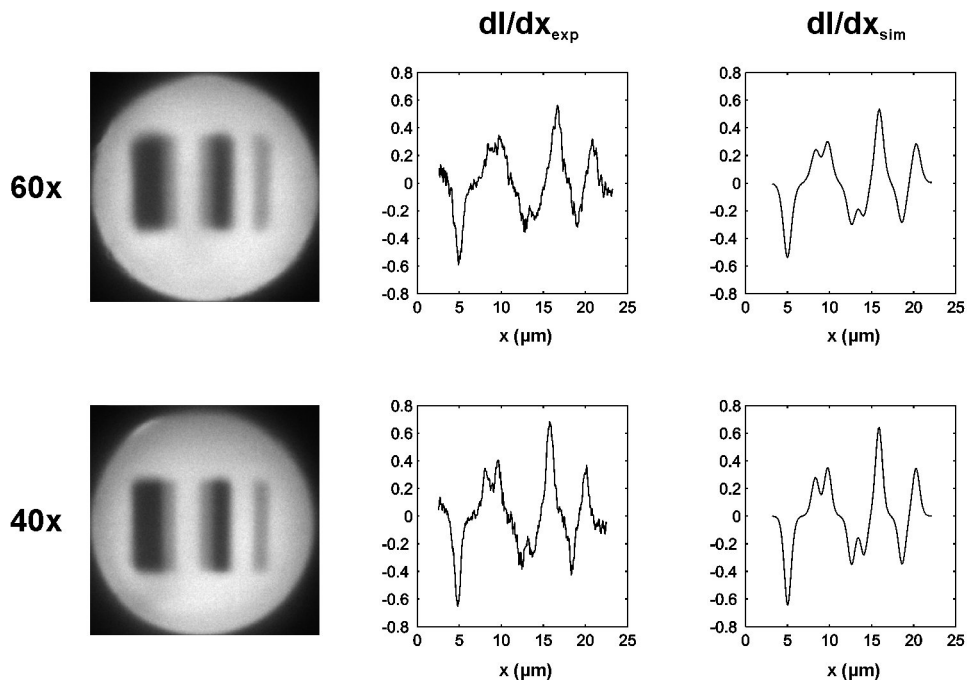


**Figure 7.13:** The three-level intensity code from Fig. 7.12 is shown at  $z_{NFP} = -1 \mu\text{m}$ . The upper code was written and imaged by the  $60\times$  lens. The lower code was written by the  $40\times$  lens and imaged by the  $60\times$  lens. The image dimensions are  $25.6 \mu\text{m} \times 25.6 \mu\text{m}$ . Because of an extended axial illumination distribution, the code bleached by the  $40\times$  lens remains better visible for the same out-of-focus distance, as can be seen from the first derivative of the corresponding intensity profile. This is also accurately predicted by the simulation program in both cases.

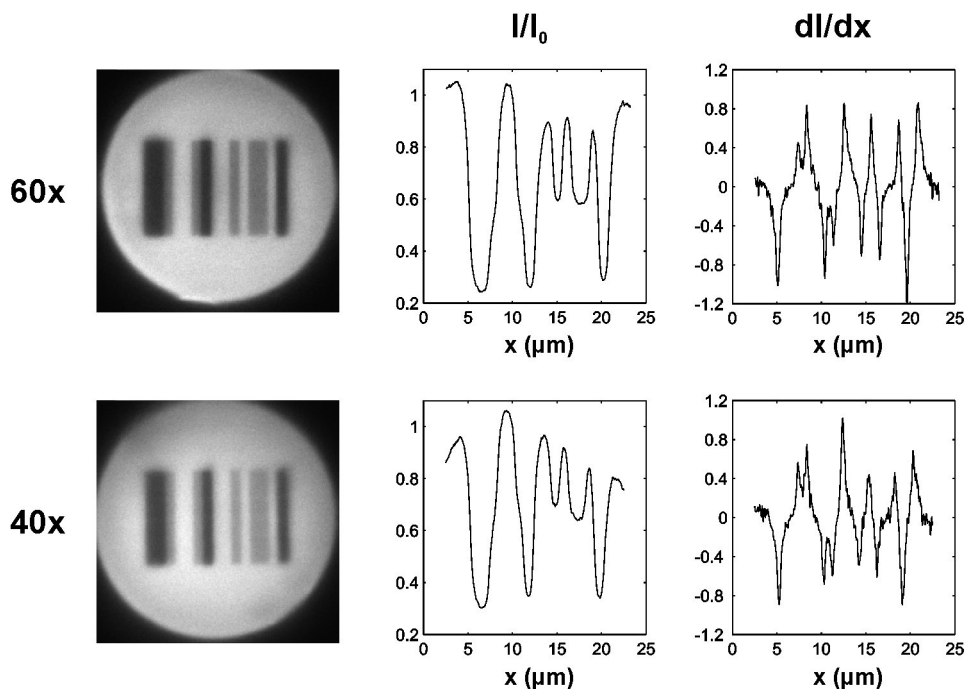


**Figure 7.14:** NODD microspheres are encoded with a barcode consisting of three intensities in combination with two bar widths. Encoding was done by the 60 $\times$  (first row) and the 40 $\times$  (second row) objective lens. The small bars have a width of 1  $\mu\text{m}$  and the wide bars a width of 1.5  $\mu\text{m}$ . A confocal Z-stack is recorded of each of the encoded microspheres with the 60 $\times$  objective lens. The ‘in-focus’ image is shown in each case. The image dimensions are 25.6  $\mu\text{m} \times 25.6 \mu\text{m}$ . The intensity profiles and their first derivative are shown for each image.

done with the 60 $\times$  and 40 $\times$  lenses and imaging with the 60 $\times$  lens. The photobleaching power in the sample was the same as for the previous code. The ‘in focus’ images are shown in Fig. 7.14, from which it is clear that still a very good contrast is obtained for all intensity levels in the focal plane. However, at an out-of-focus position of  $z_{NFP} = -1 \mu\text{m}$ , the transition from the lowest to the intermediate bleach level cannot be discriminated anymore (see Fig. 7.15). Again it is found that the situation is worse for the code bleached by the 60 $\times$  lens. In agreement with what was observed for the black and white codes, we therefore conclude that bars of 1  $\mu\text{m}$  are very well possible, but at the expense of a reduced out-of-focus readability.

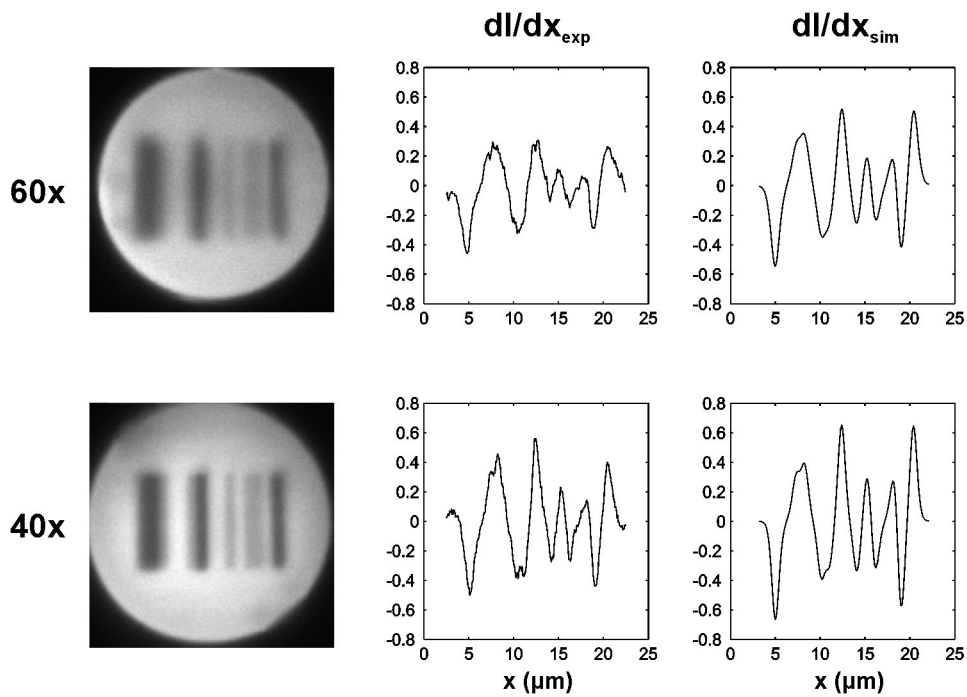


**Figure 7.15:** The three-level intensity code from Fig. 7.14 is shown at  $z_{NFP} = -1 \mu\text{m}$ . The upper code was written and imaged by the  $60\times$  lens. The lower code was written by the  $40\times$  lens and imaged by the  $60\times$  lens. The image dimensions are  $25.6 \mu\text{m} \times 25.6 \mu\text{m}$ . A good correspondence is found between the experimental and simulated result.

#### 7.4.4 Conclusions

The experiments have shown it is possible to photobleach barcodes with bars of 1  $\mu\text{m}$  wide with a good contrast between neighbouring bars. This was true for both black and white codes as well as for a three-level intensity code. However, increasing the width of the bars has the advantage of increasing the out-of-focus visibility as well. The same holds true for using multiple intensity levels. While it is very well possible to use multiple bleaching levels in the encoding scheme, the out-of-focus visibility will decrease accordingly.

The experiments have also shown that these general effects are dependent on the objective lenses that are used for writing and reading. For writing, both the 40 $\times$  and 60 $\times$  lenses gave a similar resolution in the focal plane. However, the out-of-focus readability of code was best when bleached by the 40 $\times$  lens because of its elongated axial illumination profile. For reading, at the other hand, a superior resolution and contrast was obtained for the 60 $\times$  lens. Moreover, because of its smaller deviation of the AFP from the NFP, the 60 $\times$  lens gave a much more extended out-of-focus readability.

It is therefore concluded from the experiments that writing should best be done by an intermediate NA lens (0.5 - 0.75) for extended out-of-focus readability while retaining sufficient resolution for writing. Reading at the other hand should be done by a high NA lens (and small confocal aperture) for best resolution and contrast. In addition it is best that the  $z$ -correction factor is as small as possible for the reading lens, again to maximize the out-of-focus visibility.

The Matlab computer program that was written for the simulation of writing and reading the codes, based on the theory as described in section 6.1, gave results that are in very good agreement with the experimental codes. This was true not only for a code imaged in the focal plane, but also for out-of-focus observations. First of all, comparison of the simulated and experimental codes has shown that the fundamental Gaussian illumination distribution should be used instead of the modified Gaussian. It was also found that the writing and reading resolution inside the microspheres is slightly reduced because of spherical aberrations. This is as expected, as explained in section 7.3, although the loss in resolution is all in all rather small. The simulations have also shown that the  $z$ -correction factor which is needed to relate the NFP to the AFP is in agreement with the values found in section 7.3, at least if the 'BOTTOM' values of Table 7.1 are used.



Not only was the simulation program able to accurately predict the concentration profiles, also the corresponding first derivatives were in very good agreement with the experimental results. This is important because it is the first derivative which tells us if neighbouring bars can be distinguished from one another. In addition, the first derivative may be used for automatic decoding: the peak heights reflect the transition in intensity between two neighbouring bars, while the width of the individual bars can be directly deduced from their position.

It is therefore concluded that the simulation program can be used as a convenient tool to experiment with different optical set-ups and encoding schemes. In particular it can be used to evaluate out-of-focus readability of different kinds of codes. The added feature of observing a 3D rotated code may be of value to establish the positioning and orientation accuracy necessary for successful observation of a particular code. Such experiments are very difficult to carry out in actual practice. There is an important caveat, however, in this context. At this instance, the simulation program does not take the spherical shape of the microspheres into account. In reality, the microspheres will act as a lens (at least when there is a difference in refractive index between the microsphere and its suspension medium) causing the focal plane to be bend instead of being flat. A deviation from the simulations is therefore to be expected when the code is being read at an angle far from the original orientation. To take the curvature of the focal plane inside the microspheres into account, a first order correction may be applied to the theory as described in section 6.1 by allowing the individual bars to have a certain position along the optical axis. In particular this simply means replacing the coordinate  $z$  by  $z - z_i$  in Eq. (6.5) and all subsequent expressions for  $K(\mathbf{r})$ , where  $z_i$  is the position of bar  $i$  along the optical axis. But even then the curvature of the imaging focal plane still has to be taken into account. This could be done by calculating the intersection of the simulated 3D matrix with a spherical surface. Although not excessively difficult, these corrections have not been implemented so far.

# Appendix A

## Bleaching with a scanning beam

### A.1 First-order photobleaching

We will assume that the bleaching reaction can be described by an irreversible first order reaction:

$$\frac{\partial}{\partial t}C(x, y, z, t) = -\alpha I_b(x, y, z)C(x, y, z, t), \quad (\text{A.1})$$

where  $C(x, y, z, t)$  is the spatial concentration of fluorophores at a bleach time  $t$ ,  $\alpha$  is the bleach rate which is specific for a certain type of fluorophore in a particular medium, and  $I_b(x, y, z)$  is the 3D intensity distribution of the bleaching beam. Eq. (A.1) is a valid description of the photobleaching phase as long as there is no diffusion of the fluorophores during bleaching. This is true if all fluorophores are immobile (as is ideally the case for the encoded microcarriers) or if the bleaching phase is very short compared to the diffusion process.

To describe the bleaching phase for a CSLM, Eq. (A.1) has to be solved for the bleaching beam being scanned across the sample according to a certain 2D geometry. Since a 2D geometry is scanned sequentially line by line, it is instructive to first consider the case of the bleaching along a single line.

### A.2 Bleaching of a single line segment

Let us consider the case where the bleaching beam is scanned along a single line with a constant scanning speed  $v$ . As shown in Fig. A.1, we take the  $x$ -axis to be parallel with the scanning direction. The scanned line is expressed by  $y = Y$ . While scanning across

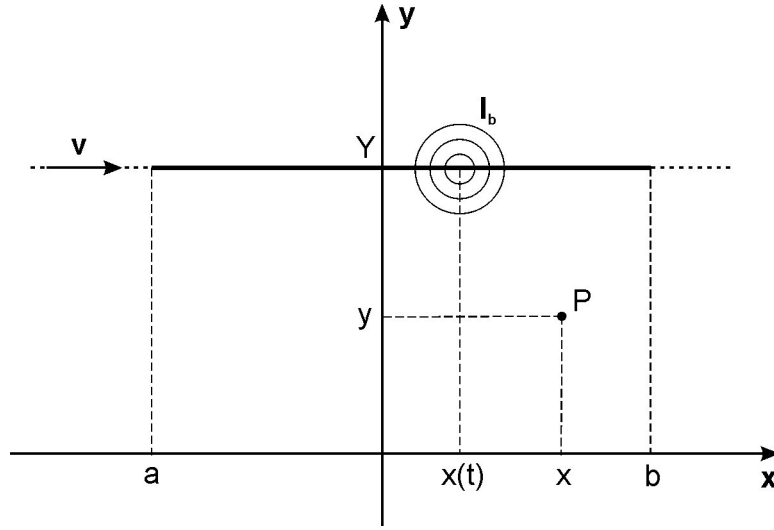


**Figure A.1:** The bleaching beam is scanned with scanning speed  $v$  along a single line. The light intensity is zero, except from position  $x = a$  to  $x = b$ .

the line, the bleaching beam has zero intensity until it reaches position  $x = a$  where the bleaching beam is switched on. At position  $x = b$  the scanning beam is again switched off. Hence, the bleaching geometry is the line

$$B(x, y) = \begin{cases} L(x)\delta(y - Y) & a \leq x \leq b \\ 0 & \text{elsewhere} \end{cases}$$

The Dirac-Delta function  $\delta(y - Y)$  is defined by the following properties:  $\delta(y - Y) = 0$  if  $y \neq Y$  and  $\int_{-\infty}^{+\infty} f(y)\delta(y - Y) dy = f(Y)$ .  $L(x)$  is the function that describes the modulation of the light intensity over the line segment  $[a, b]$  and has values between 0 and 1, where 0 means light switched off and 1 means maximum bleaching intensity. In fact,  $B(x, y)$  expresses the behaviour of the CSLM and  $B(x, y) \cdot I_b(x, y, z)$  describes the effective bleaching intensity modulation in the sample.

Now we want to know the bleaching effect at a location  $P(x, y, z)$  when the bleaching of the line segment has completed. Because of the scanning process, the  $x$ -coordinate of the bleaching intensity distribution is a function of time:  $I_b(x - x(t), y - Y, z)$ . If we take  $t = 0$  at  $x = a$ , then explicitly  $x(t) = vt + a$ . If  $T$  is the time it takes for the scanning beam to cross the bleaching line with length  $b - a$ , the scanning speed is:  $v = \frac{b-a}{T}$ .  $T$  will be called the bleaching time. If we denote the initial concentration of fluorophores (i.e. before bleaching) as  $C_0(x, y, z)$ , the concentration after a bleaching time  $T$  according to

Eq. (A.1) is:

$$C(x, y, z, T) = C_0(x, y, z) e^{-\alpha \int_0^T L(x(t)) I_b(x-x(t), y-Y, z) dt}.$$

Expressing  $t$  in terms of  $x(t)$  and renaming  $x(t)$  as  $x'$  yields:

$$C(x, y, z) = C_0(x, y, z) e^{-\frac{\alpha}{v} \int_a^b L(x') I_b(x-x', y-Y, z) dx'}.$$

The integral in the exponent is nothing else but the 2D convolution  $K(x, y, z)$  of the bleaching geometry  $B(x, y)$  with the bleaching intensity distribution  $I_b(x, y, z)$ , as can be seen from:

$$\begin{aligned} K(x, y, z) &= B(x, y) \otimes I_b(x, y, z) \\ &= \int_{-\infty}^{+\infty} \int_{-\infty}^{+\infty} B(x', y') I_b(x-x', y-y', z) dx' dy' \\ &= \int_{x=a}^b L(x') \int_{y=-\infty}^{+\infty} \delta(y'-Y) I_b(x-x', y-y', z) dx' dy' \\ &= \int_{x=a}^b L(x') I_b(x-x', y-Y, z) dx'. \end{aligned}$$

Thus we finally find that the concentration of fluorophores after bleaching of a line segment can be written as:

$$\begin{aligned} C(x, y, z) &= C_0(x, y, z) e^{-\frac{\alpha}{v} K(x, y, z)} \\ &= C_0(x, y, z) e^{-\frac{\alpha}{v} \int_a^b L(x') I_b(x-x', y-Y, z) dx'}, \end{aligned} \tag{A.2}$$

where  $K(x, y, z) = B(x, y) \otimes I_b(x, y, z)$ . As can be seen, the scanning speed  $v$  determines the extent of bleaching, rather than just the bleaching time  $T$ , as is the case for bleaching with a stationary laser beam [22, 23, 33].

### A.3 Bleaching of a 2D geometry

With a CSLM, a 2D geometry can be bleached by scanning  $N$  subsequent line segments at a regular interline spacing  $\Delta y$ , as is shown in Fig. A.2. In analogy to the previous

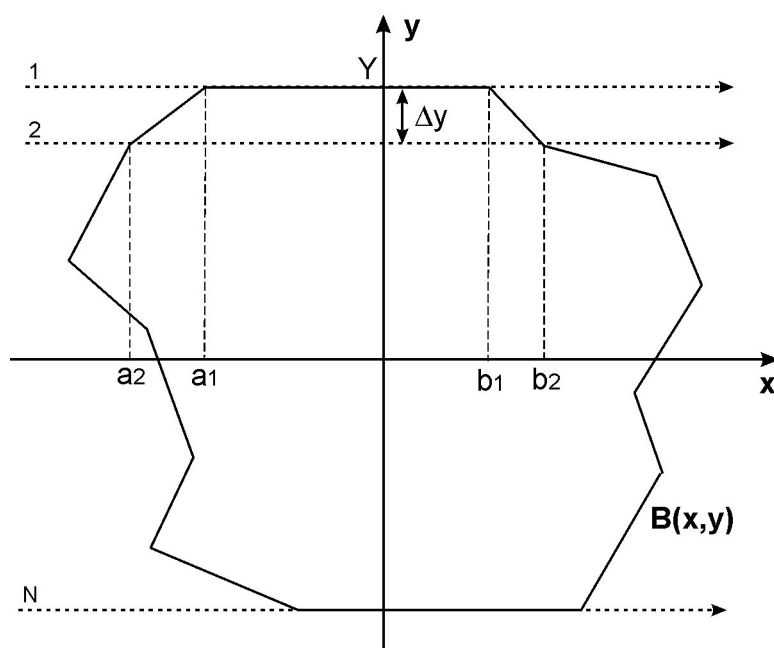


**Figure A.2:** A 2D geometry  $B(x,y)$  is bleached by scanning  $N$  adjacent line segments. The laser intensity is modulated within the geometry's boundaries and zero outside. The origin is chosen arbitrarily, whereas the  $x$ -axis is parallel to the line scanning direction. The first line  $y = Y$  is bleached from position  $x = a_1$  to  $x = b_1$ , whereas the  $i^{\text{th}}$  line  $y = Y - (i - 1)\Delta y$  is bleached from  $x = a_i$  to  $x = b_i$ .

section, let  $B(x, y)$  describe the behaviour of the CSLM to obtain the 2D bleaching geometry.  $B(x, y)$  is zero outside the geometry's boundaries, and within it describes the laser intensity modulation as a function of the spatial coordinates:

$$B(x, Y) = \begin{cases} L(x, Y)\delta(y - Y) & a_1 \leq x \leq b_1 \\ L(x, Y - \Delta y)\delta(y - (Y - \Delta y)) & a_2 \leq x \leq b_2 \\ \vdots \\ L(x, Y - (N - 1)\Delta y)\delta(y - (Y - (N - 1)\Delta y)) & a_N \leq x \leq b_N \\ 0 & \text{elsewhere} \end{cases}$$

Again we take the  $x$ -axis to be parallel with the scanning direction, whereas the origin is chosen arbitrarily. When scanning the first line at  $y = Y$ , a line segment is bleached from  $x = a_1$  to  $x = b_1$ . Upon completion we know from Eq. (A.2) that the concentration of fluorophores will be given by:

$$C_1(x, y, z) = C_0(x, y, z)e^{-\frac{\alpha}{v} \int_{a_1}^{b_1} L(x', Y) I_b(x - x', y - Y, z) dx'}$$

Next, the second line is scanned at a distance  $\Delta y$  below the first one and a line segment is bleached from  $x = a_2$  to  $x = b_2$ . The concentration  $C_1(x, y, z)$  is the initial situation for the second bleaching step. Upon completion of the second line, the concentration of fluorophores is given by:

$$\begin{aligned} C_2(x, y, z) &= C_1(x, y, z)e^{-\frac{\alpha}{v} \int_{a_2}^{b_2} L(x', Y - \Delta y) I_b(x - x', y - Y + \Delta y, z) dx'} \\ &= C_0(x, y, z)e^{-\frac{\alpha}{v} \left[ \int_{a_1}^{b_1} L(x', Y) I_b(x - x', y - Y, z) dx' + \int_{a_2}^{b_2} L(x', Y - \Delta y) I_b(x - x', y - Y + \Delta y, z) dx' \right]} \end{aligned}$$

If the bleaching geometry consists of  $N$  lines, the final concentration will be given by:

$$C_N(x, y, z) = C_0(x, y, z)e^{-\frac{\alpha}{v} \sum_{i=1}^N \int_{a_i}^{b_i} L(x', Y - (i-1)\Delta y) I_b(x - x', y - Y + (i-1)\Delta y, z) dx'} \quad (\text{A.3})$$

If the distance  $\Delta y$  is sufficiently small, the discrete summation can be approximated by an integral over a continuous variable  $y'$ , leading to a double integral over the geometry  $G$ , expressed by  $B(x, y)$ :

$$\begin{aligned} C(x, y, z) &= C_0(x, y, z)e^{-\frac{\alpha}{v} \sum_{i=1}^N \int_{a_i}^{b_i} L(x', Y - (i-1)\Delta y) I_b(x - x', y - Y + (i-1)\Delta y, z) dx' \frac{\Delta y}{\Delta y}} \\ &= C_0(x, y, z)e^{-\frac{\alpha}{v \Delta y} \iint_G L(x', y') I_b(x - x', y - y', z) dx' dy'} \\ &= C_0(x, y, z)e^{-\frac{\alpha}{v \Delta y} K(x, y, z)}, \end{aligned} \quad (\text{A.4})$$

where, again, the double integral is the convolution of the bleaching geometry and the bleaching intensity distribution:  $K(x, y, z) = B(x, y) \otimes I_b(x, y, z)$ . It is important to realize that Eq. (A.3) is always valid, whereas the continuous approximation Eq. (A.4) will only be valid if the interline distance  $\Delta y$  is sufficiently small compared to the resolution of the bleaching PSF. In the next section, some examples will be given to evaluate the validity of the replacement of the discrete summation by the continuous integral.

Finally, let it be noted, that the above reasoning can easily be extended to three (or more) dimensions.

## A.4 Discrete vs. continuous photobleaching solution

In the previous section it has been shown that bleaching of a 2D geometry by scanning multiple adjacent lines is described by Eq. (A.3). This is the exact discrete solution. It has also been shown that the discrete summation can be replaced by an integral over a continuous variable if the distance between the adjacent lines  $\Delta y$  is sufficiently small, leading to Eq. (A.4). This is the continuous approximation. We will now examine how small  $\Delta y$  has to be, relative to the resolution of the bleaching beam in the focal plane, in order for the continuous approximation Eq. (A.4) to be valid. We will do this for both the modified Gaussian intensity distribution Eq. (B.11) (see section B.2) and the fundamental Gaussian-beam solution Eq. (B.17) (see section B.3), which are identical in the focal plane:

$$I_b(x, y, z = 0) = I_{b,0} e^{-2 \frac{x^2 + y^2}{w_{0,e}^2}}. \quad (\text{A.5})$$

$w_{0,e}$  is called the radial Gaussian resolution of the bleaching beam.

Eqs. (A.3) and (A.4) are identical except for the expressions in the exponent. Therefore we will compare only those two expressions. Let us consider a rectangular bleaching region of width  $b - a$  and length  $l$  ( $a_1 = a_2 = \dots = a_N$  and  $b_1 = b_2 = \dots = b_N$ ) which is bleached by scanning  $N$  lines with a constant laser intensity ( $L(x, y) = 1$  inside the rectangle and  $L(x, y) = 0$  outside). Making use of Eq. (A.5), the exponent in the discrete

case becomes:

$$\begin{aligned}
 \frac{\alpha}{v} K(x, y, z = 0) &= \frac{\alpha}{v} \sum_{i=1}^N \int_a^b I_b(x - x', y - Y + (i - 1)\Delta y, z = 0) dx' \\
 &= \frac{\alpha}{v} I_{b,0} \int_a^b e^{-2\frac{(x-x')^2}{w_{0,e}^2}} dx' \cdot \sum_{i=1}^N e^{-2\frac{(y-Y+(i-1)\Delta y)^2}{w_{0,e}^2}} \\
 &= \frac{\alpha}{v} I_{b,0} \sqrt{\frac{\pi}{8}} w_{0,e} \left[ \operatorname{erf} \left( \sqrt{2} \frac{x - a}{w_{0,e}} \right) - \operatorname{erf} \left( \sqrt{2} \frac{x - (a + b)}{w_{0,e}} \right) \right] \\
 &\quad \cdot \sum_{i=1}^N e^{-2\frac{(y-Y+(i-1)\Delta y)^2}{w_{0,e}^2}}. \tag{A.6}
 \end{aligned}$$

For the exponent in the continuous case we find:

$$\begin{aligned}
 \frac{\alpha}{v\Delta y} K(x, y, z = 0) &= \frac{\alpha}{v\Delta y} \int_{-l/2}^{+l/2} \int_a^b I_b(x - x', y - Y + (i - 1)\Delta y, z = 0) dx' dy' \\
 &= \frac{\alpha}{v\Delta y} I_{b,0} \int_a^b e^{-2\frac{(x-x')^2}{w_{0,e}^2}} dx' \int_{-l/2}^{+l/2} e^{-2\frac{(y-y')^2}{w_{0,e}^2}} dy' \\
 &= \frac{\alpha}{v\Delta y} I_{b,0} \sqrt{\frac{\pi}{8}} w_{0,e} \left[ \operatorname{erf} \left( \sqrt{2} \frac{x - a}{w_{0,e}} \right) - \operatorname{erf} \left( \sqrt{2} \frac{x - (a + b)}{w_{0,e}} \right) \right] \\
 &\quad \cdot \sqrt{\frac{\pi}{8}} w_{0,e} \left[ \operatorname{erf} \left( \sqrt{2} \frac{y + l/2}{w_{0,e}} \right) - \operatorname{erf} \left( \sqrt{2} \frac{y - l/2}{w_{0,e}} \right) \right]. \tag{A.7}
 \end{aligned}$$

By comparing Eqs. (A.6) and (A.7), it is clear that the two expressions that have to be evaluated are:

$$\text{discrete : } \sum_{i=1}^N e^{-2\frac{(y-Y+(i-1)\Delta y)^2}{w_{0,e}^2}} \tag{A.8}$$

$$\text{continuous : } \sqrt{\frac{\pi}{8}} \frac{w_{0,e}}{\Delta y} \left[ \operatorname{erf} \left( \sqrt{2} \frac{y + l/2}{w_{0,e}} \right) - \operatorname{erf} \left( \sqrt{2} \frac{y - l/2}{w_{0,e}} \right) \right] \tag{A.9}$$

## Examples:

All distances will be related to the radial resolution  $w_{e,0}$ . Consider, for example, a rectangle of length  $l = 20w_{0,e}$ . Depending on the value of the inter-line distance  $\Delta y$ , it will take  $N = l/\Delta y + 1$  lines for bleaching of this rectangle. In the examples below we will gradually decrease the inter-line distance  $\Delta y$  and compare both Eq. (A.8) and (Eq. A.9).



- $\Delta y = 5w_{0,y}$  and  $N = 5$ : As can be seen from Fig. A.3A, there is no overlap between the neighbouring bleach lines because of the large inter-line distance. The continuous solution (dashed line) is only a poor approximation of the real situation (solid line).
- $\Delta y = 2w_{0,y}$  and  $N = 11$ : As can be seen from Fig. A.3B, the neighbouring bleach lines will start to overlap when the inter-line distance is reduced. The continuous solution (dashed line), however, still is not a good approximation of the real situation as predicted by the discrete solution (solid line).
- $\Delta y = 1.33w_{0,y}$  and  $N = 16$ : As can be seen from Fig. A.3C, the neighbouring bleach lines are mostly overlapping. The continuous approximation (dashed line) is gradually approaching the discrete solution (solid line).
- $\Delta y = w_{0,y}$  and  $N = 21$ : As can be seen from Fig. A.3D, the individual bleach lines have become nearly indistinguishable. The continuous approximation (dashed line) shows already a good correspondence to the discrete solution (solid line).
- $\Delta y = 0.5w_{0,y}$  and  $N = 41$ : As can be seen from Fig. A.3E, the individual bleach lines cannot be distinguished anymore. The bleaching profile has become uniform (solid line) and is almost identical to the continuous approximation (dashed line).
- $\Delta y = 0.1w_{0,y}$  and  $N = 201$ : When reducing the inter-line distance even further, no difference can be seen any more between the discrete solution (solid line) and the continuous approximation (dashed line).

From these examples we conclude that the continuous solution Eq. (A.4) can be used as a good approximation for the discrete bleaching solution Eq. (A.3) if the inter-line  $\Delta y$  is smaller than the radial Gaussian resolution  $w_{0,e}$ :  $\Delta y \leq w_{0,e}$ .

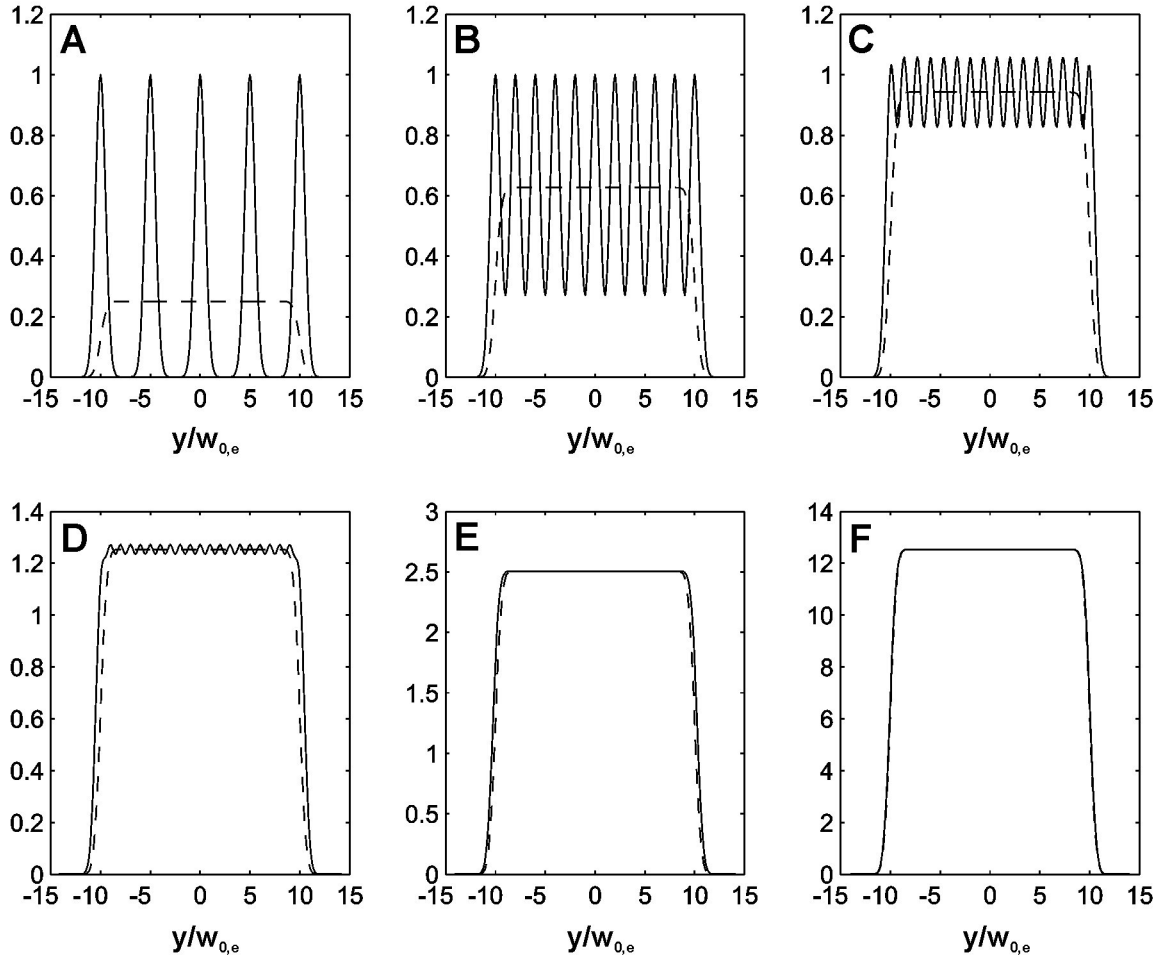


**Figure A.3:** A comparison between Eq. (A.8) (solid line) and (Eq. A.9) (dashed line) for a rectangle of length  $l = 20w_{0,e}$  and different values of the inter-line distance  $\Delta y$ : (A)  $\Delta y = 5w_{0,y}$  and  $N = 5$ , (B)  $\Delta y = 2w_{0,y}$  and  $N = 11$ , (C)  $\Delta y = 1.33w_{0,y}$  and  $N = 16$ , (D)  $\Delta y = w_{0,y}$  and  $N = 21$ , (E)  $\Delta y = 0.5w_{0,y}$  and  $N = 41$ , (F)  $\Delta y = 0.1w_{0,y}$  and  $N = 201$ .

# Appendix B

## The illumination and detection intensity distribution

When carrying out calculations on CSLM based techniques, at some point one evidently comes across the illumination and detection intensity distribution. It is sometimes difficult, though, to choose an appropriate mathematical function for those distributions. Throughout the theoretical work of this thesis, different mathematical descriptions have been chosen for the illumination and detection intensity distributions depending on the context. The different functions are described in this appendix.

### B.1 The three-dimensional light distribution near focus

A detailed description of how the three-dimensional illumination intensity distribution near the focus of a well-corrected lens is calculated, is presented in [150], pp. 484-499. The function that is calculated is the amplitude point spread function (PSF):

$$h(u, v) = -i \frac{2\pi a^2 A}{\lambda f^2} e^{i\left(\frac{f}{a}\right)^2 u} \int_0^1 J_0(v\rho) e^{-\frac{i}{2}u\rho^2} \rho d\rho, \quad (\text{B.1})$$

where, as illustrated in Fig. B.1,  $a$  is the aperture of the objective lens,  $A/f$  is the amplitude of the converging spherical wave emerging from the circular aperture and  $f$  the distance from the center of the aperture to the axial focal point (i.e. point of convergence of the spherical wave). The wavelength  $\lambda = \lambda_0/n$ , where  $\lambda_0$  is the vacuum wavelength and  $n$  the refractive index of the system.  $J_0$  is the zeroth-order Bessel function.  $v$  and  $u$  are

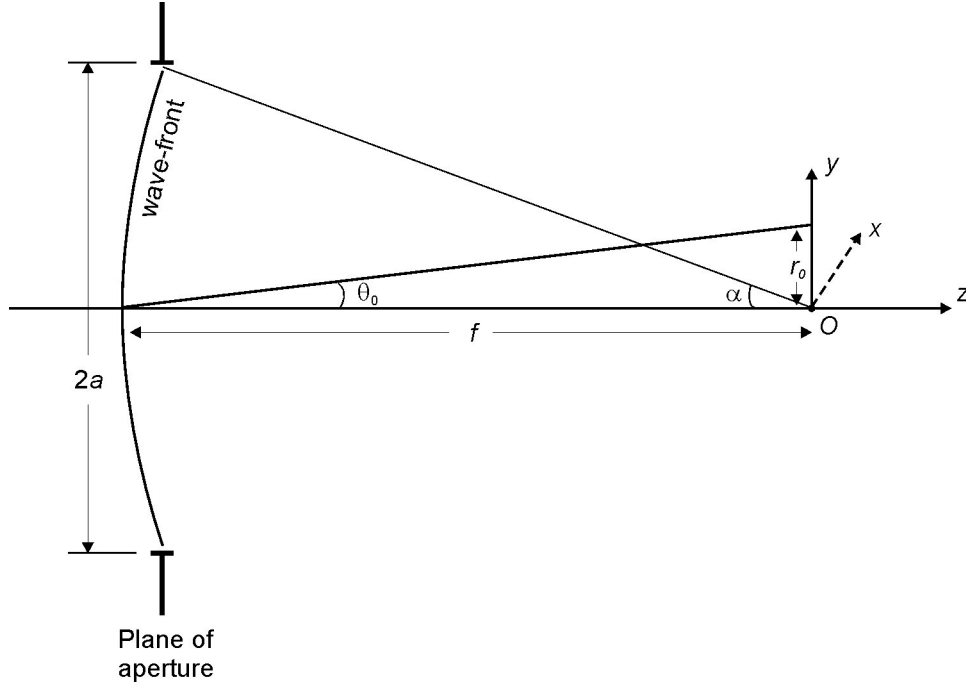


**Figure B.1:** Diffraction of a converging spherical wave at a circular aperture: notation.

normalized optical units perpendicular and parallel to the optical axis, respectively, and are given by:

$$v = \frac{2\pi ar}{\lambda f}, \quad u = \frac{2\pi a^2 z}{\lambda f^2}, \quad (\text{B.2})$$

where  $z$  is the direction of the optical axis and  $r = \sqrt{x^2 + y^2}$  is the lateral distance from the optical axis.

For microscopy it is more convenient to express Eq. (B.1) in terms of the numerical aperture  $\text{NA} = n \sin \alpha$ . The angular radius at which the diffraction pattern in the focal plane becomes zero for the first time (i.e. the first dark ring) is  $\theta_0 = 0.61\lambda/a$  [150], pp. 439-444. According to Fig. B.1, the corresponding radial distance in the focal plane is  $r_0 = f\theta_0$  because  $\theta_0$  is very small ( $\lambda \ll a$ ). At the other hand, it can also be shown that  $r_0 = 0.61\lambda/\sin \alpha$  ([150], pp.466), from which it immediately follows that  $a/f = \sin \alpha$ . Thus we find for Eq. (B.1):

$$h(u, v) = -i \frac{2\pi n A \sin^2 \alpha}{\lambda_0} e^{iu/\sin^2 \alpha} \int_0^1 J_0(v\rho) e^{-\frac{i}{2}u\rho^2} \rho d\rho, \quad (\text{B.3})$$

which is the amplitude PSF as presented in [151], pp. 101-125<sup>1</sup>. For the normalized optical units as defined in Eq. (B.2) we find:

$$v = \frac{2\pi nr \sin \alpha}{\lambda_0}, \quad u = \frac{2\pi nz \sin^2 \alpha}{\lambda_0}. \quad (\text{B.4})$$

For practical purposes it is more convenient to express the parameter  $A$  in terms of the light power  $P$  emerging from the objective lens (which is a measurable quantity). Because the wave-front at the aperture is nearly planar ( $a \ll f$ ), the power incident on the aperture can be calculated from ([150], pp484-499):

$$\begin{aligned} P &= \pi a^2 \left( \frac{A}{f} \right)^2 \\ &= A^2 \pi \sin^2 \alpha, \end{aligned}$$

or

$$A = \frac{\sqrt{P}}{\sqrt{\pi} \sin \alpha}, \quad (\text{B.5})$$

where we have used the previously found result  $a/f = \sin \alpha$ . Substitution of Eq. (B.5) into Eq. (B.6) finally gives:

$$h(u, v) = -i \frac{2\sqrt{\pi P n \sin \alpha}}{\lambda_0} e^{iu/\sin^2 \alpha} \int_0^1 J_0(v\rho) e^{-\frac{i}{2}u\rho^2} \rho \, d\rho. \quad (\text{B.6})$$

The amplitude PSF  $h(u, v)$  of a microscope is related to the strength of the electromagnetic field in the image plane when observing a point like light source. Although it is not possible to observe amplitude fluctuations directly, we can observe the intensity PSF, which is the image formed by the point source in the detector, and can be calculated from the squared modulus of the amplitude PSF:

$$|h(u, v)|^2 = h(u, v)h^*(u, v). \quad (\text{B.7})$$

This equation describes the three-dimensional intensity distribution of a beam of light focused by a lens. It equivalently describes the probability of a photon, emitted from a

---

<sup>1</sup>In this text, it seems that the amplitude parameter  $A$  has mistakenly been referred to as the ‘area of the illumination or detection aperture’.

certain location in the object, hitting a point detector in an image plane of the microscope. In these two senses, the PSFs are referred to as the illumination intensity PSF and detection intensity PSF, respectively. A confocal microscope uses both point wise illumination and point wise detection. The objective lens of a confocal fluorescence microscope forms an image of the illumination point source and the detection pinhole in their common conjugate plane: the object plane. Only the fluorophores that are in the volume shared by the illumination and detection PSFs have a reasonable chance to be both excited and detected. Since the events of excitation and detection are independent, the resulting confocal intensity PSF is the product of the illumination intensity PSF and the detection PSF:

$$|h_{confocal}(x, y, z)|^2 = |h_{det}(x, y, z)|^2 |h_{ill}(x, y, z)|^2. \quad (\text{B.8})$$

The illumination, detection and confocal intensity PSF are shown in Fig. B.2 for an oil immersion ( $n = 1.518$ ) objective lens of NA 1.3 (see figure legend for calculation details). It is important to note from Fig. B.2c that the ‘outward extensions’ of the confocal intensity PSF have a very small value ( $< 0.01$ ). For practical calculations the confocal intensity PSF is therefore often approximated by a Gaussian intensity distribution in both radial and axial directions, which corresponds to the main central oval-shaped part in Fig. B.2c: We will use a Gaussian distribution for the detection PSF:

$$|h_{confocal}(x, y, z)|^2 = I_0 e^{-2\left(\frac{x^2+y^2}{w_d^2} + \frac{z^2}{z_d^2}\right)}, \quad (\text{B.9})$$

where  $w_d$  and  $z_d$  are the radial and axial  $e^{-2}$  radii, which are called *the radial and axial (Gaussian) confocal detection resolution*.

Let us finally consider the illumination intensity in the geometrical focal plane ( $z = 0 \Rightarrow u = 0$ ). The amplitude PSF according to Eq. (B.6) becomes:

$$h(0, v) = -i \frac{2\sqrt{\pi P n \sin \alpha}}{\lambda_0} \int_0^1 J_0(v\rho) \rho d\rho.$$

Using the well-known identity [23]:

$$\int_0^w J_0(v\rho) \rho d\rho = \frac{w}{v} J_1(wv),$$

it follows that:

$$h(0, v) = -i \frac{2\sqrt{\pi P n \sin \alpha}}{\lambda_0} \frac{J_1(v)}{v},$$

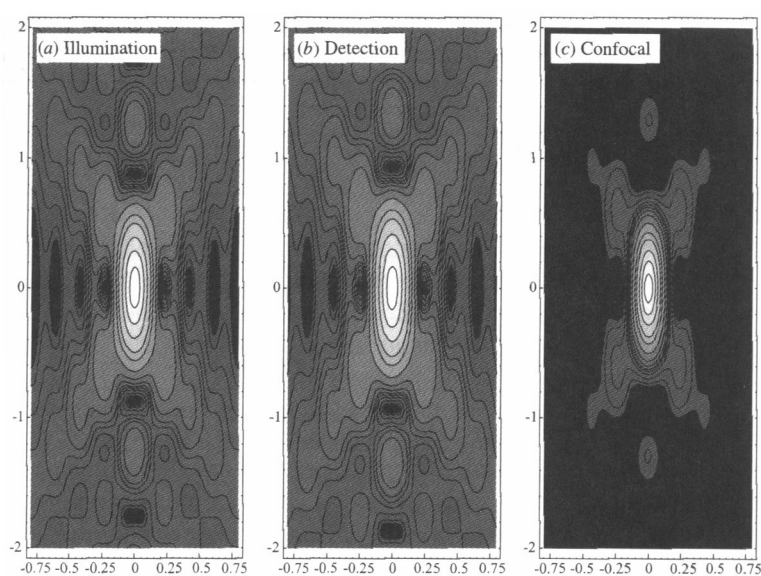


**Figure B.2:** (a) The illumination intensity PSF of a confocal microscope at  $\lambda_{ill} = 488$  nm. (b) The fluorescence detection PSF of a (confocal) microscope at  $\lambda_{ill} = 520$  nm. (c) The product of the illumination and detection PSFs yield the confocal fluorescence PSF. All PSFs are calculated for  $NA = 1.3$ ,  $n = 1.518$ . The contour lines are calculated for intensities of 0.9, 0.7, 0.5, 0.3, 0.2, 0.1, 0.05, 0.03, 0.02, 0.015, 0.01, 0.005, 0.002 and 0.001 (taken from [151], p. 105).

and the intensity illumination PSF in the focal plane becomes:

$$|h(0, v)|^2 = \frac{\pi P n^2 \sin^2 \alpha}{\lambda_0^2} \left[ \frac{2J_1(v)}{v} \right]^2, \quad (\text{B.10})$$

which is the Airy formula for Fraunhofer diffraction at a circular aperture (see, for example, [152]), as was to be expected. As shown in Fig. 2.2, the Airy pattern consists of a bright disc surrounded by concentric bright and dark rings.

## B.2 The modified Gaussian intensity distribution

The illumination intensity PSF near the focus, which follows from Eq. (B.6) and Eq. (B.7), is impractical for analytical calculations<sup>2</sup>. Instead, mathematically more convenient approximative distributions can be chosen, such as the modified Gaussian intensity distribution [31]:

$$I(\mathbf{r}) = I_0 e^{-2\frac{x^2+y^2}{w_e^2(z)}} e^{-2\frac{z^2}{w_{r,e}^2}}, \quad (\text{B.11})$$

where

$$w_e^2(z) = w_{0,e}^2 \left[ 1 + \left( \frac{z}{z_{r,e}} \right)^2 \right] \quad (\text{B.12})$$

and

$$z_{r,e} = \frac{\pi n w_{0,e}^2}{\lambda_e}. \quad (\text{B.13})$$

Although this function does take the conical shape of the focused illumination beam into account, it should be used with care, though, because it does not comply with the law of conservation of energy: an equal amount of energy in all  $xy$ -planes along the optical axis  $z$ . To see this more clearly, we will now integrate Eq. (B.11) in  $x$  and  $y$  over the infinite plane and evaluate the resulting function  $I_{xy}(z)$  along  $z$ :

$$\begin{aligned} I_{xy}(z) &= \int_{-\infty}^{+\infty} \int_{-\infty}^{+\infty} I(x, y, z) \, dx \, dy \\ &= 4I_0 e^{-2\frac{z^2}{w_{r,e}^2}} \int_0^{+\infty} e^{-2\frac{x^2}{w_e^2(z)}} \, dx \int_0^{+\infty} e^{-2\frac{y^2}{w_e^2(z)}} \, dy \\ &= I_0 \frac{\pi}{2} w_e^2(z) e^{-2\frac{z^2}{w_{r,e}^2}}, \end{aligned} \quad (\text{B.14})$$

---

<sup>2</sup>It can be used for numerical computations however.



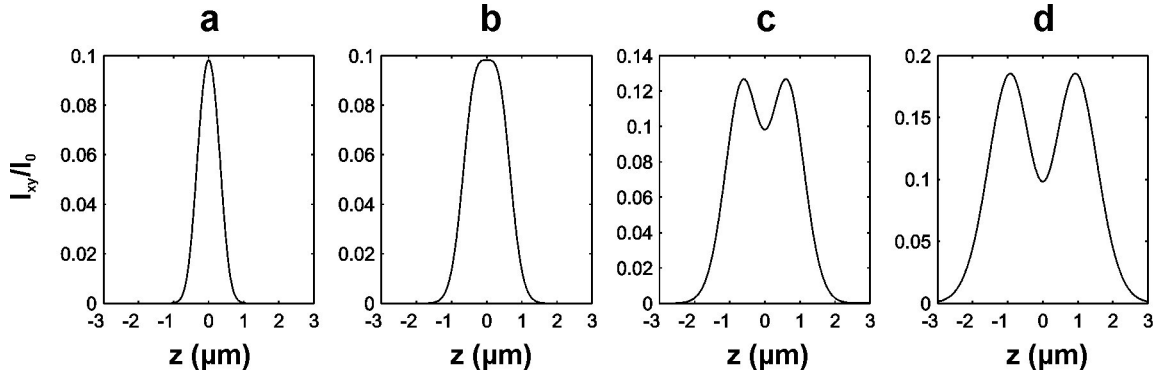


**Figure B.3:** Depending on the relative values of the radial and axial resolution  $w_{0,e}$  and  $w_{z,e}$ , the total amount of light along the optical axis can have one or three extrema according to the modified Gaussian distribution. The calculations are carried out for  $w_{0,e} = 0.25 \mu\text{m}$ ,  $\lambda_e = 0.488 \mu\text{m}$  and (a)  $w_{z,e} = 0.5 \mu\text{m}$ , (b)  $w_{z,e} = 0.757 \mu\text{m}$ , (c)  $w_{z,e} = 1.14 \mu\text{m}$  and (d)  $w_{z,e} = 1.51 \mu\text{m}$ .

where we have made use of the well-known identity  $\int_0^{+\infty} e^{-\eta^2} d\eta = \frac{\sqrt{\pi}}{2}$ . Evidently, Eq. (B.14) is not a constant, as is required by the law of conservation of energy, but a function of  $z$ . By solving  $\frac{d}{dz} I_{xy}(z) = 0$ , we find that  $z = 0$  and  $z = \pm \sqrt{w_{z,e}^2/2 - z_{r,e}^2}$ . This means that  $I_{xy}(z)$  generally has three extrema if  $w_{z,e} > \sqrt{2} \frac{n\pi}{\lambda_e} w_{0,e}^2$ . Some examples are shown in Fig. B.3. Obviously, a situation such as depicted in Fig. B.3c and d, where the focal plane would receive less energy than planes above or below, does not correspond with what is expected in reality. Therefore, the modified Gaussian intensity distribution (B.11) can only be used if the condition

$$w_{z,e} \leq \sqrt{2} \frac{n\pi}{\lambda_e} w_{0,e}^2 \quad (\text{B.15})$$

is met. This is examined for the three objective lenses of our CSLM in section 7.2).

The central intensity  $I_0$  is usually calculated from:

$$P = \int_{-\infty}^{+\infty} \int_{-\infty}^{+\infty} I(x, y, z) dx dy = I_{xy},$$

where  $P$  is the laser power in the sample, which is a constant.  $I_{xy}$  is not a constant though for the modified Gaussian intensity distribution, as is clear from Eq. (B.14), but is dependent on the position  $z$  along the optical axis. It is therefore necessary to make an additional assumption in this case to calculate  $I_0$  as a function of  $P$ . We will assume that

the power in the focal plane is equal to the laser power  $P$  in the sample  $P = I_{xy}(0)$ , from which it follows that:

$$I_0 = \frac{2P}{\pi w_{0,e}^2}. \quad (\text{B.16})$$

Eq. (B.16) corresponds to what is expected intuitively: the smaller the spot size in the focal plane, the higher the local intensity will be.

### B.3 The fundamental Gaussian-beam solution

The illumination intensity PSF as described in section B.1 is valid for nearly planar waves incident on the back aperture of the objective lens. On a confocal microscope this condition is generally fulfilled for lenses of high NA and high magnification, where the incident laser beam is overfilling the back aperture. Lenses of low magnification and low NA, at the other hand, often have a larger back aperture. In that case, the incident laser beam might be seriously underfilling the back aperture, as is the case for our  $10\times$  NA0.45 objective lens on the Bio-Rad MRC1024 confocal microscope. Since the incident laser beam usually has a Gaussian intensity distribution, it is more appropriate in that case to use the theory of the propagation of Gaussian laser beams. A rigorous treatment of this subject can be found in [153], which leads to the result (for a homogeneous medium):

$$I = I_0 \left( \frac{w_{0,e}}{w_e(z)} \right)^2 e^{-2\frac{x^2+y^2}{w_e(z)^2}}, \quad (\text{B.17})$$

where  $w_e(z)^2 = w_{0,e}^2(1 + z^2/z_{r,e}^2)$  and  $z_{r,e} = \pi w_{0,e}^2 n / \lambda_e$  ( $n$  is the refractive index of the medium). Eq. (B.17) is called the fundamental Gaussian-beam solution (of the Maxwell equations) and is valid as a paraxial approximation. This means it is valid for beams that have a small angular divergence. Hence, Eq. (B.17) can be used to describe the illumination intensity distribution for low NA objective lenses, especially when the laser beam is underfilling the back aperture of the objective lens. However, as will be demonstrated in Chapter 7, it is a valid description of the illumination intensity distribution of all three objective lenses. Unlike the modified Gaussian intensity distribution, it does meet the physical requirement of a constant laser power along the optical axis:

$$P = I_{xy} = I_0 \frac{\pi}{2} w_{0,e}^2,$$

from which it immediately follows that:

$$I_0 = \frac{2P}{\pi w_{0,e}^2}. \quad (\text{B.18})$$

# Appendix C

## Mathematical derivation of the FRAP disk model

### C.1 Diffusion after bleaching of a uniform disk

First consider an arbitrary axially symmetric initial concentration distribution  $f(r, z)$ . Fick's second law Eq. (1.14) can be solved by first applying a Hankel transform to the radial coordinate  $r$ , followed by a Fourier transform to the axial coordinate  $z$ , finally leading to the general solution (see ref. Crank):

$$C(r, z, t) = \frac{1}{4\sqrt{\pi}(Dt)^{3/2}} \int_{z'=-\infty}^{+\infty} \int_{r'=0}^{+\infty} r' f(r', z') e^{-\frac{(z-z')^2}{4Dt}} e^{-\frac{r^2+r'^2}{4Dt}} I_0\left(\frac{rr'}{2Dt}\right) dr' dz', \quad (\text{C.1})$$

where  $I_0$  is the zero order modified Bessel function. To know the fluorophore concentration at a time  $t$  after bleaching of a uniform disk, Eq. (C.1) has to be solved for the initial condition Eq. (1.9). It is somewhat more convenient to continue with the concentration of bleached molecules  $C^*(r, z, t)$ , which is related to the concentration of unbleached fluorophores  $C(r, z, t)$  through:

$$C(r, z, t) + C^*(r, z, t) = C_0(r, z, t). \quad (\text{C.2})$$

By substituting Eq. (C.2) in Eq. (1.9), the initial condition for the bleached fluorophores becomes:

$$C_b^*(r, z) = \begin{cases} C_0(r, z) \left(1 - e^{-K_0 e^{-2z^2/z_0^2}}\right) & \text{if } r \leq w \\ 0 & \text{if } r > w. \end{cases} \quad (\text{C.3})$$

From Eqs. (C.1) and (C.3) it follows that the diffusion process of the bleached molecules can be calculated from:

$$\begin{aligned}
 C^*(r, z, t) = & \underbrace{\frac{1}{2\sqrt{\pi Dt}} \int_{z'=-\infty}^{+\infty} C_0(r, z) \left(1 - e^{-K_0 e^{-2z^2/z_0^2}}\right) e^{-\frac{(z-z')^2}{4Dt}} dz'}_{\text{I}} \\
 & \cdot \frac{1}{2Dt} e^{-\frac{r^2}{4Dt}} \int_{r'=0}^w e^{-\frac{r'^2}{4Dt}} I_0\left(\frac{rr'}{2Dt}\right) r' dr'.
 \end{aligned} \tag{C.4}$$

Assuming that the fluorophores before bleaching are uniformly distributed, i.e.  $C_0$  is a constant independent of the spatial coordinates, the integral over  $z'$  becomes:

$$\begin{aligned}
 \text{I} &= \frac{C_0}{2\sqrt{\pi Dt}} \left( \int_{z'=-\infty}^{+\infty} e^{-\frac{(z-z')^2}{4Dt}} dz' - \int_{z'=-\infty}^{+\infty} e^{-K_0 e^{-z'^2/z_0^2}} e^{-\frac{(z-z')^2}{4Dt}} dz' \right) \\
 &= \frac{C_0}{2\sqrt{\pi Dt}} \left( 2\sqrt{\pi Dt} - \underbrace{\sum_{n=0}^{+\infty} \frac{(-K_0)^n}{n!} \int_{z'=-\infty}^{+\infty} e^{-2n\frac{z'^2}{z_0^2}} e^{-\frac{(z-z')^2}{4Dt}} dz'}_{\text{II}} \right),
 \end{aligned} \tag{C.5}$$

where  $e^{-K_0 e^{-z'^2/z_0^2}}$  was expanded<sup>1</sup> into  $\sum_{n=0}^{+\infty} \frac{(-K_0)^n}{n!} e^{-2n\frac{z'^2}{z_0^2}}$ . Finding a solution for the integral II is not trivial and will therefore be outlined below. The integral to be solved is of the type:

$$\int_{-c}^{+c} e^{-az'^2 - b(z-z')^2} dz', \tag{C.6}$$

with parameters  $a, b \geq 0$ . The trick is to find a suitable substitution. The integral could be solved if a substitution  $z' \rightarrow u$  could be found for which the mantissa reduces to  $-u^2 + Bz^2$ . To find this substitution, we therefore solve the equation:

$$-az'^2 - b(z-z')^2 = -u^2 + Bz^2 \quad \Leftrightarrow \quad (a+b)z'^2 - 2bzz' + (B+b)z^2 = u^2.$$

By choosing  $B = -\frac{ab}{a+b}$ , this reduces to:

$$\left( z' \sqrt{a+b} - \frac{b}{\sqrt{a+b}} \right)^2 = u^2.$$

---

<sup>1</sup>making use of  $e^x = \sum_{n=0}^{+\infty} \frac{x^n}{n!}$

Thus, by carrying out the substitution  $u = z'\sqrt{a+b} - \frac{b}{\sqrt{a+b}}$ , the mantissa reduces to  $-u^2 - \frac{ab}{a+b}z^2$ , and  $dz' = \frac{du}{\sqrt{a+b}}$ . The integral becomes:

$$\begin{aligned} \int_{-c}^{+c} e^{-az'^2 - b(z-z')^2} dz' &= \frac{1}{\sqrt{a+b}} \int_{-\frac{(a+b)c-bz}{\sqrt{a+b}}}^{\frac{(a+b)c+bz}{\sqrt{a+b}}} e^{-u^2 - \frac{ab}{a+b}z^2} du \\ &= \frac{\sqrt{\pi} e^{-\frac{ab}{a+b}z^2}}{2\sqrt{a+b}} \left[ \operatorname{erf} \left( \frac{(a+b)c - bz}{\sqrt{a+b}} \right) + \operatorname{erf} \left( \frac{(a+b)c + bz}{\sqrt{a+b}} \right) \right]. \end{aligned} \quad (\text{C.7})$$

For  $c = +\infty$ , this reduces to ( $a, b \geq 0$ ):

$$\int_{-\infty}^{+\infty} e^{-az'^2 - b(z-z')^2} dz' = \sqrt{\frac{\pi}{a+b}} e^{-\frac{ab}{a+b}z^2}, \quad (\text{C.8})$$

since  $\operatorname{erf}(+\infty) = 1$ . For  $a = 2n/z_0^2$  and  $b = 1/(4Dt)$ , integral II from Eq. (C.5) finally becomes:

$$\text{II} = \sqrt{\frac{4\pi Dt z_0^2}{8nDt + z_0^2}} e^{-\frac{2nz^2}{8nDt + z_0^2}},$$

and Eq. (C.5) becomes:

$$\text{I} = C_0 \left( 1 - \sum_{n=0}^{+\infty} \frac{(-K_0)^n e^{-\frac{2nz^2}{z_0^2(a_n-n)}}}{n! \sqrt{a_n - n}} \right), \quad (\text{C.9})$$

where we have defined  $a_n = 1 + n(1 + 2t/\tau_z)$  and  $\tau_z = z_0^2/4D$ .  $\tau_z$  is called the *axial characteristic diffusion time*. Eq. (C.4) finally becomes:

$$\begin{aligned} C^*(r, z, t) &= C_0 \left( 1 - \sum_{n=0}^{+\infty} \frac{(-K_0)^n e^{-\frac{2nz^2}{z_0^2(a_n-n)}}}{n! \sqrt{a_n - n}} \right) \\ &\quad \cdot \frac{1}{2Dt} e^{-\frac{r^2}{4Dt}} \int_{r'=0}^w e^{-\frac{r'^2}{4Dt}} \text{I}_0 \left( \frac{rr'}{2Dt} \right) r' dr'. \end{aligned} \quad (\text{C.10})$$

From Eq. (C.10) the concentration distribution of bleached fluorophores can be calculated at a time  $t$  after bleaching of a uniform disk of radius  $w$  with a bleaching beam of negligible radial resolution and Gaussian axial profile of resolution  $z_0$ .

## C.2 Fluorescence recovery after photobleaching of a uniform disk as observed by the CSLM

In FRAP we are interested in finding an expression that tells us how the fluorescence inside the disk will recover due to diffusion after photobleaching. It has to be realized, however, that the fluorescence that is observed experimentally with the CSLM does not directly reflect the concentration of the fluorophores. In general, any object that is observed by a lens-based system, such as a microscope, will be ‘deformed’ by that system’s detection point-spread function:  $I_d(x, y, z)$ . The detection PSF expresses how the light from a point source will be observed. For a more detailed discussion about the confocal detection PSF, the reader is referred to Appendix B, section B.1. The fluorescence image  $F(x, y, z, t)$  of the real concentration distribution  $C(x, y, z, t)$  will therefore be the result of the convolution product of  $I_d(x, y, z)$  and  $C(x, y, z, t)$ :

$$\begin{aligned} F(x, y, z, t) &= \int_{-\infty}^{+\infty} \int_{-\infty}^{+\infty} \int_{-\infty}^{+\infty} I_d(x', y', z') C(x - x', y - y', z - z', t) dx' dy' dz' \\ &= I_d(x, y, z) \otimes C(x, y, z, t). \end{aligned} \quad (\text{C.11})$$

We will now show that, again if the radial resolution of the detection PSF is much smaller than the disk’s radius  $w$ , the total observed fluorescence within the disk can be calculated as if the detection PSF is stationary at the disk’s position and has a uniform intensity distribution of radius  $w$ , i.e.

$$F_{tot}(t) = 2\pi \int_{z=-\infty}^{+\infty} \int_{r=0}^{+\infty} r I_d(r, z) C(r, z, t) dr dz, \quad (\text{C.12a})$$

with

$$I_d(r, z) = \begin{cases} I_{0d} Z(z) & \text{if } r \leq w \\ 0 & \text{if } r > w. \end{cases} \quad (\text{C.12b})$$

The function  $Z(z)$  expresses the axial intensity distribution of the detection PSF. This can be shown as follows. As said, we will consider a detection PSF which has a negligible radial resolution:  $I_d(x, y, z) = I_{0d} \delta(x, y) Z(z)$ . The observed fluorescence can be calculated from Eq. (C.11):

$$F(x, y, z, t) = I_{0d} \int_{-\infty}^{+\infty} \int_{-\infty}^{+\infty} \int_{-\infty}^{+\infty} \delta(x', y') Z(z') C(x - x', y - y', z - z', t) dx' dy' dz',$$

which, by making use of the property  $\int_{-\infty}^{+\infty} f(x)\delta(x)dx = f(0)$ , simplifies to:

$$F(x, y, z, t) = I_{0d} \int_{-\infty}^{+\infty} Z(z')C(x, y, z - z', t) dz'.$$

The total fluorescence within a disk of radius  $w$ , observed in the focal plane ( $z = 0$ ) is therefore:

$$F_{tot} = I_{0d} \iint_{\text{disk}} \int_{z'=-\infty}^{+\infty} Z(z')C(x, y, -z', t) dz' dx dy.$$

By making the substitution  $z = -z'$  and switching to cylindrical coordinates, it is finally found for a radial-symmetric concentration distribution  $C(r, z, t)$ :

$$F_{tot} = 2\pi I_{0d} \int_{z=-\infty}^{+\infty} \int_{r=0}^w rZ(z)C(r, z, t) dr dz,$$

q.e.d.

By combining Eqs. (C.10), (C.2) and (C.12) it follows that the total fluorescence within the disk, as observed in the focal plane by  $I_d$  according to Eq. (1.15), can be calculated from:

$$F_{tot}(t) = F_0 - 2\pi I_{0d} C_0 \underbrace{\int_{z=-\Delta z_0}^{+\Delta z_0} \left( 1 - \sum_{n=0}^{+\infty} \frac{(-K_0)^n e^{-\frac{2nz^2}{z_0^2(a_n-n)}}}{n! \sqrt{a_n-n}} \right) e^{-2z^2/z_0^2} dz}_{\text{III}} \cdot \underbrace{\frac{1}{2Dt} \int_{r=0}^w r e^{-\frac{r^2}{4Dt}} \int_{r'=0}^w e^{-\frac{r'^2}{4Dt}} I_0 \left( \frac{rr'}{2Dt} \right) r' dr' dr}_{\text{IV}}, \quad (\text{C.13})$$

where, in analogy with (ref Blonk) the finite size of the confocal pinhole for the fluorescence detection is taken into account by eliminating all light from planes above  $z = \Delta z_0$ ) and below  $z = -\Delta z_0$ .  $F_0$  is the fluorescence signal inside the disk before bleaching as measured by the CSLM. We will now calculate parts III and IV separately. After some straightforward manipulation, part III becomes:

$$\text{III} = - \sum_{n=1}^{+\infty} \frac{(-K_0)^n}{n!} \sqrt{\frac{\pi}{2a_n}} z_0 \operatorname{erf} \left( \sqrt{\frac{2a_n}{a_n-n}} \frac{\Delta z_0}{z_0} \right). \quad (\text{C.14})$$

To find a solution for part IV, we will follow the method as outlined by (ref Soumpasis). First we make use of the identity:

$$\frac{1}{2\gamma} e^{-\frac{\alpha^2 + \beta^2}{4\gamma}} I_\nu \left( \frac{\alpha\beta}{2\gamma} \right) = \int_0^{+\infty} \sigma J_\nu(\sigma\alpha) J_\nu(\sigma\beta) e^{-\gamma\sigma^2} d\sigma. \quad (\text{C.15})$$

For  $\alpha = r$ ,  $\beta = r'$  and  $\gamma = Dt$ , part IV becomes:

$$\text{IV} = \int_{r=0}^w \int_{r'=0}^w r r' \int_{\sigma=0}^{+\infty} \sigma J_0(\sigma r) J_0(\sigma r') e^{-Dt\sigma^2} d\sigma dr' dr.$$

Making use of the identity:

$$\int_0^w r' J_0(\sigma r') dr' = \frac{w}{\sigma} J_1(\sigma r), \quad (\text{C.16})$$

it follows that:

$$\text{IV} = \int_{\sigma=0}^{+\infty} \int_{r=0}^w r \sigma \frac{w}{\sigma} J_0(\sigma r) J_1(w\sigma) e^{-Dt\sigma^2} d\sigma dr.$$

Applying identity (C.16) again yields:

$$\begin{aligned} \text{IV} &= w^2 \int_{\sigma=0}^{+\infty} \frac{1}{\sigma} J_1^2(w\sigma) e^{-Dt\sigma^2} d\sigma \\ &= g(t). \end{aligned} \quad (\text{C.17})$$

Differentiating Eq. (C.17) with respect to time gives:

$$\frac{dg(t)}{dt} = -Dw^2 \int_{\sigma=0}^{+\infty} \sigma J_1^2(w\sigma) e^{-Dt\sigma^2} d\sigma,$$

and by applying identity (C.15) we obtain:

$$\frac{dg(t)}{dt} = -\frac{w^2}{2t} e^{-2\tau_r/t} I_1 \left( 2\frac{\tau_r}{t} \right),$$

where  $\tau_r = \frac{w^2}{4D}$  is the radial characteristic diffusion time. By integrating from  $t$  to  $+\infty$ , we find:

$$g(+\infty) - g(t) = -\frac{w^2}{2} \int_t^{+\infty} e^{-2\tau_r/t} I_1 \left( 2\frac{\tau_r}{t} \right) \frac{dt}{t},$$



and finally

$$\begin{aligned}
 g(t) &= g(+\infty) + \frac{w^2}{2} \int_0^{2\tau_r/t} I_1(\zeta) e^{-\zeta} \frac{d\zeta}{\zeta} \\
 &= g(+\infty) + \frac{w^2}{2} \left( 1 - e^{-2\tau_r/t} \left[ I_0 \left( 2\frac{\tau_r}{t} \right) + I_1 \left( 2\frac{\tau_r}{t} \right) \right] \right).
 \end{aligned} \tag{C.18}$$

By substituting Eqs. (C.14) and (C.18) into Eq. (C.13) we obtain for the total fluorescence inside the disk:

$$\begin{aligned}
 F_{tot}(t) &= F_0 + 2\pi I_{0d} C_0 z_0 \sqrt{\frac{\pi}{2}} \sum_{n=1}^{+\infty} \left[ \frac{(-K_0)^n}{n!} \frac{1}{\sqrt{a_n}} \operatorname{erf} \left( \sqrt{\frac{2a_n}{a_n - n}} \frac{\Delta z_0}{z_0} \right) \right] \\
 &\quad \cdot \left[ g(+\infty) + \frac{w^2}{2} \left( 1 - e^{-2\tau_r/t} \left[ I_0 \left( 2\frac{\tau_r}{t} \right) + I_1 \left( 2\frac{\tau_r}{t} \right) \right] \right) \right].
 \end{aligned} \tag{C.19}$$

$g(+\infty)$  in Eq. C.19 can be determined as follows. Until now we have been considering diffusion in a system in which all molecules are mobile. This means that the recovery inside the bleached disk will be complete after an infinite time, i.e.  $F_{tot}(+\infty) = F_0$ . Since  $I_0(0) = 1$  and  $I_1(0) = 0$ , it follows immediately from Eq. C.19 that  $g(+\infty) = 0$ . We now calculate the fluorescence inside the disk before bleaching:

$$\begin{aligned}
 F_0 &= 2\pi I_{0d} \int_{z=-\Delta z_0}^{\Delta z_0} \int_{r=0}^w C_0 e^{-2z^2/z_0^2} r \, dr \, dz \\
 &= \pi I_{0d} C_0 w^2 z_0 \sqrt{\frac{\pi}{2}} \operatorname{erf} \left( \sqrt{2} \frac{\Delta z_0}{z_0} \right).
 \end{aligned} \tag{C.20}$$

Combining Eqs. (C.19) and (C.20) we finally obtain the fluorescence inside the disk at a time  $t$  after bleaching as observed by the CSLM in the focal plane:

$$\begin{aligned}
 \frac{F_{tot}(t)}{F_0} &= 1 + \frac{1}{\operatorname{erf} \left( \sqrt{2} \frac{\Delta z_0}{z_0} \right)} \sum_{n=1}^{+\infty} \left[ \frac{(-K_0)^n}{n!} \frac{1}{\sqrt{a_n}} \operatorname{erf} \left( \sqrt{\frac{2a_n}{a_n - n}} \frac{\Delta z_0}{z_0} \right) \right] \\
 &\quad \cdot \left( 1 - e^{-2\tau_r/t} \left[ I_0 \left( 2\frac{\tau_r}{t} \right) + I_1 \left( 2\frac{\tau_r}{t} \right) \right] \right),
 \end{aligned} \tag{C.21}$$

where  $a_n = 1 + n \left( 1 + \frac{2t}{\tau_z} \right)$ ,  $\tau_z = \frac{z_0^2}{4D}$  (the axial characteristic diffusion time) and  $\tau_r = \frac{w^2}{4D}$  (the radial characteristic diffusion time). To take a mobile fraction  $k$  into account,  $F_{tot}$  according to Eq. (C.21) has to be substituted into the right part of:

$$F_{tot}(t) = F_{tot}(0) + k(F_{tot}(t) - F_{tot}(0)).$$

For numerical computations, however, there will be a problem calculating  $F_{tot}(0)$  using Eq. (C.21) directly. We will therefore calculate  $F_{tot}(0)$  separately, which can be done by considering the large argument asymptotic expansion of the radial part (see ref Soumpasis):

$$\begin{aligned} & 1 - e^{-2\tau_r/t} \left[ I_0 \left( 2\frac{\tau_r}{t} \right) + I_1 \left( 2\frac{\tau_r}{t} \right) \right] \\ &= \sqrt{\frac{t}{4\pi\tau_r}} \left( 2 - \frac{1}{2} \left( \frac{t}{4\tau_r} \right) - \frac{3}{16} \left( \frac{t}{4\tau_r} \right)^2 - \frac{15}{64} \left( \frac{t}{4\tau_r} \right)^3 - \dots \right) \quad \text{if } t \ll \tau_r, \quad (\text{C.22}) \end{aligned}$$

from which it follows that the radial part reduces to 0 at  $t = 0$ . Thus we obtain for the fluorescence right after bleaching:

$$\frac{F_{tot}(0)}{F_0} = 1 + \frac{1}{\text{erf} \left( \sqrt{2} \frac{\Delta z_0}{z_0} \right)} \sum_{n=1}^{+\infty} \left[ \frac{(-K_0)^n}{n!} \frac{1}{\sqrt{1+n}} \text{erf} \left( \sqrt{2(1-n)} \frac{\Delta z_0}{z_0} \right) \right]. \quad (\text{C.23})$$

Eq. (C.23) has to be used in numerical computations to calculate  $F_{tot}(0)$ .

# Bibliography

- [1] T. K. L. Meyvis, S. C. De Smedt, P. Van Oostveldt, and J. Demeester. Fluorescence recovery after photobleaching: A versatile tool for mobility and interaction measurements in pharmaceutical research. *Pharm. Res.*, **16**:1153–1162, 1999.
- [2] R. G. Crystal. The gene as the drug. *Nat. Med.*, **1**:15–17, 1995.
- [3] M. J. Cho and R. Juliano. Macromolecular versus small-molecule therapeutics: Drug discovery, development and clinical considerations. *Trends Biotechnol.*, **14**:153–158, 1996.
- [4] Y. Y. Rojanasakul. Antisense oligonucleotide therapeutics: Drug delivery and targeting. *Adv. Drug Deliv. Rev.*, **18**:115–131, 1996.
- [5] J. G. Weers. Colloidal particles in drug delivery. *Curr. Opin. Colloid Interface S.*, **3**:540–544, 1998.
- [6] V. P. Torchilin. Drug targeting. *Eur. J. Pharm. Sci.*, **11**:S81–S91, 2000.
- [7] N. N. Sanders, S. C. De Smedt, and J. Demeester. The physical properties of biogels and their permeability for macromolecular drugs and colloidal drug carriers. *J. Pharm. Sci.*, **89**:835–849, 2000.
- [8] N. N. Sanders, E. Van Rompaey, S. C. De Smedt, and J. Demeester. Structural alterations of gene complexes by cystic fibrosis sputum. *Amer. J. Respir. Crit. Care Med.*, **164**:486–493, 2001.
- [9] N. N. Sanders, E. Van Rompaey, S. C. De Smedt, and J. Demeester. On the transport of lipoplexes through cystic fibrosis sputum. *Pharm. Res.*, **19**:451–456, 2002.
- [10] N. N. Sanders, S. C. De Smedt, S. H. Cheng, and J. Demeester. Pegylated GL67 lipoplexes retain their gene transfection activity after exposure to components of CF mucus. *Gene Therapy*, **9**:363–371, 2002.
- [11] E. Brown, A. Pluen, C. Compton, Y. Boucher, and R. K. Jain. Measurement of diffusion coefficients in spontaneous human tumors. *Faseb Journal*, **14**:A167, 2000.
- [12] A. Pluen, Y. Boucher, S. Ramanujan, T. D. McKee, T. Gohongi, E. di Tomaso, E. B. Brown, Y. Izumi, R. B. Campbell, D. A. Berk, and R. K. Jain. Role of tumor-host interactions in interstitial diffusion of macromolecules: Cranial vs. subcutaneous tumors. *Proc. Natl. Acad. Sci. USA*, **98**:4628–4633, 2001.

- [13] S. Ramanujan, A. Pluen, T. D. McKee, E. B. Brown, Y. Boucher, and R. K. Jain. Diffusion and convection in collagen gels: Implications for transport in the tumor interstitium. *Biophys. J.*, **83**:1650–1660, 2002.
- [14] R. B. Campbell, D. Fukumura, E. B. Brown, L. M. Mazzola, Y. Izumi, R. K. Jain, V. P. Torchilin, and L. L. Munn. Cationic charge determines the distribution of liposomes between the vascular and extravascular compartments of tumors. *Cancer Res.*, **62**:6831–6836, 2002.
- [15] M Edidin. Translational diffusion of membrane proteins. In P. Yeagle, editor, *The Structure of Biological Membranes*, pages 539–572. CRC Press, Boca Raton, FL, 1992.
- [16] A. Ishihara and K. Jacobson. A closer look at how membrane-proteins move. *Biophys. J.*, **65**:1754–1755, 1993.
- [17] O. Seksek, J. Biwersi, and A. S. Verkman. Translational diffusion of macromolecule-sized solutes in cytoplasm and nucleus. *J. Cell Biol.*, **138**:131–142, 1997.
- [18] F. Umenishi, J. M. Verbavatz, and A. S. Verkman. cAMP regulated membrane diffusion of a green fluorescent protein-aquaporin 2 chimera. *Biophys. J.*, **78**:1024–1035, 2000.
- [19] S. R. Chary and R. K. Jain. Direct measurement of interstitial convection and diffusion of albumin in normal and neoplastic tissues by fluorescence photobleaching. *Proc. Natl. Acad. Sci. USA*, **86**:5385–5389, 1989.
- [20] W. M. Saltzman, M. L. Radomsky, K. J. Whaley, and R. A. Cone. Antibody diffusion in human cervical-mucus. *Biophys. J.*, **66**:508–515, 1994.
- [21] S. S. Olmsted, J. L. Padgett, A. I. Yudin, K. J. Whaley, T. R. Moench, and R. A. Cone. Diffusion of macromolecules and virus-like particles in human cervical mucus. *Biophys. J.*, **81**:1930–1937, 2001.
- [22] D. Axelrod, D. E. Koppel, J. Schlessinger, E. Elson, and W. W. Webb. Mobility measurement by analysis of fluorescence photobleaching recovery kinetics. *Biophys. J.*, **16**:1055–1069, 1976.
- [23] D. M. Soumpasis. Theoretical-analysis of fluorescence photobleaching recovery experiments. *Biophys. J.*, **41**:95–97, 1983.
- [24] A. Lopez, L. Dupou, A. Altibelli, J. Trotard, and J. F. Toccanne. Fluorescence recovery after photobleaching (FRAP) experiments under conditions of uniform disk illumination - critical comparison of analytical solutions, and a new mathematical method for calculation of diffusion coefficient-d. *Biophys. J.*, **53**:963–970, 1988.
- [25] T. T. Tsay and K. A. Jacobson. Spatial FOURIER-analysis of video photobleaching measurements - principles and optimization. *Biophys. J.*, **60**:360–368, 1991.
- [26] D. A. Berk, F. Yuan, M. Leunig, and R. K. Jain. Fluorescence photobleaching with spatial FOURIER-analysis - measurement of diffusion in light-scattering media. *Biophys. J.*, **65**:2428–2436, 1993.

- [27] G. W. Gordon, B. Chazotte, X. F. Wang, and B. Herman. Analysis of simulated and experimental fluorescence recovery after photobleaching - data for 2 diffusing components. *Biophys. J.*, **68**:766–778, 1995.
- [28] U. Kubitscheck, P. Wedekind, and R. Peters. Lateral diffusion measurement at high-spatial-resolution by scanning microphotolysis in a confocal microscope. *Biophys. J.*, **67**:948–956, 1994.
- [29] P. Wedekind, U. Kubitscheck, and R. Peters. Scanning microphotolysis - a new photobleaching technique based on fast intensity modulation of a scanned laser-beam and confocal imaging. *J. Microsc.*, **176**:23–33, 1994.
- [30] P. Wedekind, U. Kubitscheck, O. Heinrich, and R. Peters. Line-scanning microphotolysis for diffraction-limited measurements of lateral diffusion. *Biophys. J.*, **71**:1621–1632, 1996.
- [31] U. Kubitscheck, P. Wedekind, and R. Peters. Three-dimensional diffusion measurements by scanning microphotolysis. *J. Microsc.*, **192**:126–138, 1998.
- [32] R. Peters and U. Kubitscheck. Scanning microphotolysis: Three-dimensional diffusion measurement and optical single-transporter recording. *Methods*, **18**:508–517, 1999.
- [33] J. C. G. Blonk, A. Don, H. Van Aalst, and J. J. Birmingham. Fluorescence photobleaching recovery in the confocal scanning light-microscope. *J. Microsc.*, **169**:363–374, 1993.
- [34] J. Crank. *The Mathematics of Diffusion*. Clarendon Press, Oxford, UK, 2 edition, 1975.
- [35] S. C. De Smedt, A. Lauwers, J. Demeester, Y. Engelborghs, G. Demey, and M. Du. Structural information on hyaluronic-acid solutions as studied by probe diffusion experiments. *Macromolecules*, **27**:141–146, 1994.
- [36] S. C. De Smedt. *De invloed van het netwerk in hyaluronzuur-oplossingen en dextrans-glycosidymethacrylaat-hydrogelen op de diffusie van macromoleculen*. Ph.d. thesis, Ghent University, 1995.
- [37] J. E. Scott. The chemical morphology of the vitreous. *Eye*, **6**:553–555, 1992.
- [38] L. Lapcik, S. De Smedt, J. Demeester, and P. Chabreck. Hyaluronan: Preparation, structure, properties, and applications. *Chem. Rev.*, **98**:2663–2684, 1998.
- [39] T. J. Feder, I. BrustMascher, J. P. Slattery, B. Baird, and W. W. Webb. Constrained diffusion or immobile fraction on cell surfaces: A new interpretation. *Biophys. J.*, **70**:2767–2773, 1996.
- [40] Y. Cheng, R. K. Prud'homme, and J. L. Thomas. Diffusion of mesoscopic probes in aqueous polymer solutions measured by fluorescence recovery after photobleaching. *Macromolecules*, **35**:8111–8121, 2002.
- [41] G. Carrero, D. McDonald, E. Crawford, G. de Vries, and M. J. Hendzel. Using FRAP and mathematical modeling to determine the in vivo kinetics of nuclear proteins. *Methods*, **29**:14–28, 2003.

- [42] K. Braeckmans, L. Peeters, N. N. Sanders, S. C. De Smedt, and J. Demeester. Three-dimensional fluorescence recovery after photobleaching with the confocal scanning laser microscope. *Biophys. J.*, **85**:2240–2252, 2003.
- [43] L. S. Cutts, P. A. Robberts, J. Adler, M. C. Davies, and C. D. Melia. Determination of localized diffusion-coefficients in gels using confocal scanning laser microscopy. *J. Microsc.*, **180**:131–139, 1995.
- [44] C. Dietrich, R. Merkel, and R. Tampe. Diffusion measurement of fluorescence-labeled amphiphilic molecules with a standard fluorescence microscope. *Biophys. J.*, **72**:1701–1710, 1997.
- [45] A. S. Verkman. Diffusion in cells measured by fluorescence recovery after photobleaching. In G. Marriott and I. Parker, editors, *Biophotonics, Part A: Methods in Enzymology*, volume 360, pages 635–648. Academic Press, New York, 2003.
- [46] L. L. Song, E. J. Hennink, I. T. Young, and H. J. Tanke. Photobleaching kinetics of fluorescein in quantitative fluorescence microscopy. *Biophys. J.*, **68**:2588–2600, 1995.
- [47] R. Y. Tsien and A. Waggoner. Fluorophores for confocal microscopy. In J. B. Pawley, editor, *Handbook of Biological Confocal Microscopy*, pages 267–279. Plenum Press, New York, USA, 2 edition, 1995.
- [48] S. Inoué. Foundations of confocal scanned imaging in light microscopy. In J. B. Pawley, editor, *Handbook of Biological Confocal Microscopy*, book chapter 1, pages 1–17. Plenum Press, New York, 2 edition, 1995.
- [49] P. Gribbon and T. E. Hardingham. Macromolecular diffusion of biological polymers measured by confocal fluorescence recovery after photobleaching. *Biophys. J.*, **75**:1032–1039, 1998.
- [50] D. E. Koppel. Fluorescence redistribution after photobleaching - new multipoint analysis of membrane translational dynamics. *Biophys. J.*, **28**:281–291, 1979.
- [51] A. E. Cowan, D. E. Koppel, B. Setlow, and P. Setlow. A soluble protein is immobile in dormant spores of *Bacillus subtilis* but is mobile in germinated spores: Implications for spore dormancy. *Proc. Natl. Acad. Sci. USA*, **100**:4209–4214, 2003.
- [52] H. P. Kao, J. R. Abney, and A. S. Verkman. Determinants of the translational mobility of a small solute in cell cytoplasm. *J. Cell Biol.*, **120**:175–184, 1993.
- [53] D. Stoll, M. F. Templin, M. Schrenk, P. C. Traub, C. F. Vohringer, and T. O. Joos. Protein microarray technology. *Front. Biosci.*, **7**:C13–C32, 2002.
- [54] D. J. Lockhart and E. A. Winzeler. Genomics, gene expression and DNA arrays. *Nature*, **405**:827–836, 2000.
- [55] E. B. Brown, E. S. Wu, W. Zipfel, and W. W. Webb. Measurement of molecular diffusion in solution by multiphoton fluorescence photobleaching recovery. *Biophys. J.*, **77**:2837–2849, 1999.

- [56] S. C. Case-Green, K. U. Mir, C. E. Pritchard, and E. M. Southern. Analysing genetic information with DNA arrays. *Curr. Opin. Chem. Biol.*, **2**:404–410, 1998.
- [57] A. Furka and W. D. Bennett. Combinatorial libraries by portioning and mixing. *Comb. Chem. High Throughput Screen.*, **2**:105–122, 1999.
- [58] J. Ellman, B. Stoddard, and J. Wells. Combinatorial thinking in chemistry and biology. *Proc. Natl. Acad. Sci. USA*, **94**:2779–2782, 1997.
- [59] J. F. Cargill and M. Lebl. New methods in combinatorial chemistry - robotics and parallel synthesis. *Curr. Opin. Chem. Biol.*, **1**:67–71, 1997.
- [60] D. Maclean, J. J. Baldwin, V. T. Ivanov, Y. Kato, A. Shaw, P. Schneider, and E. M. Gordon. Glossary of terms used in combinatorial chemistry - (technical report). *Pure Appl. Chem.*, **71**:2349–2365, 1999.
- [61] K. S. Lam, M. Lebl, and V. Krchnak. The "one-bead-one-compound" combinatorial library method. *Chem. Rev.*, **97**:411–448, 1997.
- [62] A. Furka, F. Sebestyén, M. Asgedom, and G. Dibo. General-method for rapid synthesis of multi-component peptide mixtures. *Int. J. Pept. Protein Res.*, **37**:487–493, 1991.
- [63] M. H. J. Ohlmeyer, R. N. Swanson, L. W. Dillard, J. C. Reader, G. Asouline, R. Kobayashi, M. Wigler, and W. C. Still. Complex synthetic chemical libraries indexed with molecular tags. *Proc. Natl. Acad. Sci. USA*, **90**:10922–10926, 1993.
- [64] Z. J. Ni, D. Maclean, C. P. Holmes, M. M. Murphy, B. Ruhland, J. W. Jacobs, E. M. Gordon, and M. A. Gallop. Versatile approach to encoding combinatorial organic syntheses using chemically robust secondary amine tags. *J. Med. Chem.*, **39**:1601–1608, 1996.
- [65] V. Nikolaiev, A. Stierandova, V. Krchnak, B. Seligmann, K. S. Lam, S. E. Salmon, and M. Lebl. Peptide-encoding for structure determination of nonsequenceable polymers within libraries synthesized and tested on solid-phase supports. *Pept. Res.*, **6**:161–170, 1993.
- [66] D. S. Tan and J. J. Burbaum. Ligand discovery using encoded combinatorial libraries. *Curr. Opin. Drug. Disc. Devel.*, **3**:439–453, 2000.
- [67] M. C. Needels, D. G. Jones, E. H. Tate, G. L. Heinkel, L. M. Kochersperger, W. J. Dower, R. W. Barrett, and M. A. Gallop. Generation and screening of an oligonucleotide-encoded synthetic peptide library. *Proc. Natl. Acad. Sci. USA*, **90**:10700–10704, 1993.
- [68] X. L. Liu, L. H. Takahashi, W. L. Fitch, G. Rozing, C. Bayle, and F. Couderc. Capillary electrochromatography-laser-induced fluorescence method for separation and detection of dansylated dialkylamine tags in encoded combinatorial libraries. *J. Chromatogr. A*, **924**:323–329, 2001.
- [69] W. L. Fitch, T. A. Baer, W. W. Chen, F. Holden, C. P. Holmes, D. Maclean, N. H. Shah, E. Sullivan, M. Tang, P. Waybourn, S. M. Fischer, C. A. Miller, and L. R. Snyder. Improved methods for encoding and decoding dialkylamine-encoded combinatorial libraries. *J. Comb. Chem.*, **1**:188–194, 1999.

- [70] A. W. Czarnik. Encoding methods for combinatorial chemistry. *Curr. Opin. Chem. Biol.*, **1**:60–66, 1997.
- [71] C. L. Brummel, I. N. W. Lee, Y. Zhou, S. J. Benkovic, and N. Winograd. A mass-spectrometric solution to the address problem of combinatorial libraries. *Science*, **264**:399–402, 1994.
- [72] R. A. Zambias, D. A. Boulton, and P. R. Griffin. Microchemical structural determination of a peptoid covalently bound to a polymeric bead by matrix-assisted laser-desorption ionization time-of-flight mass-spectrometry. *Tetrahedron Lett.*, **35**:4283–4286, 1994.
- [73] R. S. Youngquist, G. R. Fuentes, M. P. Lacey, and T. Keough. Generation and screening of combinatorial peptide libraries designed for rapid sequencing by mass-spectrometry. *J. Am. Chem. Soc.*, **117**:3900–3906, 1995.
- [74] C. L. Brummel, J. C. Vickerman, S. A. Carr, M. E. Hemling, G. D. Roberts, W. Johnson, J. Weinstein, D. Gaitanopoulos, S. J. Benkovic, and N. Winograd. Evaluation of mass spectrometric methods applicable to the direct analysis of non-peptide bead-bound combinatorial libraries. *Anal. Chem.*, **68**:237–242, 1996.
- [75] B. J. Egner, M. Cardno, and M. Bradley. Linkers for combinatorial chemistry and reaction analysis using solid-phase in-situ mass-spectrometry. *J. Chem. Soc. Chem. Commun.*, **21**:2163–2164, 1995.
- [76] B. J. Egner, G. J. Langley, and M. Bradley. Solid-phase chemistry - direct monitoring by matrix-assisted laser-desorption ionization time-of-flight mass-spectrometry - a tool for combinatorial chemistry. *J. Org. Chem.*, **60**:2652–2653, 1995.
- [77] H. M. Geysen, C. D. Wagner, W. M. Bodnar, C. J. Markworth, G. J. Parke, F. J. Schoenen, D. S. Wagner, and D. S. Kinder. Isotope or mass encoding of combinatorial libraries. *Chem. Biol.*, **3**:679–688, 1996.
- [78] M. S. Shchepinov, R. Chalk, and E. M. Southern. Trityl tags for encoding in combinatorial synthesis. *Tetrahedron*, **56**:2713–2724, 2000.
- [79] G. C. Look, C. P. Holmes, J. P. Chinn, and M. A. Gallop. Methods for combinatorial organic-synthesis - the use of fast C-13 NMR analysis for gel phase reaction monitoring. *J. Org. Chem.*, **59**:7588–7590, 1994.
- [80] J. E. Hochlowski, D. N. Whittern, and T. J. Sowin. Encoding of combinatorial chemistry libraries by fluorine-19 NMR. *J. Comb. Chem.*, **1**:291–293, 1999.
- [81] J. P. Neilly and J. E. Hochlowski. Elemental analysis of individual combinatorial chemistry library members by energy-dispersive X-ray spectroscopy. *Appl. Spectrosc.*, **53**:74–81, 1999.
- [82] S. S. Rahman, D. J. Busby, and D. C. Lee. Infrared and Raman spectra of a single resin bead for analysis of solid-phase reactions and use in encoding combinatorial libraries. *J. Org. Chem.*, **63**:6196–6199, 1998.



- [83] F. Sebestyén, G. Szendrei, M. Mak, M. Doda, E. Illyes, G. Szokan, K. Kindla, W. Rapp, P. Szego, E. Campian, and A. Furka. Coloured peptides: Synthesis, properties and use in preparation of peptide sub-library kits. *J. Pept. Sci.*, **4**:294–299, 1998.
- [84] B. J. Egner, S. Rana, H. Smith, N. Bouloc, J. G. Frey, W. S. Brocklesby, and M. Bradley. Tagging in combinatorial chemistry: The use of coloured and fluorescent beads. *Chem. Commun.*, **8**:735–736, 1997.
- [85] M. Trau and B. J. Battersby. Novel colloidal materials for high-throughput screening applications in drug discovery and genomics. *Adv. Mater.*, **13**:975–979, 2001.
- [86] B. J. Battersby, G. A. Lawrie, and M. Trau. Optical encoding of microbeads for gene screening: alternatives to microarrays. *Drug Discov. Today*, **6**:S19–S26, 2001.
- [87] B. J. Battersby, D. Bryant, W. Meutermans, D. Matthews, M. L. Smythe, and M. Trau. Toward larger chemical libraries: Encoding with fluorescent colloids in combinatorial chemistry. *J. Am. Chem. Soc.*, **122**:2138–2139, 2000.
- [88] L. Grondahl, B. J. Battersby, D. Bryant, and M. Trau. Encoding combinatorial libraries: A novel application of fluorescent silica colloids. *Langmuir*, **16**:9709–9715, 2000.
- [89] R. J. Fulton, R. L. McDade, P. L. Smith, L. J. Kienker, and J. R. Kettman. Advanced multiplexed analysis with the FlowMetrix(TM) system. *Clin. Chem.*, **43**:1749–1756, 1997.
- [90] J. R. Kettman, T. Davies, D. Chandler, K. G. Oliver, and R. J. Fulton. Classification and properties of 64 multiplexed microsphere sets. *Cytometry*, **33**:234–243, 1998.
- [91] U. Prabhakar, E. Eirikis, and H. M. Davis. Simultaneous quantification of proinflammatory cytokines in human plasma using the LabMAP (TM) assay. *J. Immunol. Methods*, **260**:207–218, 2002.
- [92] T. B. Martins. Development of internal controls for the Luminex instrument as part of a multiplex seven-analyte viral respiratory antibody profile. *Clin. Diagn. Lab. Immunol.*, **9**:41–45, 2002.
- [93] F. Ye, M. S. Li, J. D. Taylor, Q. Nguyen, H. M. Colton, W. M. Casey, M. Wagner, M. P. Weiner, and J. W. Chen. Fluorescent microsphere-based readout technology for multiplexed human single nucleotide polymorphism analysis and bacterial identification. *Hum. Mutat.*, **17**:305–316, 2001.
- [94] J. D. Taylor, D. Briley, Q. Nguyen, K. Long, M. A. Iannone, M. S. Li, F. Ye, A. Afshari, E. Lai, M. Wagner, J. Chen, and M. P. Weiner. Flow cytometric platform for high-throughput single nucleotide polymorphism analysis. *Biotechniques*, **30**:661–675, 2001.
- [95] L. Yang, D. K. Tran, and X Wang. BADGE, BeadsArray for the detection of gene expression, a high-throughput diagnostic bioassay. *Genome Res.*, **11**:1888–1898, 2001.
- [96] S. A. Dunbar and J. W. Jacobson. Application of the Luminex LabMAP in rapid screening for mutations in the cystic fibrosis transmembrane conductance regulator gene: A pilot study. *Clin. Chem.*, **46**:1498–1500, 2000.

- [97] D. A. A. Vignali. Multiplexed particle-based flow cytometric assays. *J. Immunol. Methods*, **243**:243–255, 2000.
- [98] R. T. Carson and D. A. A. Vignali. Simultaneous quantitation of 15 cytokines using a multiplexed flow cytometric assay. *J. Immunol. Methods*, **227**:41–52, 1999.
- [99] R. F. Gordon and R. L. McDade. Multiplexed quantification of human IgG, IgA, and IgM with the FlowMetrix(TM) system. *Clin. Chem.*, **43**:1799–1801, 1997.
- [100] C. R. WalkerPeach, P. L. Smith, D. B. DuBois, and R. J. Fulton. A novel rapid multiplexed assay for herpes simplex virus DNA using the FlowMetrix(TM) cytometric microsphere technology. *Clin. Chem.*, **43**:21, 1997.
- [101] P. L. Smith, C. R. WalkerPeach, R. J. Fulton, and D. B. DuBois. A rapid, sensitive, multiplexed assay for detection of viral nucleic acids using the FlowMetrix system. *Clin. Chem.*, **44**:2054–2056, 1998.
- [102] K. G. Oliver, J. R. Kettman, and R. J. Fulton. Multiplexed analysis of human cytokines by use of the FlowMetrix system. *Clin. Chem.*, **44**:2057–2060, 1998.
- [103] R. Bellisario, R. J. Colinas, and K. A. Pass. Simultaneous measurement of thyroxine and thyrotropin from newborn dried blood-spot specimens using a multiplexed fluorescent microsphere immunoassay. *Clin. Chem.*, **46**:1422–1424, 2000.
- [104] P. Pantano and D. R. Walt. Ordered nanowell arrays. *Chem. Mater.*, **8**:2832–2835, 1996.
- [105] D. R. Walt. Molecular biology - bead-based fiber-optic arrays. *Science*, **287**:451–452, 2000.
- [106] K. L. Michael, J. A. Ferguson, B. G. Healey, A. A. Panova, P. Pantano, and D. R. Walt. The use of optical-imaging fibers for the fabrication of array sensors. *Polymers In Sensors*, **690**:273–289, 1998.
- [107] K. L. Michael, L. C. Taylor, S. L. Schultz, and D. R. Walt. Randomly ordered addressable high-density optical sensor arrays. *Anal. Chem.*, **70**:1242–1248, 1998.
- [108] F. J. Steemers, J. A. Ferguson, and D. R. Walt. Screening unlabeled DNA targets with randomly ordered fiber-optic gene arrays. *Nat. Biotechnol.*, **18**:91–94, 2000.
- [109] J. A. Ferguson, F. J. Steemers, and D. R. Walt. High-density fiber-optic DNA random microsphere array. *Anal. Chem.*, **72**:5618–5624, 2000.
- [110] J. A. Ferguson, T. C. Boles, C. P. Adams, and D. R. Walt. A fiber-optic DNA biosensor microarray for the analysis of gene expression. *Nat. Biotechnol.*, **14**:1681–1684, 1996.
- [111] B. G. Healey, R. S. Matson, and D. R. Walt. Fiberoptic DNA sensor array capable of detecting point mutations. *Anal. Biochem.*, **251**:270–279, 1997.
- [112] F. Szurdoki, K. L. Michael, and D. R. Walt. A duplexed microsphere-based fluorescent immunoassay. *Anal. Biochem.*, **291**:219–228, 2001.

- [113] M. Bruchez, M. Moronne, P. Gin, S. Weiss, and A. P. Alivisatos. Semiconductor nanocrystals as fluorescent biological labels. *Science*, **281**:2013–2016, 1998.
- [114] M. Y. Han, X. H. Gao, J. Z. Su, and S. Nie. Quantum-dot-tagged microbeads for multiplexed optical coding of biomolecules. *Nat. Biotechnol.*, **19**:631–635, 2001.
- [115] A. P. Alivisatos. Less is more in medicine - sophisticated forms of nanotechnology will find some of their first real-world applications in biomedical research, disease diagnosis and, possibly, therapy. *Sci. Am.*, **285**:66–73, 2001.
- [116] J. F. Keij and J. A. Steinkamp. Flow cytometric characterization and classification of multiple dual-color fluorescent microspheres using fluorescence lifetime. *Cytometry*, **33**:318–323, 1998.
- [117] J. M. Kurner, I. Klimant, C. Krause, E. Pringsheim, and O. S. Wolfbeis. A new type of phosphorescent nanospheres for use in advanced time-resolved multiplexed bioassays. *Anal. Biochem.*, **297**:32–41, 2001.
- [118] E. J. Moran, S. Sarshar, J. F. Cargill, M. M. Shabaz, A. Lio, A. M. M. Mjalli, and R. W. Armstrong. Radio-frequency tag encoded combinatorial library method for the discovery of tripeptide-substituted cinnamic acid inhibitors of the protein-tyrosine-phosphatase PTP1B. *J. Am. Chem. Soc.*, **117**:10787–10788, 1995.
- [119] K. C. Nicolaou, X. Y. Xiao, Z. Parandoosh, A. Senyei, and M. P. Nova. Radiofrequency encoded combinatorial chemistry. *Angew. Chem. Int. Ed. Engl.*, **34**:2289–2291, 1995.
- [120] R. F. Service. Chemistry - radio tags speed compound synthesis. *Science*, **270**:577, 1995.
- [121] S. H. Shi, X. Y. Xiao, and A. W. Czarnik. A combinatorial synthesis of tyrphostins via the "Directed sorting" method. *Biotechnol. Bioeng.*, **61**:7–12, 1998.
- [122] X. Y. Xiao, R. S. Li, H. Zhuang, B. Ewing, K. Karunaratne, J. Lillig, R. Brown, and K. C. Nicolaou. Solid-phase combinatorial synthesis using MicroKan reactors, Rf tagging, and directed sorting. *Biotechnol. Bioeng.*, **71**:44–50, 2000.
- [123] K. Miller. Downsizing DNA assays. *Scientist*, **16**:52, 2002.
- [124] W. Mandrecki. Multiplex assay for nucleic acids employing transponders. US Patent 6051377, 2000.
- [125] R. A. Houghten. General-method for the rapid solid-phase synthesis of large numbers of peptides - specificity of antigen-antibody interaction at the level of individual amino-acids. *Proc. Natl. Acad. Sci. USA*, **82**:5131–5135, 1985.
- [126] C. Y. Xiao, C. F. Zhao, H. Potash, and M. P. Nova. Combinatorial chemistry with laser optical encoding. *Angew. Chem. Int. Ed. Engl.*, **36**:780–782, 1997.
- [127] A. Dames, J. England, and E. Colby. Bio-assay technique. WO Patent 00/16893, 2000.

- [128] H. H. Zhou, S. Roy, H. Schulman, and M. J. Natan. Solution and chips arrays in protein profiling. *Trends Biotechnol.*, **19**:S34–S39, 2001.
- [129] B. R. Martin, D. J. Dermody, B. D. Reiss, M. M. Fang, L. A. Lyon, M. J. Natan, and T. E. Mallouk. Orthogonal self-assembly on colloidal gold-platinum nanorods. *Adv. Mater.*, **11**:1021–1025, 1999.
- [130] B.R. Martin, L.J. Dietz, B.D. Reiss, M.J. Natan, J.L. Winkler, and T.E. Mallouk. Method of manufacture of colloidal rod particles as nanobar codes. WO Patent 01/25510, 2001.
- [131] S. R. Nicewarner-Pena, R. G. Freeman, B. D. Reiss, L. He, D. J. Pena, I. D. Walton, R. Cromer, C. D. Keating, and M. J. Natan. Submicrometer metallic barcodes. *Science*, **294**:137–141, 2001.
- [132] K. Braeckmans, S. C. De Smedt, C. Roelant, M. Leblans, R. Pauwels, and J. Demeester. Encoding microcarriers by spatial selective photobleaching. *Nat. Mater.*, **2**:169–173, 2003.
- [133] S.C. De Smedt, M. Leblans, K. Braeckmans, J. Demeester, E. Gustin, and C. Roelant. Method and device for the manipulation of microcarriers for an identification purpose. WO Patent 02/33419, 2002.
- [134] K. Braeckmans, S. C. De Smedt, M. Leblans, C. Roelant, R. Pauwels, and J. Demeester. Scanning the code. *Mod. Drug Disc.*, **6**:28–32, 2003.
- [135] T. M. McHugh, R. C. Miner, L. H. Logan, and D. P. Stites. Simultaneous detection of antibodies to cytomegalo-virus and herpes-simplex virus by using flow-cytometry and a microsphere-based fluorescence immunoassay. *J. Clin. Microbiol.*, **26**:1957–1961, 1988.
- [136] J. J. Scillian, T. M. McHugh, M. P. Busch, M. Tam, M. J. Fulwyler, D. Y. Chien, and G. N. Vyas. Early detection of antibodies against rDNA-produced HIV proteins with a flow cytometric assay. *Blood*, **73**:2041–2048, 1989.
- [137] M. Geysen. Encoding scheme for solid phase chemical libraries. WO Patent 00/61281, 2000.
- [138] M.S. Wang and L. Li. Rapid screening assay methods and devices. US Patent 5922617, 1999.
- [139] H. Fenniri, H. G. Hedderich, K. S. Haber, J. Achkar, B. Taylor, and D. Ben-Amotz. Towards the DRED of resin-supported combinatorial libraries: A non-invasive methodology based on bead self-encoding and multispectral imaging. *Angew. Chem. Int. Ed. Engl.*, **39**:4483–4485, 2000.
- [140] H. Fenniri, L. H. Ding, A. E. Ribbe, and Y. Zyrianov. Barcoded resins: A new concept for polymer-supported combinatorial library self-deconvolution. *J. Am. Chem. Soc.*, **123**:8151–8152, 2001.
- [141] I. Ravkin, S. Goldbard, W.C. Hyun, and M.A. Zarowitz. Combinatorial chemical library supports having indicia at coding positions and methods of use. WO Patent 00/63419, 2000.
- [142] M. B. Meza. Bead-based HTS applications in drug discovery. *Drug Discov. Today*, Suppl.:38–41, 2000.

- [143] K. Braeckmans, S. C. De Smedt, M. Leblans, R. Pauwels, and J. Demeester. Encoding microcarriers: Present and future technologies. *Nat. Rev. Drug Disc.*, **1**:447–456, 2002.
- [144] E. H. Keller. Objective lenses for confocal microscopy. In J. B. Pawley, editor, *Handbook of Biological Confocal Microscopy*, book chapter 7, pages 111–126. Plenum Press, New York, 2 edition, 1995.
- [145] S. W. Hell and E. H. K. Stelzer. Lens aberrations in confocal fluorescence microscopy. In J. B. Pawley, editor, *Handbook of Biological Confocal Microscopy*, book chapter 20, pages 347–354. Plenum Press, New York, 2 edition, 1995.
- [146] N. Wang, J. P. Butler, and D. E. Ingber. Mechanotransduction across the cell-surface and through the cytoskeleton. *Science*, **260**:1124–1127, 1993.
- [147] K. Shibata, S. Kobatake, and M. Irie. Extraordinarily low cycloreversion quantum yields of photochromic diarylethenes with methoxy substituents. *Chem. Lett.*, **7**:618–619, 2001.
- [148] T. Fukaminato, S. Kobatake, T. Kawai, and M. Irie. Three-dimensional erasable optical memory using a photochromic diarylethene single crystal as the recording medium. *P. Jpn. Acad. B-Phys.*, **77**:30–35, 2001.
- [149] C. J. de Grauw, P. L. T. M. Frederix, and H. C. Gerritsen. Aberrations and penetration in in-depth confocal and two-photon-excitation microscopy. In A. Diaspro, editor, *Confocal and Two-Photon Microscopy*, book chapter 7, pages 153–169. Wiley-Liss, Inc., New York, USA, 2002.
- [150] M. Born and E. Wolf. *Principles of Optics*. Cambridge University Press, Cambridge, UK, 7 (expanded) edition, 1999.
- [151] J. E. N. Jonkman and E. H. K. Stelzer. Resolution and contrast in confocal and two-photon microscopy. In A. Diaspro, editor, *Confocal and Two-Photon Microscopy*, book chapter 5, pages 101–125. Wiley-Liss, Inc., New York, USA, 2002.
- [152] K. D. Mielenz. On the diffraction limit for lensless imaging. *J. Res. Natl. Inst. Stand. Technol.*, **104**:479–485, 1999.
- [153] A. Yariv. *Quantum Electronics*. John Wiley & Sons, New York, USA, 3 edition, 1989.

# Summary

In part I of this thesis, the aim was to develop FRAP models for use with the latest generation of CSLMs which have the possibility of photobleaching arbitrary user-defined regions. To allow (potential) general and widespread use of the models, it was tried to find analytical solutions to the problem which can be easily programmed into a fitting routine.

As a first step, a general formulation was derived in Appendix A for the (first-order) photobleaching process in case of a scanning beam. This was done for the bleaching of a single line segment (see Eq. (A.2)) and an arbitrary 2-D geometry (see Eq. (A.4)). It was also found that the latter expression is valid only if the distance between two neighbouring scanning lines is smaller than half the resolution of the bleaching beam. Else, the generally valid, but mathematically more complicated Eq. (A.3) has to be used instead.

Based on these results, a FRAP model was presented in Chapter 1 based on the photobleaching by a CSLM of a uniform disk. Although the mathematical derivation of the disk model takes 3-D diffusion into account, it was shown that the equivalent 2-D expression Eq. (1.18) can be used in combination with low NA objective lenses. It was shown that the disk model is valid if its radius is at least 4 to 5 times the resolution of the bleaching beam (see Figs. 1.6B and 3.6). As the bleaching resolution of low NA lenses typically varies between 1 and 2  $\mu\text{m}$ , this means that rather large disks have to be photobleached of 10 to 20  $\mu\text{m}$  diameter. This is not a problem, however, for bulk samples such as solutions, gel systems, extra-cellular matrices etc. Moreover, bleaching of large uniform disks has the advantage of having an **excellent signal to noise ratio** (see Fig. 1.3). **The diffusion coefficient and mobile fraction can therefore be measured with excellent precision and reproducibility.**

In the evaluation of the disk model, indirect evidence was found that the effective

resolution of the bleaching beam is larger than expected from the characteristics of the objective lens (see Fig. 1.4A). It was decided to examine this unexpected observation further because it may have serious implications on many FRAP models which directly depend on the precise knowledge of the resolution. **In Chapter 2, a detailed study was carried out on the photobleaching of fluorescein and FITC-dextran for different bleaching powers. By performing photobleaching experiments on FITC-dextran immobilized in acrylamide gels, we have been able to show directly that the bleaching profile expands with increasing bleaching power because the higher order diffraction rings of the focused laser beam are taking part in the photobleaching process (see Fig. 2.4).** It was possible to explain this behaviour (see Fig. 2.8) by incorporating the detailed photochemical reactions that lead to the photobleaching of the fluorescein molecules (see Table 2.1 and Eq. (2.6)) into a computer simulation program (see Fig. 2.3). **The net result of this effect in relation to FRAP is that the bleaching profiles are larger than expected theoretically from the FRAP models, as if being bleached by an expanded bleaching intensity distribution (see Fig. 2.5).** It therefore follows that the bleaching intensity distribution cannot be considered to be invariant in combination with first order photobleaching kinetics, as has always been assumed in FRAP models so far. Although this effect is not always directly evident from the FRAP experiments, neglecting it may shift the calculated diffusion coefficient by as much as over one order of magnitude.

**To be able to do FRAP measurements on small samples, such as biological cells, a second FRAP model was presented in Chapter 3, which is based on the photobleaching of a single long line segment.** Being aware of the results from the previous chapter, an independent (Gaussian) bleaching and imaging resolution were taken into account. This allows for taking a possibly expanded bleaching resolution into account without affecting the imaging resolution. **The line model can therefore be used for two purposes. First, if the effective bleaching resolution is known, it can be used to measure the diffusion coefficient. It can be used the other way round as well: if the diffusion coefficient is known, it can be used to measure directly and quantitatively the apparent bleaching resolution for a particular fluorophore as a function the bleaching power.** We have carried out such experiments for two fluorophores which are commonly used for FRAP: R-phycoerythrin and FITC-dextran. For R-phycoerythrin it was found that the apparent expansion of the bleaching beam is small for bleaching powers below 1 mW (see Fig. 3.5A). For FITC-dextran, which do not photobleach as easily as R-phycoerythrin, it was found that the effective bleaching resolution has doubled at bleaching powers between 1 and 2 mW (see Fig. 3.5B). Knowing the effective

bleaching resolution for both fluorophores, the line model was found to be able to correctly measure diffusion coefficients and mobile fractions (see Figs. 3.7 and 3.8). In order to comply with the assumption of a cylindrical bleaching profile, it was also found that the confocal aperture should be small to obtain correct diffusion coefficients in 3-D samples (see Fig. 3.4). **Compared to the disk model from Chapter 1, the line model is much more prone to noise because the recovery signal is integrated over far less pixels. The accuracy on the measured parameters is consequently not as good as for the disk model.** In particular it was found that the standard deviation on the measurements of the diffusion coefficient was typically 20 to 25 % as compared to only about 5% for the disk model. **At the other hand, it has the advantage of a smaller bleaching region compared to the disk model allowing more localized measurements. A related advantage is that the line method is much faster than the disk model because the characteristic diffusion time is proportional to the square of the bleaching geometry's dimensions. Therefore, it will depend on the size of the sample and the diffusion speed which one of those two models will be best suited.**

In part II of this thesis, the aim was to develop a new technology for the encoding of microbeads based on 'spatial selective photobleaching'. In particular this should be done in consideration of the development of an apparatus for the encoding and decoding of the microspheres at high speed. Such encoded microbeads are used for 'bead-based' assays as explained in Chapter 4, where a review on competing technologies for the encoding of microcarriers was presented as well. A distinction was made between four main categories: spectrometric encoding, electronic encoding, graphical encoding and physical encoding. Spectrometric encoding technologies have generally the advantage of being fairly easy to decode but are limited in the number of unique codes and are rather difficult to manufacture. Electronic encoded microcarriers have the advantage of an unlimited amount of unique codes. They are, however, relatively expensive and large compared to the other encoded microcarriers. Physical encoding methods seem to be the least promising as they are difficult to manufacture. Physical encoding can rather be used in combination with one of the other methods as to increase the number of uniquely encoded microcarriers. The graphical encoding techniques are the most promising because they are fairly easy to make at a low cost and offer a virtually unlimited number of unique codes. Within this category, **our method of spatial selective photobleaching seems to be the most promising because it uses low-cost poly-**



mer microbeads which are common to screening applications, thus avoiding the need for developing new chemistries.

In Chapter 5, the new method of encoding microbeads by spatial selective photobleaching (see Fig. 5.1) was discussed in detail. It was shown that the number of unique codes is virtually unlimited because it is possible to combine spatial information with several ‘gray levels’ by photobleaching (see Fig. 5.3). In spite of its clear advantages toward bead-based assays, as mentioned above, it was realized there are a number of technical challenges that will have to be dealt with in the development of a fully automated high-throughput encoding and decoding apparatus. Because the encoding is done by a scanning beam, it takes a relatively long time to photobleach a 2-D geometry, such as barcodes. **Therefore, to speed up the writing process, the possibility of replacing the barcodes by so-called ‘dotcodes’ was demonstrated (see Fig. 5.4).** The main challenge, however, will be to obtain the same position and orientation of the microbeads at read-out time as when they were encoded in order for the pattern to be clearly visible. To this end, the possibility of using ferromagnetic microbeads was evaluated. **By adding a coating of ferromagnetic CrO<sub>2</sub> particles to the polystyrene microspheres (see Fig. 5.5), we have shown it is possible to magnetize the beads by a strong magnetic field and to orient them accurately in a weak external magnetic field (see Fig. 5.6).** If the beads are magnetized by a strong magnetic field at the time they are encoded, the same orientation can be retrieved at the time they are decoded by applying the same but attenuated magnetic field.

To aid in the optimisation of the encoding and decoding of the microspheres, the writing and reading processes were looked at from a theoretical point of view in Chapter 6. The results from Appendix A for the photobleaching of a 1-D or 2-D geometry by a scanning beam were applied to the photobleaching of an arbitrary barcode (see Eqs. (6.9) and (6.10)) or dotcode (see Eqs. (6.12) and (6.13)). Special attention was paid to the bleaching intensity distribution which plays the most important role in the photobleaching process. Two different formulations were suggested, the ‘modified Gaussian distribution’ and the ‘fundamental Gaussian-beam distribution’, which have been discussed in Appendix B. Despite the fact that the modified Gaussian distribution does not obey the physical law of conservation of energy, it was chosen as a possible description of the bleaching intensity distribution in analogy with previous work on FRAP in 3-D. The fundamental Gaussian-beam distribution, at the other hand does obey the law of conservation of energy since it is derived directly from the Maxwell equa-

tions. **A computer program was written based on the theory of this chapter to simulate the photobleaching and imaging of arbitrary bar- and dotcodes (see Figs. 6.2, 6.3 and 6.4).** Some thoughts were also presented on the design of 1-D codes where it was suggested to use length-encoding, intensity encoding or a combination of both.

**In Chapter 7, the aim was to find the optimal conditions for writing and reading of the codes and to evaluate the theory of the previous chapter by comparison with the experimental results.** First it was verified if first-order photobleaching is a valid assumption for the encoding of the microbeads. Next we have examined the illumination and detection intensity distribution of three lenses separately by imaging sub-resolution fluorescent nanospheres (see Figs. 7.2, 7.3 and 7.4). The radial and axial (Gaussian) resolution was measured directly from the images for different confocal aperture settings (see Fig. 7.5). It was not possible to determine unambiguously from these experiments whether the modified or fundamental Gaussian intensity distribution shows the best correspondence with the experimental illumination intensity distributions. For small confocal apertures it was found that the confocal imaging intensity distribution can be approximated by a simple Gaussian distribution in both radial and axial directions. Next, it was demonstrated by recording  $xz$ -images through the microbeads that spherical aberrations and a focal shift play a significant role (see Fig. 7.6). These effects are primarily caused by a mismatch of the refractive index of the objective lens immersion medium and the sample. Spherical aberrations become worse when going deeper into the sample and result primarily in a deteriorated resolution and a drop in observed fluorescence intensity. The focal shift has an important consequence toward the decoding of the microbeads: a certain displacement of the microbeads along the axial direction will cause an even larger displacement of the actual focal plane inside the microbeads. The magnitude of the focal shift for a particular objective lens can be measured directly from  $xz$ -images through the microbeads (see Table 7.1). To gain insight in the optimal configuration for encoding and decoding, different kinds of codes have been written inside microspheres with different objective lenses. All codes were imaged by each of the lenses to obtain all possible combinations (see Figs. 7.7, 7.8 and 7.12). **It was found that writing of the codes should best be done by an objective lens of intermediate NA for extended out-of-focus readability while retaining sufficient resolution for writing. Reading at the other hand should be done by a high NA lens (and small confocal aperture) for best resolution and contrast. In addition it is best that the focal shift is as small as possible for the reading lens, again to maximize the out-of-focus visibility.** Comparison of the experimental codes with simulated ones showed that the fundamental Gaussian illumination distribution should be used instead of the modified

Gaussian (see Figs. 7.10 and 7.11). **When using the fundamental Gaussian distribution, the simulation program gave results that are in very good agreement with the experimental codes. This was true not only for a code imaged in the focal plane, but also for out-of-focus observations if the focal shift is taken into account (see Figs. 7.9, 7.13 and 7.15). The simulation program can therefore be used as a convenient tool in finding the optimal optical configuration in combination with a particular encoding scheme.**

# Samenvatting

In Deel I van deze thesis was het doel FRAP modellen te ontwikkelen die toegepast kunnen worden op CSLM's van de laatste generatie die de mogelijkheid hebben om willekeurige patronen te bleken. Om een zo algemeen en eenvoudig mogelijk gebruik van deze modellen toe te laten, was bovendien vooropgesteld om een analytisch eindresultaat te vinden dat gemakkelijk in een fitting-routine kan verwerkt worden.

Daarom is allereerst een algemene wiskundige formulering opgesteld die het (eerste-orde) fotobleeringsproces beschrijft voor een scannende bleekstraal zoals dat het geval is voor een CSLM (zie Appendix A). Dit is zowel voor de bleking van een enkelvoudig lijnstuk gedaan (zie Vgl. (A.2)) als voor een willekeurig 2-D patroon (zie Vgl. (A.4)). In het bijzonder is daarbij vastgesteld dat deze laatste vergelijking, die een continue benadering is van het discontinue scanproces, slechts geldig is wanneer twee opeenvolgende scanlijnen op een afstand van minder dan de halve resolutie van de bleekstraal uiteen liggen. Anders dient de algemeen geldige, maar wiskundig gecompliceerdere uitdrukking (A.3) gebruikt te worden.

Vertrekkend van deze algemene formulering is vervolgens in Hoofdstuk 1 een FRAP model opgesteld dat gebaseerd is op het bleken van een uniforme schijf met een CSLM. Hoewel in de afleiding de drie ruimtelijke dimensies in rekening gebracht zijn, is aangetoond dat de equivalente 2-D uitdrukking Vgl. (1.18) kan gebruikt worden wanneer gewerkt wordt met objectieflenzen met een lage numerieke apertuur (NA). Experimenteel hebben we vastgesteld dat de straal van de gebleekte schijf 4 tot 5 keer groter dient te zijn dan de resolutie van de bleekstraal opdat een correcte diffusiecoëfficiënt gemeten zou worden (zie de Figures 1.6B and 3.6). Aangezien de resolutie van de bleekstraal voor lage NA lenzen typisch tussen de 1 en 2  $\mu\text{m}$  ligt, zullen met dit model relatief grote schijven dienen gebleekt te worden met een diameter tussen de 10 en 20  $\mu\text{m}$ . Dit is echter geen probleem voor het meten van diffusiecoëfficiënten in volumineuze stalen zoals oplossingen,

gel-systemen, extra-cellulaire matrices e.d. Bovendien heeft het bleken van dergelijke grote geometrieën het voordeel dat een **uitstekende signaal-ruis verhouding** bekomen wordt (zie Fig. 1.3). **De diffusiecoëfficiënt kan daarom met een grote precisie en een uitstekende reproduceerbaarheid gemeten worden.**

Bij de experimentele evaluatie van het schijfmodel was indirect vastgesteld dat de effectieve resolutie van de bleekstraal groter is dan men verwacht op basis van de lenseigenschappen (zie Fig. 1.4A). Dit fenomeen werd verder onderzocht omdat dit belangrijke consequenties kan hebben op de vele FRAP modellen die rechtstreeks steunen op een precieze kennis van de resolutie van de bleekstraal. In het bijzonder werd dit onderzocht voor fluoresceïne en FITC-dextranen bij verschillende bleekvermogens in Hoofdstuk 2. **Door fotoblekingstudies uit te voeren op FITC-dextranen die geïmmobiliseerd waren in acrylamide gels, hebben we rechtstreeks kunnen aantonen dat het bleekprofiel groter wordt met stijgende bleekvermogens omdat de hogere orde diffractieringen van de gefocuseerde bleekstraal deel gaan nemen in het bleekproces (zie Fig. 2.4).** We hebben dit fenomeen theoretisch kunnen verklaren (zie Fig. 2.8) door alle deelreacties in beschouwing te nemen die een rol spelen in het fotochemisch bleekproces van fluoresceïne (zie Tabel 2.1 en Vgl. (2.6)). **Het uiteindelijke effect naar FRAP toe is dat de bleekstraal een groter bleekprofiel teweegbrengt dan theoretisch verwacht volgens de FRAP modellen. Of anders gezegd, de bleking wordt *schijnbaar* veroorzaakt door een bleekstraal met een geëxpandeerde intensiteitsdistributie (zie Fig. 2.5).** Daaruit volgt dat de intensiteitsdistributie van de bleekstraal niet langer als invariant kan beschouwd worden in combinatie met de eenvoudige eerste-orde fotoblekingskinetiek waarvan steeds uitgegaan wordt in de FRAP modellen. Hoewel de aanwezigheid van dit fenomeen in praktijk niet steeds op evidente wijze merkbaar is, kan het leiden tot een afwijking van de gemeten diffusiecoëfficiënt met een factor 10.

**Om FRAP metingen op kleine objecten zoals cellen mogelijk te maken, hebben we in Hoofdstuk 3 een ander FRAP model voorgesteld voor gebruik met de CSLM, gebaseerd op het bleken van een lang lijnsegment.** Bewust zijnde van de resultaten van het vorige hoofdstuk, hebben we in dit model een onafhankelijke bleek- en detectieresolutie in rekening gebracht. Dit laat toe om een mogelijk geëxpandeerde intensiteitsdistributie van de bleekstraal in rekening te brengen zonder daarbij de detectieresolutie te beïnvloeden. **Dit lijnmodel kan daarom voor twee doeleinden aangewend worden. Enerzijds, indien de effectieve (geëxpandeerde) bleekresolutie gekend is, kan uit de FRAP metingen de diffusiecoëfficiënt bepaald worden.**

Anderzijds, indien de diffusiecoëfficiënt gekend is, kan het lijnmodel gebruikt worden om de expansie van de bleekstraal rechtstreeks quantitatief te meten voor een welbepaald fluorofoor in functie van het bleekvermogen. Dergelijke experimenten hebben we uitgevoerd op twee types fluoroforen: R-phycoërythrine en FITC-dextranen. Voor R-phycoërythrine hebben we gevonden dat de schijnbare expansie van de bleekstraal klein is voor bleekvermogens beneden 1 mW (zie Fig. 3.5A). Voor het FITC-dextraan kwamen we tot de vaststelling dat dit moeilijker bleekt dan R-phycoërythrine. Daarom waren bleekvermogens nodig van minstens 1 tot 2 mW met als resultaat dat de schijnbare bleekresolutie verdubbeld was (zie Fig. 3.5B). Met een gekende effectieve bleekresolutie voor beide fluoroforen, hebben we kunnen aantonen dat het lijnmodel inderdaad in staat is om correcte absolute diffusiecoëfficiënten en mobiele fracties te meten (zie Figuren 3.7 en 3.8). Voorts hebben we vastgesteld dat de confocale irisopening klein dient te zijn voor FRAP metingen in 3-D stalen om in overeenstemming te zijn met de theoretische veronderstelling dat de lijn gebleekt is door een cilindrische bleekstraal. **In vergelijking met het FRAP model uit hoofdstuk 1, zijn de FRAP experimenten met het lijnmodel meer onderhevig aan ruis. De meetwaarden zijn dan ook minder nauwkeurig als met het schijfmodel.** Dit komt omdat het fluorescentiesignaal gemeten wordt over heel wat minder beeldpixels in vergelijking met het schijfmodel. Concreet is vastgesteld dat de standaarddeviatie op de diffusiecoëfficiënt typisch 20 tot 25% bedraagt met het lijnmodel, terwijl dit slechts ongeveer 5% is voor het schijfmodel. **Anderzijds heeft het lijnmodel het voordeel dat het kan toegepast worden op kleinere objecten wegens een kleinere bleekgeometrie. Daarmee gaat ook samen dat de metingen met het lijnmodel veel sneller zijn aangezien de diffusietijd evenredig is met het kwadraat van de grootte van de bleekgeometrie. Daarom zal het voornamelijk afhangen van de grootte van het sample en de diffusiesnelheid welk van beide modellen het meest aangewezen is.**

In deel II van deze thesis was het doel vooropgesteld om een nieuwe techniek voor het coderen van microsferen, eveneens gebaseerd op fotobleking, verder uit te werken. Specifiek diende dit te gebeuren met het oog op de uiteindelijke ontwikkeling van een apparaat waarmee automatisch en aan hoge snelheid microsferen gecodeerd en gedecodeerd kunnen worden. Zulke gecodeerde microsferen zijn van belang voor zogenaamde ‘bead-based’ assays, zoals besproken in Hoofdstuk 4. Bij het in beschouwing nemen van alle bestaande technologieën voor het coderen van microdragers, hebben we een onderscheid kunnen maken tussen vier

hoofdcategorieën: spectrometrische, elektronische, grafische en fysische codeermethodes. Spectrometrisch gecodeerde microsferen hebben in het algemeen het voordeel dat ze relatief gemakkelijk uitgelezen kunnen worden, maar ze zijn eerder beperkt in het aantal unieke codes. Elektronisch gecodeerde microdragers hebben het voordeel van een quasi onbeperkt aantal unieke codes, maar zijn dan weer relatief duur en groot in vergelijking met de andere soorten. De fysische codeermethodes schijnen de minst realistische te zijn aangezien ze moeilijk praktisch te verwezenlijken zijn. Eerder kunnen ze gebruikt worden in combinatie met één van de andere methodes om het aantal uniek gecodeerde microdragers nog te vergroten. De grafisch gecodeerde microdragers blijken het meeste potentieel te hebben omdat ze relatief gemakkelijk in grote aantallen gefabriceerd kunnen worden tegen een lage kostprijs. Bovendien bieden ze een quasi onbeperkt aantal unieke codes. **Binnen deze categorie blijkt onze nieuwe methode van ‘spatiaal selectieve fotobleking’ het meeste voordelen te bieden naar bead-based assays toe ondermeer omdat gebruik gemaakt wordt van goedkope polymeer-microsferen. Polymeermaterialen worden immers sinds lang frequent gebruikt in screening toepassingen en zodoende is de vaste-fase chemie voor het binden van moleculen op een polymeeroppervlak reeds goed gekend.**

In Hoofdstuk 5 zijn de verschillende aspecten verbonden aan de nieuwe methode voor het coderen van microsferen d.m.v. fotobleking meer in detail voorgesteld. We hebben aangetoond dat het aantal unieke codes daadwerkelijk zo goed als onbeperkt is wegens de mogelijkheid om spatiale codering met intensiteitscodering te combineren (zie Fig. 5.3). Ondanks de duidelijke voordelen van dit type microsferen naar bead-based assays toe, hebben we tevens onderkend dat er een aantal technologische uitdagingen zijn die overwonnen dienen te worden om tot een geautomatiseerd codeer/decodeer apparaat te komen. Aangezien de codering door middel van een scannende beweging van de bleekstraal gebeurt, duurt het voor deze toepassing te lang om een 2-D geometrie zoals een barcode te schrijven. **Daarom hebben we de mogelijkheid aangetoond om te werken met ‘puntcodes’ (zie Fig. 5.4) die geschreven kunnen worden door een enkelvoudige scanbeweging.** De grootste uitdaging is echter de oriëntatie en positionering van de microsferen. Om een correcte uitlezing van de code te verzekeren dienen de microsferen bij het uitlezen dezelfde positie en oriëntatie te hebben als bij het coderen. Om dit mogelijk te maken hebben we het gebruik van ferromagnetische microsferen voorgesteld. **We hebben aangetoond dat polystyreen microsferen waarop een laag ferromagnetische CrO<sub>2</sub> partikels aangebracht is (zie Fig. 5.5), magnetiseerbaar zijn in een sterk magnetisch veld en precies oriënteerbaar zijn met een zwak magnetisch veld zonder hun magnetisatie te verliezen (zie Fig.**

**5.6).** Indien dergelijke microsferen gemagnetiseerd worden bij de codeerstap, dan zal bij het uitlezen dezelfde oriëntatie terug verkregen kunnen worden door eenzelfde zwakker magnetisch veld aan te leggen.

Om een goede optimalisatie van het coderen en decoderen van de microsferen mogelijk te maken, zijn het schrijf- en leesproces bekeken vanuit een theoretisch standpunt in Hoofdstuk 6. Eerst zijn de algemene resultaten van Appendix A voor het bleken van een 1-D of 2-D geometrie d.m.v. een scannende bleekstraal toegepast op het fotobleken van een willekeurige barcode (zie Vgl. (6.9) en (6.10)) of puntcode (zie Vgl. (6.12) en (6.13)). Er is daarbij in het bijzonder aandacht besteed aan de intensiteitsdistributie van de bleekstraal die een primaire rol speelt in het codeerproces. Twee verschillende formuleringen zijn beschouwd geweest, de zogenaamde ‘gemodificeerde Gauss distributie’ en de ‘fundamentele Gauss distributie’. Beiden zijn apart besproken in Appendix B. Hoewel de gemodificeerde Gauss distributie niet voldoet aan de wet van behoud van energie, was ze toch gekozen als een mogelijke beschrijving van de bleekintensiteitsdistributie in analogie met vroeger FRAP werk in 3-D door anderen. De fundamentele Gauss distributie, anderzijds, voldoet wel aan de wet van behoud van energie aangezien ze rechtstreeks van de wetten van Maxwell afgeleid is. **De theorie van dit hoofdstuk is verwerkt in een computerprogramma om het schrijven en uitlezen van de codes te simuleren (zie Figuren 6.2, 6.3 en 6.4).** Tot slot van dit hoofdstuk hebben we ook enkele beschouwingen gemaakt over welke codes kunnen gebruikt worden: lengtecodering, intensiteitscodering of een combinatie van beide.

Het doel in Hoofdstuk 7, tenslotte, was om daadwerkelijk experimenteel inzicht te krijgen in de optimale condities voor het schrijven en uitlezen van de codes. Bovendien konden de experimenten gebruikt worden om de theorie van het vorige hoofdstuk te valideren. Daartoe is eerst experimenteel geverifieerd of het bleekproces in de microsferen inderdaad kan benaderd worden door een eerste-orde proces. Vervolgens hebben we de belichtings- en detectie-intensiteitsdistributie nader bekeken van drie verschillende lenzen m.b.v. sub-resolutie fluorescente nanosferen (zie Figuren 7.2, 7.3 en 7.4). Uit deze beelden werd de (Gaussiaanse) resolutie bepaald voor verschillende instellingen van de confocale iris. Met deze experimenten bleek het echter niet mogelijk te zijn om eenduidig uit te maken of de gemodificeerde of fundamentele Gauss distributie de beste overeenkomst vertoont met de experimentele belichtingsdistributies. Wel vonden we bevestiging dat de detectiedistributie goed benaderd kan worden door een ‘gewone’ Gauss distributie bij een kleine confocale iris. Vervolgens hebben we de aanwezigheid van sferische aberraties en een focale shift in de microsferen aangetoond d.m.v.  $xz$ -opnames



doorheen de microsferen (zie Fig. 7.6). Beide effecten worden in eerste instantie veroorzaakt door het verschil in brekingsindex tussen het immersiemedium van de objectieflens en het microsfeer-materiaal (polystyreen). De sferische aberraties worden erger naarmate dieper in de microsferen gefocuseerd wordt met een daling in resolutie en waargenomen intensiteit tot gevolg. De focale shift heeft een belangrijke consequentie naar de uitleesstap toe: een zekere verplaatsing van de microsfeer in de  $z$ -richting veroorzaakt een nog grotere verplaatsing van het werkelijk focaal vlak in de microsfeer. De grootte van de focale shift kon rechtstreeks bepaald worden uit de  $xz$ -beelden voor elk van de lenzen (zie Tabel 7.1). Vervolgens werden verschillende types codes geschreven in microsferen. De codes werden geschreven met elk van de drie objectieflenzen en vervolgens ook bekeken met elk van deze lenzen (see Figs. 7.7, 7.8 and 7.12). Zo hebben we vastgesteld dat het schrijven van de codes best gebeurt met een objectieflens met middelmatige NA om een redelijke ‘uit-focus’ zichtbaarheid van de codes te verzekeren terwijl toch voldoende resolutie overgehouden wordt voor het coderen zelf. Uitlezen van de codes gebeurt echter beter met een hoge NA lens (en een kleine confocale iris) om een optimale resolutie en contrast te bekomen. Bovendien wordt de focale shift best zo klein mogelijk gehouden, opnieuw om een zo groot mogelijke uit-focus zichtbaarheid te bekomen. Vergelijk van de experimentele codes met gesimuleerde heeft overduidelijk getoond dat de gemodificeerde Gauss distributie niet geldig is om het bleekproces te beschrijven. **Met de fundamentele Gauss verdeling werd daarentegen wel een goede overeenkomst gevonden (zie Figuren 7.10 en 7.11). Dit was niet alleen zo wanneer de codes ‘in focus’ bekeken werden, maar ook voor uit-focus observaties indien de focale shift in rekening gebracht werd (zie Figuren 7.9, 7.13 en 7.15). Het simulatieprogramma kan daarom gebruikt worden als een zeer handig hulpmiddel bij het optimaliseren van de optische opstelling voor een welbepaalde code.**

## Curriculum Vitae

### Personalialia

Naam: Kevin Braeckmans  
Geboren te: Mechelen op 12 februari 1976  
Nationaliteit: Belg  
Burgerlijke staat: gehuwd  
Kinderen: Sebastiaan & Elewout  
Adres: Vondelstraat 9, 9160 Lokeren  
Tel: 09/252.15.41  
E-mail: Kevin.Braeckmans@UGent.be

### Studies

#### Middelbaar onderwijs

**1994:** diploma van het secundair onderwijs, behaald aan het Sint-Lodewijkcollege te Lokeren

#### Universitaire opleidingen

**1997:** de academische graad van Kandidaat in de Natuurkunde, behaald met onderscheiding aan de Universiteit Gent

**1999:** de academische graad van Licentiaat in de Natuurkunde, behaald met grote onderscheiding aan de Universiteit Gent

#### Wetenschappelijke loopbaan

**Van 1 augustus 1999 tot 31 juli 2003:** doctoraatsbursaal van het Labo Algemene Biochemie en Fysische Farmacie, Universiteit Gent.

**Van 1 augustus 2003 tot op heden:** wetenschappelijk medewerker van het Labo Algemene Biochemie en Fysische Farmacie, Universiteit Gent.

## List of publications

### International journals with referee system

Braeckmans K., Peeters L., Sanders N.N., De Smedt S.C., and Demeester J. Three-dimensional fluorescence recovery after photobleaching with the confocal scanning laser microscope. *Biophysical Journal* **85**:2240-2252 (2003).

Braeckmans K., De Smedt S.C., Roelant C., Leblans M., Pauwels R., and Demeester J. Encoding microcarriers by spatial selective photobleaching. *Nature Materials* **2**:169-173 (2003).

Braeckmans K., De Smedt S.C., Leblans M., Pauwels R., and Demeester J. Encoding microcarriers: Present and future technologies. *Nature Reviews Drug Discovery* **1**:447-456 (2002).

Stubbe B.G., Braeckmans K., Horkay F., Hennink W.E., De Smedt S.C., and Demeester J. Swelling pressure observations on degrading dex-HEMA hydrogels. *Macromolecules* **35**:2501-2505 (2002).

Lucas B., Remaut K., Braeckmans K., Haustraete J., De Smedt S.C. and Demeester J. Studying pegylated DNA-complexes by dual color fluorescence fluctuation spectroscopy. *Macromolecules*, accepted.

### International journals without referee system

Braeckmans K., De Smedt S.C., Roelant C., Leblans M., Pauwels R., and Demeester J. Scanning the code. *Modern Drug Discovery* **6**:28-32 (2003).

### Abstracts of meetings

Braeckmans K., and De Smedt S.C. New generation of encoded microcarriers. *Biochemistry* **42**:209 (2003).

Braeckmans K., De Smedt S.C., Demeester J., Leblans M., Roelant C., Gustin E. New generation of encoded microcarriers. *Abstr. Pap. Am. Chem. S.* **226**:209-BIOL Part 1 (2003).

## **Patents**

Braeckmans K., De Smedt S.C., Roelant C., Gustin E., Leblans M., and Demeester J.  
Method and device for the manipulation of microcarriers for an identification purpose.  
WO0233419 (2002).